Theses and Dissertations

Fall 2015

Simulating the hydrologic impact of distributed flood mitigation practices, tile drainage, and terraces in an agricultural catchment

Nicholas Wayne Thomas
University of Iowa

Recommended Citation

SIMULATING THE HYDROLOGIC IMPACT OF DISTRIBUTED FLOOD

MITIGATION PRACTICES, TILE DRAINAGE, AND TERRACES IN AN

AGRICULTURAL CATCHMENT

by

Nicholas W. Thomas

A thesis submitted in partial fulfillment
of the requirements for the Doctor of Philosophy
degree in Civil and Environmental Engineering
in the Graduate College of
The University of Iowa

December 2015

Thesis Supervisors: Professor Larry J. Weber
                     Adjunct Assistant Professor Keith E. Schilling

Graduate College
The University of Iowa
Iowa City, Iowa

CERTIFICATE OF APPROVAL

_____

PH.D. THESIS

_____

This is to certify that the Ph.D. thesis of

Nicholas W. Thomas

has been approved by the Examining Committee
for the thesis requirement for the Doctor of Philosophy degree
in Civil and Environmental Engineering at the December 2015 graduation.

Thesis Committee: _____
                   Larry J. Weber, Thesis Supervisor

                  _____
                   Keith E. Schilling, Thesis Supervisor

                  _____
                   A. Allen Bradley

                  _____
                   Witold F. Krajewski

                  _____
                   Matthew J. Helmers

academic achievements. If not for her support, calming presence, and needed distractions, the product of this research and the direction of my life would forever be diminished.

ABSTRACT

In 2008 flooding occurred over a majority of Iowa, damaging homes, displacing residents, and taking lives. In the wake of this event, the Iowa Flood Center (IFC) was charged with the investigation of distributed flood mitigation strategies to reduce the frequency and magnitude of peak flows in Iowa. This dissertation is part of the several studies developed by the IFC and focused on the application of a coupled physics based modeling platform, to quantify the coupled benefits of distributed flood mitigation strategies on the reduction of peak flows in an agricultural watershed.

Additional investigation into tile drainage and terraces, illustrated the hydrologic impact of each commonly applied agricultural practice. The effect of each practice was represented in numerical simulations through a parameter adjustment. Systems were analyzed at the field scale, to estimate representative parameters, and applied at the watershed scale.

The impact of distributed flood mitigation wetlands reduced peak flows by 4 % to 17 % at the outlet of a 45 km^2 watershed. Variability in reduction was a product of antecedent soil moisture, 24-hour design storm total depth, and initial structural storage capacity. The highest peak flow reductions occurred in scenarios with dry soil, empty project storage, and low rainfall depths. Peak flow reductions were estimated to dissipate beyond a total drainage area of 200 km^2, approximately 2 km downstream of the small watershed outlet.

A numerical tracer analysis identified the contribution of tile drainage to stream flow (Q_T/Q) which varied between 6 % and 71 % through an annual cycle. Q_T/Q responded directly to meteorological forcing. Precipitation driven events produced a strong positive logarithmic correlation between Q_T/Q and drainage area. The addition of precipitation into the system saturated near surface soils, increased lateral soil water

movement, and reduced the contribution of instream tile flow. A negative logarithmic trend in Q_T/Q to drainage area persisted in non-event durations.

Simulated gradient terraces reduced and delayed peak flows in subcatchments of less than 3 km^2 of drainage area. The Hydrographs were shifted responding to rainfall later than non-terraced scenarios, while retaining the total volumetric outflow over longer time periods. The effects of dense terrace systems quickly dissipated, and found to be inconsequential at a drainage area of 45 km^2.

Beyond the analysis of individual agricultural features, this work assembled a framework to analyze the feature at the field scale for implementation at the watershed scale. It showed large scale simulations reproduce field scale results well. The product of this work was, a systematic hydrologic characterization of distributed flood mitigation structures, pattern tile drainage, and terrace systems facilitating the simulation of each practices in a physically-based coupled surface-subsurface model.

PUBLIC ABSTRACT

In 2008 flooding occurred over a majority of Iowa, damaging homes, displacing residents, and taking lives. In the wake of this event, the Iowa Flood Center was charged with the investigation of distributed flood mitigation strategies to reduce the frequency and magnitude of floods in Iowa. This work focused on the application of a numerical model to quantify the flood reductions induced by flood mitigation strategies in an agricultural watershed. Floods were estimated to be reduced in magnitude by 4 % to 17 % at the outlet of a 45 km^2 watershed. Variability in reduction was a product of soil wetness and rainfall. The highest reductions occurred in scenarios with dry soil and light rainfall. The influence of flood mitigation strategies were estimated to no longer impact stream flow at 2 km downstream of the watershed outlet.

Additional investigation into commonly applied agricultural practices led to a new method to incorporate fine scale features into coarse models. Through this approach terraces were found to delay and reduce the peak flows from the watershed at small drainage areas. Over large catchment areas the impacts of terraces were unnoticeable. Agricultural tile drainage is typically applied to reduce excess near surface water, and was found to significantly impact surface water flow. The quantity of rainfall and evapotranspiration altered the influence of tile drains over varying drainage areas. This research led to a number of unique outcomes related to large flood reductions which are applicable to agricultural catchments common in Iowa.

TABLE OF CONTENTS

LIST OF TABLES

LIST OF FIGURES

1.0 INTRODUCTION

Significant flood and drought events in the Central U.S. have led to the loss of lives, displaced residents, and billions in economic damages to agricultural communities and private property (NCDC 2014; US-EPA 2012; Villarini et al. 2013). The impact of these extreme events is further complicated by the increased frequency and magnitude of floods (Peterson et al. 2013), interrupted by prolonged periods of drought (Grigg 2014). This region is particularly vulnerable to extreme events due to the increase in cultivated lands causing amplification of flood and drought conditions (Villarini and Strong 2014; Woodhouse and Overpeck 1998).

In 2008 flooding occurred over a majority of Iowa, USA, damaging homes, displacing residents, and taking lives. This event was described by Governor Culver as "the worst disaster in the state's history," after declaring 85 of the 99 counties federal disaster areas. Whether this event and many like it were the effect of climatic change specifically in extreme events or anthropogenic changes in the landscape is an increasingly sought after research question. Regardless of the diver, Iowa in recent years is experiencing increasingly variable flows, and a trend of increasing mean daily discharge (Steffens and Franz 2012). Since 2008 Iowa has experienced varying degrees of flooding in 2009, 2010, 2011, and 2013, while 2012 was reported as one of the driest years on record.

1.1 Iowa Watershed Projects (IWP)

In 2010, Iowa received $8.8 million (US) from the U.S. Department of Housing and Urban Development (HUD) to assist with ongoing disaster recovery programs following the devastating floods of 2008. The Iowa Flood Center (IFC), a unit of the University of Iowa's IIHR–Hydroscience & Engineering, led the effort to evaluate methods to increase soil water holding capacity, reduce soil erosion, and manage upland runoff under saturated soil moisture conditions. The IWP's goal was to alter the

hydrologic system in Iowa's watersheds enabling them to better alleviate flood risk. The project was completed in two phases, which split the modeling effort into two scales. In Phase I, large-scale hydrologic simulations were developed for five Iowa watersheds (1,400 km^2 to 4,400 km^2) representing Iowa's variability in topography, soils, and land use (Fig. 1.1). The simulations assessed the current drainage infrastructure in chosen basin scale watersheds. Phase I modeled stream flows from historically and statistically significant rainfall events. The primary purpose of large scale hydrologic modeling was to identify locations of high runoff potential, where mitigation efforts may provide the greatest benefits.

Smaller catchments within the Phase I watersheds were identified for construction of flood mitigation projects. Within the subcatchments, specific flood prevention strategies were chosen based on a further hydrologic understanding of catchment specific characteristics. In Phase II, researchers evaluated the flood mitigation performance of potential projects, through monitoring and detailed modeling. Small-scale hydrologic simulations (40 km^2 to 100 km^2), including a more detailed representation of physical processes, were developed for areas selected for pilot project implementation. Construction projects took place at the small scale catchments with the intent to impact the peak discharge through the larger watershed. Approximately $5.1 million of the original HUD allocations was directed to construction of distributed flood reduction activities. Project locations and specific flood reduction strategies were identified through private landowner engagement and a nested hydrologic modeling approach. The watershed projects were monitored prior to, during, and post project construction. The distributed projects were evaluated after project completion to show their impact and effectiveness within the watershed, and estimate the implications at a larger scale.

This research was funded by the Iowa Watershed Project, as part of the detailed modeling and evaluation preformed in Phase II. The remainder of this study focused on the hydrologic modeling advancements in the Beaver Creek watershed (Fig. 1.1).
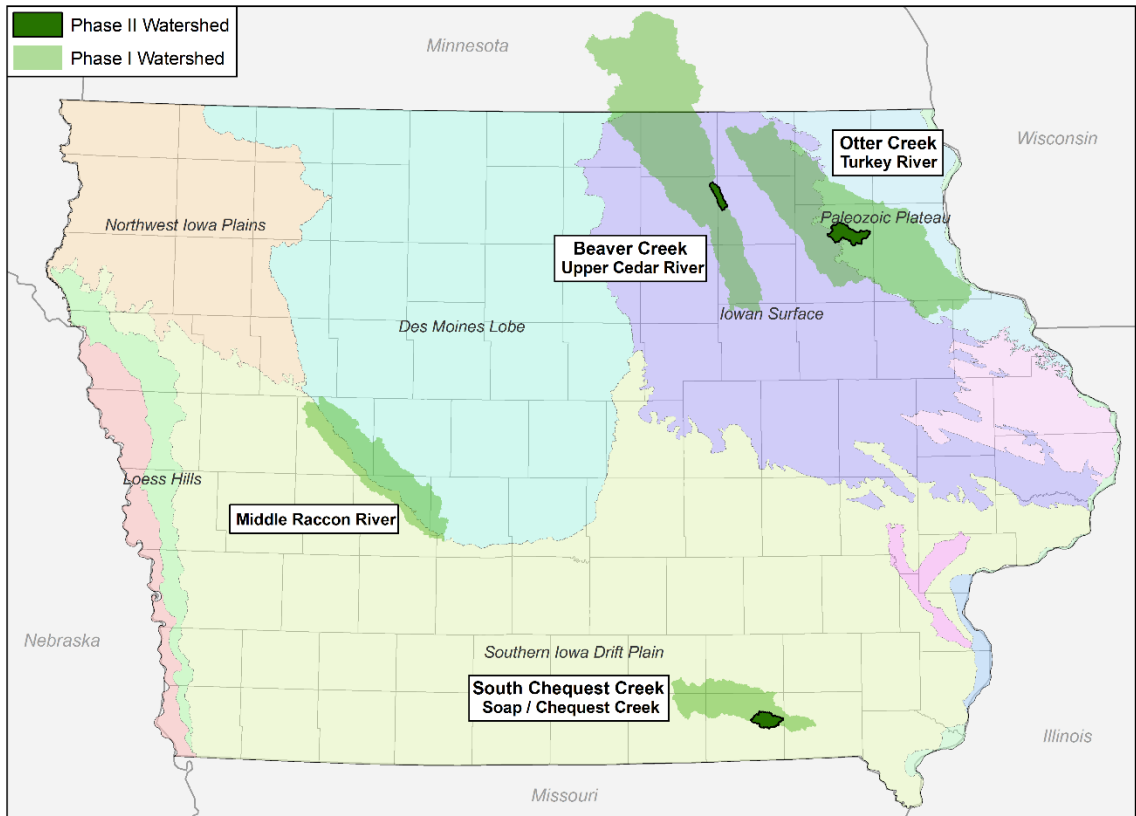
Figure 1.1 Iowa Watersheds Project, Phase I and Phase II selected watersheds.

1.2 Objectives

Goal: Quantify the coupled benefits of distributed flood mitigation strategies on the reduction of peak flows in an agricultural watershed. To achieve the goal stated above, a number of objectives need to be met:

Objective 1: Develop a physically based surface-subsurface hydrologic model of the Beaver Creek Watershed (BCW) to determine the benefits of flood mitigation strategies. The model should incorporate appropriate spatial resolution of surface and subsurface properties, providing a viable numerical experimentation tool.

Objective 2: Analyze the spatiotemporal impact of flood mitigation strategies. Investigate the variability of project based peak discharge reductions influenced by antecedent soil moisture, rainfall intensity, and relative structural storage.

Objective 3: Investigate surface and subsurface features unique to agricultural watershed hydrology (terraces, and pattern tile drainage). Develop and test approaches to produce an equivalent hydrologic response at the watershed scale from field scale experimentation.

This section provided context for further investigation of distributed flood mitigation strategies. A coupled surface-subsurface model, HydroGeoSphere (HGS), was chosen as the numerical platform for hydrologic investigation, Section 2 provided a literature review of coupled surface-subsurface modeling. Section 3 discussed the mathematical model HGS, and the relevant features applied to this research. Section 4 described the Beaver Creek watershed study location. Construction of the surface-subsurface model of BCW was provided in Section 5. Section 6 discussed model initialization and integrated watershed validation. The following Sections 7 to 9 described the major contributions to the scientific community, each containing a literature review, and discussion of results specific the respective topic. Section 6 incorporated the planned flood mitigation projects into the numerical model and described project impacts under varied initial conditions and rainfall events at multiple scales. Section 8 and Section 9 investigated equivalent approaches to incorporate tile drainage networks, and terraces at the watershed scale. Section 10 described a future effort to calibrate and validate watershed scale models through numerical column experiments. Section 11 summarized and concluded this research, and pointed towards future areas of study.

2.0 SCIENTIFIC REVIEW OF COUPLED HYDROLOGIC MODELING

Detailed hydrologic modeling offers a quantitative insight into transient flow processes at various scales. Many approaches have been applied to compute watershed hydrology, in this study a physics-based hydrologic model was chosen for investigative purposes. This modeling approach, which rigorously accounts for all of the relevant flow processes, enables the direct investigation of surface and subsurface flow variables.

Hydrologic computation has significantly evolved over the past several decades. Spatially averaged, conceptual process driven models have been supplanted in recent years by a physics based distributed description of watershed hydrology (Singh and Woolhiser 2002). Physics based modeling platforms in the template of Freeze and Harlan (1969), are becoming increasingly common due to advancements in computational efficiency and data acquisition. Distributed physically based models aim to rigorously account for all of the interactions within the water cycle by applying the fundamental formulation of each hydrologic process (Kollet et al. 2010). These models are recognized as complex to set up, requiring large amounts of time and data to initialize, and significant computational time to solve.

New modeling capabilities allow for investigation of fluid flow in a coupled 2-D surface, 3-D variably saturated subsurface environment. Evapotranspiration can be added for a comprehensive analysis of the hydrologic cycle. These models readily simulate fractures, channels, and wells (Panday and Huyakorn 2004; Therrien and Sudicky 1996; Therrien and Sudicky 2000). Expanding on the movement of water, non-reactive (Blessent et al. 2014; Dueri and Therrien 2003), as well as reactive (Graf and Therrien 2008), chemical species can be transported through the subsurface and surface domains. This work has been further extended into the modeling of density driven flows (Graf and Simmons 2009; Graf and Therrien 2007; Graf and Therrien 2008), heat-transport (Graf and Boufadel 2011), and energy balance (Brookfield et al. 2009).

Studies at large scales historically have required a spatially coarse numerical description. This stretches the applicability of the governing equations, often developed at the field scale or smaller. Simulations at the basin scale have still been shown to reasonably reproduce subsurface hydraulic heads and surface outflows (Goderniaux et al. 2011; Jones et al. 2008; Li et al. 2008). Advancement in computational power has enabled the use of coupled surface-subsurface models to expand simulations from field scale to large spatial extents. Kollet et al. (2010) demonstrated the application of high resolution hydrologic simulations at the regional scale, while significantly reducing computation times through parallel computing.

Simulation modeling offers a fast and inexpensive approach to investigate hydrologic processes through numerical experimentation (Soltani and Hoogenboom 2007). Advanced models offer the capability of a comprehensive evaluation of agricultural practices on coupled flow. The goal of this project was to evaluate distributed flood mitigation reservoirs on peak flow reduction though detailed coupled surface-subsurface modeling. Answering the question of, "What is the cost of peak flow reduction?" While remaining a valid and important question, the construction of this model enables the investigation into many other aspects of agricultural watershed hydrology in a detailed physics based approach.

3.0 MATHEMATICAL MODEL DESCRIPTION

To improve the understanding of the dynamic surface and subsurface response to hydrologic forcing, a coupled surface-subsurface hydrologic model was constructed. HydroGeoSphere (HGS) was the numerical platform selected for watershed modeling. HGS provides a 3-D subsurface, 2-D surface, 1-D pipe, fully integrated approach to solving flow and mass transport through heterogeneous landscapes (Fig. 3.1). Due to the increased computational requirements of HGS, previously published coupled applications have been most commonly applied to experimental plots or small subcatchments (Cornelissen et al. 2013; De Schepper et al. 2015; Heppner et al. 2006; Hofer et al. 2011; Jones et al. 2006; Loague and Vanderkwaak 2002; Pebesma et al. 2005; Perez et al. 2011; Rozemeijer et al. 2010; VanderKwaak and Loague 2001) with a few applications to larger scale basins (Goderniaux et al. 2011; Jones et al. 2008; Li et al. 2008; Sciuto and Diekkruger 2010).

The following briefly describes the major modeling components of HGS, for a detailed description, see Therrien et al. (2013).
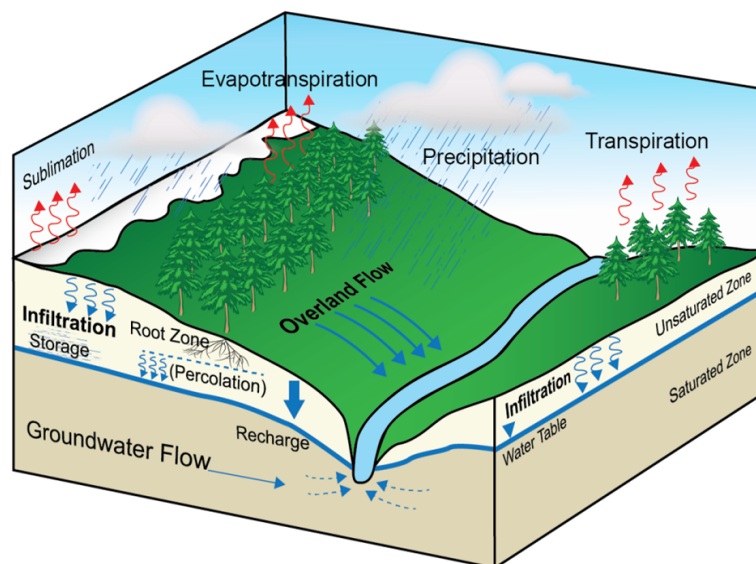
Figure 3.1 Conceptual diagram of hydrologic processes simulated by HGS.

3.1 Subsurface Flow

The subsurface flow regime is described by the Richard's Equation representing a variably-saturated porous medium in 3-D, Eq. [3.1].

$$\frac{d}{dx}\left(K_{xx}k_{rw}\frac{dh_G}{dx}\right) + \frac{d}{dy}\left(K_{yy}k_{rw}\frac{dh_G}{dy}\right) + \frac{d}{dz}\left(K_{zz}k_{rw}\frac{dh_G}{dz}\right) + \sum\Gamma_{ex} \pm Q = \varphi\frac{dS_w}{dt} + S_wS_s\frac{dh_G}{dt} \quad [3.1]$$

Where x, y, and z are in the Cartesian coordinate system having saturated hydraulic conductivities in the x, y, and z directions of K_{xx}, K_{yy}, and K_{zz} (ms^{-1}), respectively. k_{rw} (-) represents the relative permeability of the porous medium as a function of water saturation defined by the relative permeability curve, Eq. [3.2]. h_G (m) is the total hydraulic head, a combination of the pressure head and the elevation head. Γ_{ex} (m^{3}m^{-3}s^{-1}) represents the volumetric fluid exchange rate between the subsurface domain and all other domain types (i.e. surface, wells, tiles drains, discrete fractures, and dual continuum). Q (m^{3}m^{-3}s^{-1}) is the fluid exchange into and out of the modeling domain, typically represented by specified boundary conditions. φ (-) is volumetric fraction of the total porosity occupied by the porous medium. S_w (-) is the water saturation level as a function of the pressure head determined by the moisture retention curve. S_s (m^{-1}) is the specific storage of the subsurface.

The primary variable for solution of nonlinear subsurface flow is the pressure head, where constitutive relationships describe the connection between the pressure head and the other unknown parameters, S_w and k_{rw}. The constitutive relationships applied were established by Van Genuchten (1980), Eq. [3.2] and Eq. [3.3].

$$k_{rw} = S_e^{\frac{1}{2}}\left[1 - \left(1 - S_e^{\frac{1}{v}}\right)^v\right]^2 \qquad\qquad\qquad [3.2]$$

$$S_e = \frac{S_w - S_{wr}}{1 - S_{wr}} = \frac{1}{[1+(\alpha\psi)^\beta]^v} \qquad \text{for } \psi < 0 \qquad\qquad [3.3]$$

$$S_e = 1 \qquad\qquad \text{for } \psi \geq 0$$

Where S_e (-) is the effective saturation, and S_{wr} (-) is the residual saturation. The relationship between v and β is $v = 1 - 1/\beta$. The parameters α (m⁻¹) and β (-) are empirically derived parameters for the moisture retention and relative permeability functions. α and β are typically obtained through laboratory measurements, soil type identification, or soil database analysis.

3.2 Surface Flow

Areal overland flows are simulated using a 2-D depth averaged form of the St. Venant's equations, known as the diffusion-wave approximation, Eq. [3.4].

$$\frac{dh_o}{dt} - \frac{d}{dx}\left(dk_x \frac{dh_o}{dx}\right) - \frac{d}{dy}\left(dk_y \frac{dh_o}{dy}\right) + d\Gamma \pm Q = 0 \qquad\qquad [3.4]$$

Where $h_o = d + z_o$ (m), d (m) is the water depth, and z_o (m) is the bed elevation. k_x (ms⁻¹), and k_y (ms⁻¹), are surface flow conductance terms described by a manipulation of Manning's equation Eq. [3.5]. Γ (m³m⁻³s⁻¹) represents the volumetric fluid exchange rate between the surface domain and the subsurface domain. Q (m³m⁻³s⁻¹) is the fluid exchange into and out of the modeling domain, represented by specified boundary conditions.

$$k_i = \frac{d^{\frac{2}{3}}}{n_i} \frac{1}{\left[\frac{dh_o}{ds}\right]^{\frac{1}{2}}} \quad (i = x, y) \qquad\qquad [3.5]$$

The friction slopes in Eq. [3.5] are described by Manning's roughness coefficient n. Where i = x or y coordinate directions, and s (m) is the length along the direction of maximum local slope.

Surface and subsurface components are coupled by a dual node approach. A thin layer is assumed to exist between the porous media and the surface. A Darcy flux scaled by the coupling length and hydraulic conductivity enable fluid to from one domain to the other, Eq. [3.6].

$$d\Gamma = \frac{k_r K_{zz}}{l_{exch}}(h - h_o) \qquad\qquad [3.6]$$

Where the subsurface water head is h (m), and h_o (m) is the surface water head. The relative permeability for the exchange flux is represented by k_r (-), K_{zz} (ms^{-1}) is the vertical saturated hydraulic conductivity of the porous medium, and l_{exch} (m) is the coupling length, discussed in further detail by (Ebel et al. 2009).

3.3 Tile Drain Flow

Tile drains are represented by 1-D linear elements along which flow along the element axis (l) is described by Eq. [3.7].

$$-\frac{\partial}{\partial_l}(Q_{1D}) + Q_{pm}\delta(l - l_p) = \frac{\partial}{\partial_t}(A_f) \qquad\qquad [3.7]$$

Where Q_{1D} ($m^3 s^{-1}$) is the fluid flux along the 1-D element, Q_{pm} ($m^3 s^{-1}$) represents the tile flow interaction with the porous media domain at a given point l_p, and A_f (m^2) is the tile cross sectional area.

3.4 Boundary Conditions

Boundary conditions for subsurface flow include: prescribed head, sources or sinks, infiltration or recharge, evapotranspiration, and seepage faces. In the current

simulation an assumption is made that the surface water boundary is also the subsurface water boundary, as such a no flow boundary condition is placed on all outer subsurface nodes.

Surface flow boundary conditions include prescribed head, and flux conditions like the subsurface, and further include critical depth and zero-depth gradient outflow conditions. Q in Eq. [3.4] is given by a surface flux per unit width normal to the flow direction, where Eq. [3.8] and Eq. [3.9] represent the critical depth and zero-depth gradient outflow conditions respectively. Each the critical depth and the zero-depth gradient are defined here in terms of Manning's coefficient:

$$Q = \sqrt{gd^3} \qquad\qquad [3.8]$$

$$Q = \frac{1}{n}d^{\frac{5}{3}}\sqrt{s_o} \qquad\qquad [3.9]$$

Rainfall is input as a prescribed flux applied to the surface modeling domain. Interception, evaporation, and transpiration are modeled using the Kristensen and Jensen (1975) approach, removing water through a combination of plant and climactic fluid losses. Interception is the retention of rainfall on the leaves or branches of vegetation and on buildings or other constituents above the ground with water holding capacity. The process of interception is simulated by a simple bucket model. Interception storage S_{int} varies between zero and S_{max} (m) the maximum storage capacity. The maximum storage depends on the type of plant or storage device and the maturity of the vegetation, Eq. [3.10].

$$S_{int}^{Max} = c_{int}LAI \qquad\qquad [3.10]$$

Where c_{int} (m) is the canopy storage parameter, and the leaf area index (LAI) (m^3m^{-3}) is a measure of the leaf coverage over an area and can vary temporally. The storage is calculated at the beginning of each time step and is depleted by evaporation.

Evapotranspiration is modeled as a combination of plant transpiration and evaporation from the surface and subsurface flow domains. Transpiration occurs down to the bottom of the root zone, with the rate of transpiration described by a depth dependent function, Eq. [3.11].

$$T_p = f_1(LAI)f_2(\theta)\left[E_p - E_{can}\right] \tag{3.11}$$

Where $f_1(LAI)$ is a function of the LAI, Eq. [3.12], $f_2(\theta)$ is a function of θ (m^3m^{-3}) the nodal water content, Eq. [3.14], E_p (m^3s^{-1}) is the reference evapotranspiration typically defined by a climactic factors with the Penman (1948) model, and E_{can} (m^3s^{-1}) is the canopy evaporation.

$$f_1(LAI) = \max\{0, \min[1, (C_2 + C_1 LAI)]\} \tag{3.12}$$

$$RDF = \frac{\int_{z'_1}^{z'_2} r_F(z')dz'}{\int_0^{L_r} r_F(z')dz'} \tag{3.13}$$

$$f_2(\theta) = \begin{cases} 0 & \text{for } 0 \leq \theta \leq \theta_{wp} \\ 1 - \left[\frac{\theta_{fc}-\theta}{\theta_{fc}-\theta_{wp}}\right]^{c_3} & \text{for } \theta_{wp} \leq \theta \leq \theta_{fc} \\ 1 & \text{for } \theta_{fc} \leq \theta \leq \theta_o \\ \left[\frac{\theta_{an}-\theta}{\theta_{an}-\theta_o}\right]^{c_3} & \text{for } \theta_o \leq \theta \leq \theta_{an} \\ 0 & \text{for } \theta_{an} \leq \theta \end{cases} \tag{3.14}$$

Where C_1, C_2, and C_3 (-) are dimensionless fitting parameters, L_r (m) is the effective root length, z' (m) is the depth from the soil surface, θ_{wp}, θ_{fc}, θ_o, θ_{an} (m^3m^{-3}) are the moisture

contents at wilting point, field capacity, oxic limit, and anoxic limit respectively, RDF is the root distribution function, Eq. [3.13], r_F (m^3s^{-1}) is the root zone extraction function, which varies logarithmically with depth.

Evaporation occurs only if the reference evapotranspiration has not been removed by the process of canopy evaporation and plant transpiration, Eq. [3.15] and Eq. [3.16].

$$E_s = \alpha^* \left(E_p - E_{can} - T_p \right) EDF \qquad [3.15]$$

$$\alpha^* = \begin{cases} \frac{\theta - \theta_{e2}}{\theta_{e1} - \theta_{e2}} & \text{for } \theta_{e2} \leq \theta \leq \theta_{e1} \\ 1 & \text{for } \theta > \theta_{e1} \\ 0 & \text{for } \theta < \theta_{e2} \end{cases} \qquad [3.16]$$

Where θ_{e1} and θ_{e2} (m^3m^{-3}) are the upper and lower energy limiting moisture contents, where above θ_{e1} evaporation occurs at full capacity and below θ_{e2} evaporation does not occur. To incorporate evaporation at depth an evaporation density function EDF prescribing energy penetration into the soil for evaporation to occur variably with depth over a soil column.

3.5 Contaminant Transport

Solute transport is solved by the classic advection-dispersion equation, Eq. [3.17].

$$-\nabla(qC - \theta SD\nabla C) + [\theta SR\lambda C]_{par} + \sum \Omega_{ex} \pm Q_c = \frac{d(\theta SRC)}{dt} + \theta SR\lambda C \qquad [3.17]$$

Where C (kgm^{-3}) is the solute concentration of the current species, λ (m^{-1}) is the first-order decay constant. *par* represents the parent species for the decay chain, with a straight decay chain there is only one parent species, degrading organics often have multiple complex chains. Q_c ($kgm^{-3}s^{-1}$) represents solute exchange though the boundary conditions, while Ω_{ex} ($kgm^{-3}s^{-1}$) represents the mass exchange rate of the solutes between

the subsurface domain and all other domains in the model. The retardation factor R (-) describes the fraction of solute in a mobile state and originated from Freeze and Cherry (1979), Eq. [3.18].

$$R = 1 + \frac{\rho_b}{\theta S} K' \qquad [3.18]$$

Where ρ_b (kgm^{-3}) is the bulk density of the porous medium, and K' (kgm^{-3}) is the equilibrium distribution coefficient describing a linear Freundlich adsorption isotherm. The hydrodynamic dispersion tensor is given by Eq. [3.19].

$$\theta SD = (\alpha_l - \alpha_t)\frac{qq}{|q|} + \alpha_t|q|I + \theta S\tau D_{free}I \qquad [3.19]$$

Where α_l and α_t (m) are the longitudinal and transverse dispersivities, $|q|$ (-) is the magnitude of the Darcy flux, τ (-) is the tortuosity of the matrix, D_{free} (m^{2}s^{-1}) is the free solution diffusion coefficient, and I is the identity tensor. In the unsaturated zone the tortuosity changes with saturation (Millington and Quirk 1961), given by Eq. [3.20].

$$\tau = \frac{(S\theta)^{\frac{7}{3}}}{\theta^2} \qquad [3.20]$$

The surface domain is discretized into a 2-D depth averaged transport equation, Eq. [3.21].

$$-\bar{\nabla}(q_oC_o - D_o\varphi_oh_o\nabla C_o) + [\varphi_oh_oR_o\lambda C_o]_{par} - d_o\Omega_o = \frac{d}{dt}(\varphi_oh_oR_oC_o) + \varphi_oh_oR_o\lambda C_o \qquad [3.21]$$

Where C_o (kgm^{-3}) is the concentration in the water on the surface of the domain, D_o (m^{2}s^{-1}) is the hydrodynamic dispersion tensor of the surface flow domain, and $\bar{\nabla}$ is the

vertically integrated 2-D gradient operator. Expressions for D_o and R_o are analogous to those in Eq. [3.18] and Eq. [3.19] from the subsurface domain.

3.6 Numerical Methods

HGS utilizes a fully-implicit coupling approach to conserve mass and to ensure strong interaction between flow domains. A control volume finite element method is employed to discretize both the surface and subsurface flow domains. The standard Galerkin finite element method or the control volume finite element method can be used to solve the transport equations. The nonlinear equations are solved by linearizing and applying the Newton Raphson technique. The solver utilizes an adaptive time stepping scheme to automatically control the time steps to increase precision during rapid alterations in fluid fluxes (Therrien and Sudicky 1996). Calculations are performed on irregular tetrahedral and triangular meshed for the subsurface and surface domains, respectively.

4.0 SITE DESCRIPTION

The focus of this study was the Beaver Creek Watershed (BCW), a 45 km^2 catchment, located in the agriculturally dominated central U.S. Land use in the BCW is predominantly row crop agriculture (corn and soybeans), constituting 72 % of the catchment. The remaining land is a mix of grasslands in the south and deciduous forests in riparian areas (27 %). Urban type land uses attribute less than 1 % of the total area (Fig. 4.1a).

BCW is located in the Iowan Surface geologic formation (Fig. 1.1), where the now visible rolling hills, low relief, and well developed drainage were produced through glacial weathering and leveling during the last glacial period (Prior et al. 1991). Shallow Devonian-age limestone bedrock, covered by thin layers of loamy glacial deposits, are the result of widespread erosion from a landscape dominated by pre-Illinoian glacial drift (NRCS 2012; Squillace et al. 1996). Areas of shallow carbonate bedrock are present in the western half of the catchment. As a result, karst geologic features including sinkholes, springs, and weathered and fractured bedrock sporadically exist. Coland and Clyde type clay loams comprise the alluvial deposits in mildly sloping (0 % to 2 %) streams. Readlyn, Floyd, and Bassett type loams are draped over mild to moderately sloped (2 % to 5 %) uplands (NRCS 2014) (Fig. 4.1b).

Elevations range from 364 m AMSL in the uplands to 305 m AMSL at the outlet. The watershed tends towards milder slopes in the northern uplands, and relatively steeper slopes in the south (Fig. 4.1c).

The BCW lies in a humid continental climactic region, characterized by large temperature and precipitation variations. Average annual precipitation ranges from 850 mm to 910 mm (Hutchinson et al. 2013), with approximately 75 % lost to evaporation (Sanford and Selnick 2013; Schilling et al. 2008). Of the average annual precipitation, 70 % occurs between March and July, with approximately half of that occurring in March

and April. This provides evidence that spring rainfall and snowmelt processes are significant sources of increased runoff. Groundwater is extracted for residential use, but it is not required for irrigation purposes as frequent rainfall provides enough water to satisfy agricultural needs. The rural watershed contains approximately 500 people, with the total ground water extraction for residential assumed to be negligible.

Figure 4.1 BCW site description. a) Land use (FSA 2013). b) Soil texture (NRCS 2014). c) Topography (IGWS 2010).
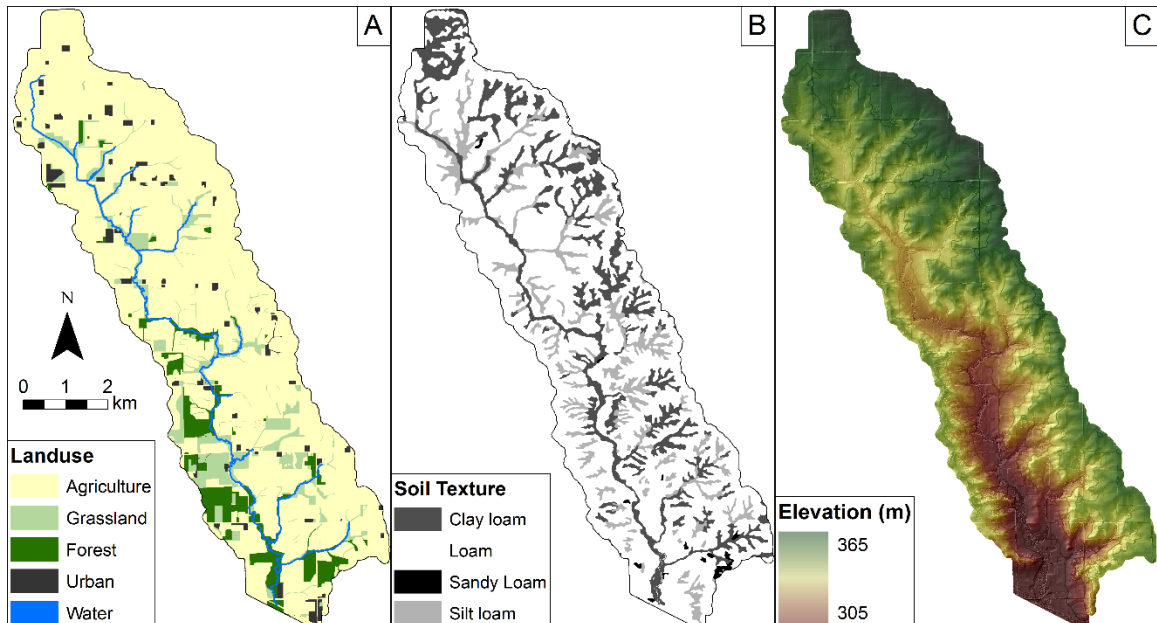
4.1 Data collection

In the spring of 2014 rain gauge and soil moisture (RGSM) platforms (3), stream stage sensors (3), shallow ground water wells (6), and water quality sensors (2) were installed in the BCW (Fig. 4.2).
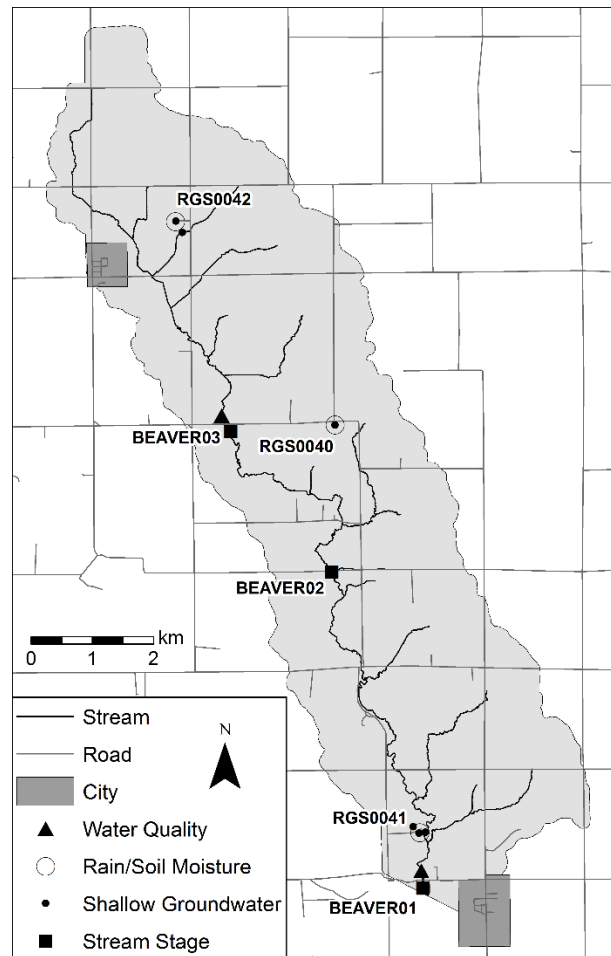
Figure 4.2 Monitoring locations in BCW from spring 2014 installation. Displayed in this figure are RGSM platforms (3), stream stage sensors (3), water quality stations (2), and shallow groundwater wells (6).

At each RGSM platform location, soil water content at 5 cm, 10 cm, 20 cm, and 50 cm was measured with horizontally installed Campbell Scientific CS655 Water Content Reflectometers. Dual MetOne 380 precipitation gages were collocated with the soil moisture sensors. When temperatures were below 0 °C the precipitation gauges were removed, and soil moisture measurements were considered unreliable, as moisture near the surface freezes. Each of the sensors were located in short grass open areas adjacent to agricultural activity.

Shallow groundwater wells were collocated with the RGSM platforms (3), in nearby floodplains (2), and at a local elevation peak (1). Each well was constructed from

5.08 cm PVC pipe drilled to a depth ranging from 4.57 m to 6.10 m. Well screens were installed in three meter increments, beginning at depth of 1.52 m, down to 4.57 m. Each site was backfilled with bentonite and equipped with a Decagon CTD-10 water level transducer.

Stream stage sensors were mounted at three road crossings, and acoustically measure the distance to the water surface. An approximation of the bed elevation enabled the estimation of water depth.

Water quality stations were collocated with BEAVER01 and BEAVER03 stream stage sensors (Fig. 4.2). The sensor platform consisted of Hach Nitratax SC Nitrate Sensor, FTS DTS-12 Turbidity Sensor and Ott-Hydromet Hydrolab DS5X Sonde. The Hydrolab multiprobe sensors were configured to measure water temperature, specific conductance, chlorophyll a, pH, and dissolved oxygen.

Each monitoring system consisted of an IIHR Hydroscience & Engineering developed datalogger, battery, solar panel, and cellular modem. Data were collected, transmitted, and ingested into severs located at The University of Iowa on a 15 minute schedule. Monitoring data was incorporated into event validation, and calibration of soil moisture in Section 10.

<u>4.2 Data Manipulation for Simulation</u>

Measured meteorological data for 2014 from the BCW was applied for all annual simulations. This section describes the exact alterations to the raw data for input into numerical simulations.

Precipitation was measured at 3 locations within the BCW beginning May 15, 2014 at 15 minute increments (Fig. 4.2). The raw data was aggregated to the hourly time step and Thiessen polygon weighted over the BCW. This produced a uniformly distributed rainfall at hourly time steps from May 15, 2014 to December 31, 2014. From January 1, 2014 to May 15, 2014 hourly, liquid equivalent precipitation data was

downloaded from the Iowa State University AgClimate weather station at Nashua (ISU 2015) (Fig. 4.5). The precipitation data from Nashua, and from within BCW were combined and applied as a surface flux input for annual model simulations of 2014 (Fig. 4.3). Precipitation was aggregated spatially as to remove rainfall variability from the catchment response. Similarly, the raw 15 minute data was aggregate to an hourly time step in an effort to reduce the impact of variable rainfall inputs on the basin response.
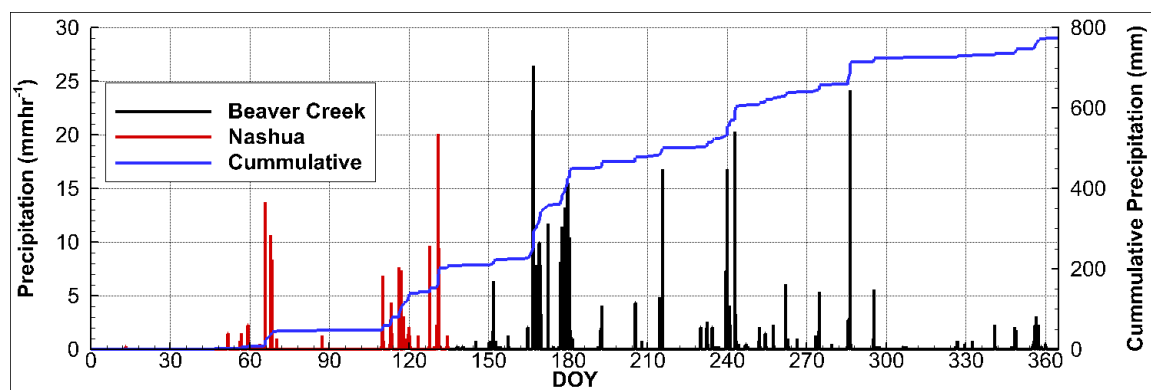
Figure 4.3 Hourly aggregated precipitation data for the year of 2014. Precipitation data from Nashua (Fig. 4.5) was used from DOY 1 to DOY 135 (red) when BCW sensors were installed (black) and used from DOY 135 until the end of 2014.

Daily potential evapotranspiration (PET) based on the Penman-Monteith approach and downloaded from the Iowa State AgClimate station at Nashua, IA (ISU 2015). A gap in PET data from April 1, 2014 to August 18, 2014 required supplemental PET data (Fig. 4.4a). Supplemental data was calculated with the Penman-Monteith approach, with weather data from Charles City, (Bradley 2014). The Charles City and Nashua PET data were combined for further preprocessing.

PET data was modified to take into account the dominant land use, agriculture. A crop coefficient (K_c) was applied to each daily PET estimated based on the cumulative growing degree day base 50 (GGD50) method (HPRCC 2015; ISU 2015) (Fig. 4.4b). K_c take into account the ground cover, canopy properties, and aerodynamic resistance of the specific crop (Allen et al. 1998). K_c increased PET during growing seasons, otherwise K_c

reduced the PET (Fig 4.5c). Due to model simplifications only a single PET value can be applied to the simulations. As a result the PET* K_c from corn was applied uniformly over the watershed (Fig 4.5c).

Table 4.1 Corn growth stages based on GDD50 and associated K_c (Allen et al. 1998).

Growth Stage	K_c	GDD50
2 leaves	0.1	0
4 leaves	0.18	240
6 leaves	0.35	360
8 leaves	0.51	480
10 leaves	0.69	600
12 leaves	0.88	720
14 leaves	1.01	840
16 leaves	1.1	960
Silks	1.1	1200
Blister	1.1	1440
Dough	1.1	1680
Early Dent	1.1	1920
Full Dent	0.98	2160
Black Layer	0.6	2400
Full Mature	0.1	2450
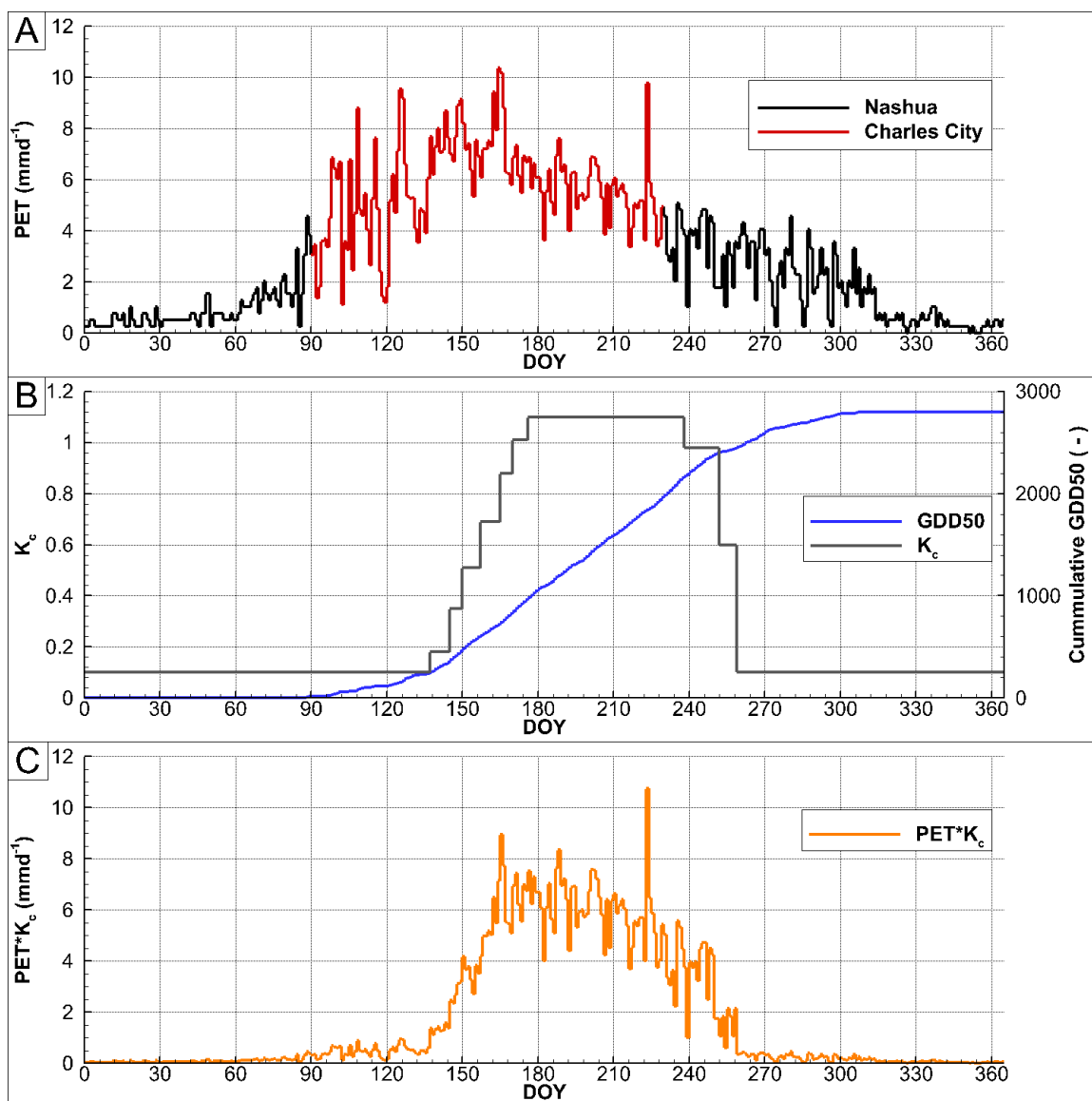
Figure 4.4 PET data for the year 2014. a) Raw PET data aggregated from two research locations Nashua (black) and Charles City (red) (Fig. 4.5). b) Cumulative GDD50 was used to calculate the K_c based on growth stage (Table 4.1). c) PET as input for numerical simulations incorporating the K_c.

4.3 Meteorological Input for Hydrologic Simulation 2014

Precipitation in 2014 totaled 773 mm for a combination of in-catchment measurements and measurements from a nearby rain gage at Nashua (Fig. 4.5). Two major storms (beginning DOY 110 and DOY 165) produced more than half of the annual

cumulative precipitation. The maximum rainfall occurred on day 167 at a rate of 26.4 mmhr^{-1}.

PET accumulated 1134 mm over the entire year (Fig 4.4a). K_c reduced the cumulative PET to 630 mm (Fig. 4.4c). The impact of the K_c reduced PET in the winter, spring, and late fall and increased it in the summer months. The PET* K_c was at its peak from DOY 165 to DOY 215.
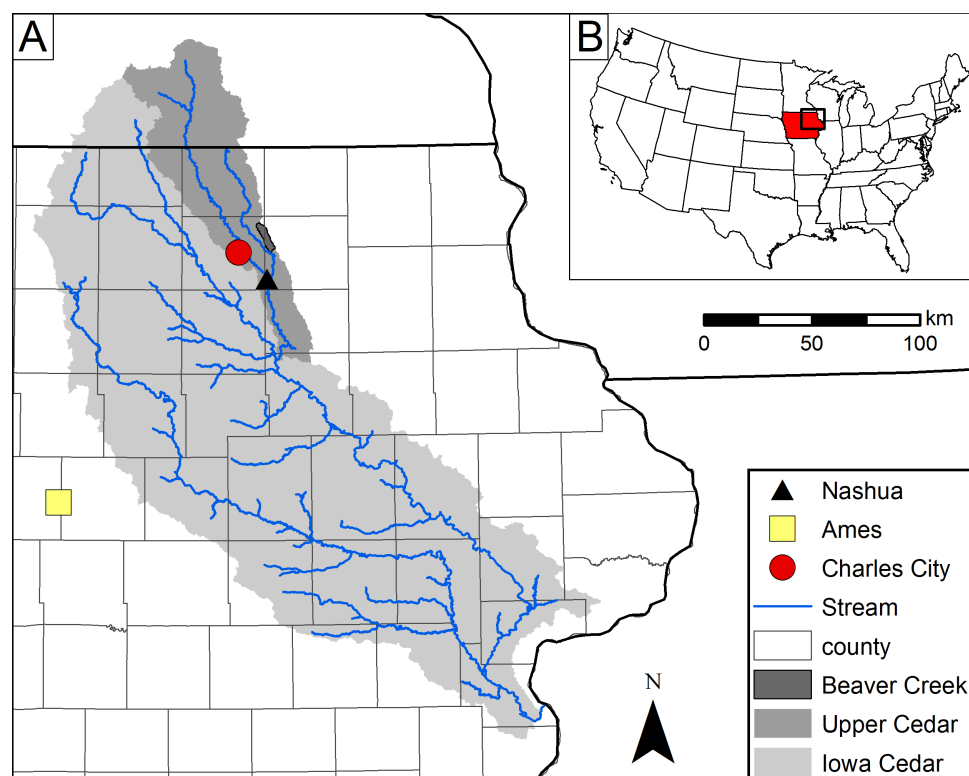
Figure 4.5 Data collection sites in Iowa. Ames SCAN – long term water content (yellow), Charles City - supplemental meteorological data for PET calculation (red), Nashua – PET data and supplemental hourly rainfall (black).

4.4 Long Term Soil Water Content Record

Long term measured soil water content data was available at only a few locations in the state of Iowa. Soil Climate Analysis Network (SCAN) was developed to gain insight into the soil-climate dynamics through the NRCS (NRCS 2004; NRCS 2015). A

nearby SCAN site in Ames, IA, measured continuous soil water content data from 2002 to 2012. Soil water content was measured at 5 cm, 10 cm, 20 cm, 50 cm, and 100 cm using a dielectric measuring device (NRCS 2004). The data was used to identify long term soil moisture trends and as initial conditions to investigate antecedent moisture controls.

SCAN soil water content data was shown to vary with depth, and temporally (Fig. 4.6, Fig. 4.7, and Fig. 4.8). Shallower soils were shown to have increased variability, with lower median soil water content values. At the 5 cm soil depth (Fig. 4.6), measured hourly soil water ranged from 0.67 to 0.12. Median soil water content tended to increase with depth, and soil water tended to exhibit less variability. In the 10 cm (Fig. 4.7), and 20 cm (Fig. 4.8) depths soil water content ranged from 0.59 to 0.18 and 0.58 to 0.21, respectively. At 50 cm and 100 cm depths measured soil water content tended to vary little or not at all (not shown here). The highest median soil water values and lowest variability occurred in the months of March, April, and May, due to spring snowmelt, and rainfall. June, July, and August were attributed with the highest variability and lowest median water content values due to high ET. Temporal variability held true with depth, albeit a more muted response occurred.

Section 7.0 investigated the exceedance probability of nine antecedent moisture conditions on peak flow and peak flow reductions of distributed flood mitigation wetlands. SCAN data provided a reasonable representation of the frequency and magnitude of soil wetness in central Iowa. These conditions vary with soil type, soil stratigraphy, and location.

Raw data was aggregated from multiple sources and manipulated to provide reliable measurements of hydrologic variables in close proximity to BCW. BCW annual 2014 simulation were driven with the data described in the section.
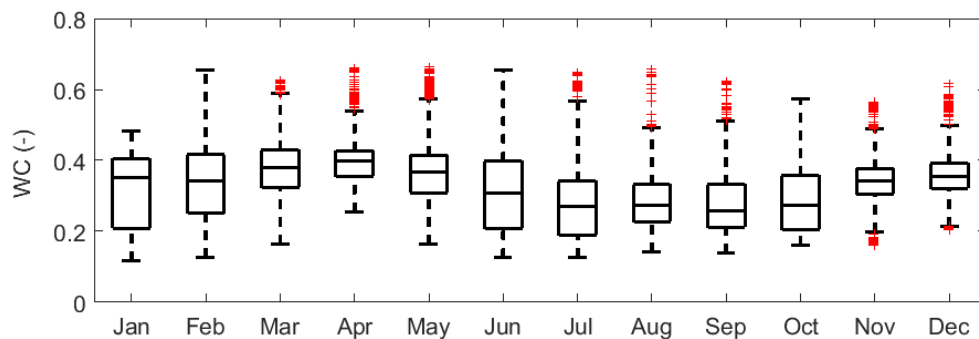
Figure 4.6 Measured monthly 5 cm aggregated water content from the Ames, IA SCAN location (Fig. 4.5).
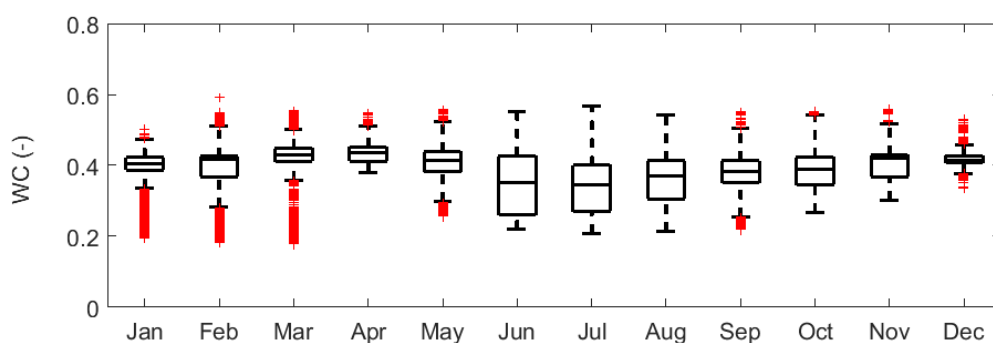
Figure 4.7 Measured monthly 10 cm aggregated water content from the Ames, IA SCAN location (Fig. 4.5).
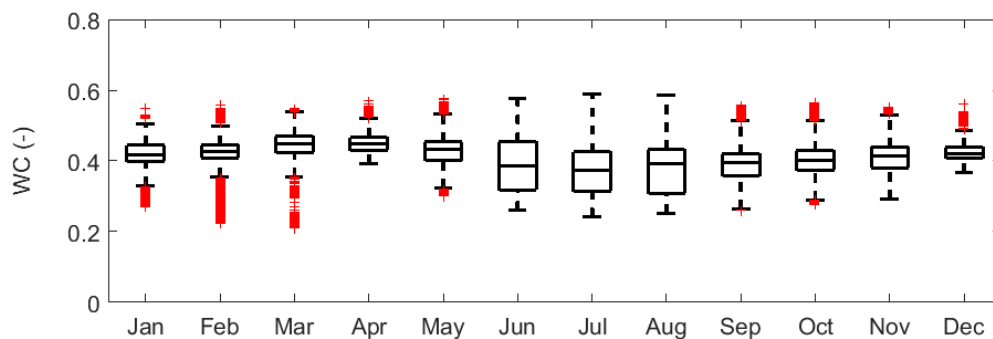
Figure 4.8 Measured monthly 20 cm aggregated water content from the Ames, IA SCAN location (Fig. 4.5).

5.0 MODEL CONSTRUCTION

This section describes the construction of a finite element mesh, conceptual allocation of surface and subsurface properties, and associated parameters.

5.1 Numerical Discretization

The objectives of this study required investigation surface, and near surface water flow processes. A 2-D unstructured finite element mesh was created using Gridgen V15 (Pointwise Inc. 2003). Gridgen automatically generated mesh elements inside of designated boundaries through Delaunay Triangulation (Guibas and Stolfi 1985).

For this study a comprehensive and adaptable mesh was produced from the watershed boundary, stream centerlines, roadways, and hydraulic structure locations. The watershed boundary was identified as the local topographic high, draining all internal area to a single outlet location. This boundary acts as the lateral edge of both the surface and subsurface domains. BCW is located in a region known for its mildly sloped agricultural expanses, divided only by elevated roadways and incised stream channels. During heavy rainfall events elevated roadways act as topographic divides, forcing rainfall into nearby drainage ditches and then into Beaver Creek. HGS extracts elevation information from nodal locations. Through allocating mesh generation boundaries to a topographic feature, Gridgen places nodes at the same locations ensuring the topographic inclusion of the boundaries. Roadways were included as mesh generation boundaries guaranteeing the important topographic features were retained. Stream centerlines were delineated and incorporated to ensure continuous flow to the catchment outlet, maintaining travel times, and realistically capturing surface-subsurface interactions (Li et al. 2008). To increase computation efficiency mesh elements were coarsened to 200 m in overland mildly sloped areas, and refined near streams and constructed projects to 25 m. The final 2-D surface grid contained 12,529 nodes, and 24,764 triangular elements (Fig. 5.1).
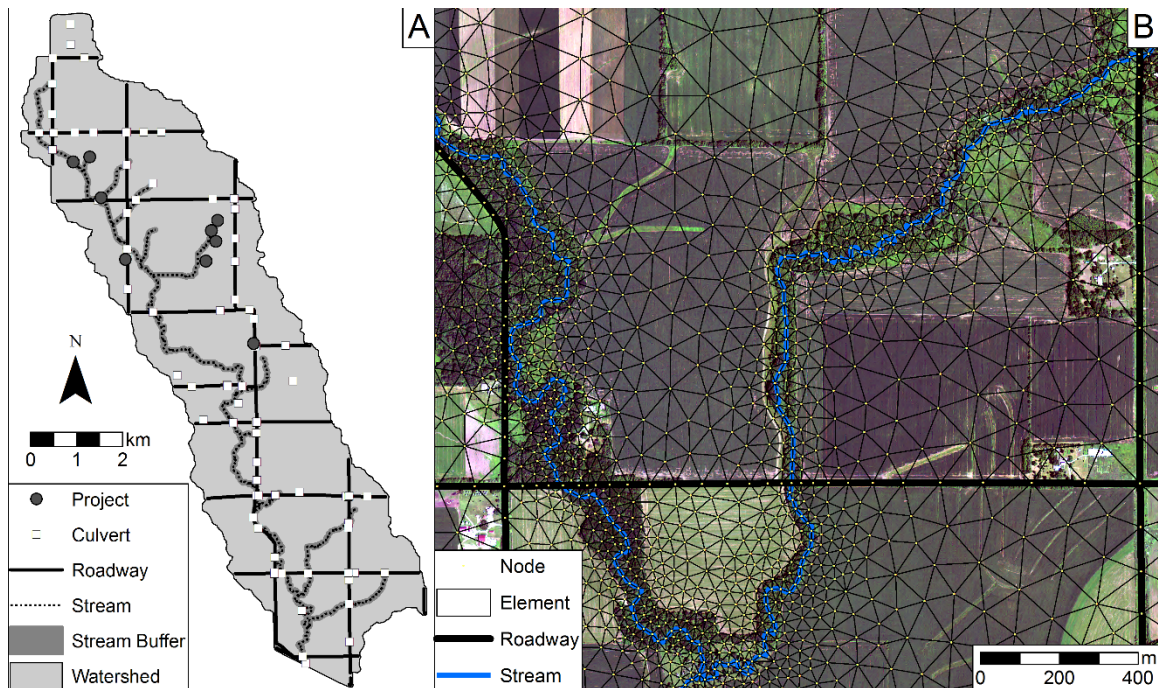
Figure 5.1 BCW surface domain grid generation a) Boundaries for mesh generation. b) Example location of the completed 2-D finite element grid.

The completed 2-D surface mesh was projected downward to an impermeable layer, described in Section 5.2.3, to form 3-D subsurface layers. The subsurface was divided into two zones, from the surface down one meter, and from a one meter depth to the impermeable layer. Vertical nodes were allocated to each soil water content measurement depth (5 cm, 10 cm, 20 cm, and 50 cm). A numerical layer was added between each sensor location to ensure water content dynamics at each observation point varied independently. This vertical allocation of nodes produced a total of 10 layers in the top one meter of the subsurface (Fig. 5.2). The remaining domain was divided into 5 layers increasing in thickness from 0.6 m to 1.7 m near the impermeable layer. The finer vertical discretization near the surface represents more accurately the interactions between the surface and subsurface domains (Fig. 5.2). Downer and Ogden (2004) identified that at vertical resolutions greater than 2 cm near the surface can result in a misrepresentation of infiltration, producing physically incorrect solutions to the Richard's

equations. Representation of evapotranspiration fluxes were better represented as root

and evaporation depths were distributed over multiple numerical layers (Sciuto and

Diekkruger 2010). The product of mesh generation was a 16 layer, 212,993 node, and

371,460 element 3-D finite element grid.
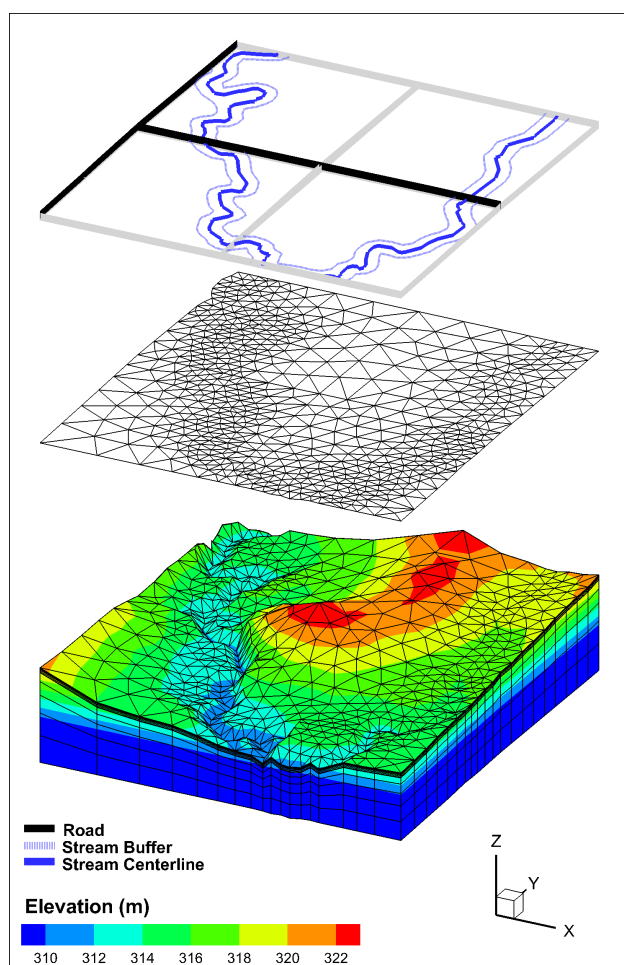
Figure 5.2 Generation of 2-D and 3-D mesh. Conceptual mesh generation though incorporation of important boundaries (top), to produce a 2-D mesh (middle), which was projected downwards to create a 3-D tetrahedral mesh (bottom). Vertical axis at 10:1 ratio.

5.2 Basin Characterization

Publically available land use, soil type, and well log data was used to spatially

describe surface and subsurface classifications. Subsurface stratigraphy was divided into

surficial soils and deeper geologic soils. The surficial one meter of soil depth was described by the Soil Survey Geographic (SSURGO) database (NRCS 2014) (Fig. 4.1b). The remaining deeper soil layers were described by historical well log stratigraphy (Fig. 5.3). Surface and subsurface physical properties were derived from combinations of literature values and though publically available classifications. This section describes the process of characterizing and parameterizing the generated mesh with appropriate values.

5.2.1 Surficial Soils

The SSURGO soil database contains spatially variable surficial soil data used to describe the top one meter of model domain (NRCS 2014) (Fig. 4.1b). The data was derived through a combination of soil sampling and visual survey to estimate areas consistent in soil type. Surficial soils were assigned unique spatial values in the plan view, but were assumed vertically homogeneous for the top one meter of soil.

Soil water retention functions following the Van Genuchten approach were estimated from SSURGO texture classification through the ROSSETTA pedotransfer function (Schaap and Leij 1998; Schaap and Leij 1998; Schaap and Leij 2000; Schaap et al. 2001). The saturated hydraulic conductivity of the surficial soils was increased by one order of magnitude from literature values following (De Schepper et al. 2015), as preferential flow pathways permeate the oxidized near surface soils in the agricultural, clay landscape (Johnson 1995; Mohanty et al. 1996).

Table 5.1 Surficial soil and averaged geologic soil properties estimated from SSURGO texture classification through the ROSSETTA pedotransfer function (Mohanty et al. 1994; NRCS 2014; Schaap et al. 2001)

Soil Type	Area (%)	K_{sat} (cmd^{-1})	θ_s (m^{3}m^{-3})	α (m^{-1})	β (-)	θ_r (m^{3}m^{-3})
Loam	69.2	12	0.44	1.11	1.47	0.06
Clay Loam	23.7	8	0.46	1.58	1.42	0.08
Silt Loam	0.4	18	0.50	0.51	1.66	0.07
Sandy Loam	6.7	38	0.45	2.67	1.45	0.04
Geologic Soils	N/A	8	0.32	1.11	1.42	0.05

5.2.2 Geologic Soils

Geologic formations below the top one meter of soil were described by historical well logs at 86 sites across the watershed and surrounding area (IGS 2015) (Fig. 5.3a). The stratigraphic units were digitized vertically and interpolated onto a 3-D representation of the watershed up to a 100 m depth (Fig. 5.3b). General trends in the geologic interpolation indicated variable layering of till, loess, and clay over confining layers of sedimentary carbonates, and siliciclastics. The geologic formation contains intermittent sand and gravel lenses.

Geologic soil stratigraphic units were assigned saturated hydraulic conductivity and porosity values from the ROSSETTA pedotransfer function for soil textures (Schaap and Leij 1998; Schaap and Leij 1998; Schaap and Leij 2000; Schaap et al. 2001). The saturated soil properties were volume weighted to produce an aggregated representation of geologic properties. The deeper subsurface was represented by the above described homogeneous representation of hydraulic properties from one meter deep to the impermeable layer.

5.2.3 Lower Geologic Boundary

Well logs indicated the depth to an unoxidized soil varied spatially across the watershed, from 1 m to 18 m. Measured saturated hydraulic conductivities in unoxidized

soils of this region were measured to be greater than an order of magnitude less than surficial soils (Bakhsh et al. 2004; Eidem et al. 1999; Seo 1996). The subsurface beneath the oxidized soil was not included in the modeling domain due to reduced porous media movement, the lack of subsurface characterization, the lack of deep numerical discretization, and the overall interest in surface and near surface water fluxes. A minimum threshold of a 5 m depth to the impermeable layer was imposed. Model testing indicated an unrealistically low representation of base flow occurred without sufficient subsurface depth. The depth to an assumed impermeable layer was inverse distance interpolated onto the 2-D mesh and applied as the bottom of the discretized domain (Fig. 5.4).
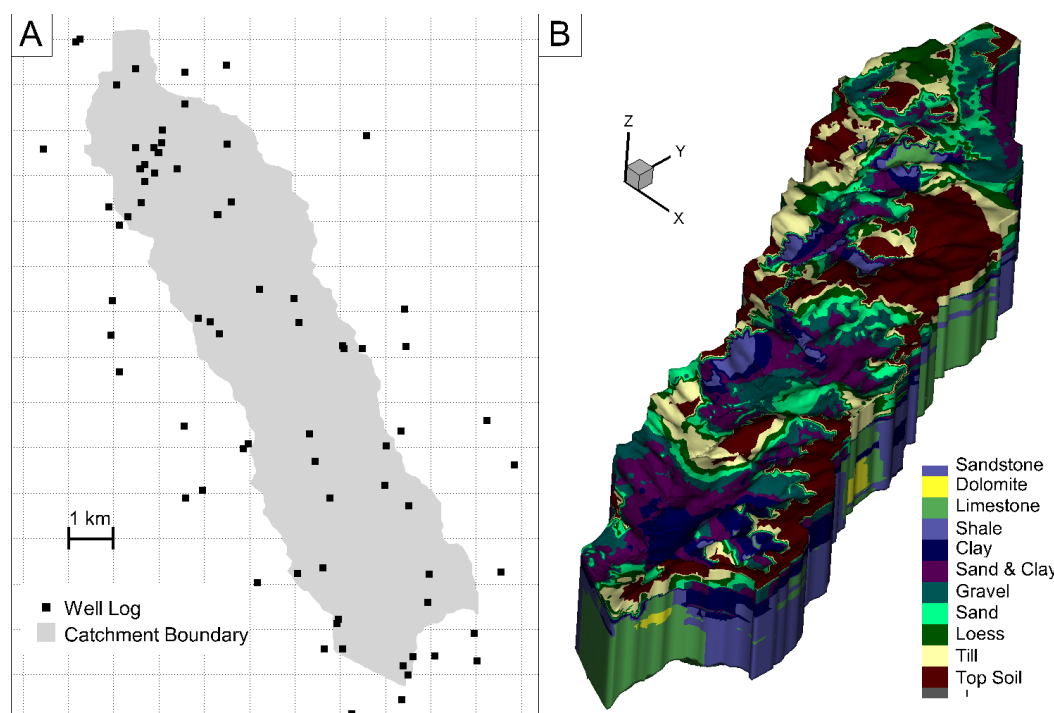
Figure 5.3 a) Geologic well log locations (86) within BCW and the surrounding area. b) Inverse distance interpolation of well log points onto the mesh up to 100 m deep.
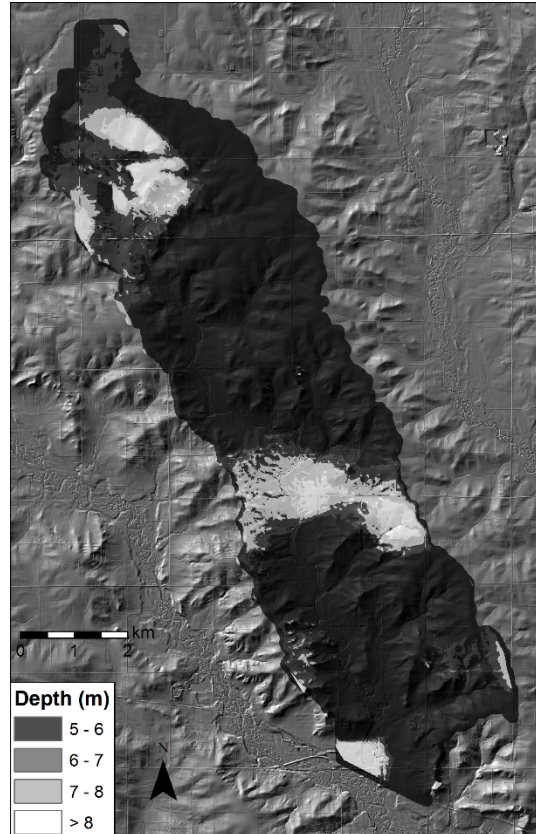
Figure 5.4 Depth to impermeable layer defining the bottom no flow boundary of the modeling domain.

5.2.4 Land Use

Spatially variable land use classifications were provided by the Common Land Unit (CLU) 2013 dataset from the United States Department of Agriculture. The CLU dataset delineates field boundaries, fence lines, waterways, tree lines, and roadways, by use of aerial photography to a spatial tolerance of three meters (FSA 2013). Land classifications were simplified into five classifications, agriculture, grassland, forest, developed, and water from the CLU and assigned to each elemental area (Fig. 4.1a).

The five surface land use classifications related surface elements to overland flow resistance parameters and vegetation properties (Table 5.2). Surface frictional roughness was described by a Manning's roughness coefficient. Sub grid scale roughness was represented by the depression storage parameter applied in a spatially uniform manner

over all land classifications. Depression storage restricts surface water conductance until water depth increases above the depression threshold (0.002 m) (Li et al. 2008). The surface and subsurface domains were connected though the coupling length, which was applied uniformly across the entire domain (0.01 m) (Ebel et al. 2009; Sciuto and Diekkruger 2010). The parameters used to calculate the actual evapotranspiration (Kristensen and Jensen 1975), were described thoroughly by Li et al. (2008) (Table 5.2 and Table 5.3). Transpiration and canopy evaporation rates were described as a function of LAI (Section 3.4). Values of LAI for each land use classification were derived from a combination of sources to identify maximum LAI values, and the associated temporal distribution (Fig. 5.5).
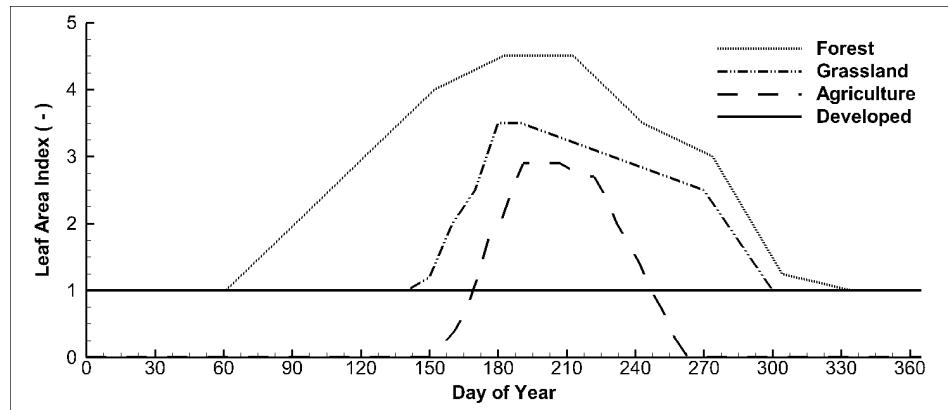
Figure 5.5 LAI for each land classification over an annual cycle. Data sources which described agriculture (Kim et al. 2012), prairie grassland (Breuer et al. 2003; Fang et al. 2008) , and forested areas (Breuer et al. 2003; Fang et al. 2008).

Table 5.2 Spatially varying properties based on land use classification, n was derived from (Chow 1959; Mattocks and Forbes 2008), and R_D was derived from *(Breuer et al. 2003).

Land Use	Area (%)	n (sm$^{-1/3}$)	R_D (m)
Agriculture	77.1	0.07	*1.00
Grassland	8.5	0.07	*0.93
Forest	6.2	0.12	*2.00
Developed	3.6	0.10	1.00
Stream	4.5	0.04	0.00

Table 5.3 Evapotranspiration parameter values for all land classifications (Li et al. 2008), where the limiting saturations θ_{wp}, θ_{fc}, θ_o, θ_a, θ_{e1}, and θ_{e2} (m^3m^{-3}), the transpiration fitting parameters C_1 (-), C_2 (-), and C_3 (mmd^{-1}), and c_{int} (m).

Description	Value
Transpiration Limiting Saturation	
θ_{wp}	0.2
θ_{fc}	0.32
θ_o	0.76
θ_a	0.9
Transpiration Fitting Parameter	
C_1	0.3
C_2	0.2
C_3	20
Evaporation Limiting Saturation	
θ_{e1}	0.4
θ_{e2}	0.3
c_{int}	0.00005

5.2.5 Topography

Light detection and ranging (LiDAR) datasets were aggregated for the entire state of Iowa between 2007 and 2010 (IGWS 2010). One meter Digital Elevation Models (DEM) of bare ground surface data was derived from the LiDAR products. The LiDAR products have an 18.5 cm RMS vertical precision, increasing to 37 cm in dense vegetation. A high spatial resolution DEM enabled accurate identification of stream, roadway centerlines, watershed boundaries, and culvert locations for mesh generation. Nodal elevation data representing the land surface was extracted directly from the one meter resolution DEM. Mesh generation boundaries ensured that the extracted elevation data coincided with roadways, and stream centerlines.

5.3 Boundary Conditions

Boundary Conditions for the surface domain were defined as follows: time and space variable surface Neumann boundary conditions forcing a transient solution (i.e.

rainfall, evapotranspiration), critical depth outflow around all exterior edges enabling

excess nonphysical ponded water to exit the system, and uniform depth flow from the

outlet. No flow boundary conditions were assigned to all bottom and lateral subsurface

boundaries. Dual node surface subsurface coupling was used to link the two domains by a

thin numerical boundary, which estimates exchange between the domains by differences

in head at the overlapping surface-subsurface nodes (Fig. 5.6).
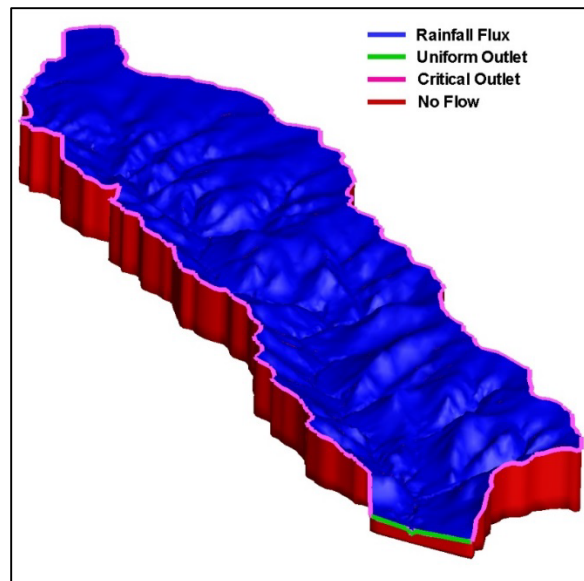
Figure 5.6 Boundary conditions for the surface and subsurface domains.

6.0 MODEL INITIALIZATION

The performance of a distributed surface-subsurface model is largely dependent upon proper initialization (Ajami et al. 2014). As models become more complex, as do the required input parameters and related state variables (Goderniaux et al. 2009). Physics based descriptions of more processes offers a wider range of observation data for calibration, validation, and initialization (Ebel and Loague 2006). Surface flow measurements are well distributed (USGS continuous stream flow), but are lagged by available groundwater data. As briefly described above, the spatial variability of a catchment's hydrologic state is rarely known, as observations are often sporadic in time and space (Ajami et al. 2015).

The fidelity of dynamic unsaturated and saturated watershed simulations are significantly impacted by antecedent condition of the model state variables (Ajami et al. 2014). Identification of a realistic initial condition for hydrologic simulation is required to produce realistic results. An appropriate initial condition allows simulation results to offer insight into the hydrologic processes independent of antecedent conditions (Seck et al. 2015). In an ideal scenario, an initial condition would be the product of a comprehensive field campaign to collect data providing the modeler with an initial snapshot of a given watershed state. Without a data driven initialization, a number of methodologies have been proposed.

Various procedures have been applied to initialize coupled hydrologic models. (1) Initial conditions were be forced by long term averaged rainfall until the hydrologic system reached a steady state in large (greater than 286 km^2) (Goderniaux et al. 2009; Li et al. 2008), and small (27 ha) (Sciuto and Diekkruger 2010) catchments. (2) Initial subsurface head was set equal to the surface elevation. No transient forcing was applied. The subsurface was allowed to drain onto the surface and out of the system, until agreement was found between simulated and observed values (Jones et al. 2008;

VanderKwaak and Loague 2001). (3) An annual cycle of precipitation and evapotranspiration data was applied to a model prior to an event. The goal of transient forcing was to eliminate the system memory of the initialization (Perez et al. 2011; Sciuto and Diekkruger 2010). (5) Analogous to the preceding approach, an annual time series of meteorological data was applied recursively until convergence of hydraulic heads and stream flow was achieved (Ajami et al. 2014; Ala-Aho et al. 2015; Kollet and Maxwell 2008; Rihani et al. 2010). Iteration of transient forcing often produced realistic initial conditions, but requires significant computational time to achieve (Ajami et al. 2015). Iterative forcing has been noted to drive surficial and near surface storages to equilibrium faster than deeper groundwater storages.

In this study a recursive spin up of the year of interest was performed to a 1.0% change threshold in the saturated and unsaturated groundwater storages, and stream flow. Ajami et al. (2014) showed that to achieve a 1.0% change threshold required 2 to 14 recursive years of spin up. In an effort to reduce the recursive spin up time, this study was pre-initialized with a two-step approach. First the ground water table was assumed to be equal to the land surface, the basin was allowed to drain for one year to reach realistic surface base flow conditions. A constant PET of 8.4 mmd^{-1} was applied to the watershed in the absence of precipitation, allowing surficial soils to reach approximately field capacity. This two-step approach acted as an initial condition to 5 years of recursive 2014 atmospheric forcing (rainfall and evapotranspiration). Section 6.1 describes the initial condition convergence results in more detail.

Integrated measures of watershed storage were separated into three components, surface, unsaturated subsurface, and saturated subsurface. To monitor alterations in surface fluxes and subsurface storages, groundwater monitoring wells (15), soil water content monitoring locations (3) at four depths, and a surface flow observation location at the outlet were incorporated into the model (Fig. 6.1).

Flux (surface outlet), water content (soil water), and head (groundwater table) measurements were output for each simulated time step. Water table measurements were Thiessen polygon weighted, resulting in an averaged depth to water table at each time step. An estimate of the total soil water content in the soil column at each of the three sites was produced by assuming each observation location was valid for half of the depth between the next observation location above and below a given observation depth (i.e. the 10 cm sensor is valid from 7.5 cm to 15 cm deep) (Fig. 6.2), Eq. [6.1]. The depth averaged water content estimate was then Thiessen polygon weighted resulting in an averaged estimated volume of water at each time step. For the remainder of this section the surface, unsaturated, and saturated storages will refer to the surface flux, depth and Thiessen weighted soil water volumes, and depth to water table respectively.

Graphical and statistical measures were applied to initialization results, describing the error associated with each annual iteration. Plots for surface, unsaturated, and saturated storages and the associated relative error graphically depicted error trends (Fig. 6.5, Fig 6.6, and Fig. 6.7) Eq. [6.2]. The initialization analysis was completed by investigating the variation in the surface, unsaturated, and saturated storages due to initialization. Each iteration of the 2014 meteorological forcing was compared to the final iteration (5). Each measure was based on changes in a spatially integrated catchment response to recursive forcing. Equilibrium state at the annual time scale was identified by average and maximum relative error from each successive iteration to iteration 5.

$$\theta_d = [(0.075)\theta_{5cm} + (0.75)\theta_{10cm} + (0.20)\theta_{20cm} + (0.45)\theta_{50cm}]\theta_s \qquad [6.1]$$

$$\varepsilon = \left[\frac{S_5 - S_i}{S_5}\right] 100 \qquad [6.2]$$

Where ε is the relative error (%), S_5 is the storage (surfaces, unsaturated, or saturated) for iteration 5, and S_i is the storage for each iteration (1 to 4). The depth weighted water

content is θ_d (m^{3}m^{-3}), θ_{5cm} is the water content at 5 cm (m^{3}m^{-3}), θ_{10cm} is the water content at 10 cm (m^{3}m^{-3}), θ_{20cm} is the water content at 20 cm (m^{3}m^{-3}), θ_{50cm} is the water content at 50 cm (m^{3}m^{-3}), and θ_s is the porosity of the given soil texture (m^{3}m^{-3}).
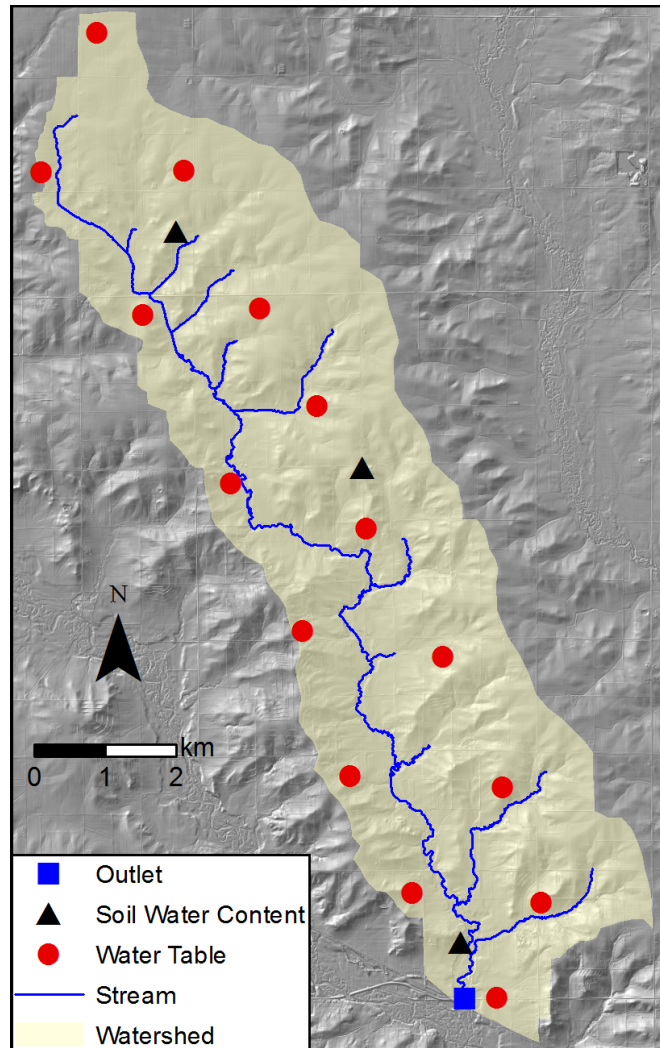
Figure 6.1 Monitoring points for recursive spin up initialization. The depth to the groundwater table was measured continuously at 15 locations (red). Soil water content was measured at 3 locations and 4 depths (5 cm, 10 cm, 20 cm, and 50 cm) (black). Surface water outflow was is monitored at the outlet (blue).
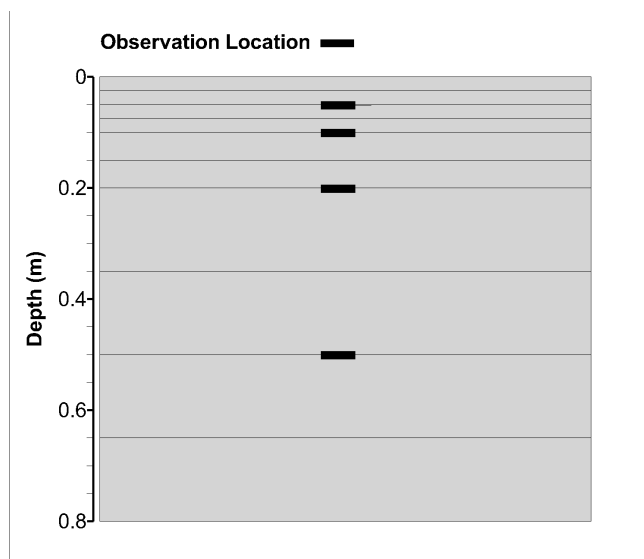
Figure 6.2 Conceptual description of the unsaturated zone and observation depths.

6.1 Recursive Initialization Results and Discussion

Improper initialization of a simulation can result in significant alterations to model storages. The behavior of a model spin up period is directly linked to the initial condition (Seck et al. 2015). A wet initial condition relies on the model's ability to release water from the subsurface, which is dependent on the hydraulic conductivity and water retention functions. A dry initial condition requires atmospheric forcing (precipitation) to increase water storages (Seck et al. 2015). The above deviation from equilibrium and the associated impact has been termed the watershed's "memory" (Lo and Famiglietti 2010; Wu and Dickinson 2004).

Prior to beginning the recursive spin up analysis, the hydrologic system was pre-initialized to a state closely resembling a hydrologic equilibrium. The groundwater table was set equal to the surface, and allowed for free gravity drainage for a year (Jones et al. 2008; VanderKwaak and Loague 2001; Vivoni et al. 2007) (Fig. 6.4 a). Free drainage resulted in a lowering of the water table 2.1 m from the surface, and the soil moisture from 0.40 m^3m^{-3} to 0.23 m^3m^{-3} (Fig. 6.3). Soil moisture and water table levels reached asymptotic behavior quickly. A high intensity PET was applied for one week. This final

week further reduced soil moisture to an average of approximately field capacity (0.14 m^3m^{-3}), and the water table by an additional 0.3 m. High elevation locations and points furthest from the stream drained the most rapidly, with isolated locations achieving a depth to water table of 4.5 m (Fig. 6.4). The pre-initialization described was analogous to combined approaches of drainage and meteorological forcing by De Schepper et al. (2015) and Rozemeijer et al. (2010).
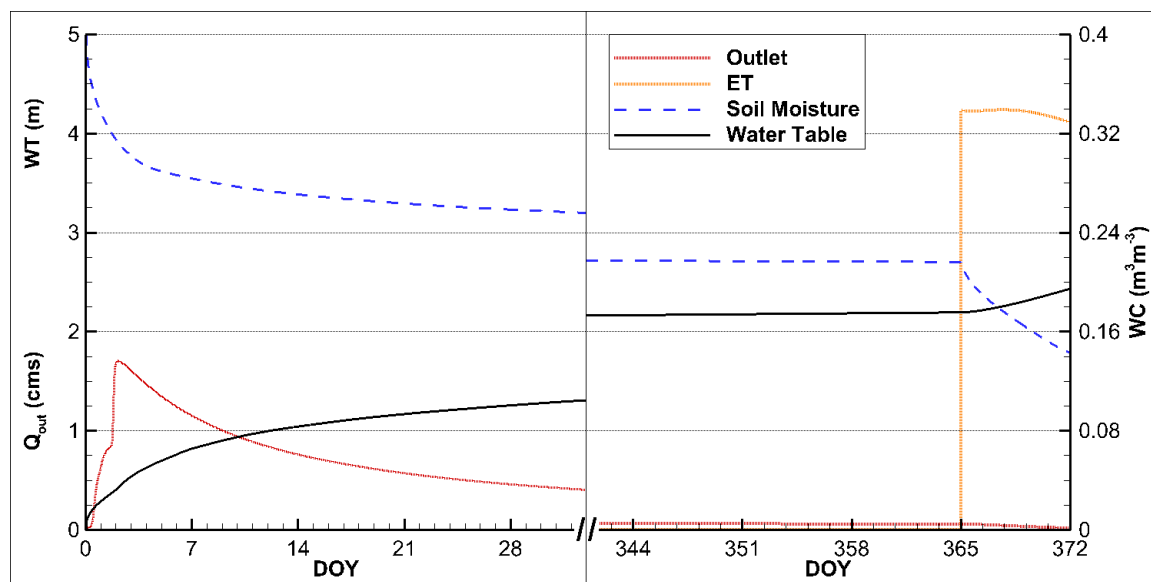
Figure 6.3 Pre-initialization to recursive spin up. One year of drainage beginning from a fully saturated condition (0 d to 365 d). One week of PET at a constant rate of 8.6 mmd^{-1}. Plot depicts beginning 32 days and final 32 days of output. The left vertical axis represents outflow from the basin's surface outlet and from evapotranspiration (cms), and the depth to water table (m).
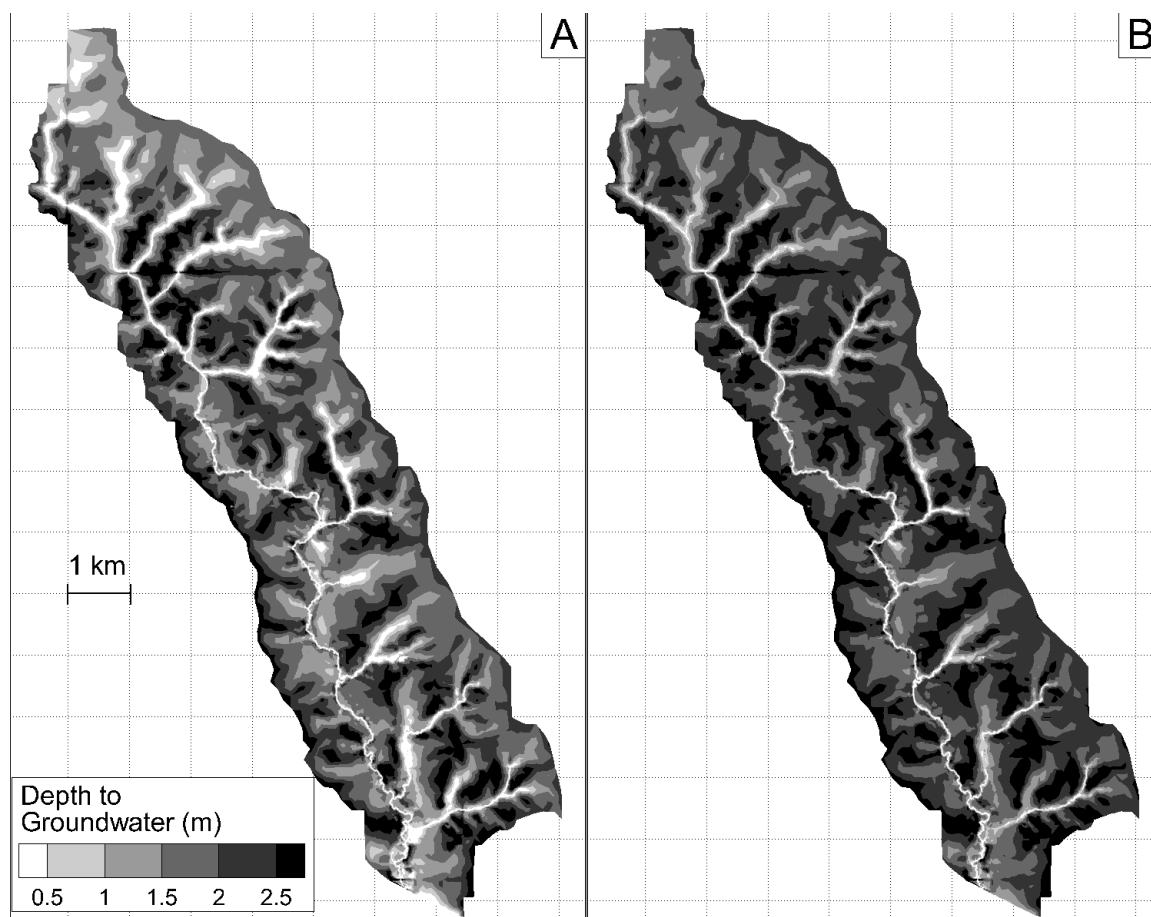
Figure 6.4 Depth to the ground water table for the pre-initialization recursive spin up. One year of drainage beginning from a fully saturated condition, followed by one week PET at a constant 8.6 mmd^{-1}. a) After 365 days of drainage b) After 365 days of drainage and 7 days of PET at a constant rate of 8.6 mmd^{-1}.

To verify that the HGS solutions were independent of initialization, a recursive spin up analysis was performed. The year of 2014 precipitation and PET was recursively input to force the hydrologic model for 5 repeated years. Each successive year of simulation converged to a pseudo steady state.

Integrated ε from the surface and unsaturated zone asymptotically decreased as the simulation time increased. The saturated zone exhibited the opposite behavior, decreasing with each successive iteration. Behavior of the surface flow, and soil moisture were likely initialized too dry, indicated through a large initial negative ε. The depth to the water table was likely too high, lowering with each successive model iteration, noted

by the reducing ε (Table 6.1). Surface flow was initialized the furthest from equilibrium and reacted the fastest to recursive forcing. Surface flow converged to a 1 % change from one year to the next in 3 iterations, and less than 0.1 % in 5 iterations. Soil moisture and water table measures began much closer to equilibrium than surface flow. The water table responded slowly to recursive forcing as compared to soil moisture and surface water. Each measure reached a ε of 1 % after 4 iterations (Table 6.1).

Table 6.1 ε (%) from start to end of each annual iteration of 2014 for a recursive spin up of 5 years. Q, SM, and WT, represent surface flow, soil moisture, and water table errors, respectively.

Year	Q	SM	WT
1	-82.0	-23.4	20.7
2	-6.9	-1.9	6.3
3	-1.1	-0.3	1.0
4	-0.1	0.0	0.2
5	0.0	0.0	0.0

Surface flows peaked at 18.5 cms at DOY 131, due to intense spring rainfall. High evapotranspiration and low precipitation in the summer produced the lowest flow at DOY 232 (Fig. 6.5). ε in surface runoff was always negative, indicating an increase in flow as iterations increased. The global maximum of surface water ε occurred in the first iteration within 10 days of the start of the recursive spin up. The initial large deviation indicated the solution was far from equilibrium. From the initial high ε a decreasing trend in ε occurred from the beginning to the end of each successive iteration. Locally, ε peaked in response to rainfall. Average ε decreased with each iteration to below 1.0 % after iteration 3 (Table 6.2).
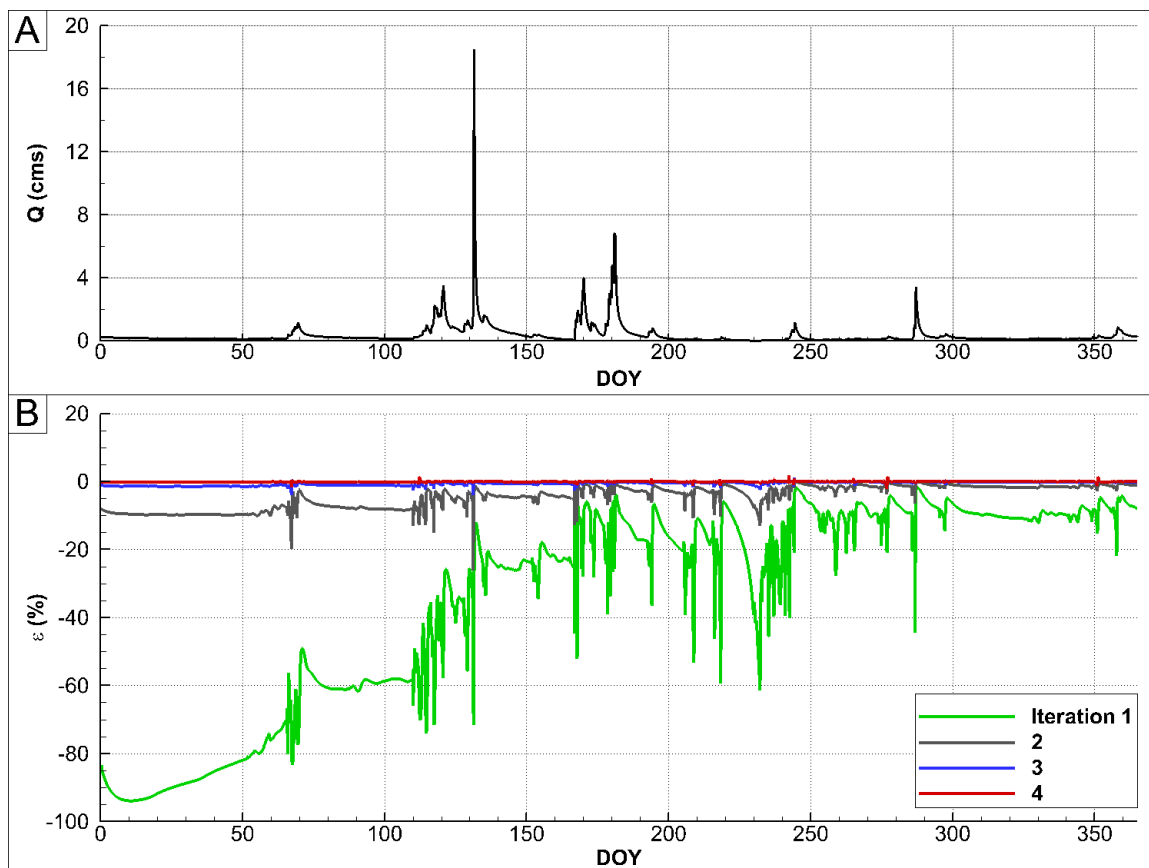
Figure 6.5 Surface outflow for each iteration of 2014 meteorological forcing as compared to iteration 5 during recursive spin up. a) Surface outflow (Q) for iteration 5. b) ε (%) with iteration 5 as reference Eq. [6.2].

Spatial and depth averaged soil water content values ranged from 0.17 m^3m^{-3} to 0.32 m^3m^{-3}, the porosity of loam type soils is 0.40 m^3m^{-3}. Soil moisture responded to rainfall in a similar manner as surface flow (Fig. 6.6). Soil moisture response varied with depth, in timing and magnitude of peak water content. Near surface soil water content (5 cm) had a much larger variability, rapidly changing in response to precipitation and evapotranspiration. Near surface soil moisture observations were muted through depth averaging the observations with the lower magnitude variability of the 10 cm, 20 cm, and 50 cm observation depths. The maximum ε in averaged water content occurred at the onset of simulation, stemming from the pre-initialization period. Peak maximum and minimum local ε occurred in response to precipitation. With each successive iteration the

average and peak ε exhibited an asymptotic reduction. After 4 iterations the average and

peak ε were below 0.1 %. (Table 6.2)
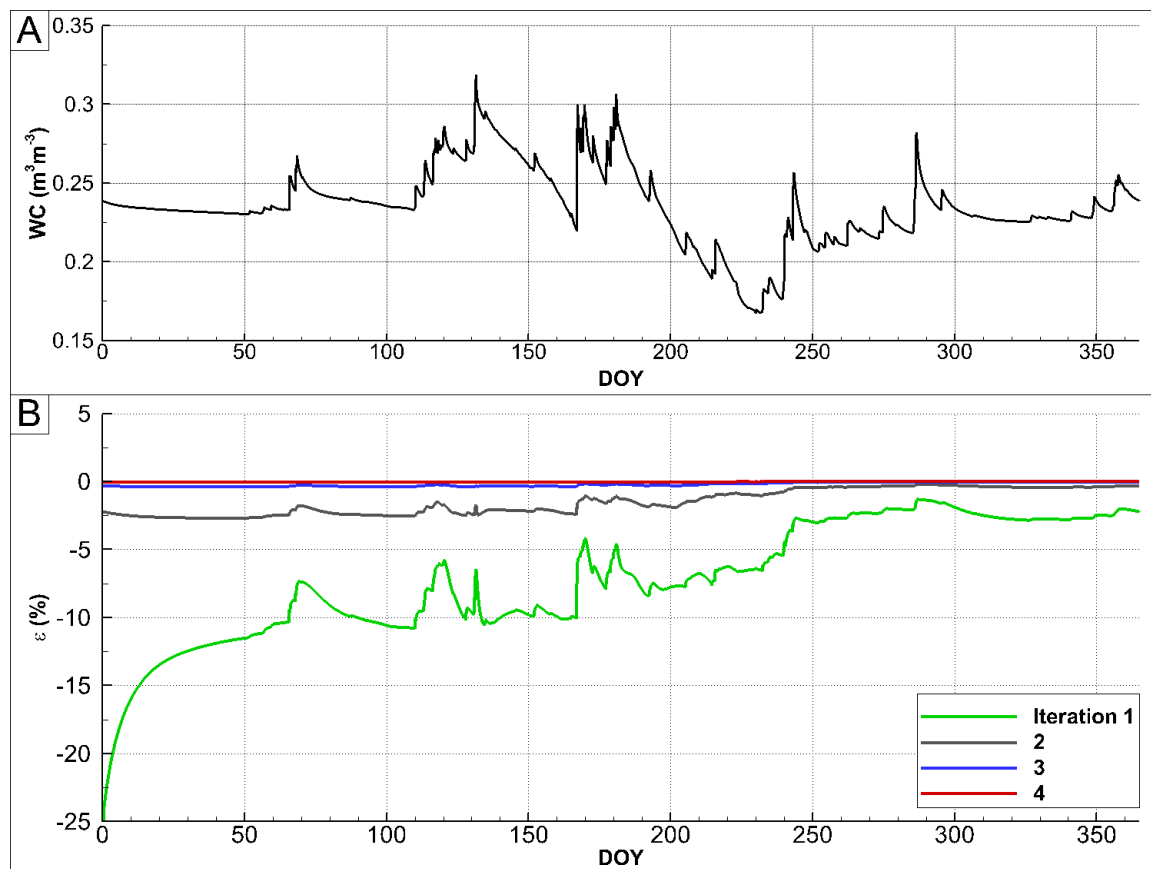
Figure 6.6 Soil water content (maximum of 0.40 m^{3}m^{-3}), for Thiessen polygon weighted average of 3 observation locations and 4 measurement depths, for each iteration of 2014 meteorological forcing as compared to iteration 5 during recursive initialization. a) Soil water content (WC) for iteration 5. b) ε (%) with iteration 5 as reference, Eq. [6.2].

Depths to the spatially averaged groundwater table varied from 0.9 m to 2.9 m

below the surface (Fig. 6.7). Groundwater was closest to the surface in spring and

summer in response to precipitation events. Water slowly drained out of subsurface

storages in response to low precipitation volumes relative to evapotranspiration from

DOY 190 to DOY 250. Subsurface drainage trends only responded to significant volumes

of precipitation. E in depth to water table were largest in the first iteration in response to

significant rainfall events at DOY 120 and DOY 130 (68 %). The lowest ε occurred when

precipitation was low and evapotranspiration was high. E decreased in each successive
iteration to an average of 0.08 % and a maximum of 0.91 % in iteration 4 (Table 6.2).
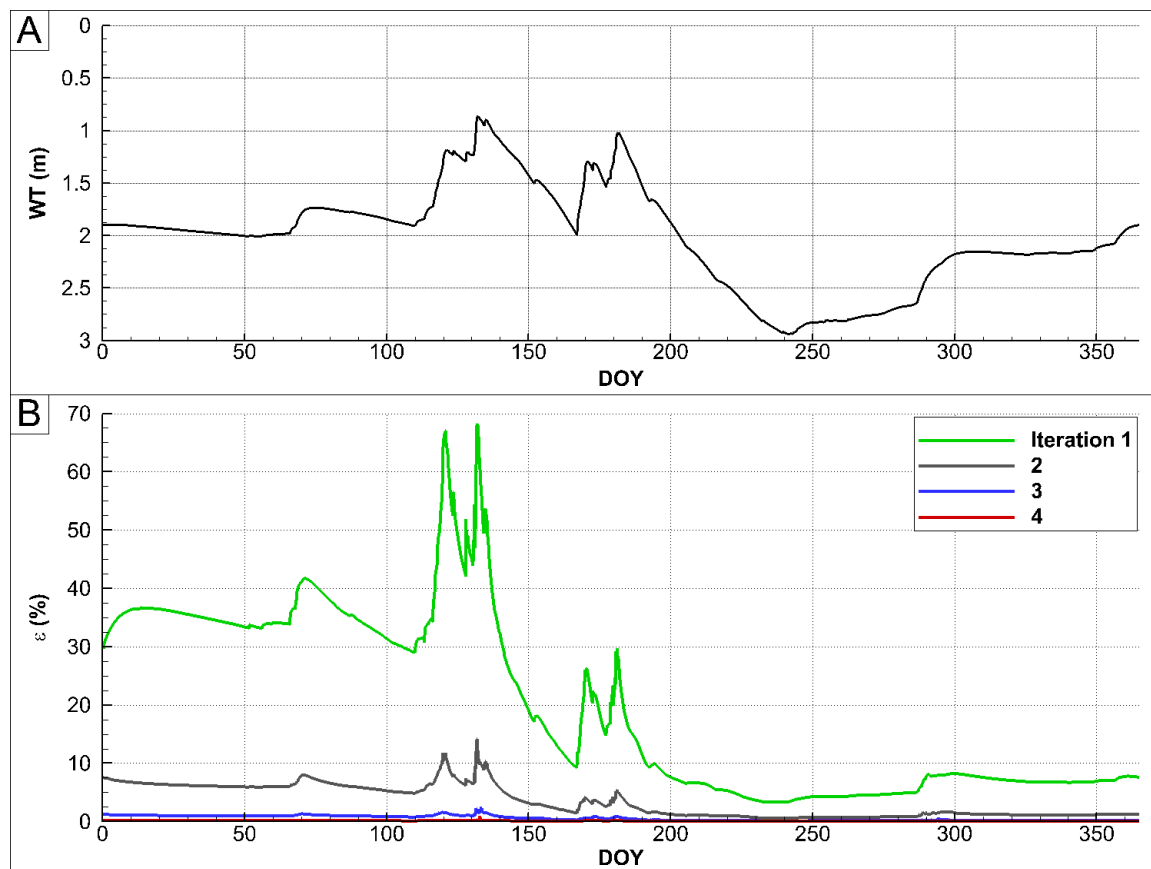
Figure 6.7 Depth to water table for Thiessen polygon weighted average of 15 wells at
each iteration of 2014 meteorological forcing as compared to iteration 5 during recursive
initialization. a) Average depth to water table (WT) for iteration 5. b) ε (%) with iteration
5 as reference Eq. [6.2].

Table 6.2 Summary of ε at each iteration of 2014 meteorological forcing as compared to
iteration 5 during recursive initialization. Q, SM, and WT, represent surface flow, soil
moisture, and water table errors, respectively. Δ_{max} is the maximum ε achieved during the
given iteration. Δ_{ave} is the average ε over a given iteration.

Year	Q		SM		WT	
	Δ_{max}	Δ_{ave}	Δ_{max}	Δ_{ave}	Δ_{max}	Δ_{ave}
1	-94.0	-34.5	-25.1	-7.2	68.2	19.8
2	-26.0	-4.5	-2.7	-1.5	14.2	3.4
3	-3.9	-0.7	-0.5	-0.2	2.3	0.5
4	-2.1	-0.1	-0.1	0.0	0.9	0.1

The pre-initialization of the model began with the surface and unsaturated storages too dry, and the saturated storage too wet. Additional drainage without evapotranspiration and a reduced evapotranspiration flux could offer a pre-initialization closer to equilibrium. Visual analysis indicated a strong linkage between the surface and subsurface model components. Significant rainfall and evapotranspiration impacted each storage zone in a predictable manner, increasing with precipitation and decreasing with evapotranspiration. The surface responded much faster than the soil water, which responded faster than the ground water table. Near surface soils dynamically retard the response of surface and groundwater trends. The dynamic relationships showed that simplified initialization methods may not adequately represent model equilibriums. These linkages indicated the need to spin up model with atmospheric forcing, positive (precipitation) and negative (evapotranspiration) to achieve a proper initialization.

 A convergence threshold of 1.0 % in ε between successive years has been applied to indicate model equilibrium as review by Ajami et al. (2014). Through recursive initialization average component ε were less than 0.2% after 4 years, and less than 0.7 % after 3 years (Table 6.2). A wet model achieved equilibrium faster than a dry initial state as the model is dependent upon its own drainage capacity to reach equilibrium (Seck et al. 2015). Dry models require atmospheric forcing to gain water and reach equilibrium. As a corollary to Seck et al. (2015) a wet year may have the capacity to achieve equilibrium faster.

After 3 successive iterations the model storages converged to an equilibrium state. As compared to Ajami et al. (2015) this was a more rapid response than expected. The rapid response could be due to a successful pre-initialization. After 3 years the model can be applied as an initial condition for other simulations without a significant impact on model solutions. Repeated forcing allowed for direct comparison between years, producing an indication of convergence. Although this may be a pseudo-steady state for

this set of meteorological forcing, a watershed is never realistically in a steady state. Thus, initial condition derived from these analyses offer an initialization which won't drive simulations results, but may not be realistic for a given year.

6.2 Validation of Water Balance Components

The objectives of this study do not require the exact prediction of water balance components, peak flows, or soil water content values. Rather, the study was viewed as a numerical experiment. Through application of physics based modeling and appropriate parameterization, the model provided insight into the impact of various flood mitigation, and common agricultural practices. Furthermore, without commonly accepted calibration targets (outlet, and internal stream flow measurements), fitting parameters to other, approximate estimates was deemed inappropriate. Without calibration, the model was validated to ensure catchment processes were adequately described. Quantitative measures of validity included a partitioning of rainfall into stream flow (Q/P) and evapotranspiration (ET/P), and evapotranspiration into its components.

A recursive spin up through application of 2014 meteorological forcing, was described in Section 6.1 and iteration three was used for model validation. Iteration 3 from the recursive initialization described in Section 6.1 was chosen as convergence to a 1 % threshold was achieved in the surface and subsurface components.

Precipitation in 2014 totaled to 774 mm, of which 248 mm was lost through the surface outlet, and 522 mm was lost through evapotranspiration (Table 6.3). Schilling et al. (2008) calculated ET/P values ranging from 0.75 to 0.85 for a watershed in central Iowa (9,364 km^2). Sanford and Selnick (2013) estimated that ET/P ratios ranged from 0.60 to 0.69 for northern Iowa over a 30 year period (100 km^2 to 1,000 km^2). In this study ET/P was 0.67 which is within the range identified by Sanford and Selnick (2013) and lower than Schilling et al. (2008). In a steady state year the water balance components were in equilibrium, as indicated by a Q/P of 0.33 for this study. Making the same

assumption of the previous two studies Schilling et al. (2008) estimated a Q/P of 0.15 to 0.25, and Sanford and Selnick (2013) of 0.31 to 0.4. Tomer et al. (2003) indicated that watershed response varied at scales with two internal subcatchments, producing a larger response than at the watershed outlet. A result reciprocated through observed data in Ohio (King et al. 2014).

Evapotranspiration represented 522 mm of the precipitation, which was partitioned between canopy evaporation (29 mm), surface evaporation (11 mm), porous media evaporation (149 mm), and transpiration (333 mm). The partitioning of transpiration (T) from total ET (T/ET) was 0.64 (Table 6.4). This result compares well to other studies which indicated an annual average of 0.61 to 0.77 (Kang et al. 2003; Schlesinger and Jasechko 2014; Wang et al. 2013). This transpiration rate has been noted to vary predictably with LAI, from T/ET of 0.0 in pre plant growth periods to 0.9 when LAI was greater than 3.0 m^3m^{-3} (Kang et al. 2003).

Table 6.3 Water balance components annually integrated for iteration 3 of recursive spin up for year 2014. Parenthesis indicate a ratio of each component to precipitation.

Component	Depth (mm)
P	774 (1.00)
Q	248 (0.33)
ET	522 (0.67)

Table 6.4 Evapotranspiration components annually integrated for iteration 3 of recursive spin up for year 2014. Parenthesis indicate a ratio of each component to total ET. E_c represents the canopy evaporation, E_s represents the surface evaporation, and E_{pm} represents the porous media evaporation.

Component	Depth (mm)
ET	522 (1.00)
E_c	29 (0.06)
E_s	11 (0.02)
E_{pm}	149 (0.29)
T	333 (0.64)

It should be noted that the BCW HGS model has not been calibrated to surface or subsurface measurements as none were available. Herein described the partitioning of water balance components which indicated a reasonable allocation of rainfall into runoff and evapotranspiration. The definitive instantaneous values of the simulation outputs from subsequent analyses, should not be directly abstracted from this work without caveat. Calibration and validation of the model for predictive purposes has yet to be investigated. However, the model was shown to adequately simulate water balance partitioning for the year of 2014, wet and dry seasons, and event rainfall partitioning. It was deemed reasonable to study the changes between various scenarios, and in relative water balance components.

7.0 IMPACT OF DISTRIBUTED PROJECTS

In history, the problem of flood mitigation has been described simply as: How large does a reservoir need to be to meet a given inflow demand? (Simonovic 1992). Could it be restated as how many distributed projects are needed to meet a given demand? Distributed flood mitigation through structural or nonstructural measures is not a new concept (Andoh and Declerck 1997; Kurz et al. 2007; Montaldo et al. 2004), typically applied to urban drainages (Emerson and Traver 2008; Emerson et al. 2005; Hamel et al. 2013; Ravazzani et al. 2014). The objective behind a distributed flood mitigation approach is to store excess flood water in upland basins, and soils, reducing the accumulation of downstream discharge.

Recurring floods in 1993, and 2008, 2010, and 2013 have caused billions in damages to the Central U.S., and more specifically Iowa. As described in Section 1.0, the IWP was funded for the purpose of reducing the magnitude and frequency of flooding in Iowa. Per Phase II of the same study, a detailed investigation of distributed a flood mitigation approach was investigated. This section represented the findings of Phase II of the IWP.

It is common hydrologic knowledge that reservoirs reduce and attenuate inflow hydrograph peaks. Runoff water is stored up to a set maximum capacity. The available storage dictates the magnitude which high flows can be mitigated. After the reservoir capacity has been reached, water is released at a rate equal to inflow through an emergency spillway. Prior to exceeding the maximum storage capacity, discharge is released through control structures, moderating storage levels and downstream discharge. Often in large structures the outflow is actively managed to maintain obligatory pool levels or downstream discharges. In small distributed structures the normal pool level is dictated by either an orifice pipe outlet, or a weir structure. In each case, a reservoir built

for the purpose of flood mitigation modifies the downstream flood frequency (Ayalew et al. 2013).

Distributed storage analyses have often been applied to storm water management of urbanization areas, described as source control (Hamel et al. 2013; Petrucci et al. 2013). Impervious surfaces associated with urban development prevent infiltration of rainfall, as a result runoff volumes and peak flow rates increase. To mitigate these negative effects, networks of storm water detention basins retain and reduce total runoff volume and peak. These structures are often multifunction adapting to sediment and nutrient loss from urban landscapes.

These same concepts can be applied to agriculturally developed areas, also producing more runoff than natural conditions (Babbar-Sebens et al. 2013). Kurz et al. (2007) discussed the use of current roadway and culvert infrastructure modified for flood storage. Each upstream structure mitigates the impacts of intense rainfall at the location where they occur. The target of this approach was to control water at the source, reducing the storm flows to match the downstream system capacity. Distributed structures attenuated peak flows across the basin, at a 50% cost reduction as compared to a single reservoir (Andoh and Declerck 1997), and decentralizing the risk of structural failure. Systems of distributed reservoirs either in parallel or in series have been shown to systematically reduce flood peaks throughout the catchment with distributed models (Del Giudice et al. 2014; Montaldo et al. 2004; Perez-Pedini et al. 2005; Ravazzani et al. 2014), and simplified analytic solutions (Del Giudice et al. 2014).

Peak flow reductions in these studies ranged widely from 0.3 % to 36 % (Emerson et al. 2005; Perez-Pedini et al. 2005; Ravazzani et al. 2014; Wang and Yu 2012). Studies investigating retention basins indicated a dependence of peak flow reduction on pre-event storage conditions (Ayalew et al. 2013; Hancock et al. 2010; Montaldo et al. 2004), precipitation intensity (Hancock et al. 2010), event duration (Levy

and McCuen 1999; Petrucci et al. 2013), and catchment characteristics (Del Giudice et al. 2014; Emerson et al. 2005; Wang and Yu 2012).

Precipitation intensity and duration directly impact runoff volume and timing of peak flow production (Hewlett et al. 1984; Levy and McCuen 1999; Petrucci et al. 2013; Radatz et al. 2013). Levy and McCuen (1999) indicated significant effects of design storm duration and depth, on peak flows and storm volumes. Typically, design storms are such that the precipitation is in excess of soil infiltration capacity. Under normal conditions, infiltration excess is a requirement for watershed scale runoff production (Dunne and Black 1970). Without heavy precipitation, only topographically convergent regions of the watershed contributed to surface flow (Dunne and Black 1970; Grayson et al. 1997; James and Roulet 2007; Meyles et al. 2003; Penna et al. 2011).

Many studies have shown an influence of antecedent moisture on the fraction of rainfall transformed into runoff (De Michele and Salvadori 2002; Descroix et al. 2002; James and Roulet 2007; Meyles et al. 2003; Nishat et al. 2010; Penna et al. 2011; Radatz et al. 2013; Sahu et al. 2007). The predictability of hydrologic response is predicated on the knowledge of soil moisture prior to an event (James and Roulet 2007; Meyles et al. 2003). Small drainages in a dry initial state exhibited a dominant vertical movement of soil water movement, a result of increased infiltration. Any water able to exfiltrate back to the surface was reabsorbed by downslope drier soils (Meyles et al. 2003). This produces a disconnection between hillslope and stream response (Dunne and Black 1970; Penna et al. 2011). In a wet state the subsurface responds in unison with surface runoff producing a progressively increasing response as water moves downstream, unable to reabsorb into subsurface materials (Grayson et al. 1997; Meyles et al. 2003). A soil moisture threshold differentiating wet and dry basin response conditions has been estimated at a soil saturation of 49 % (James and Roulet 2007), 70 % (Grayson et al. 1997), 75 % (Meyles et al. 2003), 80 % (Radatz et al. 2013), and 90 % (Penna et al. 2011).

This sections attempts to assess the impacts of distributed flood mitigation detention basins. This broad question was further divided into the effects of antecedent moisture state, available storage, and design storm depth, and at multiple investigation points. A coupled hydrologic model forced with synthetic design storm precipitation was applied to investigate the combined stated effects. The manner in which all these factors compound determined the total effectiveness of the flood mitigation efforts.

7.1 Study Methodology

BCW was selected for Phase II detailed hydrologic assessment as part of the IWP (Fig. 7.1). BCW was selected from the larger, Phase I, Upper Cedar River Watershed (UCRW) (IFC 2014). As compared to other UCRW subcatchments, BCW produced relatively small runoff volumes alone to draw interest as a flood risk. A combination of land owner engagement, further paired funding sources, and an overall high runoff potential of the entire UCRW, indicated that the BCW was the optimal choice. A coupled HGS hydrologic model was constructed, parameterized, and validated for annual water balance simulations, Section 5.0. In this section, nine flood detention structures were added to the model. Simulations were run for single event, variable exceedance probability design storms. Initial soil moisture values were systematically varied to incorporate antecedent conditions into flood reduction estimates. Five design storm depths, nine initial soil antecedent conditions, and three project initial storage scenarios totaled 135 simulation runs applied to envelope project induced peak flow reductions.

7.1.1 Hydrologic Model and Structure Implementation

Prior to the IWP, three constructed multi-purpose wetland type projects, existed in the BCW. Two of the projects were funded by the Conservation Reserve Enhancement Program (CREP) for nutrient reduction purposes (Fig 7.1). The CREP structures were built with a standing pool elevation, saturating the soils and enhancing denitrification. These structures have an emergency spillway at approximately one meter above the

permanent pool elevation, designed for a 0.04 annual exceedance probability rainfall event. The CREP structures were located in the upper one third of the catchment area, draining the least sloped most heavily cultivated areas. In 2015, six new projects were built as dual purpose denitrification and flood mitigation structures. The project designs were completed by private consulting firms and were built to National Resource Conservation Service (NRCS) Conservation Practice Codes No. 410 (NRCS 1985), No. 378 (NRCS 2011), and Iowa Department of Natural Resources (IDNR) Technical Bulletin No. 16 (IDNR 1990).

Section 5.2 described the construction of a 2-D surface grid for BCW consisting of 24,764 elements. Each of the nine structures were incorporated into the mesh through two components, the structural embankment centerline, and the estimated inundation limits of the emergency spillway (Fig. 7.2a). Elevation contours at the emergency spillway elevation were extracted from the DEM and incorporated into the mesh. The mesh was refined in proximity to the detention structures, ensuring the appropriate representation of inundation, flow, and storage.

Flood detention embankments were incorporated into the grid as uniform three node cross sections, positioned perpendicular to the stream centerline. One node was allocated to the embankment centerline at a 10 m spacing across the embankment length. Two additional nodes were allocated 10 m upstream and downstream of the embankment centerline node (Fig. 7.2). Elevations along centerline nodes were assigned a value equal to the top of dam elevation. Elevations of nodes at the normal pool elevation outlet, and the emergency spillway were assigned per design specifications, respectively (Fig. 7.2). Upstream and downstream nodes remained consistent with the original LiDAR derived elevation data.

Structures of ID1-3 were designed as CREP style wetlands, draining on average greater than 200 ha (Table 7.1). These structures were built to maintain a large shallow permanent pool encouraging anaerobic conditions conducive to denitrification. On

average these structures offered 14,000 m^3 of permanent pool storage, and an additional

32,000 m^3 of storage up to the emergency spillway. ID5-9 drained on average 60 ha,

maintained 5,500 m^3 of permanent pool storage, with an additional 18,000 m^3 storage up

to the emergency spillway. In normalizing the additional flood detention storage by the

drainage area (DA) of each project. The IWP funded projects offered more than a factor

of 3 increase in flood storage per unit DA. Each of the IWP, aside from ID 2, were

constructed for the purpose of flood retention. The hypothesis was that ID5-9 projects

would produce a larger reduction in peak flow than the CREP style wetlands (ID1-3).
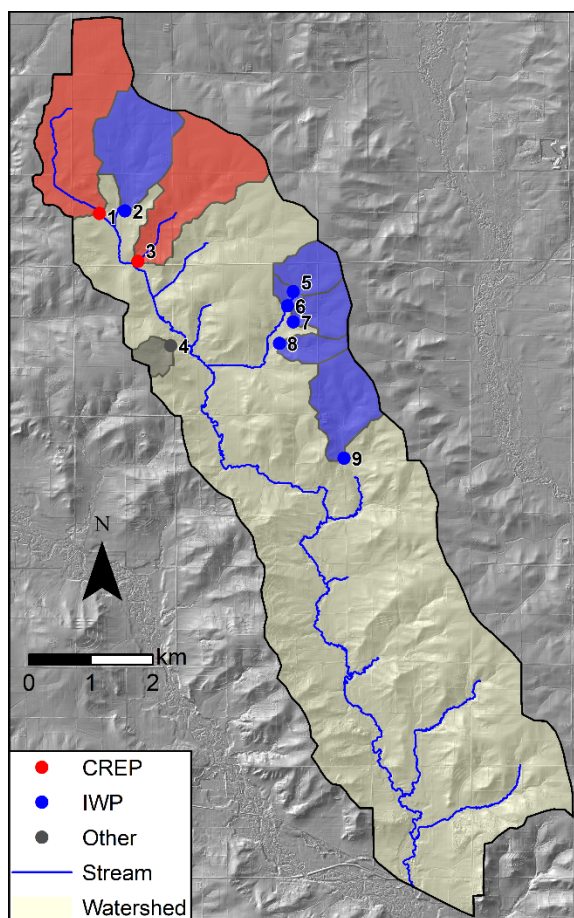
Figure 7.1 BCW structure locations and upstream drainage area. Colors indicate funding source and numbers correspond to Table 7.1.

Table 7.1 Project Specifications. ID corresponds to Fig. 7.2. PP represents permanent pool descriptions, and ES represents emergency spillway descriptions. *Only estimated costs were included in the summary table. Cost for the IWP funded structures were averaged from the total cost of all six projects.

ID	Type	DA (ha)	Elevation (m)		Storage (m³)		Cost
			PP	ES	PP	ES	
1	CREP	263	343.5	344.4	13,800	52,600	$ 162,000
2	IWP	186	344.7	345.3	15,300	40,000	$ 227,000
3	CREP	222	340.4	341.3	14,000	46,200	$ 87,000
4	Other	26	341.3	341.8	7,300	12,200	-
5	IWP	64	351.4	352.6	5,400	26,200	$ 227,000
6	IWP	15	347.4	348.9	4,300	23,300	$ 227,000
7	IWP	56	347.4	348.6	5,400	25,500	$ 227,000
8	IWP	44	343.5	344.1	4,700	13,100	$ 227,000
9	IWP	118	338.0	338.9	7,500	30,800	$ 227,000
Mean		111	-	-	8,600	30,000	$ 201,000
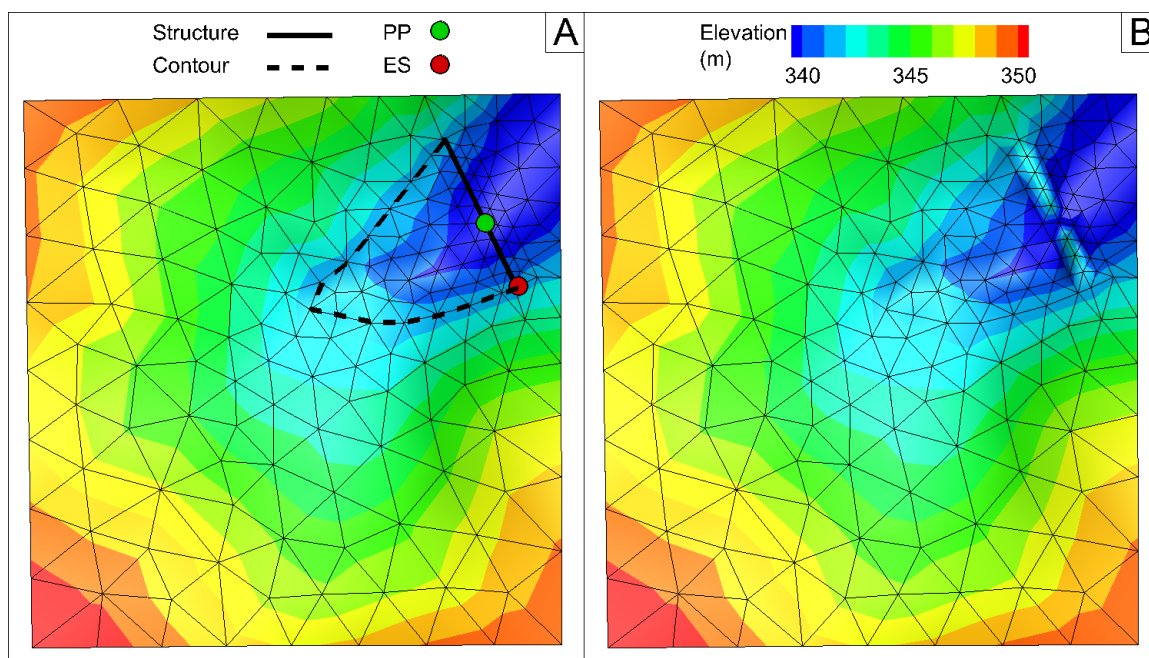
Figure 7.2 Example detention basin implementation at project IC4 (Fig. 7.1, Table 7.1). a) Elevation prior to project implementation with specific mesh and elevation features highlighted. b) Mesh and elevation contour after incorporation of project specific alterations.

7.1.2 Detention Basin Initial Storage

Ayalew et al. (2013) conceptually and numerically investigated the impact of a single reservoir on flood frequency, discharge from the structures was dependent upon the initial storage. Three project conditions were chosen to adequately encompass the detention basin initial conditions, no projects (NP), full projects (FP), and empty projects (P). These conditions represent a control (NP), and maximum peak flow reduction potential (P), and a minimum peak flow reduction potential (FP).

FP simulations were initialized with water up to the permanent pool outlet. The surface water depth initial conditions were achieved by initializing a simulation with 3 m of water depth over the entire surface and allowed to drain for 100 days. The initial depth was enough to fill all natural surface depressions and all of the available storage behind each project. FP simulations were initialized with 93,900 m^3 of surface water.

With the same approach as FP surface initialization, NP surface initialization was completed to fill the natural depressions left on the surface, not attributed to project locations. NP scenarios were initialized with 9,600 m^3 of surface water. This same volume was applied to P simulations, where no water was initially stored behind each structure. The P scenario which allows for all of the storage available is unlikely. This case allows researchers to reasonably capture the maximum magnitude of peak flow reduction this suite of practices is capable of.

NP initialization added 9,600 m^3, and the FP initialization added 93,900 m^3 surface water to each respective scenario. FP initialization incorporated an additional 84,300 m^3 beyond NP scenarios. This volume was attributed to the project storage capacity. The added surface water was larger than design specifications detailed (77,000 m^3) (Table 7.1). The increased volume was due to the sparse elevation sampling in model construction, which occurred at nodal locations. This 9.5 % increase in surface storage could allow for greater peak flow reductions than the projects may achieve in reality.

7.1.3 Subsurface Initial Condition

Accounting for antecedent soil moisture conditions (AMC) prior to event simulations has been recognized as an important factor in peak flow production (Ajami et al. 2015; Berthet et al. 2009; De Michele and Salvadori 2002; Descroix et al. 2002; Grayson et al. 1997; Haga et al. 2005; Heggen 2001; James and Roulet 2007; Meyles et al. 2003; Nikolopoulos et al. 2011; Nishat et al. 2010; Pathiraja et al. 2012; Penna et al. 2011; Radatz et al. 2013; Sahu et al. 2007; Seck et al. 2015). An increased initial soil moisture reduces the available soil pore space to accommodate precipitation, producing larger runoff volumes. Common methods for incorporating AMC into event based models include: Soil Conservation Service-Curve Number (SCS-CN) AMC method (Ponce and Hawkins 1996), the Antecedent Precipitation Index (API) (Heggen 2001), and continuous moisture accounting (Berthet et al. 2009; Grayson et al. 1997; Pathiraja et al. 2012; Sahu et al. 2007) among others. The former two approaches accumulate precipitation depth in the time preceding an event, and relate the depth to a moisture state, altering rainfall-runoff parameters. The latter approach requires an empirical or physical representation of soil water accumulation during rainfall, and loss from ET, lateral flow and seepage.

Without prior knowledge of a distribution to represent soil moisture variability, a non-parametric approach was applied. This study treated initial soil water content as an independent variable over a range of exceedance probabilities based on an estimated cumulative distribution function (CDF) of measured soil water content. Soil water content data was aggregated for a 10 year period beginning January 1, 2002 from the Soil Climate Analysis Network (SCAN, Ames location) (NRCS 2015) (Fig. 4.5). The SCAN data included 5 cm, 10 cm, 20 cm, 50 cm, and 100 cm deep soil water data at hourly time intervals. SCAN soil water content data was shown to vary with depth, and temporally (Fig. 4.6, Fig. 4.7, and Fig. 4.8). Shallower soils were shown to have increased variability, with lower median soil water content values. As measurement depth

increased, median soil water content increased, with variability decreased. The highest median soil water values and lowest variability occurred in the months of March, April, and May, due to spring snowmelt, and rainfall. June, July, and August were attributed with the highest variability and lowest median water content values due to high ET. Temporal trends held true at each depth. Fig. 4.6, Fig. 4.7, and Fig. 4.8 were reproduced for HGS input saturation values discussed in the remainder of this section. Each plot displayed the same median, and variability with time and depth as discussed in Section 4.4 (Fig. 7.8, Fig. 7.9, and Fig. 7.10).

The hourly soil water content data was ranked and plotted for each measured soil depth (Fig. 7.3). Per the SCAN procedure the soil column at each site was characterized, including estimation of soil water retention parameters (NRCS 2004; NRCS 2015). Soil water in HGS was input as a percent saturation, with 1.0 constituting the maximum saturation for each soil type. The estimated soil saturated water content for each measurement depth was abstracted from the SCAN soil characterization (Fig. 7.4). The abstracted values were used to normalize the measure water content values into HGS accepted inputs, ranging from 0 to 1.0. Measured water content values above 0.99 cumulative frequency (Fig. 7.3) for the 5 cm, 10 cm, and 20 cm depths often exceeded saturated water content measurements. Time domain reflectometry was the method applied to measure soil water content at the SCAN site. It measured the dielectric permittivity of a soil water volume, and determined soil water content based on the significant difference between soil, water, and air permittivity values. High clay content, near surface temperature variability, and near surface porosity variability, induced variability in measured dielectric permittivity (Or and Wraith 1999; Seyfried et al. 2005). Soil water content values exceeding the measured saturated water content at each depth were assumed fully saturated and assigned a value of 1.0. This assumption impacted less than 1.0 % of all measured values. At the 100 cm depth, the soil water content was

always above the estimated soil water content. The 100 cm depth was therefore assumed to be always under saturated conditions.

Fig. 7.5 displays the saturation percent values at all levels including horizontal indicators of nine exceedance probabilities input as soil water initial conditions. These initial conditions were extracted and displayed in Fig. 7.6 and Table 7.2, for each exceedance probability against depth. Depths below 100 cm were assumed equal to 1.0 for these simulations. Each exceedance probability was identified under the assumption that the least likely condition was near saturation. In reality, the same approach could be applied to identify exceedance probabilities of an exceedingly dry condition. This study investigated flooding, known to be magnified under wet conditions.

Soil water initial conditions were uniformly distributed across the basin (Fig. 7.7a). Near stream channels the soil was assumed to have a saturation value of 1.0 for the profile depth (Fig. 7.7b). Streams in the BCW were perennial in nature, indicating the subsurface immediately below was likely saturated. Initializing a simulation with an unsaturated stream channel would induce a slower, muted streamflow response.

Nine soil saturation conditions were selected based the estimated CDF (Fig. 7.5), for 0.02, 0.05, 0.10, 0.15, 0.20, 0.25, 0.30, 0.40, and 0.50 exceedance probabilities. These soil moisture initial conditions herein were described by SM02, SM05, SM10, SM015, SM20, SM25, SM30, SM40, and SM50, respectively. These soil saturation values describe the range from exceedingly wet (SM02), to normal wetness conditions (SM50).
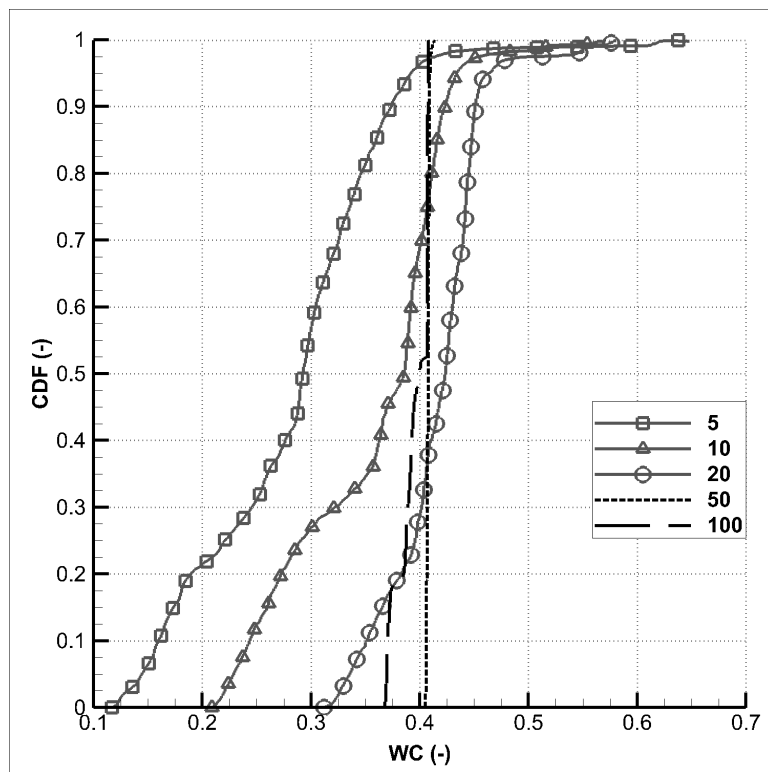
Figure 7.3 CDF of the hourly soil water content (m^3m^{-3}) at 5 cm, 10 cm, 20 cm, 50 cm, and 100 cm depths for the Ames SCAN site (NRCS 2015) (Fig. 4.5).
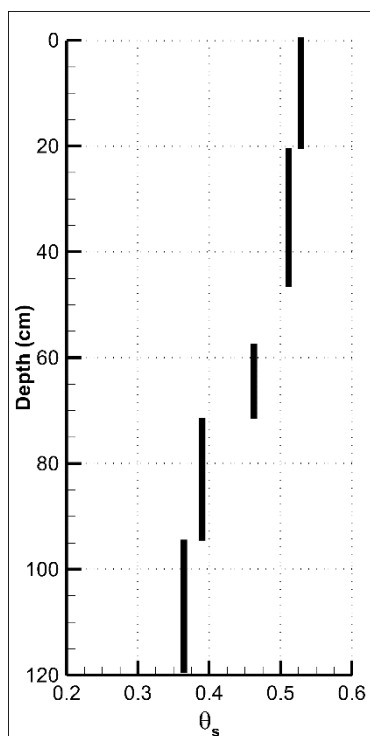
Figure 7.4 Measured saturated soil water content (θ_s) (m^3m^{-3}) describing the depth range over the soil water content sensor depths, from soil water retention curves (NRCS 2015).
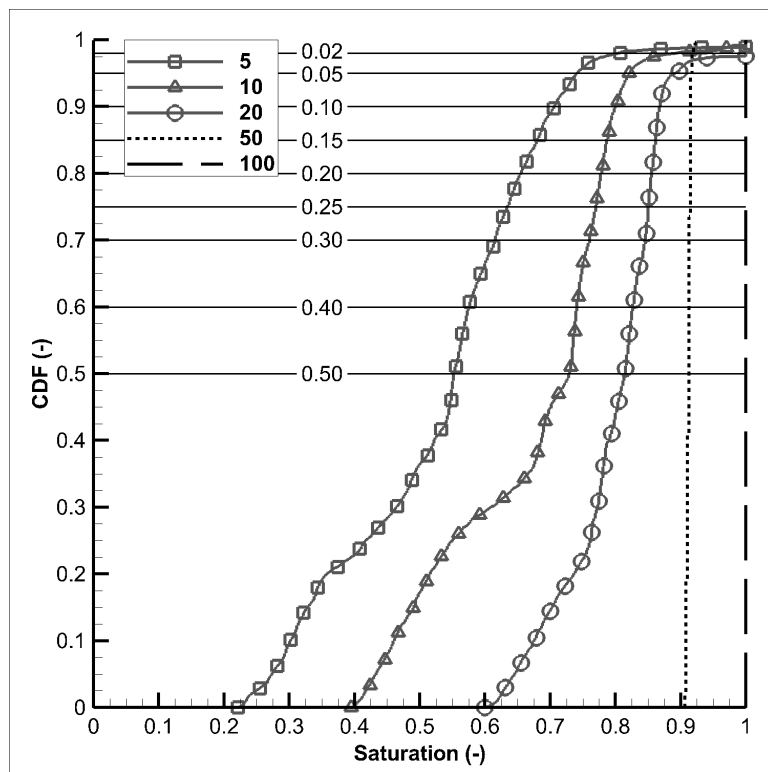
Figure 7.5 CDF of saturation values at 5 measured depths. Horizontal lines represent the initial conditions for event simulation (SM02, SM05, SM10, SM15, SM20, SM25, SM30, SM40, SM50).
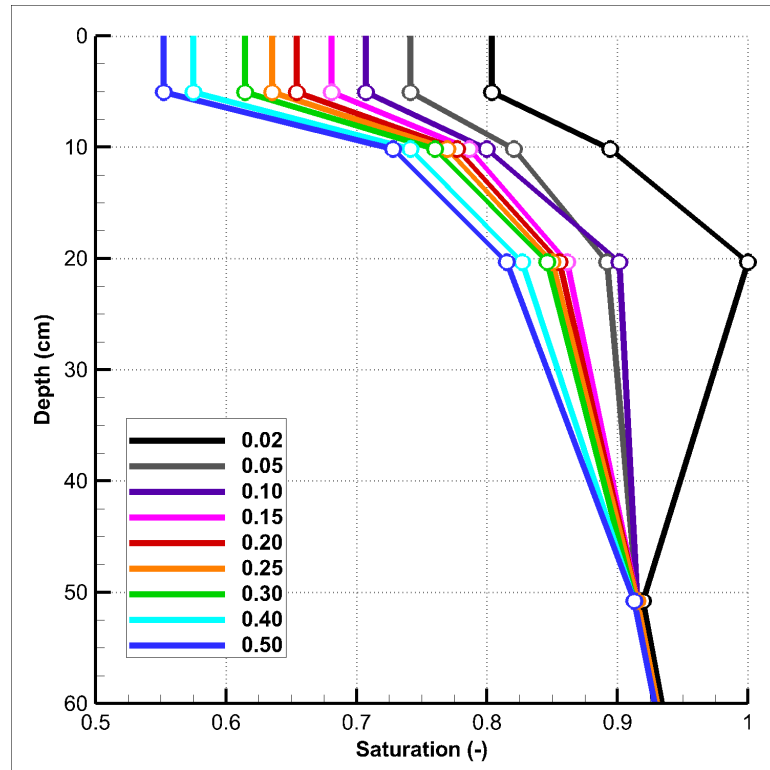
Figure 7.6 Soil water initialization saturation for SM02, SM05, SM10, SM15, SM20, SM25, SM30, SM40, and SM50 over the first 50 cm. 100 cm initialization state was equal to 1.0 for all chosen exceedance probabilities. Circles indicate soil measurement location, lines indicate linearly interpolated HGS input values.

Table 7.2 Arithmetic mean of input saturation over the 5 cm, 10 cm, and 20 cm soil moisture depths for each saturation exceedance probability.

Exceedance Probability	Mean Saturation (-)
0.02	0.83
0.05	0.77
0.10	0.74
0.15	0.72
0.20	0.70
0.25	0.68
0.30	0.66
0.40	0.63
0.50	0.61
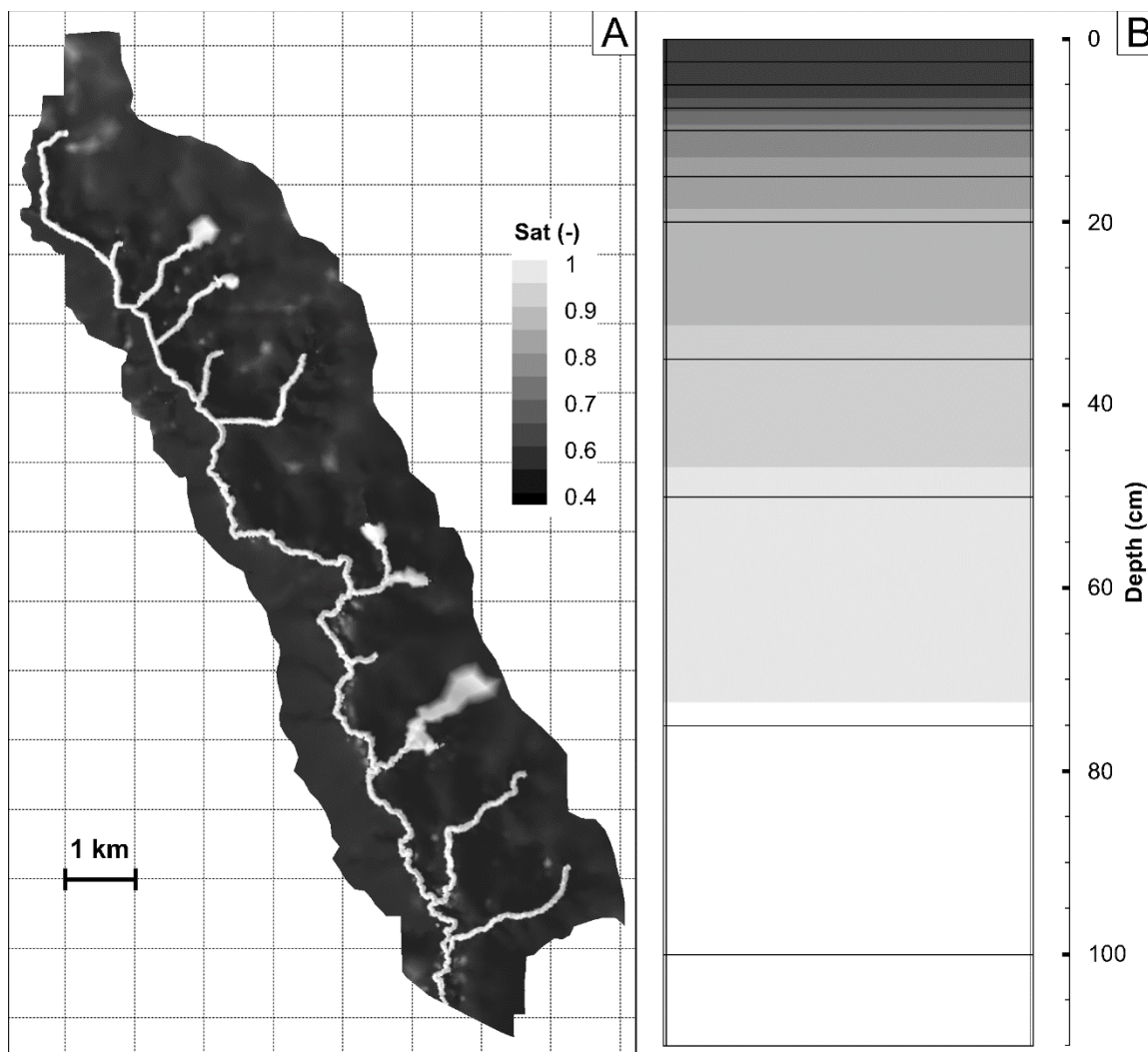
Figure 7.7 Watershed scale model soil water initialization for SM50. a) Plan view of surface saturation. b) X-Z view of 100 cm depth saturation.
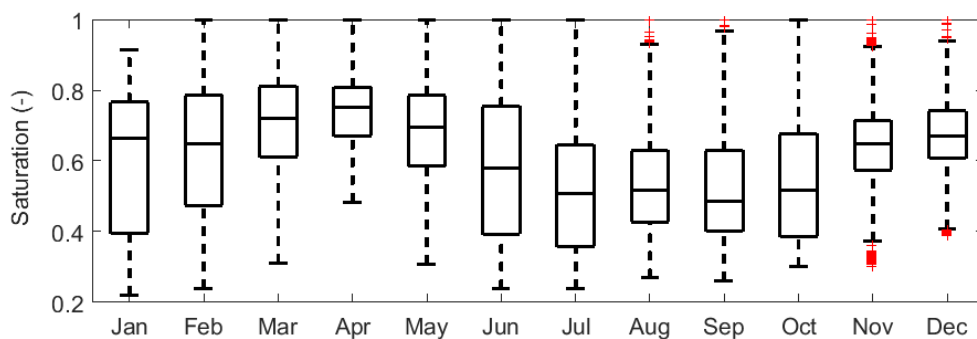
Figure 7.8 Measured monthly 5 cm aggregated saturation from the Ames, IA SCAN location, (Fig 4.5).
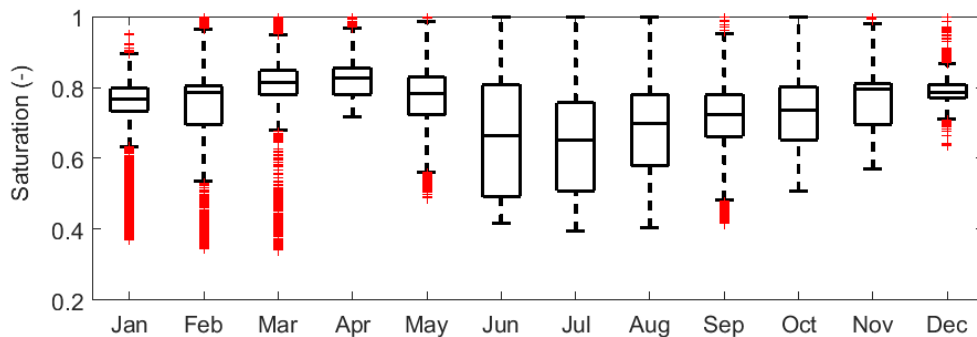
Figure 7.9 Measured monthly 10 cm aggregated saturation from the Ames, IA SCAN location, (Fig 4.5).
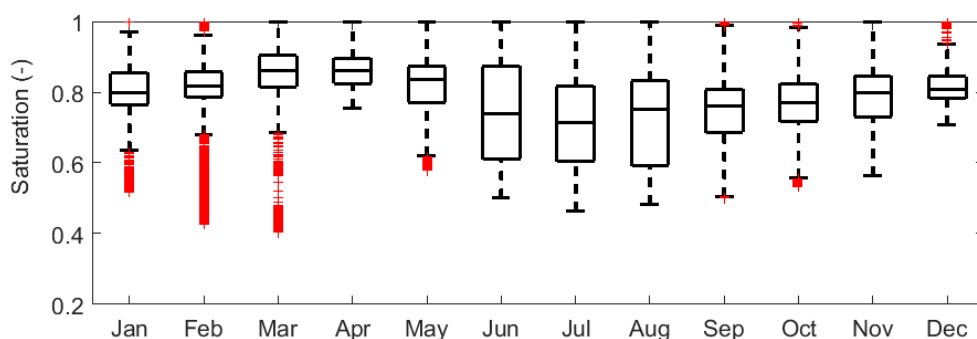
Figure 7.10 Measured monthly 20 cm aggregated saturation from the Ames, IA SCAN location, (Fig 4.5).

7.1.4 Design Storm Precipitation Analysis

The objective of this study was to investigate peak flows in a probabilistic manner (Maidment 1993). A synthetic design storm analysis was chosen in this study to represent the risk of a given event. An annual 24-hour duration, center loaded storm was identified as representative of the basin wide response to storm events (Levy and McCuen 1999). NOAA Atlas 14 point precipitation depth frequency estimates for the 0.2, 0.1, 0.04, 0.02, and 0.01 24-hour annual recurrence frequency rainfall events were selected for simulation (Perica et al. 2013) (Table 7.3). Design storm rainfall depths were allocated temporally by the SCS type II distribution (McCuen 2005) (Fig. 7.11), and uniformly in space (Huff and Angel 1992). Point precipitation frequency estimates were collected at the basin centroid. Spatial rainfall characteristics of heavy rainfall events in the Midwest indicated

that point precipitation estimates were only applicable for areas up to 25 km^2 (Huff and Angel 1992). The area of BCW is just larger than the lower recommend areal reduction factor limit. The recommend areal reduction was minimal and not incorporated into this study.

Five 24-hour design storm precipitation depths associated with the 0.01, 0.02, 0.04, 0.10, and 0.20 exceedance probabilities were selected for simulation forcing. Herein the design storms were referred to as DS01, DS02, DS04, DS10, and DS20, respectively. The maximum rainfall intensity of each design storm was in excess of the soil infiltration capacity (Fig. 7.11b). This range of precipitation depths represent medium to high intensity events, descriptive of possible flood scenarios.
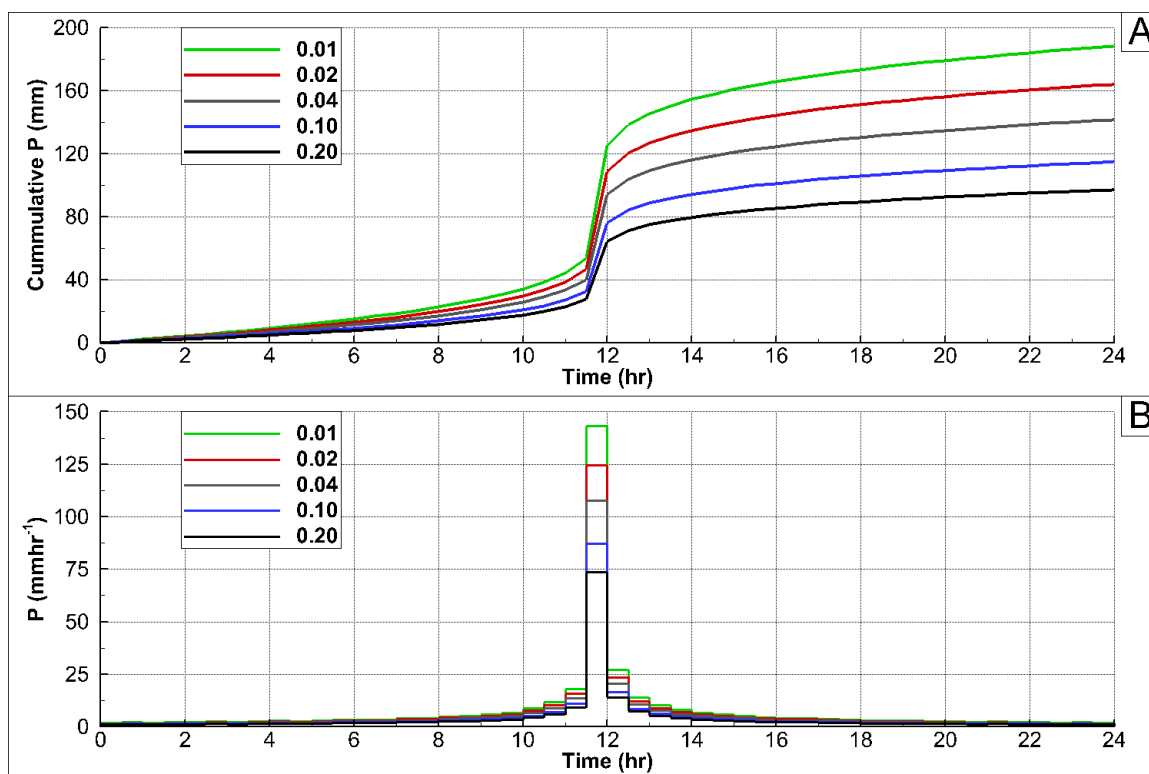
Figure 7.11 Design storm temporal distribution for 24-hour for the five design storms (DS01, DS02, DS04, DS10, DS20). a) Cumulative precipitation depth. b) Precipitation intensity.

Table 7.3 Depth of 24-hour design storm for each simulated annual recurrence frequency (Perica et al. 2013).

Recurrence Frequency	Depth (mm)
0.20	97
0.10	115
0.04	141
0.02	164
0.01	188

7.1.5 Analysis Approach

Each of the five design storm quantiles were simulated, with nine soil saturation initial conditions, and NP, P, and FP storage scenarios. This totaled 135 HGS simulations which encompassed medium to heavy rainfall, normal to saturated soil conditions, and most to least available pond storage. Each simulation was run for the 24-hour design storm window, along with an additional 3 days to ensure stream flow response at all locations had receded to near base flow conditions. Simulated hydrographs were observed at the outlet of each project (9) and along the main channel of Beaver Creek (MC 1-10) (Fig. 7.12). MC observation points were located downstream of each major tributary, such that each individual point was not repetitive.
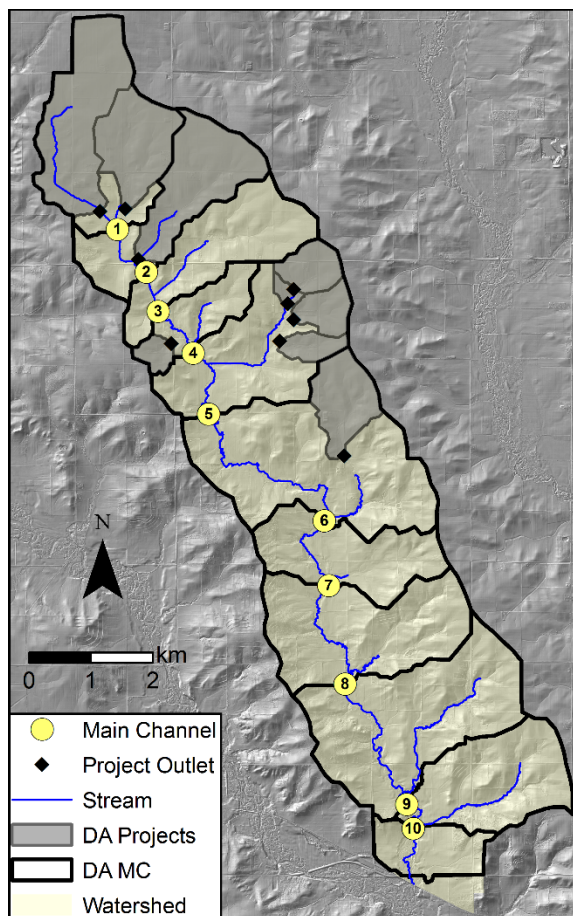
Figure 7.12 BCW observation locations at project locations and on the main stem of Beaver Creek, and contributing DA. MC points are numbered.

Maximum observed discharge values were extracted from each of the 19 observation points, for each of the 135 scenarios. The influence of soil moisture, initial storage, and precipitation depth were investigated in relation to the magnitude of the peak discharge. The downstream 5 observation locations (MC6-10) were isolated, as all detention structures were located upstream. Tributaries to these locations did not have flood reduction structures, so discharge from these regions were unabated, attenuating the upstream peak flow reductions. The rate at which NP, P, and FP scenarios converged as DA increased, offered insight into the peak flow benefits outside of the basin. To extrapolate peak flows beyond the BCW, a flood scaling approach was applied. Flood scaling refers to the scale invariance of peak discharges for an independent, basin wide

events in nested catchments. The capability of this model to observe flow at any nodal location makes this a prime simulation platform to apply this approach. There have been many studies describing the scale invariance in observed natural systems (Ayalew et al. 2015; Furey and Gupta 2005; Furey and Gupta 2007; Gupta et al. 2010; Mandapaka et al. 2009; Ogden and Dawdy 2003), and simulated systems (Ayalew et al. 2014; Ayalew et al. 2015; Ayalew et al. 2014; Gupta et al. 1996; Mantilla et al. 2006; Menabde and Sivapalan 2001), giving credence to this area of study. A power law trend was fit the MC6-10 locations Eq. [7.1]. The least squares fit was extrapolated for NP, P, and FP simulations. At the point of intersection between the NP and P or NP and FP scenarios, the peak flow reduction was assumed to be negligible. This offered the capability to estimate the DA at which the BCW peak reductions were no longer important.

$$Q_p(A) = \alpha DA^\theta \qquad\qquad [7.1]$$

Where Q_p (m^3s^{-1}) is the peak discharge from a single design storm, soil moisture initial condition, and initial storage simulation. DA (km^2) is the drainage area, α (m^3s^{-1}) is the scaling intercept equal to the peak discharge at 1 km^2, and θ (-) represents the scaling exponent.

Peak flow reduction (Q_R) Eq. [7.2] was then investigated for NP and P or FP pairs for a given design storm and initial soil condition. The influence of soil moisture, initial storage, and precipitation depth were investigated in relation to Q_R. The downstream five locations (MC6-10) were isolated and the respective Q_R were fit with a linear trend to better differentiate the effects of varying conditions.

$$Q_R = \left[\frac{Q_{P(NP)} - Q_{P(P)}}{Q_{P(NP)}}\right] 100 \qquad\qquad [7.2]$$

Where Q_R (%) is the peak discharge reduction resulting from a single design storm, soil moisture initial condition, and initial storage set. $Q_{P(NP)}$ (m^3s^{-1}) is the maximum measured discharge at a given observation location for the NP scenario, and $Q_{P(P)}$ (m^3s^{-1}) is the maximum measured discharge at the same observation location for the P or FP initial storages.

7.2 Results

This study investigated the influence of design storm recurrence frequency and soil water initial conditions on Q_p. Further, it investigated how each of these factors influenced Q_R through distributed flood mitigation projects at 19 observation locations within the BCW. This section is divided into four parts. Q_p was investigated for NP scenarios under variable rainfall and soil moisture initial conditions. The following subsection studied the influence of detention structures under varying storage conditions on Q_R. Proceeded by an extrapolation of NP, P, and FP Q_p results beyond the BCW, to identify the relative impact of these projects on downstream flooding. Finally, estimated project costs and Q_R were scaled up to the UCRW.

7.2.1 Peak flow Response to Variable Rainfall and Soil
Water Conditions

This investigation began by isolating the impact of antecedent soil moisture on Q_p at each of the 19 observation locations (Fig. 7.12). Precipitation input was held constant at DS04, while the soil moisture initial condition was systematically varied from 0.50 to 0.02 exceedance probabilities. Each simulation was investigated for the NP scenario (Fig. 7.13). Under this arrangement at the largest DA, increased initial soil wetness increased Q_p. The range of Q_p at MC10 varied from 128 cms for SM50 to 201 cms for SM02, a 36 % difference with SM02 as reference. The largest incremental increase in Q_p occurred between SM05 and SM02. A 5 % saturation increase (Table 7.2) produced an 18% increase in Q_p. As DA increased so did the Q_p. A scale break was apparent at

approximately 20 km^2, below which Q_p increased with DA at a rapid rate. The influence of soil the initial condition held consistent throughout all DA, decreasing in magnitude with a reduction in DA. The distribution of impacts remained approximately 37% variability from SM02 to SM50 at each observation point.
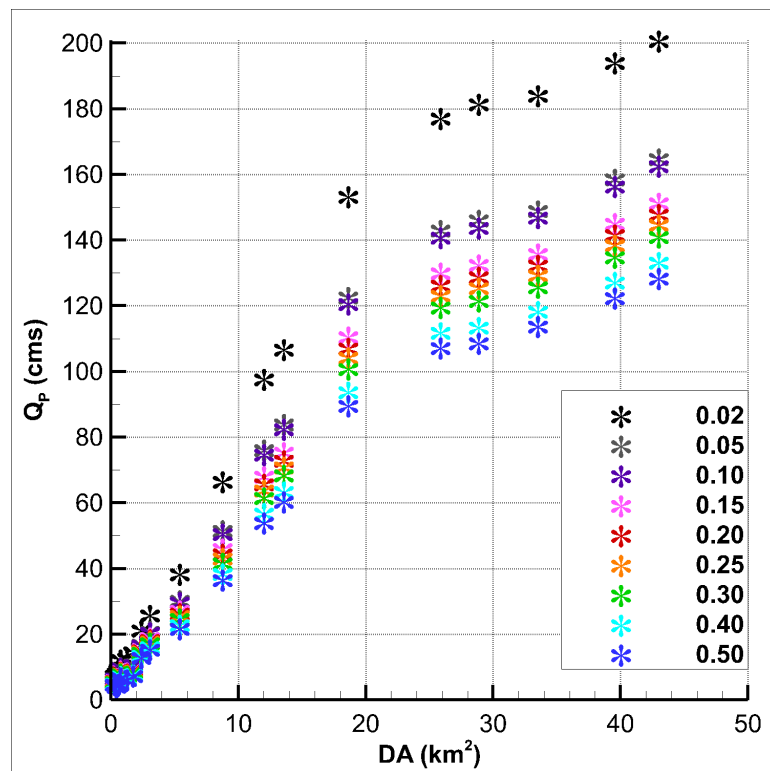
Figure 7.13 Q_p at each observation point, with DS04 over the nine soil saturation initial conditions (SM02, SM05, SM10, SM15, SM20, SM25, SM30, SM40, SM50).

To investigate precipitation depth on Q_p at each observation location, the soil initial condition was held constant at SM20, and the design storm quantiles were systematically varied from DS20 to DS02. Each simulation was investigated for the NP scenario (Fig. 7.14). Under this arrangement at the largest DA an increase in precipitation depth caused an increase in Q_p. At MC10 Q_p varied from 60 cms (DS20) to 260 cms (DS01), representing a 71 % increase with DS01 as reference. As the design storm depth increased, an appreciable increase in Q_p was observed. These observations held

consistent in a relative manner at decreased DA. The scale break identified in Fig. 7.13 was apparent in Fig. 7.14, increasing in severity with increased precipitation depth. The scale break remained at a constant DA for all antecedent soil and precipitation quantiles.
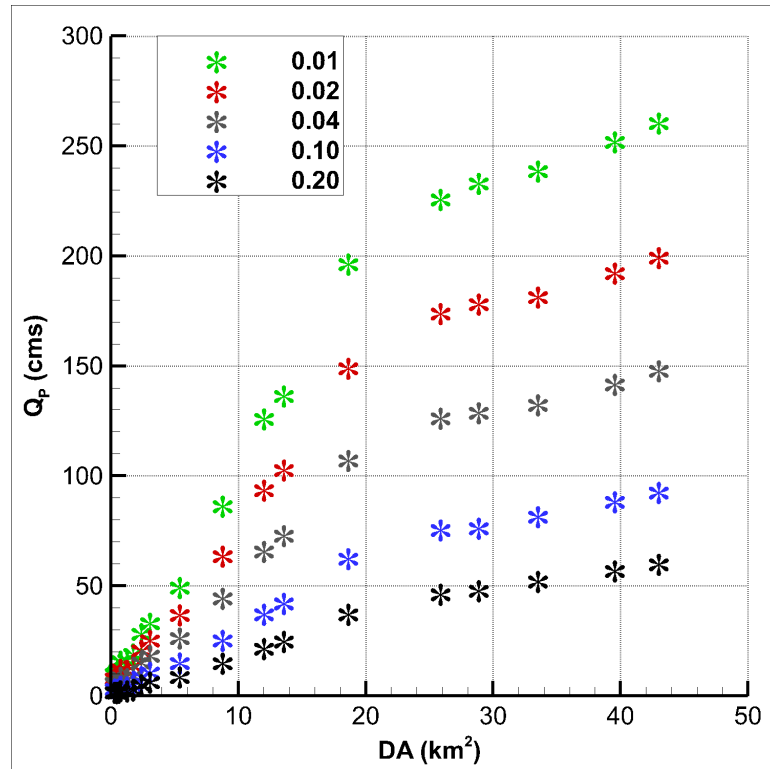
Figure 7.14 Q_p at MC10 for SM20 for the five design storm rainfall quantiles (DS01, DS02, DS04, DS10, DS20).

Fig. 7.15 incorporated both soil initial condition and design storm systematic variation. The input design storm temporal distribution was such that over 45 % of the precipitation depth was input in 0.5 hours, beginning at simulation hour 11.5. Q_p in each scenario always occurred after simulation hour 12. Q_p at upstream smaller DA responded faster to rainfall than downstream MC points (Fig. 7.15). Upstream hydrographs were more peaked than downstream locations. Increased precipitation depth caused an increase in Q_p at each observation location (Fig. 7.15. a, d, g). Stream flow responded faster to larger rainfall depths. Increased initial soil water content produced higher, faster

responses in stream flow (Fig. 7.15 a, b, c). The largest Q_p occurred in response to high

rainfall depths on near saturated soils.
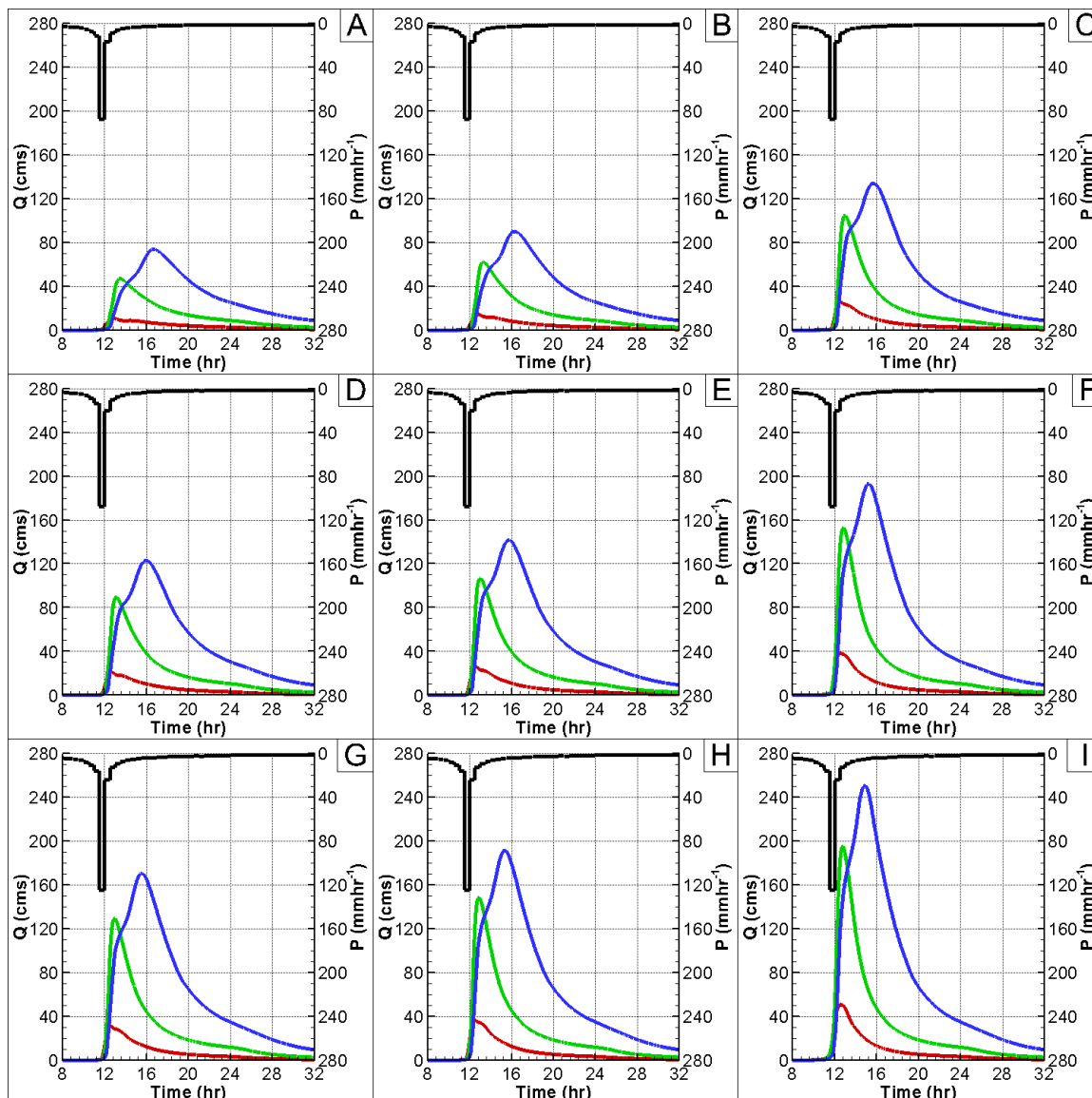
Figure 7.15 Stream response for NP simulations at MC1 (red), MC5 (green), and MC10 (blue). Column 1 represents SM50 (a, d, g), column 2 represents SM20 (b, e, h), and column 3 represents SM02 (c, f, i). Row 1 represents DS10 (a, b, c), row 2 represents DS04 (d, e, f), and row 3 represents DS02 (g, h, i).

Regional flood-frequency equations are commonly applied in the US to predict

annual exceedance discharges at ungauged, or poorly gauged locations. The USGS

regularly publishes methods to calculate extreme events based on hydrologic region and drainage area. Most recently Eash et al. (2013) published a report developing regional regression peak flow prediction equations for Iowa. The current design storm approach leans on the hypothesis that a given annual exceedance probability rainfall event leads to the formation of the equivalent annual exceedance probability discharge (Camici et al. 2011; Viglione et al. 2009). Fig. 7.16 displays USGS hydrologic region and DA based annual exceedance discharge values for each of the five design storm quantiles in this study. USGS estimates were plotted against, the associated design storm simulated Q_p peak for each of the nine soil wetness initial conditions from this study. Simulated and USGS Q_p estimates overlapped under small exceedance probability events for SM50 and SM60 wetness conditions. As the rainfall depth, and subsequent Q_p increased, as did the difference between the simulated and USGS predicted values (Table 7.4).

Table 7.4 Q_p estimates and scaling parameters, Eq. [7.1], for USGS regional regression applied to BCW for only DA as an explanatory variable (Eash et al. 2013).

Recurrence Frequency	α (cms)	θ (-)	Q_p (cms)
0.20	11	0.53	46
0.10	17	0.50	69
0.04	26	0.48	101
0.02	34	0.46	125
0.01	43	0.45	153
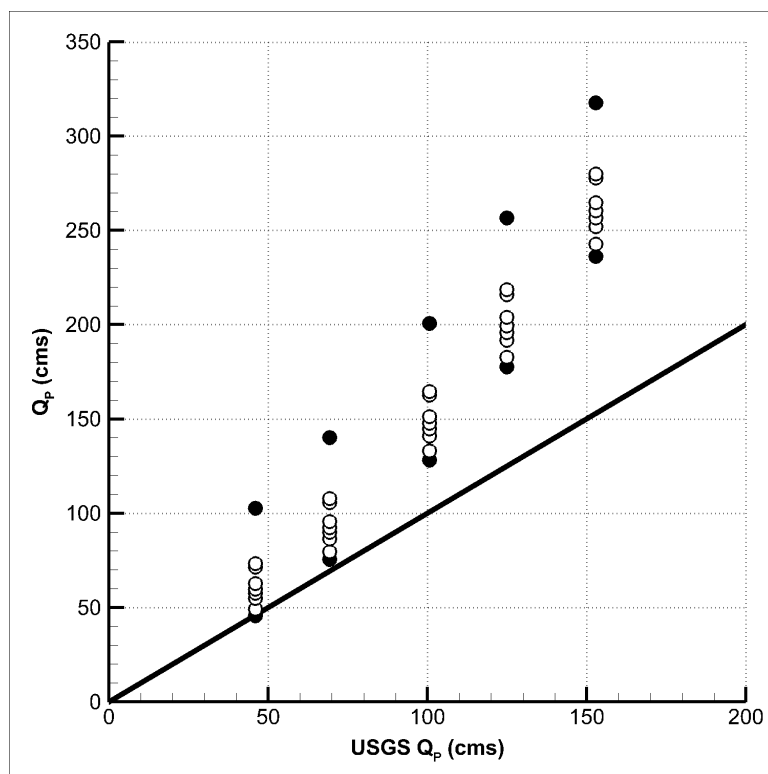
Figure 7.16 Simulated Q_p at MC10 for each exceedance probability soil initial wetness and each design storm depth as explained by the USGS annual exceedance discharge value (Eash et al. 2013), associated with each design storm quantile. Filled circles represent SM50 and SM98 peak discharges, black line represents a 1 to 1 correlation.

7.2.2 Project Induced Peak Flow Reduction

Flood detention structures were distributed across the upper half of BCW, at locations of less than 3 km^2 of upstream DA. The distribution of structures was investigated under the same design storm and soil wetness conditions described previously. The projects were initialized in an empty or full state. These analysis allowed for a complete description of Q_p impacts due to the addition of nine structures.

Q_p increased with response to increased soil wetness, and rainfall depth for P and FP scenarios, consistent with the Q_p of NP simulations. The BCW stream flow response for P and FP scenarios exhibited the same patterns of increased Q_p, and slower response time with increased DA (Fig. 7.17). The remainder of this section focused on the difference of Q_p of P and FP scenarios from NP simulations Eq. [7.2].

Flood detention structures at all observation locations reduced Q_p, and increased the time to peak as compared to NP simulations. Fig. 7.16 isolated DS04 under SM50 and SM02 conditions as an example of P and FP influence on peak flow hydrographs. P simulations reduced Q_p in SM50 simulations, from 128 cms to 126 cms (Q_R of 1.5 %) and 112 cms (Q_R of 12.5 %) for FP and P simulations at MC10, respectively. Increased Q_p was a product of increased saturation conditions. For a SM02 condition Q_p was observed at MC10 to be 200 cms, 189 cms (Q_R of 2.4 %), and 180 cms (Q_R of 10 %), for NP, FP, and P simulations, respectively. In all simulations, at all observation locations, P scenarios reduced peak flow hydrographs in a consistent manner (Fig. 7.17, Fig. 7.18). This held true for FP scenarios, but to a lesser Q_R magnitude than P scenarios.
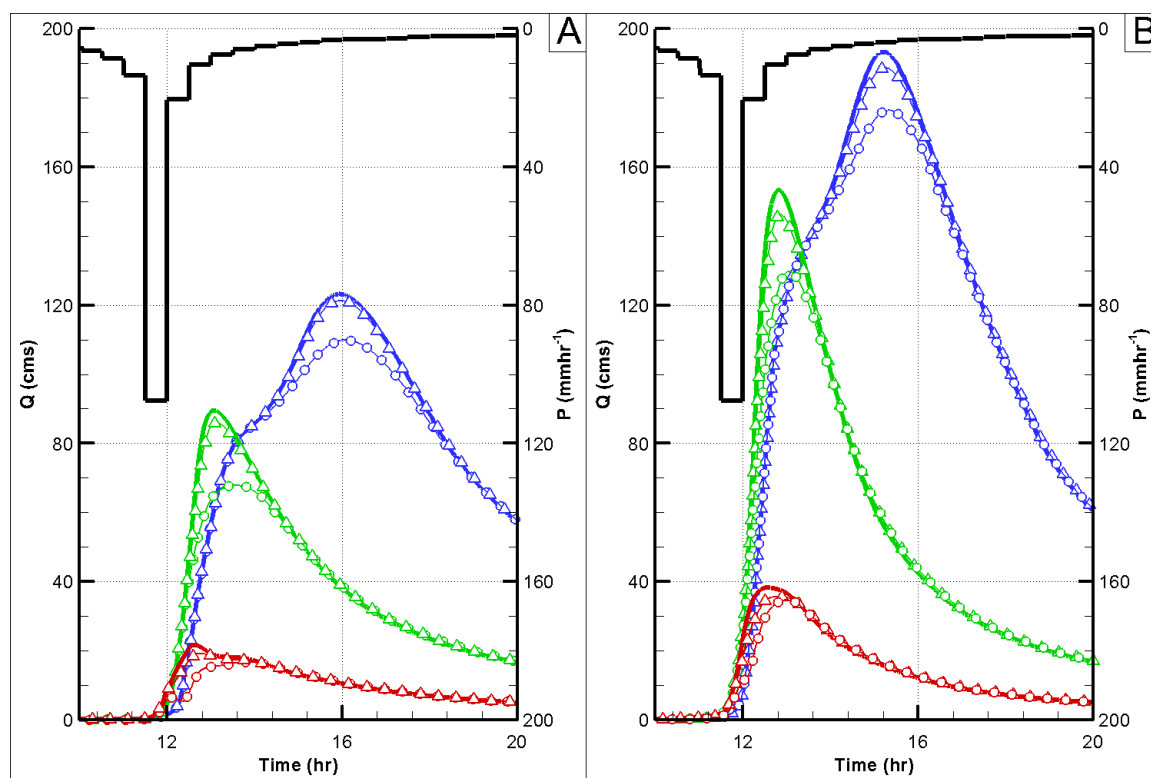
Figure 7.17 Stream response for NP (solid), P (circles), and FP (triangles) scenarios. MC1 (red), MC5 (green), and MC10 (blue). a) DS04, SM50. b) DS04, SM02.
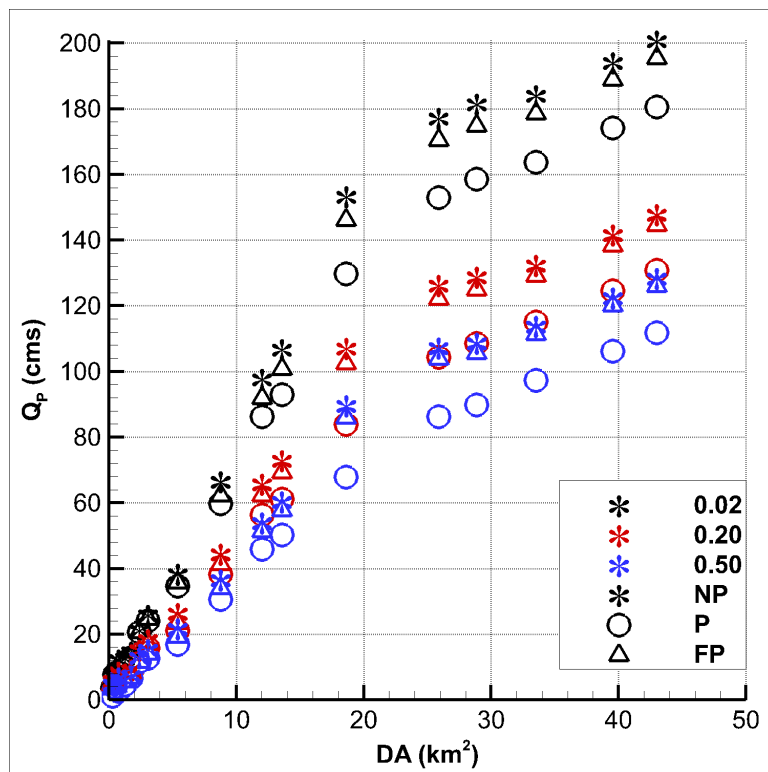
Figure 7.18 Q_P at MC10 for NP (star), P (circle), and FP (triangle) scenarios. For DS04, SM02 (black), SM20 (red), and SM50 (blue).

Fig. 7.19 shows a decrease in Q_R as the as the design storm quantile increased. Larger rainfall depths decreased the effectiveness of projects. The expectation of increased Q_R as the ratio of area drained to a project was not obvious over the entire channel length. Isolating the most downstream observation locations (MC6-10) where projects were no longer added, the expected trend was clearly visible. As the ratio of area upstream of the projects reduced, the Q_R due to P and FP scenarios were overcome by uncontrolled overland runoff.

Extreme variability was observed at the outlet of each project. The large variability in Q_R at the outlet of each project was clear in Fig. 7.19 at the ratio of area upstream of a project of 1.0. Downstream of these locations at MC1-5, an increase in Q_R was observed as the ratio of area upstream of a project increased. This trend was a function of two basin specific features, individual project design, and the DA to each

project. The most upstream three projects (ID1-3, Fig. 7.1) above MC2, were designed as CREP wetlands. These projects have a constant pool elevation and no addition flood storage. These wetland type structures were frequently overcome by large events, but affected the hydrograph peak through delay and attenuation. The projects funded by this research (ID 5-9, Fig. 7.1) were designed with flood mitigation as a primary goal. These structures were more capable in producing larger Q_R than the wetland type designs. There was a large discrepancy of DA to each project, as the wetland style projects (ID 1-3) drained on average 3.5 times more area than the IWP project locations (ID 5-9). Projects which were not designed for flood control received larger amounts of storm water, further decreasing the effects during large rainfall events.
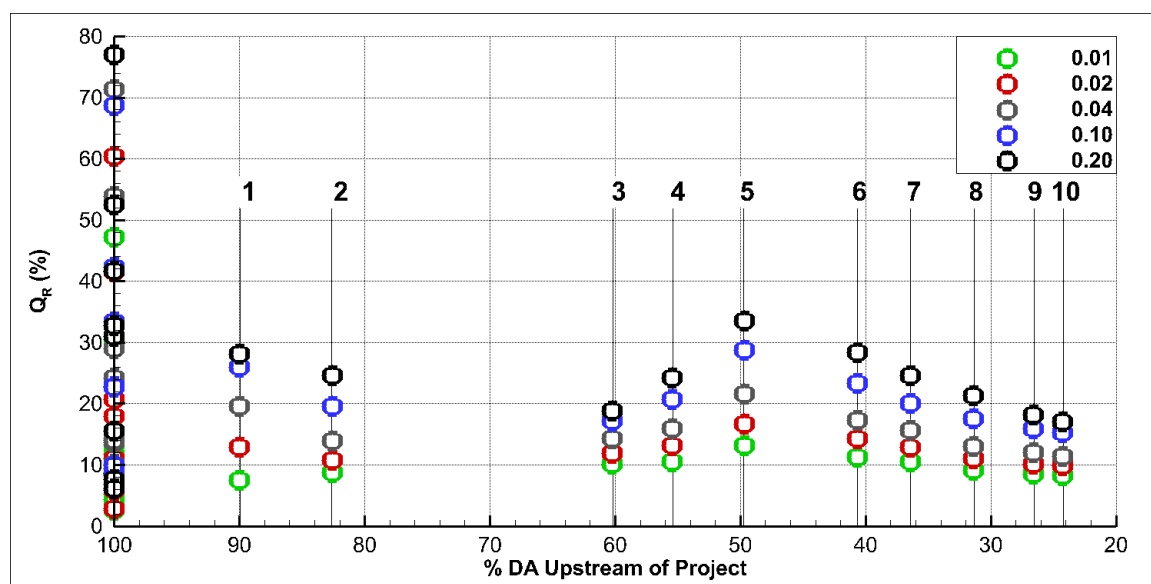
Figure 7.19 Q_R (%) of P scenarios initialized with SM20 for all five design storm rainfall quantiles (DS01, DS02, DS04, DS10, DS20) as explained by the ratio of upstream drainage area that is upstream of a project location for MC1-10 (Fig. 7.10). The number above each set of points correlates to the MC observation number in Fig. 7.13.

Beyond MC6 there were no additional structures added to the MC of BCW. MC6-10 were isolated for further investigation of the attenuation of Q_R. A trend in Q_R for P and FP scenarios was produced with reference to the ratio of upstream area draining to a

project location. Ordinary Least Squares (OLS) regressions were performed and plotted against observations (Fig. 7.20). OLS lines fit the data well, always achieving an R^2 greater than 0.95. Q_R were always the largest at the largest ratio of area upstream of a project. In SM50 (28%) and in SM02 (23 %) Q_R was observed for DS20. Q_R decreased with decreased area upstream of a project and increased rainfall depth. In FP scenarios Q_R was always less than 4 % with a mildly sloping OLS regression line from MC6-10.

Linear regression slopes decreased with increased rainfall depth, and tended to decrease with increased soil wetness (Fig. 7.21b). Inversely the intercept increased with increased rainfall depth, trends amongst the SM initial condition were less distinct (Fig. 7.21b).
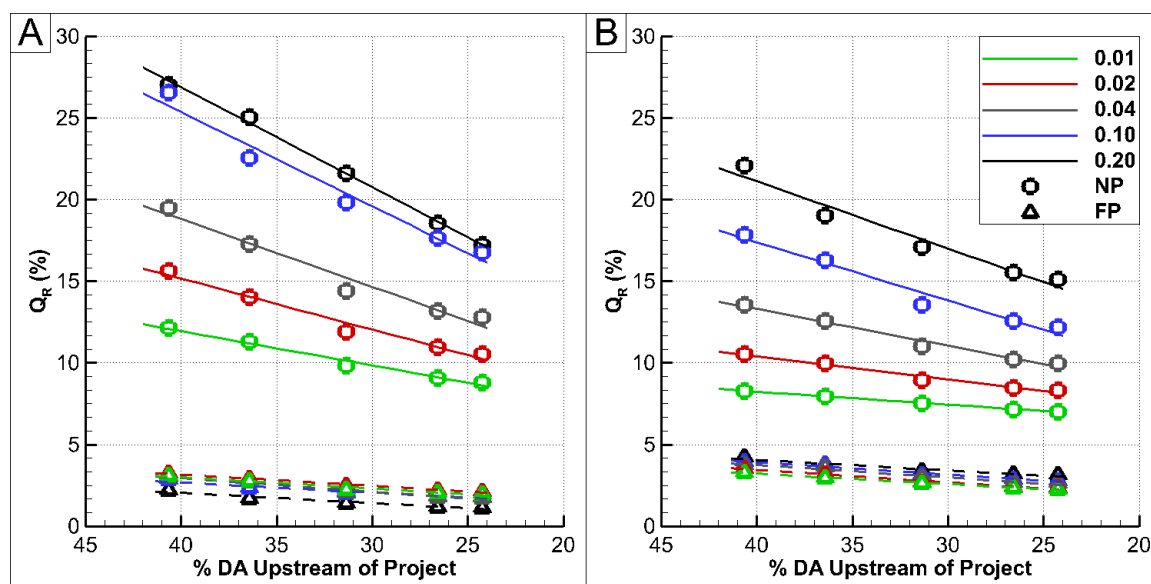
Figure 7.20 Q_R (%) for P (circle) and FP (triangle) for MC6-10 observations and each of the five design storm quantiles (DS01, DS02, DS04, DS10, DS20). Explained by the ratio of upstream drainage area that is upstream of a project location. OLS regression lines described the approximate variability for the P (solid) and FP (broken) scenarios. a) SM50. b) SM02.
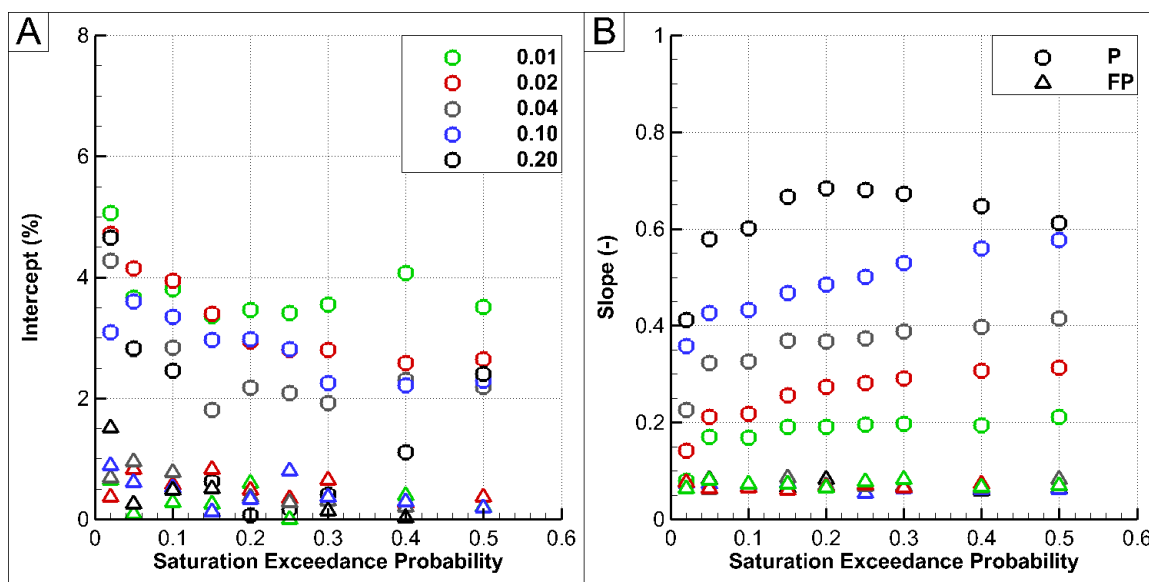
Figure 7.21 OLS regression of Q_R on the ratio of upstream area drained to a project. Results for variable design storm depths (DS01, DS02, DS04, DS10, DS20), and soil initial conditions (SM02, SM05, SM10, SM15, SM20, SM25, SM30, SM40, SM50). a) Intercept. b) Slope.

7.2.3 Extrapolation of Peak Discharge Reduction beyond

BCW

Many studies have discussed the scaling of peak flows in response to varying rainfall conditions, eluding to the influence of antecedent soil moisture and basin characteristic as explanatory variables (Ayalew et al. 2014; Ayalew et al. 2015; Ayalew et al. 2014; Furey and Gupta 2005; Furey and Gupta 2007; Gupta et al. 1996; Gupta et al. 2010; Mandapaka et al. 2009; Mantilla et al. 2006; Menabde and Sivapalan 2001; Ogden and Dawdy 2003). The same has yet to be investigated for Q_R due to the incorporation of flood detention projects. Here we look to investigate the tail of the empirical data, investigating the decay of Q_R influence. This was analyzed under the assumption that the scale invariance can be reasonably estimated from five points, and that the parameters obtained for a power law regression hold beyond the DA of BCW. As a thought experiment, Q_p scaling trends for each scenario were extrapolated beyond the 45 km^2 BCW, to estimate the attenuation effects at larger scales. This process looked to identify the location where projects no longer influence downstream discharges.

A power law least squares regression was performed on MC6-10 for each of the 135 SM, DS, and project combinations. Power law scaling intercept (α) and slope (θ) are displayed for P and NP simulations (Fig. 7.22). A combination of consistently greater α and lower θ of NP simulations as compared to P and FP scenarios ensured the intersection of best fit lines. Each the P, FP, and NP scenarios responded in the same manner to varied soil initial conditions and design storm depth. α increased with increased excess precipitation from 4 cms at DS20, to 82 cms at DS01. As precipitation depth decreased the differences in θ between NP and P reduced. With increasing soil wetness α also increased in a near linear manner. A significant increase in α occurred at the wettest SM02 initial condition. Inversely, with increasing rainfall depth θ decreased. DS01 and DS02 produced approximately the same θ. This could imply a convergence to the minimum possible θ under larger precipitation depths. As soil initial wetness increased the θ decreased in a nearly linear manner. This decrease was greater under lower rainfall depths, and nearly constant at DS01. A significant decrease in θ was achieved with increased soil wetness from SM05 to SM02 in a similar, but opposite manner as α.

Regression based α and θ allowed for extrapolation of Q_p with DA. Q_p was extrapolated from 25 km^2 up to the point of intersection between NP and P scaling relationships (Fig. 7.23, Fig 7.24, and Fig. 7.25). The largest Q_R at MC10 occurred under SM50 and DS20 conditions. These same conditions produced the lowest extrapolated Q_p intersection. This was an intuitive result as the largest difference between in θ derived from P and NP scenarios, and the lowest difference in α occurred for the SM50 and DS20 combination. Under P scenarios, the DA of intersection generally increased with increasing soil wetness, and design storm depth. The largest extrapolated DA was 589 km^2 for DS01 and SM02, the least frequent scenario. This value was an outlier from other extrapolated DA of the remaining combinations of soil wetness and design storm. Typically, these values varied from 90 km^2 to 170 km^2. FP scenario DA intersections

were not distinguishable from each other by soil wetness or precipitation depth. These results generally ranged from 70 km^2 to 180 km^2.
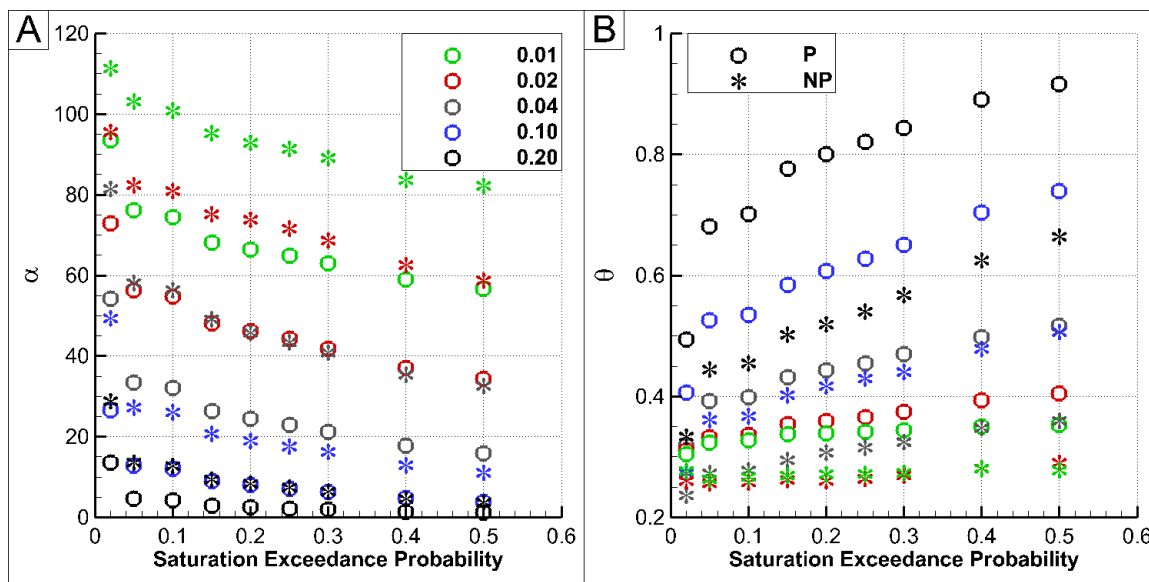
Figure 7.22 Power law regression of Q_p on DA resulting parameters for variable design storm quantiles (DS01, DS02, DS04, DS10, DS20), and soil initial conditions (SM02, SM05, SM10, SM15, SM20, SM25, SM30, SM40, SM50). a) α. b) θ.
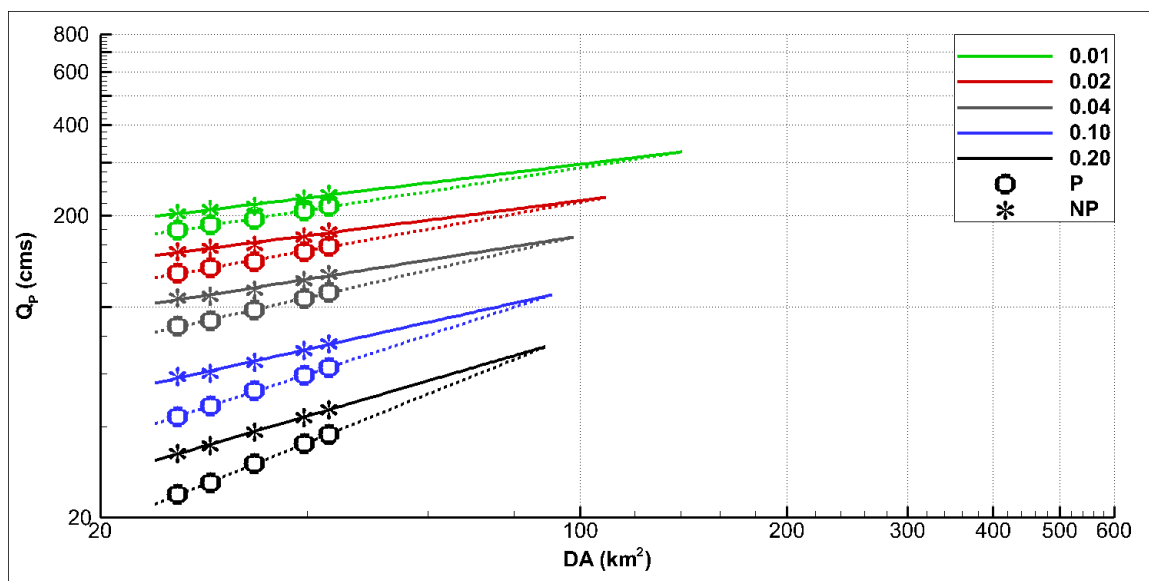
Figure 7.23 Q_p for soil initial condition SM50 of P (circle) and NP (star) scenarios for MC6-10 and each design storm quantile (DS01, DS02, DS04, DS10, DS20). Power law least squares regression lines described the approximate variability for the P (solid) and NP (broken) scenarios. Trend lines terminate at the point of intersection between NP and P extrapolated Q_p.
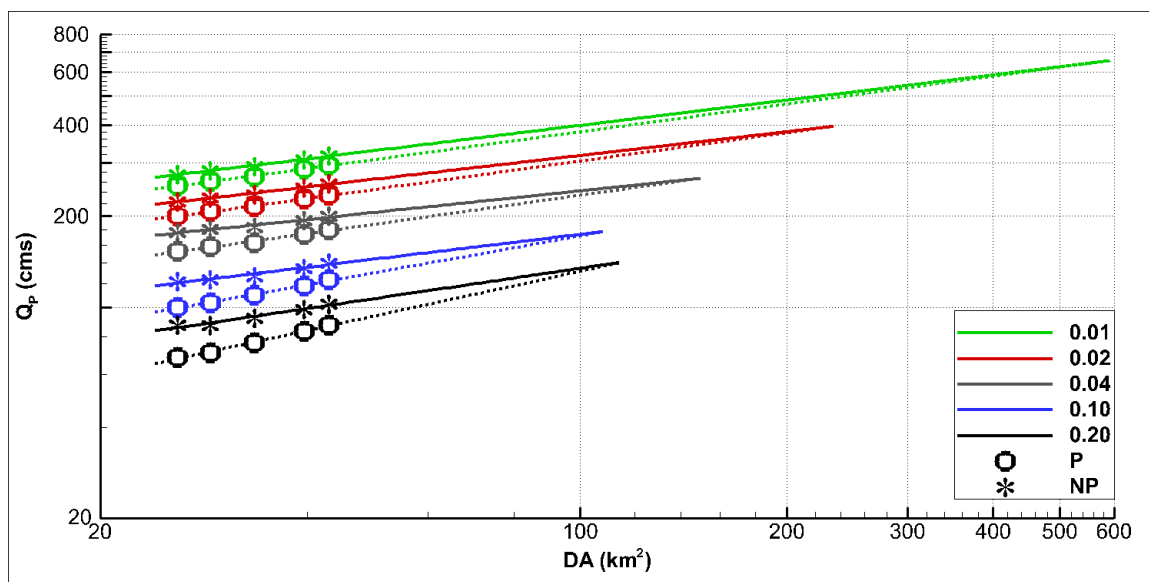
Figure 7.24 Q_p for soil initial condition SM02 of P (circle) and NP (star) scenarios for MC6-10 and each design storm quantile (DS01, DS02, DS04, DS10, DS20). Power law least squares regression lines described the approximate variability for the P (solid) and NP (broken) scenarios. Trend lines terminate at the point of intersection between NP and P extrapolated Q_p.
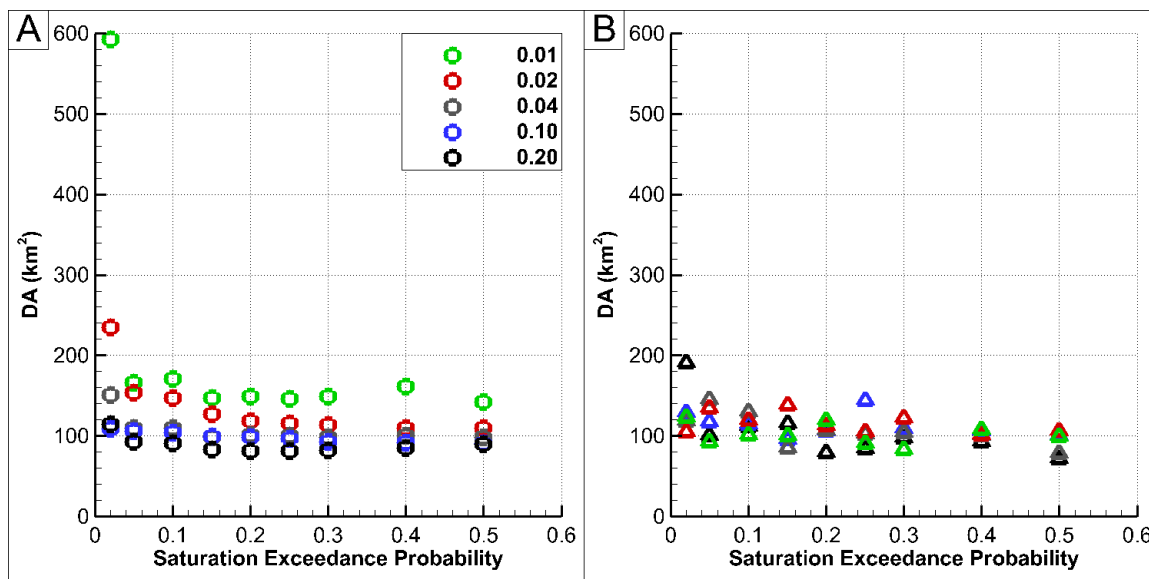
Figure 7.25 Q_p intersection DA for each set of extrapolated power law regression simulations for MC6-10 and each of the design storm quantile (DS01, DS02, DS04, DS10, DS20), plotted against the exceedance probability of each soil moisture initial condition (SM02, SM05, SM10, SM15, SM20, SM25, SM30, SM40, SM50). a) P to NP intersection DA. b) FP to NP intersection DA.

Adding context to the extrapolated DA, Fig. 7.26 displays the UCRW along with major confluence locations downstream of BCW. The first major confluence is located 2 km downstream of BCW. The DA at this location is 50 km^2 most of which represents the BCW. At this location Beaver Creek meets the Little Cedar River totaling 750 km^2 of DA. Under the approximations made in this section, the influence of nine projects in the BCW would not extend beyond this point even under ideal conditions.
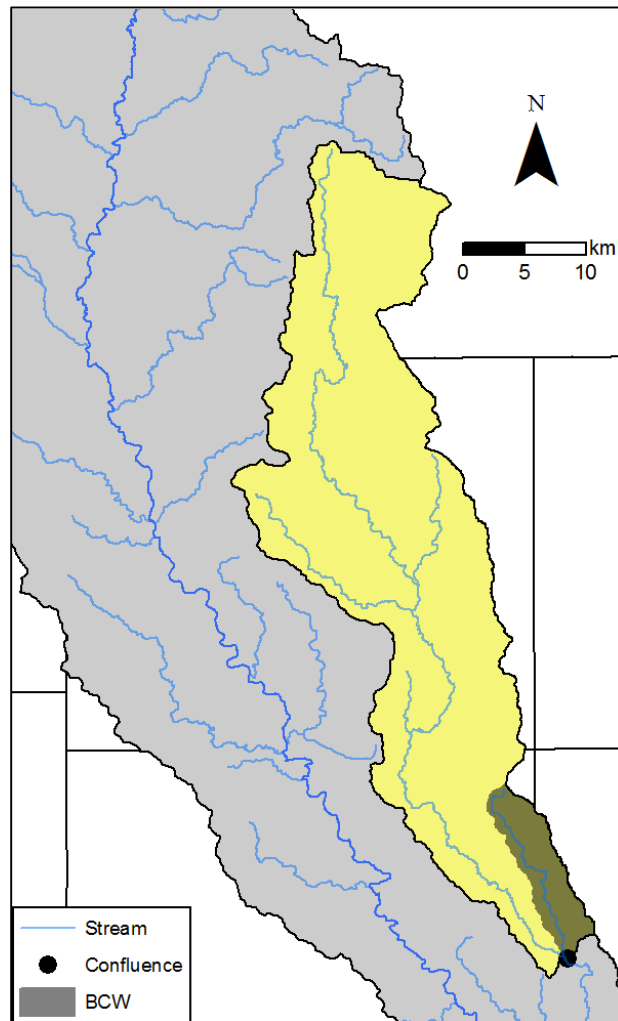
Figure 7.26 Extrapolation of Q_R beyond the BCW. Confluence point indicates the location where Q_R have dissipated. Grey watershed represents the UCRW (Fig. 7.27).

7.2.4 Cost of Peak Discharge Reductions for the Upper

Cedar River Watershed

BCW resulting Q_R was applied as a surrogate in an effort to estimate the quantity of projects required to produce a similar influence at the outlet of the UCRW. BCW was selected for detailed analysis for a number of reasons identified in Section 7.1, one of which was its relative similarity to the UCRW as a whole. Land use, soil type, slope, and physical characteristics such as the aspect ratio were consistent among the two watersheds.

Under the assumption that Q_p in the UCRW can be replicated by BCW. BCW was applied as a scale model of the UCRW. Q_p was normalized to Q_R and DA was normalized to ratio of DA upstream of a project. MC6-10 observation locations were isolated, as indicators of the effects of upstream projects. The ratio of DA to a project ranged from 40 % to 25 % from observation locations MC6 to MC10. In the BCW the average structure incurred a cost of $201,000 and drained 1.1 km^2. These costs and DA were scaled to the UCRW.

The total DA upstream of Janesville, the outlet of the UCRW, is 4,350 km^2. The number of projects and associated construction costs were estimated for systematically varied levels of downstream protection. The area upstream of a project at Janesville was varied from 25% to 40 %. Table 7.5 offers a summary of the calculations to identify the total number of projects required ranges from 974 to 1,559, and costing $196 million to $313 million. If these analyses hold true, Fig. 7.20 can be applied to describe the range of Q_R benefits the detention structures could offer the UCRW. These benefits vary from a maximum of 28 % Q_R to less than 3% Q_R, based on design storm depth and initial soil wetness conditions.

Phase I of the IWP investigated the potential influence of typical NCRS designed detention basins on the UCRW (IFC 2014). 372 prototypical ponds were placed across the watershed in headwater subbasins. Each pond drained 5 km^2 and represented 22.6 %

of the DA upstream of the UCRW outlet. At Janesville, resulting Q_R values produced

through a design storm quantile analysis ranged from 2.5 % to 3%, 4.5 % to 7 %, and 7.5

% to 10 % for varied pond storage capacities. Q_R for Phase I were within the expected Q_R

range of this study, tending towards no available storage BCW results.

 If these benefits were applied to the UCRW as a whole, the downstream impact

could affect the major communities of Waterloo, Cedar Falls, and Cedar Rapids, amongst

other smaller communities (Fig. 7.27). The funding source for the IWP came in the wake

of the 2008 flood which devastated Cedar Rapids. A week of storms progressively

impacting locations lower and lower in the Iowa-Cedar River basin continually increased

stream flow, cresting in Cedar Rapids. The intent of this investigating this location was to

forecast appreciable benefits at Cedar Rapids amongst the other communities, property,

and people of Iowa.

Table 7.5 UCRW percent of area upstream of a flood detention project estimated cost
based on BCW built structures.

Drainage Scenario	Project DA (km^2)	# of Projects	Total Cost
25%	1082	974	$ 195,832,000
30%	1298	1169	$ 235,039,000
35%	1514	1364	$ 274,245,000
40%	1730	1559	$ 313,452,000
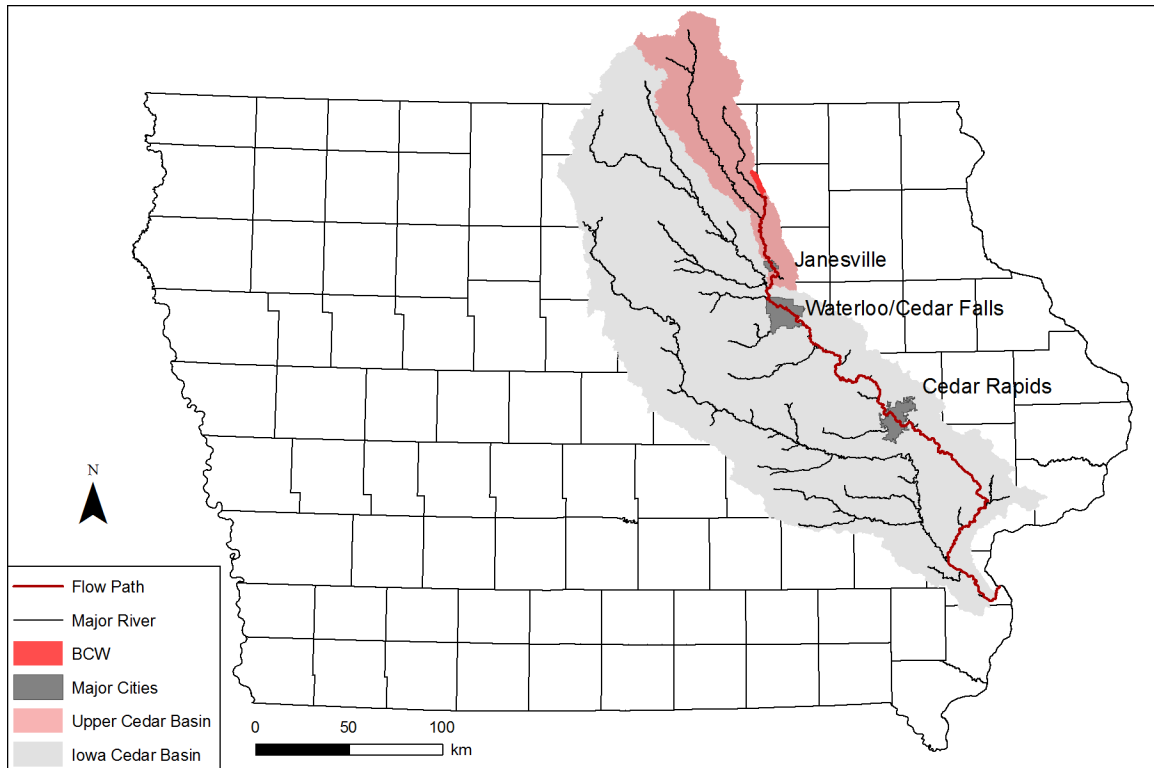
Figure 7.27 Flow path from BCW through the Iowa-Cedar River Basin to the Mississippi River. Flow path indicates potential locations flood mitigation in BCW influence.

7.3 Discussion

This study systematically investigated the influence of initial soil wetness conditions, and rainfall depth on Q_p in a synthetic, probabilistic manner. Q_p increased with increasing rainfall depth, and increasing initial soil wetness conditions, consistent with (Nikolopoulos et al. 2011). A scale break in Q_p was consistently visible at approximately 20 km^2, below which Q_p increased rapidly with DA, and muted above. This scale break was more pronounced under larger rainfall depths. Q_p was consistently higher than USGS annual exceedance predicted discharges for each rainfall design storm.

The addition of flood retention projects reduced Q_p at MC10 by between 3 % and 17 % depending on deign storm depth, initial pond storage, and initial wetness condition. Q_p for P and NP simulations were fit with a power law relationship between Q_p and DA. These values were extrapolated beyond the DA of BCW to locate the point of peak

reduction depreciation. These values ranged from 70 km^2 to 200 km^2 for the majority of NP, P, and FP sets. The extrapolated results divulged that Q_p would be unnoticeable beyond the confluence of Beaver Creek with the Little Cedar River 2 km downstream.

Q_R due to projects observed in this study were well within the variability indicated in literature (0.3 % to 36 %) (Emerson et al. 2005; Perez-Pedini et al. 2005; Ravazzani et al. 2014; Wang and Yu 2012). A strong dependency of Q_R on pre-event storage conditions (Ayalew et al. 2013; Hancock et al. 2010; Montaldo et al. 2004), and precipitation intensity (Hancock et al. 2010) were observed in this study. While, heterogeneity in catchment characteristics became less important with increasing DA (Del Giudice et al. 2014; Emerson et al. 2005; Wang and Yu 2012).

7.3.1 Analysis of the Antecedent Condition

In rainfall design storm analysis, it is assumed that the simulated Q_p has the same return period as the input storm quantile for small impervious drainages (Bradley and Potter 1992; Packman and Kidd 1980). This does not hold true at larger scales and pervious surfaces, where antecedent soil moisture, and spatial and temporal rainfall cannot be assumed uniform (Bradley and Potter 1992; Brocca et al. 2008; Castillo et al. 2003; Huff and Angel 1992; Levy and McCuen 1999; McCuen 2005). The antecedent conditions for design storm analysis are usually assumed in an "average antecedent condition" for the catchment (Pilgrim and Cordery 1973). This assumption minimizes the variability encountered as their probability of occurrence of either higher or lower values is the same. A clear methodology has yet to be proposed for initialization of physically based models in design storm simulations. This is likely due to physically based models incurring initialization and spin up errors.

In this study, a probabilistic approach based on hourly measured soil water content was applied, producing average soil saturation values of 0.83, 0.77, 0.74, 0.72, 0.70, 0.68, 0.66, 0.63, and 0.61. Q_p simulation for each SM initial condition displayed a

threshold value between 0.77 and 0.83, average surface soil saturation. At the highest SM quantile a sharp increase in Q_p was observed. A shift in the calculated fitting parameters for linear and power law regression, and the runoff coefficient (not show here) were clear. This threshold range aligns well with that reported by Radatz et al. (2013), identifying an 80 % soil saturation threshold. This consistency was likely due to similar physical characteristics of the Tama silt loam soil series to those found in the BCW.

This threshold finding may be skewed by the design storm temporal distribution. As the rainfall peak occurs 11.5 hours after the initiation of rainfall. An accumulation of 28 % of the total rainfall depth occurs prior to the peak. Under high total rainfall depths, or high initial soil wetness levels pre-peak event rainfall can cause significant runoff. In the situation where pre-event rainfall does not cause infiltration excess runoff, infiltration of precipitation increased the initial soil moisture. To elude this issue, a front loaded cumulative precipitation distribution could be used. This approach has been noted to decrease the flood peak (Levy and McCuen 1999). To further investigate the effects of pre-peak rainfall a detailed infiltration analysis would be required, identifying the point of mass runoff production. Or through a systematic analysis, investigating a single temporally uniform intense rainfall event to evaluate the runoff threshold.

7.3.2 Occurrence of Peak Flow Opportunities

The largest flows observed in in Iowa and much of the central U.S. have been a product of summertime convective storm systems or rain on snow spring events (IFC 2014; Villarini et al. 2011; Villarini et al. 2011). In the northern portions of the state annual maximum flows most frequently occurred in the spring months (IFC 2014), while the highest ranked Q_p often occurred over the summer. Total precipitation in northeast Iowa averages 900 mm each year with the largest volumes occurring in the summer (June, July, August) months (Huff and Angel 1992; IFC 2014; Villarini et al. 2011; Villarini et al. 2011). In a rainfall frequency analysis of the central U.S., Huff and Angel

(1992) identified that 72.1 % of top ranked 1-day storms occurred in the summer months, with August as the most frequent. This study was completed with data prior to 1986. In a more recent study, Villarini et al. (2011) noted that the peak rainfall depths occurred in a unimodal distribution peaking in June and July. The floods of record in more recent years have occurred in exceedingly wet summer months of 1993 and 2008.

Antecedent soil moisture conditions are well known to impact peak flow magnitude and duration. A further investigation of the SCAN soil moisture data from Ames Iowa (Fig. 7.8, 7.9, and 7.10) indicated that the soil was typically the wettest in the spring months of March, April, and May. This was true for each of the sensors in the top 20 cm. In the summer months, extreme variability in soil moisture was observed, with upper and lower quartile of 21 % and 100% saturation. The extreme variability was in part due to increased ET lowering median values, and high soil saturations due to the frequent summer rainfall events increasing soil wetness.

Increased soil moisture in the spring months reciprocates the increase in the quantity of spring time Q_p. While, increased rainfall occurring in the summer months has produced most frequently the floods of record. It seems that the pattern of increased soil wetness and increased rainfall were independent. Extraction of the median soil saturation values for each of the summer months at each of the top three soil moisture depths, was approximately equivalent to the SM50 condition. This soil wetness was indicative of an averaged wetness. SM50 produced the lowest Q_p for each design storm quantile. The effects of soil moisture on runoff and peak high flow events have been documented (De Michele and Salvadori 2002; Descroix et al. 2002; James and Roulet 2007; Meyles et al. 2003; Nishat et al. 2010; Penna et al. 2011; Radatz et al. 2013; Sahu et al. 2007). Under extreme rainfall conditions studies have indicated a lack of correlation between rainfall and soil moisture, noting that Q_p became independent of the initial soil state (Bronstert and Bardossy 1999; Castillo et al. 2003). This study agrees with the former, where larger Q_p occurred in response to increased soil wetness, even in extreme events. Although, it

must be mentioned that the design storm temporal distribution incurs rainfall 12 hours prior to the major peak producing event, possibly wetting near surface soils and altering soil moisture impacts. In this study it was found that rainfall recurrence frequency tended to have a larger impact on peak flows than soil wetness.

Although these analyses do not point to the correlation of median rainfall and soil moisture as important flood producing event. Rare events are often flood producing. In this vein the increased variability of summer month soil moisture leads the larger likelihood of increased antecedent wetness. Furthermore, future work in the investigation of exceedingly dry soil conditions could benefit the investigation of Q_p variability.

7.3.3 Scaling Components of Peak Flows

The study of Q_p across scales has become an increasingly sought after topic. Research in this area has become increasingly robust, provided through empirical analysis, and rainfall runoff modeling. This study was the first to investigate Q_p scaling with a fully integrated coupled surface-subsurface modeling platform. This platform also offered the capability to systematically investigate the role of antecedent wetness on Q_p. The wetness of a given basin has been proposed as a driver to Q_p scaling variability (Ayalew et al. 2014; Furey and Gupta 2005), but has yet to be directly investigated. Although this was not the proposed topic of investigation study, the findings added to previous work in this area.

In this study, only the downstream MC6-10 points were investigated for scale invariance, as projects were no longer added beyond this location. A pronounced scale break was identified at a consistent DA of approximately 20 km^2. The scale break depends on the duration of excess rainfall, which drives the quantity of upstream DA directly contributing to outlet (Ayalew et al. 2014; Ayalew et al. 2014). In the design storm analysis only one rainfall peak produces infiltration excess rainfall. The rainfall

peak always had a 0.5 hr duration which produced the stagnant scale break DA, consistent with the previous study.

Ayalew et al. (2014) systematically investigated excess rainfall duration and intensity, and channel and hillslope velocities on the scaling θ and α of Q_p in three catchments (254 km^2, 520 km^2, and 1082 km^2). Although subsurface processes were ignored in these studies by assuming excess rainfall characteristics, similar scaling parameter variability was extracted from this study. The peak rainfall intensity of each selected design storm quantile was in excess of infiltration, from 25 mmhr^{-1} to 110 mmhr^{-1} dependent upon soil type and design storm depth, a similar range to that of Ayalew et al. (2014). The study linked α with Q_p magnitude, and θ with the proportion of the catchment contributing to the outlet. In this study, α increased with increasing excess precipitation depth from 29 cms to 112 cms for NP scenarios at SM02. The variability of α described Q_p produced at 1 km^2, increasing with excess precipitation. Similarly, at SM02 θ decreased only under high excess rainfall depths (DS01, DS02, and DS04), and increased for DS10 and DS20, under exceedingly wet conditions. This inconsistency in θ response could be a function of infiltration excess occurring prior to the single event peak, increasing the excess rainfall depth producing an ill posed comparison.

Furey and Gupta (2005) and Ayalew et al. (2014) identified antecedent wetness as a possible driver of inter-event variability in scaling parameters through empirical and simulated studies, respectively. This was abundantly clear in this study, as soil wetness decreased from SM02 to SM50, both α and θ responded in a predictable fashion. An increase in initial soil wetness was akin to increasing the runoff coefficient, and total volume of water allocated to the surface. Increased excess rainfall depth in the upland hillslopes decreased the hillslope response time, in a comparable manner to Ayalew et al. (2014). As the initial soil wetness increased α increased, and θ decreased. Large excess rainfall depths produced a near constant θ. Consistency was found between low infiltration results of Furey and Gupta (2005), and Ayalew et al. (2014) and in this study

under exceedingly high initial soil wetness. More generally, this study agreed with results that a variability in hill slope velocity was speculated to correspond to runoff coefficient and soil wetness (Ayalew et al. 2014).

This study was further compared to regional annual exceedance flood quantile studies put forth by the USGS, most recently of Eash et al. (2013). These flood frequency equations take the same power law form as the peak flow analyses in this study. A review of the scaling parameters of the USGS equations displayed the same increasing pattern of α and decreasing θ with increasing flood quantile (Table 7.4). Annual exceedance discharge estimation does not directly take into account antecedent conditions. This became clear in Fig. 7.16, through a direct comparison of Q_p quantiles. Q_p was calculated with a the power law parameters of Table 7.4 and Eq. [7.1], and compared to Q_p simulation in this study at MC10. An agreement was achieved under median wetness conditions at low frequency Q_p events. Beyond DS20, the USGS equations consistently underestimated Q_p. BCW was well within the accepted DA range of application (0.2 km^2 to 20,000 km^2). The median DA in the USGS study for the representative hydrologic region was 118 km^2, nearly a factor of three larger than BCW. The increased DA of the typical USGS gauge location likely skewed results towards slower, lower peaks of larger basins. This did not compare well with the rapid response at the BCW scale. This comparison also assumed the design storm quantiles were equivalent to USGS regression.

In the process of investigating peak flow scaling structure dependency, Mandapaka et al. (2009) identified that the effects of rainfall variability on Q_p were scale depended. This was also found true for spatially heterogeneous rainfall, runoff coefficient, and roughness properties (Ayalew et al. 2014). Each study suggested that small to medium sized catchments were largely effected by heterogeneities, which aggregated and smoothed as DA increased. Projects reduced and attenuated Q_p locally, disturbing Q_p scaling at small DA. With increased DA, P and NP scenarios converged to

a similar solution. This was the feature discussed in the extrapolation method, whereby the intersection of these two with and without local heterogeneities were investigated.

7.3.4 Challenges and Future Work

The overarching goal of this study was to identify the Q_R capability of a set of structures built in the BCW. Q_p have been noted to occur under exceedingly wet antecedent soil conditions, heavy rainfall events, or both. To that end this research completed the task, identifying a range of Q_R under variable rainfall, soil, and project storage conditions. This work could be expanded through the analysis of historical events, and continuous modeling. Performing this experiment under a continuous mode over a long time series would offer a different probabilistic view of Q_R.

This study focused on normal to excessively wet initial conditions, which were conceptualized to produce larger magnitude Q_p. An expansion of this work into excessively dry simulations could offer a wider more realistic variability of Q_p. Additionally, the largest observed Q_p in Iowa typically occurred in the summer months, where commonly normal to excessively dry conditions are abundant. USGS regression quantile estimates of peak discharge values do not take into account time of year or antecedent condition. The investigation of dry conditions could also lead to a greater consistency with USGS regression estimates.

This study investigated the central loaded SCS 24-hour design storm temporal distribution for five quantile depths. Variability in design storm duration and temporal distribution, would subsequently alter infiltration and runoff characteristics of the basin. An expansion of this work into a systematic investigation of the duration of event, could identify the critical duration design storm and the associated Q_p and Q_R induced by projects.

Although not the main objective of this study a number of important discussion directions ensued from this work, each requiring further investigation to fully encompass.

These topics included the runoff generation thresholds due to antecedent moisture controls and peak flow scaling parameters.

The role of antecedent moisture thresholds have most commonly been investigated through field scale measurement campaign (Grayson et al. 1997; James and Roulet 2007; Meyles et al. 2003; Nikolopoulos et al. 2011; Penna et al. 2011; Radatz et al. 2013). With simulation studies focusing on proper estimation of antecedent conditions for design storm analysis (Brocca et al. 2008; Camici et al. 2011) or the influence of soil moisture spatial variability on flow (Bronstert and Bardossy 1999). These studies have yet to systematically investigate the possible driving factors behind the antecedent runoff threshold. Through application of a uniform rainfall distribution, an investigation could parse key variables likely to influence runoff thresholds. These could encompass infiltration capacity, rainfall depth and duration, basin shape, and basin scale.

As noted by Furey and Gupta (2005) and Ayalew et al. (2014) antecedent soil wetness has been weakly linked to variability of power law scaling parameters. In a similar manner to Ayalew et al. (2014) and Ayalew et al. (2014) a comprehensive analysis of antecedent moisture conditions would offer insight into Q_p scaling parameter variability. Furthermore, the application of a couple physically based model would be assessed for its capability to hold true to the power law scaling observed in empirical studies. This effort would also provide confidence in the extrapolation approach to estimate the impact of the BCW projects outside the DA.

Finally, this systematic approach can be applied to a number of other distributed structural or nonstructural flood mitigation practices. In this sense, the model of BCW would be applied as a numerical experiment, altering practice types and locations to best optimize the basins response to heavy rainfall.

7.4 Summary of Findings

In this study, attention was given to antecedent soil wetness, rainfall depth, and the subsequent impact on Q_p and Q_R through project implementation at various scales. A systematic increase of antecedent soil wetness, precipitation depth, and structure initial storage offered a global perspective on Q_R capabilities of nine projects in the BCW.

Q_p increased with increasing soil wetness and rainfall depth, a combination of the two produced the highest Q_p. The addition of flood mitigation projects reduced Q_p in downstream MC observation for each combination of soil wetness and rainfall depth. Initializing structures as empty produced the highest Q_R, consistently higher than FP scenarios. Q_R varied at the outlet of BCW from 17 % to 3 % dependent upon soil wetness, project initial storage, and rainfall depth. An estimate of Q_R influence outside of BCW was produced through an extrapolation of the most downstream MC observation points, through a power law scaling fit. Q_R under most conditions were no longer noticeable beyond 200 km^2. In the context of the BCW, this extrapolation led to a termination at 2 km downstream, where Beaver Creek met the much larger Little Cedar River. Finally, the Q_R estimates at BCW were scaled to the UCRW by the ratio of area drained upstream of a project. Under similar conditions, the UCRW at 4,350 km^2 would require between 950 and 1,600 projects costing \$196 million to \$313 million to exhibit a similar Q_R response as the BCW.

Beyond investigation of peak flow benefits offered by detention structures under various scenarios, this work touched on peak flow scale invariance and antecedent thresholds for peak flow production. Limited investigation of these two additional directions offered brief insight and consistency with previous studies. Each of these areas offer a new direction for analysis on this modeling platform.

This work proposed a methodology for initialization of physically based models in design storm simulations. The systematic investigation of antecedent moisture

conditions in this study offered an added understanding to the role in Qp in design storm analysis.

With these results and measured field based soil moisture and rainfall information offered by the IFC at 3 locations in the BCW (Fig. 4.2) an approximation of large magnitude flows can be estimated, and the associated peak flow benefits incumbent on the introduced projects. The main object of this study was to investigate peak flow reduction under various conditions in the BCW and to scale these benefits beyond BCW for the IWP. These needs were met though a thorough and systematic investigation. This work provided the investigation of distributed flood mitigation practices per Phase II of the IWP.

8.0 TILE DRAINAGE

Subsurface tile drainage significantly alters flow pathways within hydrologic systems (Eidem et al. 1999; Hansen et al. 2013; Hirt et al. 2011; King et al. 2014; Macrae et al. 2007; Rozemeijer et al. 2010; Schilling et al. 2012; Singh et al. 2006; Stamm et al. 2002; van den Eertwegh et al. 2006; van der Velde et al. 2010). Tile drainage improves conditions for agricultural productivity by providing a fast flow route for excess water though subsurface pipe networks. Drainage systems increase infiltration, reduce surface runoff and erosion, and improve agricultural yield (Blann et al. 2009; Skaggs et al. 1994; Stillman et al. 2006; Strock et al. 2010; Zucker and Brown 1998). Subsurface drainage is used extensively throughout the agriculturally dominated central U.S. to drain more than 37 % of the soils (Zucker and Brown 1998). The dominance of row crop agriculture and heavy soil types in central Iowa has led to a wide distribution of tile drainage (Fig. 8.1). Tile drainage is often spaced uniformly from 10 m to 100 m across entire fields (Strock et al. 2010), beyond recommended values.
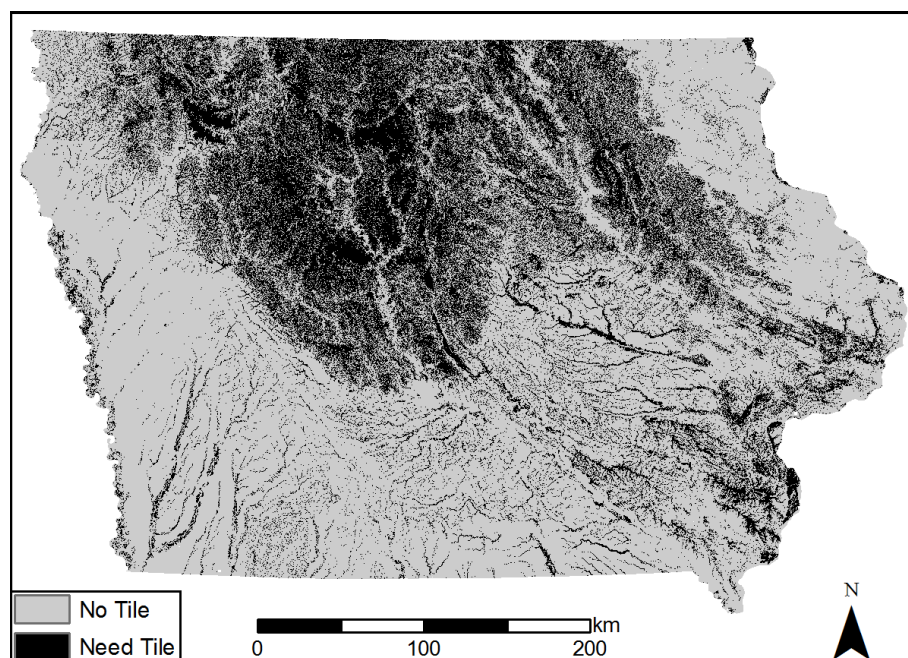
Figure 8.1 Soils requiring drainage for full productivity (IDNR 2015; IGS and IDNR 2008).

Artificial flow paths through drained systems impact the risk of floods and droughts (O'Connell et al. 2007), and the transport of agrochemicals (Jaynes et al. 2001; Stamm et al. 2002). Tile drainage has been shown to increase base flow (Schilling et al. 2012; Schilling and Libra 2003), reduce groundwater travel times (Schilling and Helmers 2008), and increase annual flow volume (Blann et al. 2009; Haitjema 1995; Magner et al. 2004). The impacts of subsurface drainage on peak flows vary with scale (Blann et al. 2009). Added storage provided above the drains increases infiltration and reduces surface runoff, resulting in lower peak flows at the watershed scale (Blann et al. 2009; King et al. 2014; Skaggs et al. 1994). At small scales, excess surface water is dictated by spatial heterogeneities in soil water retention characteristics and antecedent moisture conditions, as reviewed by Skaggs et al. (1994). Rapid subsurface routing offers a pathway for soluble nitrate to bypass natural groundwater flow paths, increasing concentrations in streams (Blann et al. 2009; Jaynes et al. 2001; Rozemeijer et al. 2010; Skaggs et al. 1994; van den Eertwegh et al. 2006). The addition of subsurface storage reduces overland surface flow, subsequent field based erosion and phosphorous transport, as reviewed by Sims et al. (1998).

Studies expanding from the field scale to the watershed scale have indicated a wide range of tile drainage contribution to stream flow dynamics (Carluer and De Marsily 2004; Eastman et al. 2010; Hirt et al. 2011; King et al. 2014; Macrae et al. 2007; Sims et al. 1998; van den Eertwegh et al. 2006; van der Velde et al. 2010). Tile drainage contribution to watershed outflow ranges from 0 % to 90 % varying with season (3 km^2) (Macrae et al. 2007), and 30 % to 61 % (4 km^2) (King et al. 2014). At field locations without surface flow measurements, tile flow represents 19 % to 73 % of volumetric precipitation (0.060 km^2 to 0.078 km^2). Tile discharge is also strongly correlated with the size of the contributing drainage area (King et al. 2014; van der Velde et al. 2010). Further research is needed on the impact of tile drainage contribution to hydrologic flow

processes at the watershed scale (Eidem et al. 1999; King et al. 2014; Macrae et al. 2007; Schilling et al. 2012).

Numerical modeling of coupled surface-subsurface systems provides insight into the effects of tile drainage on various hydrologic processes. Hydrograph recession, base flow, travel times, and flow during events (De Schepper et al. 2015; Hofer et al. 2011; van der Velde et al. 2010) have been investigated through various modeling approaches. Hydrologic modeling of tile flow ranges from the root zone (DRAINMOD), to basin scale linear reservoir hydrologic representations (SWAT), to fully integrated 3-D subsurface simulations (HGS), as reviewed by (Hansen et al. 2013). Recent approaches to modeling coupled surface-subsurface systems in a physically based framework were discussed in Section 2.0. Adding a realistic representation of tile drainage into numerical models is important to investigate subsurface flow pathways (Kiesel et al. 2010). The complexity of methods to include tile drains varies greatly. The most advanced modeling includes an explicit 2-D surface flow, 3-D subsurface flow, and 1-D tile flow simulations (De Schepper et al. 2015; Rozemeijer et al. 2010). With the added numerical burden of these complex systems, approximate methods have been found to represent tile drainage impacts. Carlier et al. (2007) presented an equivalent medium approach, where regularly spaced drainage systems were represented by a highly permeable horizontal layer. Rozemeijer et al. (2010) applied this approach as a boundary condition for an internal explicit drain tile representation. De Schepper et al. (2015) compared numerous simplifications to tile drainage representation at the subcatchment scale, finding that an equivalent medium approach was able to represent surface outflow and subsurface hydraulic heads adequately. De Schepper et al. (2015) noted a significant increase in computation speed derived from a reduced resolution mesh, and simplified internal boundary conditions.

The goal of this study was to investigate the impact of pattern tile drainage systems at the catchment scale. HGS a coupled surface-subsurface hydrologic model was

applied to the BCW. BCW is defined by a landscape dominated by tile drained agriculture (Fig. 8.3). An annual meteorological time series was chosen to force the numerical model, expanding on previous single event based studies. The annual time series was dissected to investigate the spatiotemporal dependency of tile drainage contribution to surface flow. Precipitation and evapotranspiration were investigated as key components driving tile drain flow variability.

8.1 Study Methodology

The impact of explicit tile drainage systems was evaluated at the field scale for application at the watershed scale. Coupled surface-subsurface modeling at large scales requires simplifications to the mesh, and tile drainage components (De Schepper et al. 2015). Comparable tile response to events was achieved through calibration of an equivalent highly permeable medium at the field scale. Field scale results were implemented at the watershed scale, enabling the study of tile drainage impacts at varying temporal and spatial scales.

8.1.1 Field Scale Tile Modeling Through Explicit and
Equivalent Approaches

A 120 m^2 artificial test catchment based on (Abdul 1985), was used to investigate the impact of tile drainage density on tile outflow (Fig. 8.2 a). The surface topography and 2-D grid were adapted from Therrien et al. (2013) and Abdul (1985). The field scale test model is an elongated (8:1, length: width) mildly sloping channel and localized drainage area. The elevation change from the high point to the outlet is 1.65 m. The 2-D numerical grid contains 188 triangular surface elements, with an average area of 0.64 m^2. This model was originally produced to replicate a field experiment, testing the surface-subsurface hydrologic interactions for an artificial rainfall event (Abdul 1985). Therrien et al. (2013) utilized this experiment as verification of flow and transport processes in a coupled HGS model.

8.1.1.1 Explicit Tile Drainage Incorporation

The test basin was modified to assume the same vertical discretization as the watershed scale model (Section 5.1), with 16 subsurface layers. Ten numerical layers were allocated to the top meter of the subsurface domain. One layer, from 1.0 m to 1.1 m below the surface was incorporated for the explicit and equivalent medium representations of tile drainage. This field study assumed a flat bottom to the subsurface domain, which ranges from 5.0 m to 6.7 m below the surface. Five additional subsurface layers were allocated to the remaining subsurface depth below the tile layer. Numerical layers range in thickness from 1.7 m near the bottom to 0.025 m near the surface (Fig 8.2a).

Tile drains were simulated as 1-D pipes following element edges, see Section 3.3 and Therrien et al. (2013) for further numerical details of tile simulation. Variations in tile drainage were quantified in terms of Tile Drainage Density (TDD). TDD was calculated as the total length of tile drainage per unit drainage area (Schilling et al. 2012). Each tile drainage configuration consisted of a main collector along the stream centerline, with regularly spaced parallel laterals. Drain spacing refers to the approximate distance between parallel laterals. Tile drains were assumed 0.1 m in diameter, and with Manning's n of 0.055. Tile drainage was incorporated at TDD ranging from no drainage (0.0 m^{-1}) to a maximum density of 0.17 m^{-1} or a 10 m lateral spacing. This range described the expected spacing in Iowa soils (Melvin et al. 2012) (Fig. 8.2 b, c, d).

The subsurface domain was parameterized with uniform loam type surficial soils, and geologic soils for the domain deeper than 1.1 m (Table 5.1). The surface parameters were applied uniformly as an agricultural classification (Table 5.2). For a further description of surface and subsurface parameter values, refer to Section 5.3 and Section 5.4.

A constant head boundary condition was applied to the tile outlet, equal to its elevation (Fig. 8.2 a) (De Schepper et al. 2015). The remaining boundaries were

established in the same approach as the watershed scale model (Section 5.4). The outlet edge for the surface domain was assigned a uniform gradient boundary, the remaining surface boundaries were represented as critical depth. All remaining subsurface boundaries were no flow. Evapotranspiration and rainfall were omitted from field scale simulations.

The test basin simulations began with the groundwater table equal to the surface elevation. The simulation was allowed to run for 10 days, draining subsurface water through the head outlet boundary condition. Measured flow out of the head boundary condition was monitored and used for equivalent parameter estimation.

8.1.1.2 Equivalent Medium Field Scale Tile Drainage

Equivalent medium field scale simulations were completed on the same numerical grid, and parameter distributions described in Section 8.1.1.1. Main collector and lateral drains, were removed from the subsurface domain and replaced by an equivalent medium. The equivalent medium was allocated to the depth of drain tile in the explicit representation (1.0 m), with a thickness corresponding to the diameter of the tile drains (0.1 m).

To simulate flow out of the drainage layer, all nodes belonging to the layer along the downstream boundary of the domain were assigned a prescribed head equal to their elevation (Fig. 8.2a) (De Schepper et al. 2015). The remaining boundary conditions, and initial conditions remained consistent with the previous section. The domain was allowed to drain for 10 days, monitoring outflow from the drainage layer for calibration targets.

The hydraulic conductivity of the drainage layer was iteratively estimated using the Parameter Estimation (PEST) software (Doherty 2010). PEST is a model independent parameter optimization software, which minimizes a user defined objective function through a Gauss-Marquardt-Levenberg method of nonlinear parameter estimation. Physically-based coupled models are known to contain numerous parameters, many of

which are difficult to determine through field measurements. Automated parameter estimation has been used for data intensive physically based modeling, offering a close approximation of model dynamics during the calibration window (Verbist et al. 2012). The objective function was described by a 10 d volumetric integration of outflow from the subsurface head boundary condition. PEST iteratively altered the hydraulic conductivity of the equivalent layer, until the explicit and equivalent objective function was minimized. Lower and upper parameter limits for hydraulic conductivity estimation were set to 0.121 md^{-1}, and 12,100 md^{-1}, respectively. PEST calibration was performed for each explicitly incorporated drainage configuration.

A relationship between TDD and hydraulic conductivity was the product of this analysis. Resulting calibrated parameters from the artificial test basin were then applied at the watershed scale.
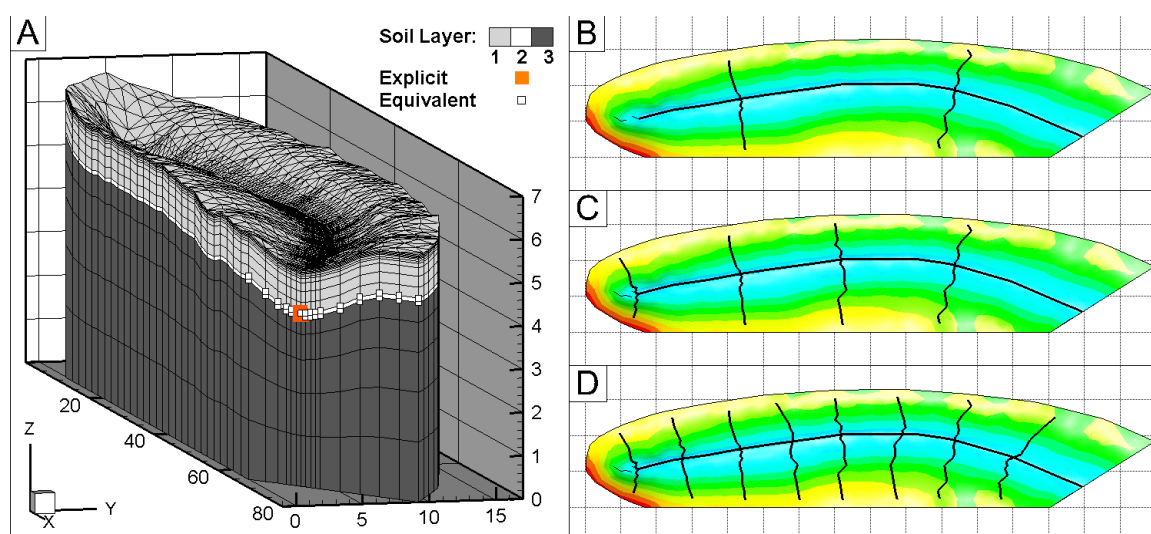
Figure 8.2 a) Numerical test basin, isometric view including soil property layering equivalent to application at the watershed scale. b) TDD of 0.088 m^{-1} (40 m explicit tile spacing). c) TDD of 0.111 m^{-1} (20 m explicit tile spacing). d) TDD of 0.166 m^{-1} (10 m explicit tile spacing).

8.1.2 Watershed Scale Tile Drainage application

The focus of this study was on the watershed scale implementation of tile drainage in the BCW. The predominance of row crop agriculture (> 70%) (Fig. 7.3), finely textured soil types (loam and clay loam > 90%) (Fig. 5.3 a), and relatively flat topography lends the BCW to widespread application of subsurface drainage. Tile drainage systems reduce soil water logging and surficial ponding during rainfall events, improving conditions for agricultural productivity. Tile drainage systems were installed across the watershed scale model uniformly. The objective was to identify the impact of tile drainage on surface flow, with respect to temporal and spatial scale.
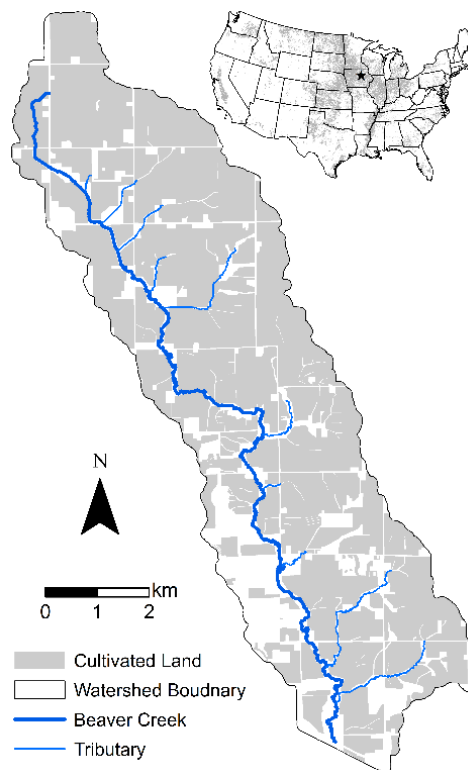
Figure 8.3 BCW location and agricultural land classification (FSA 2013).

The exact distribution of tile drainage in the BCW was unknown. Through aerial photography after rainfall events tile drainage systems have been mapped (Naz et al. 2009; Verma et al. 1996). The mapping procedure is based on the knowledge that soil

over a tile drains unsaturates faster after a rainfall event. The increased soil dry

subsequently increases the infrared reflectance (Naz et al. 2009). Aerial photography for

a portion of BCW from the 1980's after a rainfall event provided evidence of the

extensive drainage network (Fig. 8.4). Recent work in GIS mapping of drainage indicates

that tile drainage is likely more wide spread than originally estimated by Zucker and

Brown (1998).
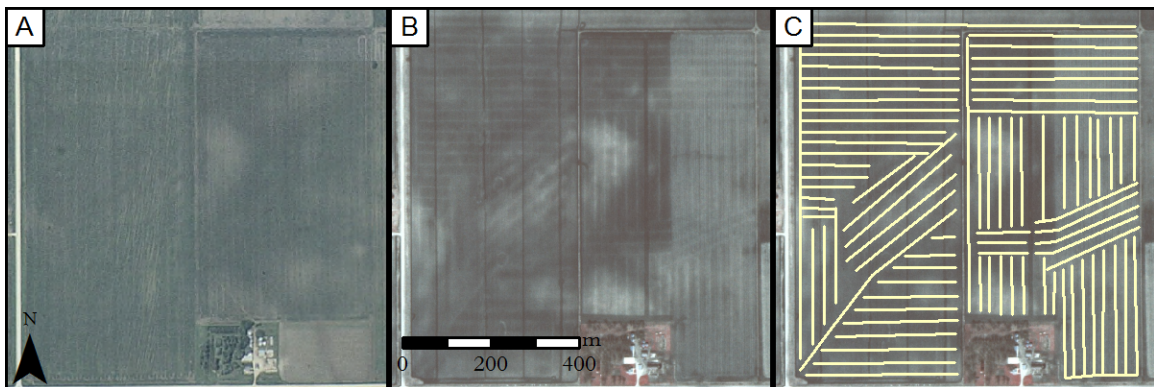
Figure 8.4 a) Aerial photograph 2005 per the National Agricultural Imagery Program (NAIP) (IDNR 2015), b) Color Infrared (CIR) photograph 1980's per the NAIP (IDNR 2015), c) Digitized tile lines from CIR imagery. Located in the farthest north section of BCW.

To investigate tile drainage at the watershed scale, HGS was applied to the 16

layer, 212,993 node, and 371,460 element 3-D grid, produced in Section 5.2. Basin

characterization, parameter identification, and boundary conditions for model simulations

were described in Section 5.0. Initial conditions were the product of iterative

meteorological forcing, described in Section 6.1.

Surface elements in the watershed scale model average 0.18 ha, making them too

coarse to explicitly incorporate tile drainage networks at TDD for the region. To preserve

efficient computational times, elements could not be exhaustively distributed. The

addition of an equivalent medium at 1.0 m below the surface, uniformly throughout the

watershed was implemented. A TDD of 0.111 m^{-1} (20 m spacing) was assumed for the

entire watershed, an average value representative of the watershed per Melvin et al. (2012). The hydraulic conductivity of the stream bed, from the surface to the drainage layer, was increased to 6.4 md^{-1}. This represented an increased connection between the tile network and the stream.

Although it is know that tile drainage systems were not installed in many of the grassland or forested regions of the watershed, the equivalent medium was still incorporated beneath them. Non-agricultural land represented 23 % of the total land area (Table 5.2).Tile drainage systems propagate water through field laterals into collector mains and then into channels. Varying the equivalent tile drainage properties with land use could impact the connectivity of the drainage layer in agricultural lands to the streams. Removal of a few key elements at field edges throughout the system would stop subsurface fast flow in the riparian areas, halting connectivity to the stream. Connectivity of the subsurface layer was no a feature studied here.

To parse tile flow from total stream flow a numerical tracer was applied to the nodes representing the tile drainage layer. A specified concentration boundary condition known as a first-type, Dirichlet, or constant concentration boundary condition of 1.0 was applied to the drainage layer. Nodes allocated to the stream centerline were not included in the constant concentration boundary condition (Fig. 8.5). The inclusion of these nodes would bias the simulation towards higher contribution of tile flow, as any water interacting within the stream bed would be identified as tile flow. Below the tile layer, the concentration was specified as zero to separate base flow from tile flow.

Observation points continuously measuring surface flow and surface water concentration at 29 locations were allocated to locations along the main channel and tributaries (Fig. 8.6). Each point drained at least 1 km^2, drained more than 100 elements upstream, and was located within an element specified as a stream channel land use. These additional points allowed for a spatial representation of tile flow.
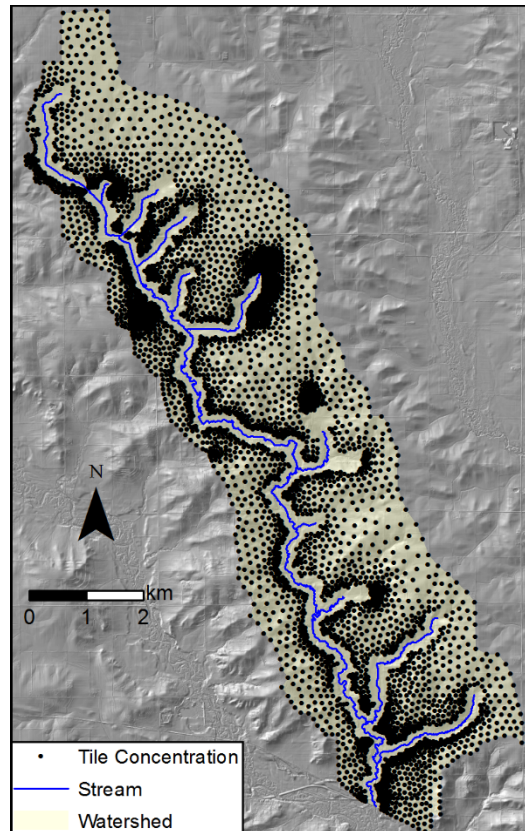
Figure 8.5 Spatial representation of the specified concentration boundary condition located at a depth of 1.0 m to investigate tile contribution to stream flow.
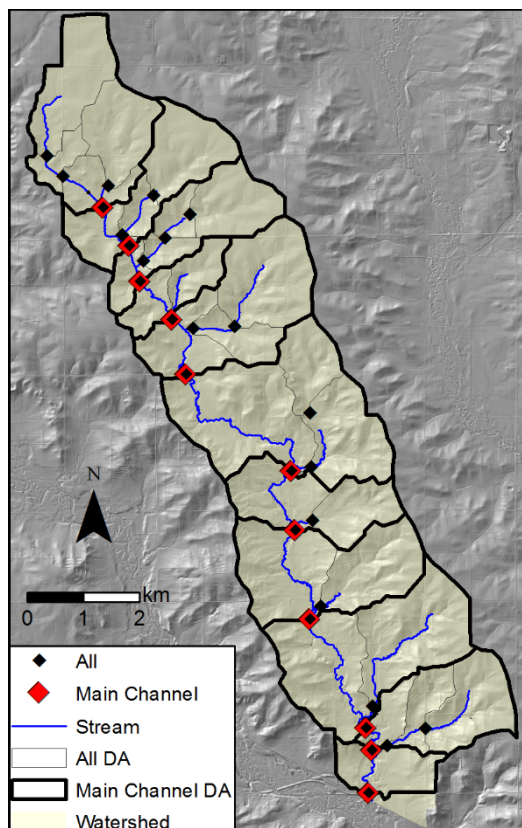
Figure 8.6 Observation locations for flow and concentration along the main stream and tributaries.

Simulations were run with the initial condition described in Section 6.1 for the year of 2014. The initial condition for surface and subsurface concentrations was a product of the same methodology. Spatiotemporal variability in hydrologic conditions with respect to tile drainage contribution to stream flow was described in Section 8.2.2.

8.2 Simulation Results

Tile drainage at the field scale was investigated to assess the applicability of a calibrated equivalent medium representation of tile drainage. The hydraulic conductivity of the equivalent medium was calibrated with PEST, for multiple TDD. The year of 2014 was simulated at the watershed scale with an equivalent tile drainage layer. A tracer was applied to the nodes representing the equivalent tile drainage layer. The main objective

was to quantify the contribution of tile drainage to surface flow for varying spatial scales and time periods.

8.2.1 Field Scale Tile Drainage Results

The equivalent drainage layer conductivity was calibrated to represent explicit tile drainage through the cumulative drainage volume after 10 days. PEST required between 26 and 165 HGS simulation runs to converge on a hydraulic conductivity for each of the drain spacing arrangements. Calibrated hydraulic conductivity values are depicted in Table 8.1.

Calibrating the equivalent medium altered the soils natural ability to transport water. Each PEST model outcome increased the hydraulic conductivity of the drainage layer. Calibrated values for each specific tile drainage arrangement ranged from 164 md^{-1} to 530 md^{-1} increasing the hydraulic conductivity by at least three orders of magnitude from the predominant soils in BCW (Table 5.1). The altered hydraulic conductivity was associated with a TDD, allowing an extrapolation to other regions based on land and soil characteristics.

PEST calibration results compared well to explicit incorporation of tile drains after 10 days of drainage. Calibrated parameters resulted in a faster response to drainage in the first 3 days of each calibration except the 10 m spacing (Fig. 8.7). Over the remaining seven days of simulation the equivalent medium slightly over estimated flow from the head boundary condition. The combination produced an asymptotically convergence to the same volumetric accumulation. Each calibration resulted in total drained volumes within 2% of calibration targets (Table 8.1).

The average depth to the groundwater table (GWT) after 2 days (Table 8.1), indicated a faster response of the equivalent medium when compared to the explicit tile model in all but the 10 m spacing (Fig. 8.8). Depth to GWT in the equivalent drainage simulations was deeper near the head outlet boundary (~0.9 m), and shallower in the

upstream areas (~0.3 m) (Fig. 8.8 b, d, f, h). The simulated GWT began to more evenly distribute after 4 days (Fig. 8.8). The explicit inclusion of tile drainage systems offer a spatially varying water table elevation, producing an elliptical pattern between drains, while the equivalent medium offers an averaged representation of depth to GWT (Fig. 8.9).

Table 8.1 PEST calibration results for five calibration scenarios, $K_{s(eq)}$ is the equivalent saturated hydraulic conductivity, $V_{D(ex)}$ is the volume drained for explicit tile drainage, $V_{D(eq)}$ is the volume drained for the equivalent tile drainage, $W_{T(ex)}$ is the arithmetically averaged depth to groundwater table for explicit drainage, and $W_{T(eq)}$ is the arithmetically averaged depth to groundwater table for equivalent drainage. V_D values correspond to t = 10 d (Fig. 7.7), and W_T values correspond to t = 2 d (Fig. 7.8). *For no tile simulation estimated $K_{s(eq)}$ is that of a loam soil type.

Distance	TDD	$K_{s(eq)}$	$V_{D(ex)}$ (10 d)	$V_{D(eq)}$ (10 d)	$W_{T(ex)}$ (2 d)	$W_{T(eq)}$ (2 d)
(m)	(m^{-1})	(md^{-1})	(m^3)	(m^3)	(m)	(m)
10	0.17	530	77	77	1.13	1.06
20	0.11	325	68	68	0.97	0.94
40	0.09	235	61	62	0.87	0.87
Collector	0.06	164	54	55	0.77	0.79
No Tile	0.00	0.12*	13	13	0.34	0.34
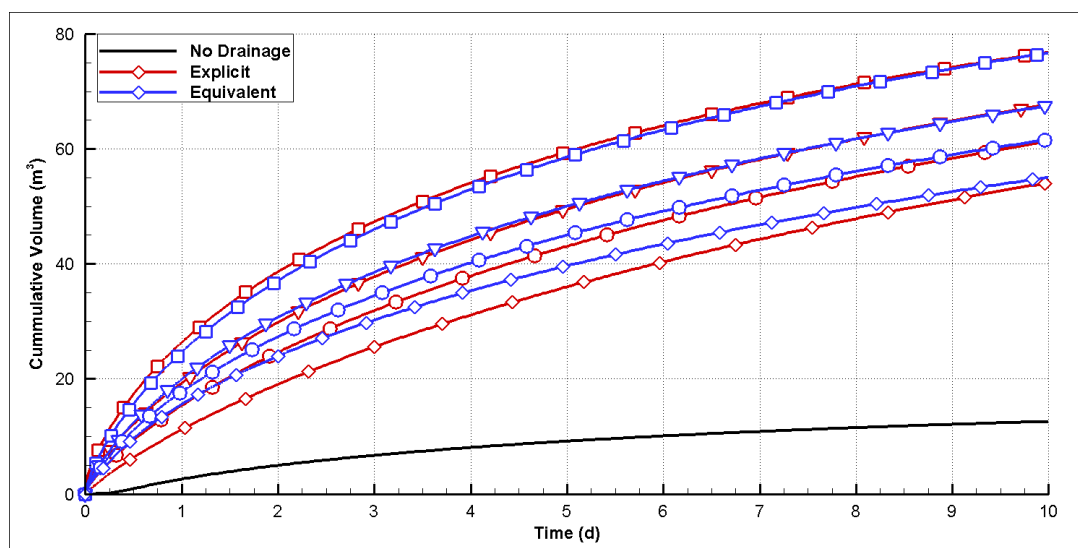
Figure 8.7 Cumulative volume comparison of explicit tile drainage incorporation (red) and calibrated equivalent medium (blue) for five levels of spacing, 10 m (square), 20 m (gradient), 40 m (circle), and only the collector located under the channel (diamond).
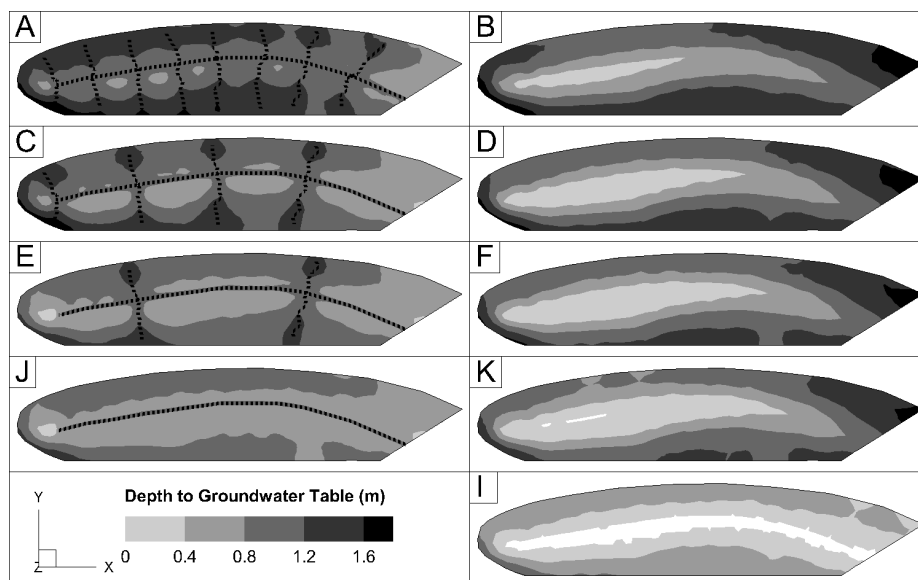
Figure 8.8 Depth to the water table at t = 2 d. a, c, e, g) explicit tile drainage for a spacing of 10 m, 20 m, 40 m, and collector, respectively. b, d, f, h) Equivalent medium final calibration for drainage for a spacing of 10 m, 20 m, 40 m, and collector, respectively. i) No tile drainage.
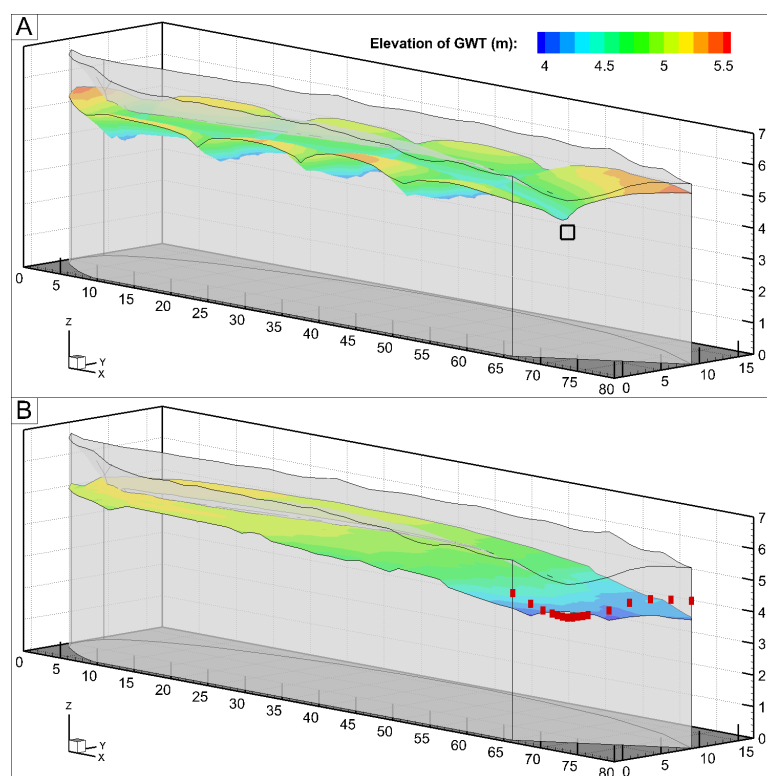
Figure 8.9 Estimated GWT after 4 days of drainage (10 m tile spacing). a) Explicit tile drainage GWT, as produced by a saturation contour at 0.99. b) Equivalent drainage layer GWT, as produced by a saturation contour at 0.99.

Calibration of equivalent tile drainage layer properties to explicit incorporation of tile drainage resulted in a relationship between TDD and equivalent hydraulic conductivity (Fig. 7.10). Points on the curve were a product of five TDD simulations. A second order polynomial function was used to describe the relationship (Fig. 8.10). This conceptual incorporation of tile drainage enabled a simplification of the mesh to for a wide variety of TDD, providing an approximate hydrologic impact. The results of parameter estimation were incorporated into watershed scale simulations to investigate tile drainage induced alterations in flow.
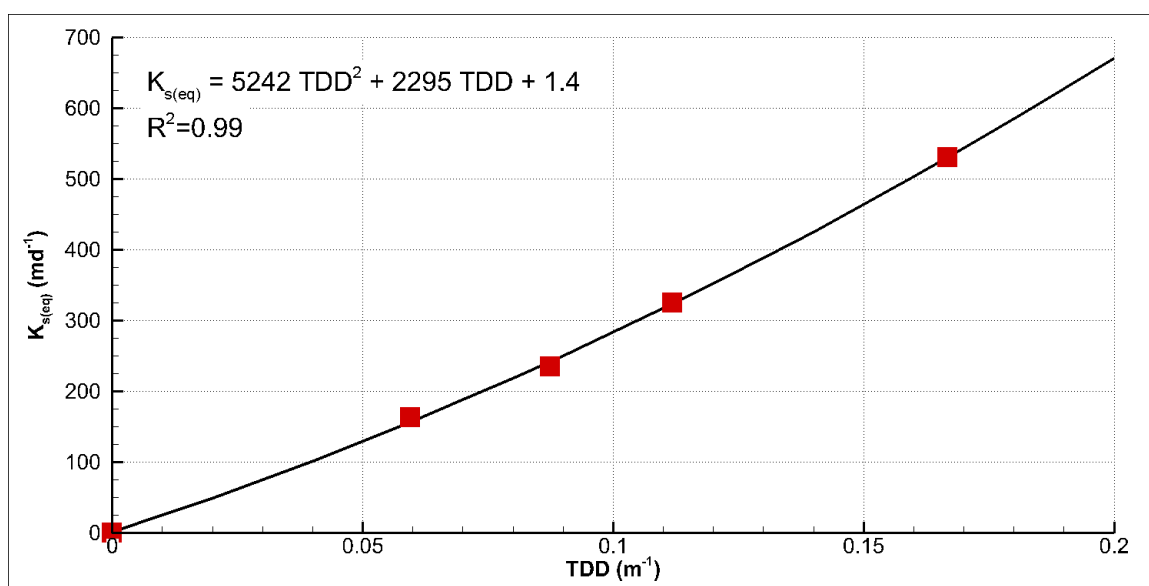
Figure 8.10 Equivalent saturated hydraulic conductivity ($K_{s(eq)}$) resulting from parameter estimation as described by TDD. Quadratic regression describes the relationship between TDD and $K_{s(eq)}$.

8.2.2 Watershed Scale Tile Drainage Results

Contribution of tile drainage to surface flow was aggregated over annual, seasonal (S), event (E), and non-event (NE) time periods. Over each time period the ratio of tile drainage flow to streamflow (Q_T/Q) was investigated at 29 observation locations (Fig. 8.6). Observation points were categorized as part of the main channel of Beaver Creek

(MC), or a tributary. Logarithmic lines of best fit were calculated by least squares criteria to all 29 observation points Eq. [8.1], and independently to the 11 points identified as MC. Best fit parameters (m, b) and R^2 values were reported for each regression. Semi-log plots of the tile flow to total flow ratio (Q_T /Q) vs. drainage area (DA) were depicted, and logarithmic fits were investigated for scale dependency of tile drainage contribution to stream flow.

$$\frac{Q_T}{Q} = m \log DA + b \qquad [8.1]$$

Where Q_T (mm) represents the tile flow volume, Q (mm) represents the flow volume, DA (km^2) is the upstream drainage area, m is the slope, and b is the intercept.

8.2.2.1 Annual Contribution of Tile Drainage

Precipitation (P) and PET forced coupled HGS simulations of the BCW for the year of 2014. A pseudo-steady state in watershed storages was achieved after 3 years of recursive simulation (Section 6.1). Convergence of tile drainage contribution to stream flow was calculated through the same methodology. After 3 recursive years of model simulation, total volume, and year start to end error reduced to below a1.0 % threshold. The last year (3) of this simulation was the object of analysis for this study.

Over the year 2014 input P totaled 774 mm (Table 8.2). The incoming P was partitioned into 522 mm evapotranspiration (ET), and 248 mm Q. The system produced a Q/P ratio of 0.32 and an ET/P ratio of 0.67. Q_T at the outlet was 97 mm, corresponding to 39 % of the total Q. As described in Section 4.3, approximately half of the P occurred over two distinct events beginning on DOY 131 and DOY 167 (Fig. 8.11). The maximum input precipitation intensity was 26.1 mmhr^{-1}. These two distinct rainfall events produced Q peaks of 18.5 cms and 6.8 cms, respectively. Modeled ET remained below 1 mmd^{-1} from DOY 0 to DOY 134 and again after DOY 260. The maximum daily ET rate was

9.35 mmd[-1], which occurred at DOY 225. Over the growing season, DOY 150 to DOY 250, ET averaged greater than 4 mmd[-1]. In response to high ET, Q dropped to a low of 0.0014 cms at DOY 232. Q_T /Q varied from 0.06 to 0.71. The largest fluctuations in Q_T /Q occurred immediately after rainfall events. The largest sustained Q_T contributions occurred beginning on DOY 0 and DOY 305 and lasting for 100 d and 40 d, respectively. The high Q_T /Q values occurred in non-event, low ET time periods.

At approximately 3 km^2 a strong increasing trend of Q_T /Q to DA was achieved. A comparison of Q_T /Q to DA (Fig. 8.12), showed decreasing variability with increasing DA. Logarithmic regression for all of the observation points, produced a slope of approximately zero, indicating a lack of a relationship between DA and Q_T /Q. The regression for the MC points exhibited a slight increasing trend with increasing DA of m=0.12, from Q_T /Q of 0.29 at 5.5 km^2 to 0.39 at 44.5 km^2. The MC regression produced a good log-linear fit achieving an R^2 of 0.98.
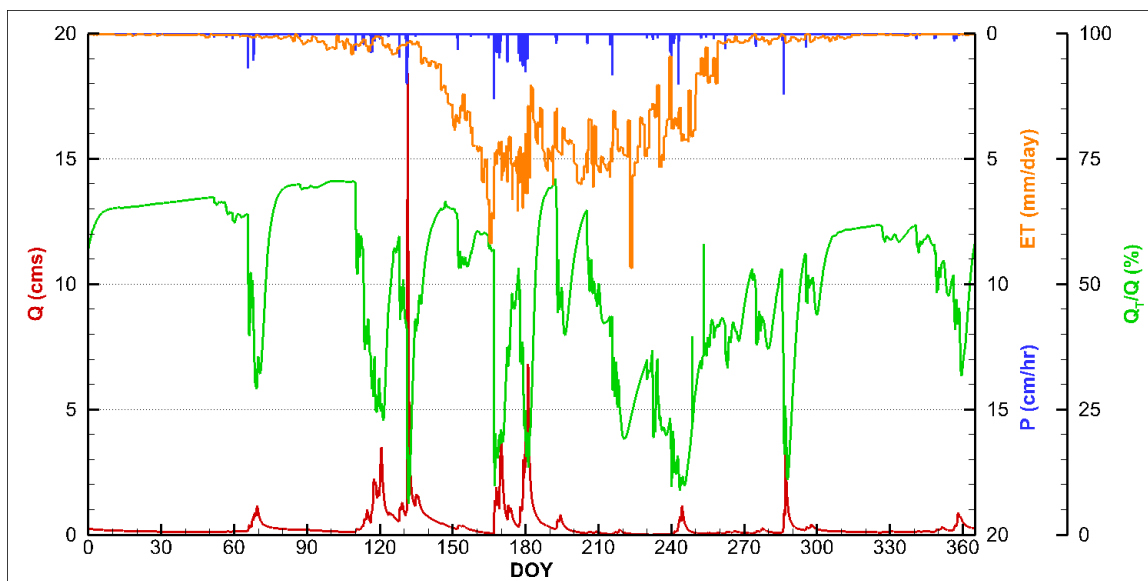
Figure 8.11 Annual water balance components for the year of 2014. Components represented - Q (red), P (blue), ET (orange), and Q_T /Q (green).

Table 8.2 Annual integration of water balance components for 2014, values in parentheses represent the ratio of each water balance component to P (i.e. ET/P = 0.67).

Start (DOY)	Length (d)	P (mm)	ET (mm)	Q (mm)	Q_T (mm)	Q_T/Q
0.0	365.0	774	522 (0.67)	248 (0.32)	97 (0.13)	0.39
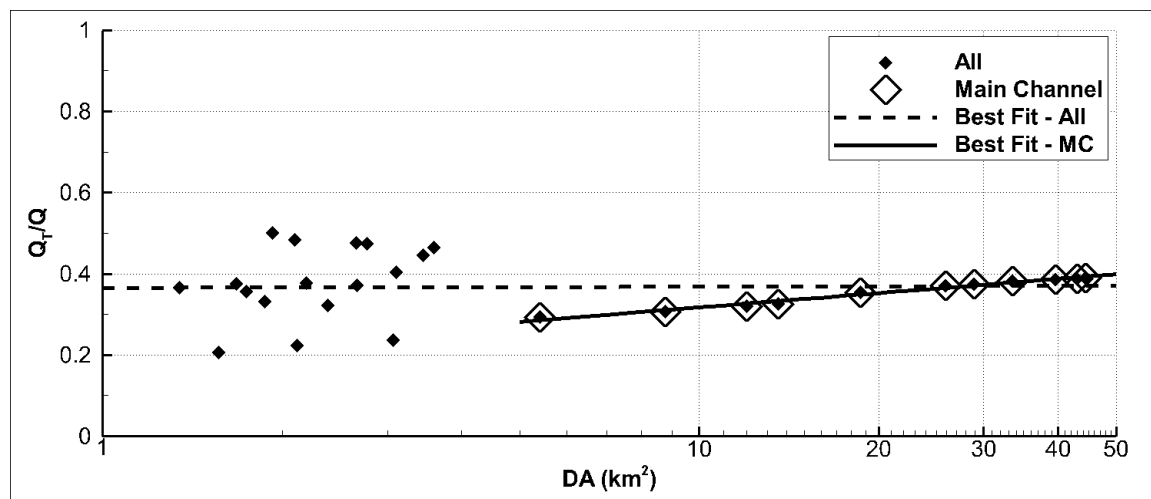
Figure 8.12 Annual Q_T/Q at 29 observation points (Fig. 8.6) on a semi-log plot with logarithmic regression lines for all observation points (dashed) and for the observation points identified as MC (solid).

Table 8.3 Annual logarithmic regression parameters for MC points.

m	b	R^2
0.12	0.20	0.98

8.2.2.2 Seasonal Contribution of Tile Drainage

The simulation was divided into four seasons each representing a three month time period (90 to 92 days). For the duration of this section the time periods from January to March, April to June, July to September, and October to December were referred to as S1, S2, S3, and S4, respectively. S1 incurred the least P, ET, and Q, and produced the highest Q/P of 0.70, and Q_T/Q of 0.59 (Table 8.4). S2 incurred the largest P depth of 400 mm, which produced the largest Q and Q_T, 141 mm and 48 mm, respectively (Table 8.4), (Fig. 8.13). The largest peak Q of 18.5 cms also occurred in S2. In S3 the majority of the

ET volume was extracted, removing 314 mm of water. Q_T/Q was the most stable during S1, and S4. Concurrently, in S1 and S4 Q_T/Q (0.59, 0.44) ratios were higher than S2 and S3 (0.34, 0.36). The largest variability in Q_T/Q occurred when larger volumes of P were input into the system, or a large volume of ET was removed from the system.

For just MC points a consistent increasing trend of Q_T/Q to DA was achieved (m = 0.07 to 0.15). S2 was attributed the highest slope of 0.15 (Table 8.5) (Fig. 8.14). Best fit lines m for the tributaries and MC observations differ significantly, from the MC only trends. Best fit lines for all observation points displayed muted slopes when compared to those from only the MC points. DA of less than 3 km^2 displayed the most variability in Q_T/Q (Fig. 8.14). All of the observation points produced similarly flat sloped regression lines. Each best fit line displayed slight increasing or decreasing trends with drainage. For all observations, the trend lines were heavily skewed by the large variability at small scales. For the remainder of this section the MC log-linear regression was primarily discussed.
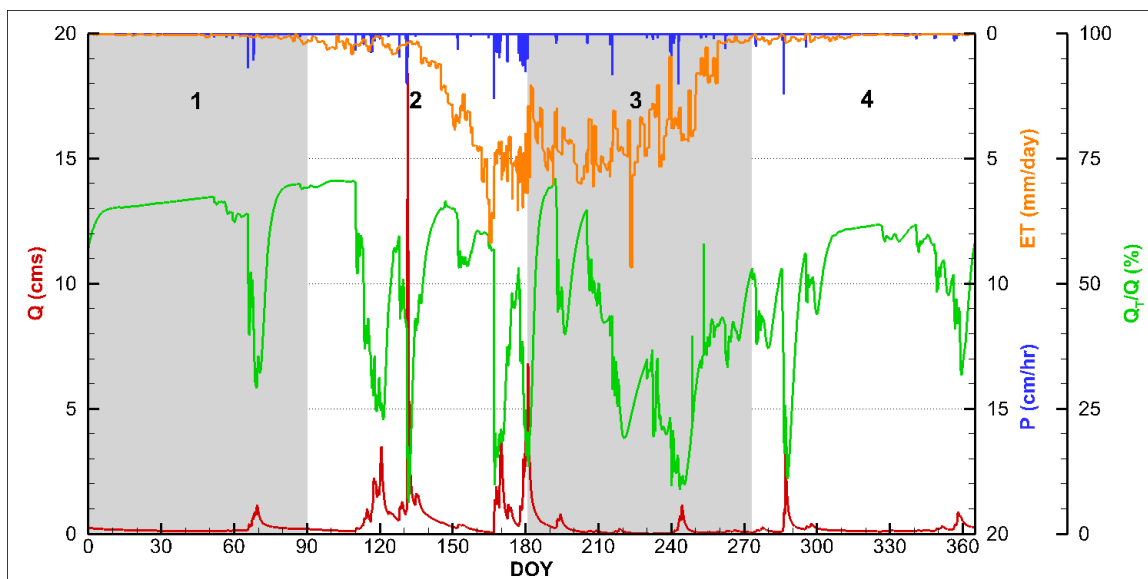
Figure 8.13 Seasonal water balance components for the year of 2014. Grey and white backgrounds denote varying seasons. Components represented - Q (red), P (blue), ET (orange), and Q_T/Q (green).

Table 8.4 Seasonal integration of water balance components for 2014, values in parentheses display the ratio of each water balance component to P.

Name	Start (DOY)	Length (d)	P (mm)	ET (mm)	Q (mm)	Q_T (mm)	Q_T/Q
S1	0	90	47	8 (0.16)	33 (0.7)	19 (0.41)	0.59
S2	90	91	400	190 (0.47)	141 (0.35)	48 (0.12)	0.34
S3	181	92	194	314 (1.62)	38 (0.2)	13 (0.07)	0.36
S4	273	92	133	10 (0.07)	37 (0.28)	16 (0.12)	0.44
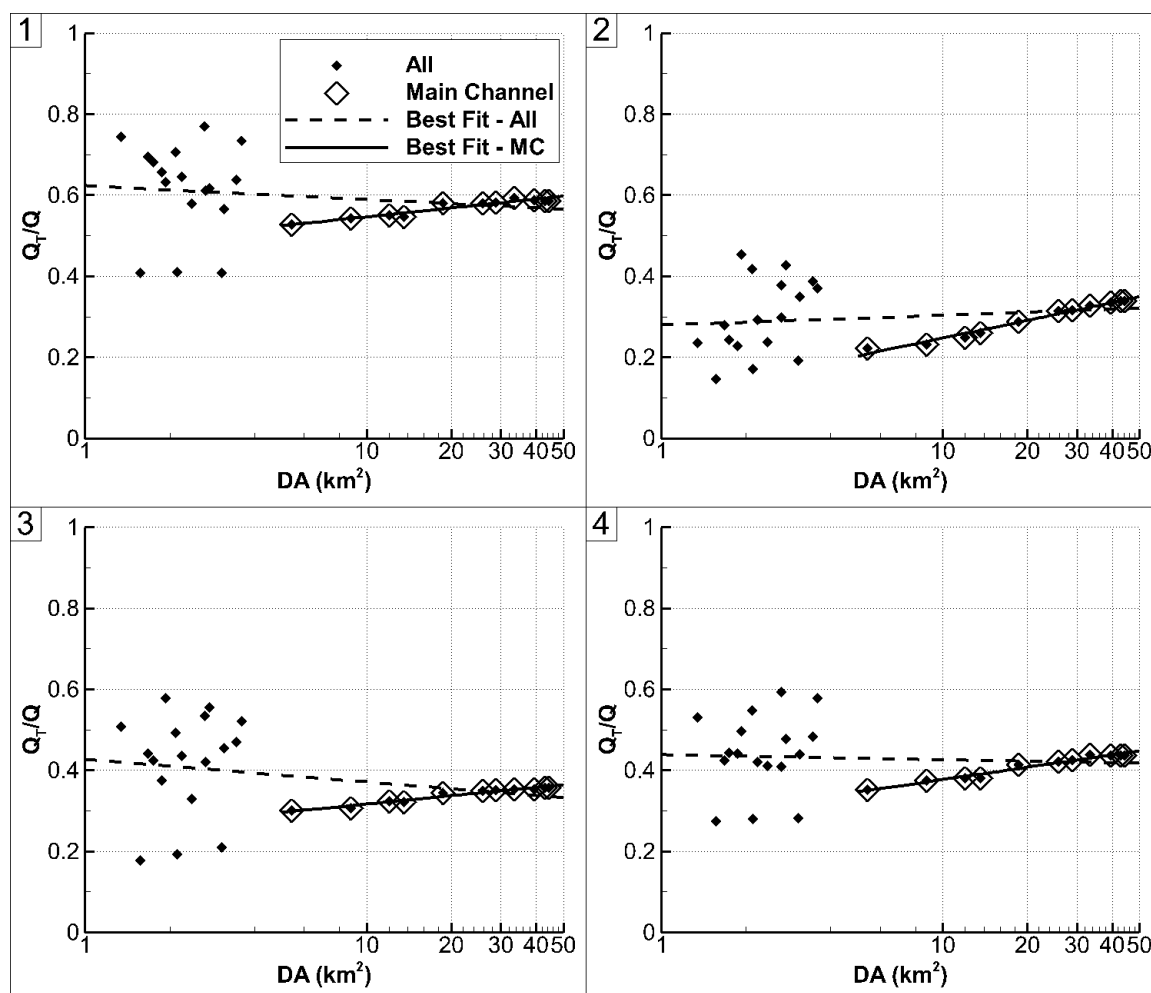
Figure 8.14 Seasonal Q_T/Q at 29 observation points (Fig. 7.6) on a semi-log plot with logarithmic regression lines for all observation points (dashed) and for the observation points identified as MC (solid). The name in the top left corner correlates with the name in Fig. 8.13, Table 8.4, and Table 8.5.

Table 8.5 Seasonal logarithmic regression parameters for MC points.

Name	m	b	R^2
S1	0.07	0.47	0.90
S2	0.15	0.10	0.98
S3	0.07	0.25	0.94
S4	0.10	0.28	0.96
Mean	0.10	0.27	0.94

8.2.2.3 Event Contribution of Tile Drainage

The hypothesis that trends in Q_T/Q with DA differ with respect to meteorological forcing required a division of the year, into high P events (E), and low P non-events (NE). The start of an event was defined as any P accumulation in excess or equal to 10 mm over a 3 hour duration. This accumulation of P was chosen such that a response was evident in stream flow at the outlet. The uniformly distributed P applied to the watershed ensured that a response at the outlet would guarantee the same at smaller scales. The end of an event was identified with a lag time of 5 days after that last accumulation of 10 mm of P in 3 hours. The end time was chosen such that Q_T/Q rebounded to approximately pre-event levels. This definition of a P dominated time period resulted in 14 events totaling 113.4 days of the year (Fig. 8.15).

Events were label E1 to E14, denoting the order in which they occurred. The mean event length (L) was 8.1 d with a minimum and maximum of 5.2 d and 19.0 d, respectively (Table 8.6, Fig 8.16). 12 of the 14 events clustered between DOY 110 and DOY 300. The largest peak Q and Q/P of 0.67 occurred during E3. The event occurred early in the year (DOY 128), prior to large ET rates significantly altering near surface soils. E5 had the longest L of 19.0 d and accumulated the largest P (222 mm), ET (88 mm), Q (57 mm), and Q_T (15 mm) values. From DOY 150 to DOY 250, the increased ET caused a reduction of Q and Q_T volumes with equivalent P, reducing Q/P (Table 7.6). The average event had low mean Q_T/Q of 0.30 as compared to an annual Q_T/Q of 0.39.

The total P accumulation and low Q_T/Q ratio provided evidence of precipitation-surface flow dominated system during events (Table 8.2).

Total Q_T volume increased during Es to an average of 4 mm per event (Fig. 7.16). Absolute Q_T was the largest for E1-E5 prior to large ET rates. Large Q_T occurred in concert with large P, and Q volumes. As P and more specifically P/L increased, Q_T/Q decreased. Surface and near surface flow from increased P rates diluted Q_T to an average of 0.30 for all events.

Q_T/Q varied significantly with DA (Fig. 8.17). Similar to the annual and seasonal time period descriptions, trends in MC points were well defined with logarithmic best fit lines averaging $R^2 = 0.84$ (Table 8.7). Q_T/Q was lower than ET driven periods. MC trend lines all increased with increasing drainage area, except E10. This indicated that during events there was a large contribution of Q_T at the outlet as compared to upstream points. Slopes (m) for 10 of the 14 events could not be identified as significantly different from the mean of the 14 E periods. This indicated the slope of the line or general pattern of increasing Q_T /Q as DA increased remained consistent amongst Es. The intercept incurred a large variability (0.05 to 0.48). With a consistent m value amongst Es, the b value represent the variability from one event to the next. An increase in b corresponded to a vertical shift in the scaling of Q_T/Q over DA. An increase in b represented an intensification of Q_T, a decreased represented a dilution of Q_T.

Slopes for E1, E4, E7, and E10 were all identified as significantly different from the mean of the events. Q for E4, E7, and E10 was narrowly differentiable from pre-event flow rates. E4, and E7 occurred readily after two major events, heavily impacted by antecedent conditions. E1 occurred after a long NE low ET period, where small P produced a large response in Q relative to the rest of the year. Each event incurred variability due to antecedent conditions or atypical atmospheric forcing.
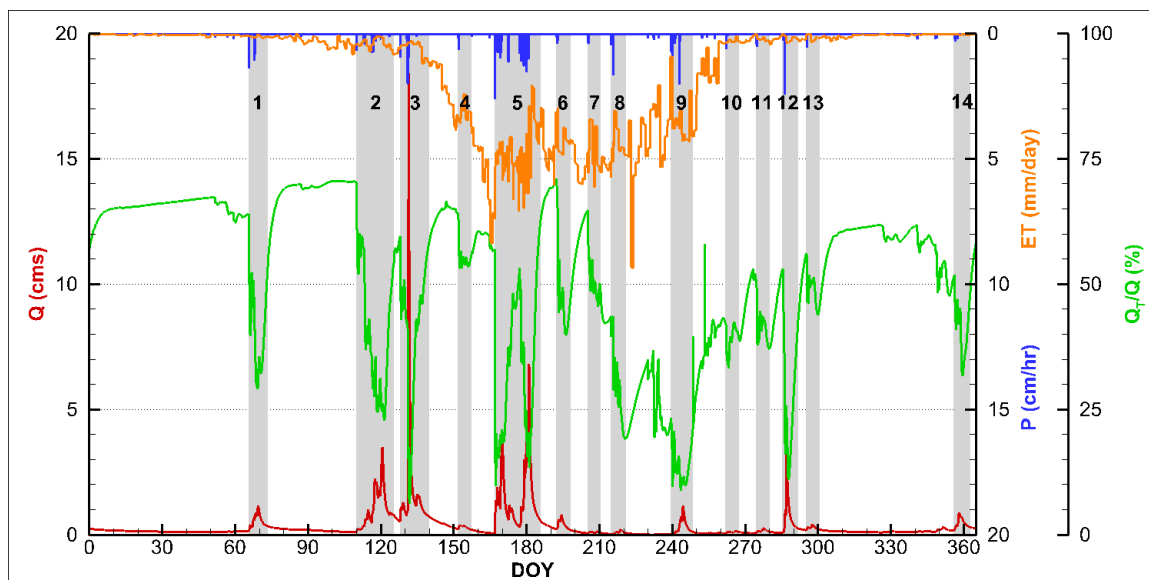
Figure 8.15 Event water balance components for the year of 2014. Grey areas denote start and end of individual events labeled (1-14). Components represented - Q (red), P (blue), ET (orange), and Q_T/Q (green).

Table 8.6 Event integration of water balance components for 2014, values in parentheses is the ratio of each water balance component to P.

Name	Start (DOY)	Length (d)	P (mm)	ET (mm)	Q (mm)	Q_T (mm)	Q_T/Q
E1	66	7.6	37	1 (0.03)	8 (0.22)	3 (0.08)	0.38
E2	110	15.3	95	6 (0.07)	31 (0.33)	10 (0.11)	0.33
E3	128	11.8	65	7 (0.11)	44 (0.67)	12 (0.19)	0.28
E4	152	5.4	12	17 (1.42)	3 (0.27)	2 (0.15)	0.55
E5	167	19.0	222	88 (0.4)	57 (0.26)	15 (0.07)	0.26
E6	192	5.7	16	24 (1.52)	5 (0.29)	2 (0.14)	0.47
E7	205	5.3	13	24 (1.95)	1 (0.08)	0 (0.04)	0.50
E8	215	6.1	22	26 (1.21)	1 (0.05)	0 (0.01)	0.27
E9	240	8.8	85	31 (0.36)	5 (0.06)	1 (0.01)	0.12
E10	262	5.2	16	1 (0.09)	1 (0.07)	0 (0.03)	0.39
E11	275	5.3	14	1 (0.09)	2 (0.12)	1 (0.05)	0.41
E12	285	6.2	54	1 (0.02)	9 (0.16)	2 (0.03)	0.20
E13	295	5.4	11	1 (0.09)	3 (0.28)	1 (0.13)	0.49
E14	356	6.5	23	0 (0.01)	6 (0.25)	2 (0.1)	0.40
Mean		8.1	49	16 (0.34)	13 (0.26)	4 (0.08)	0.30
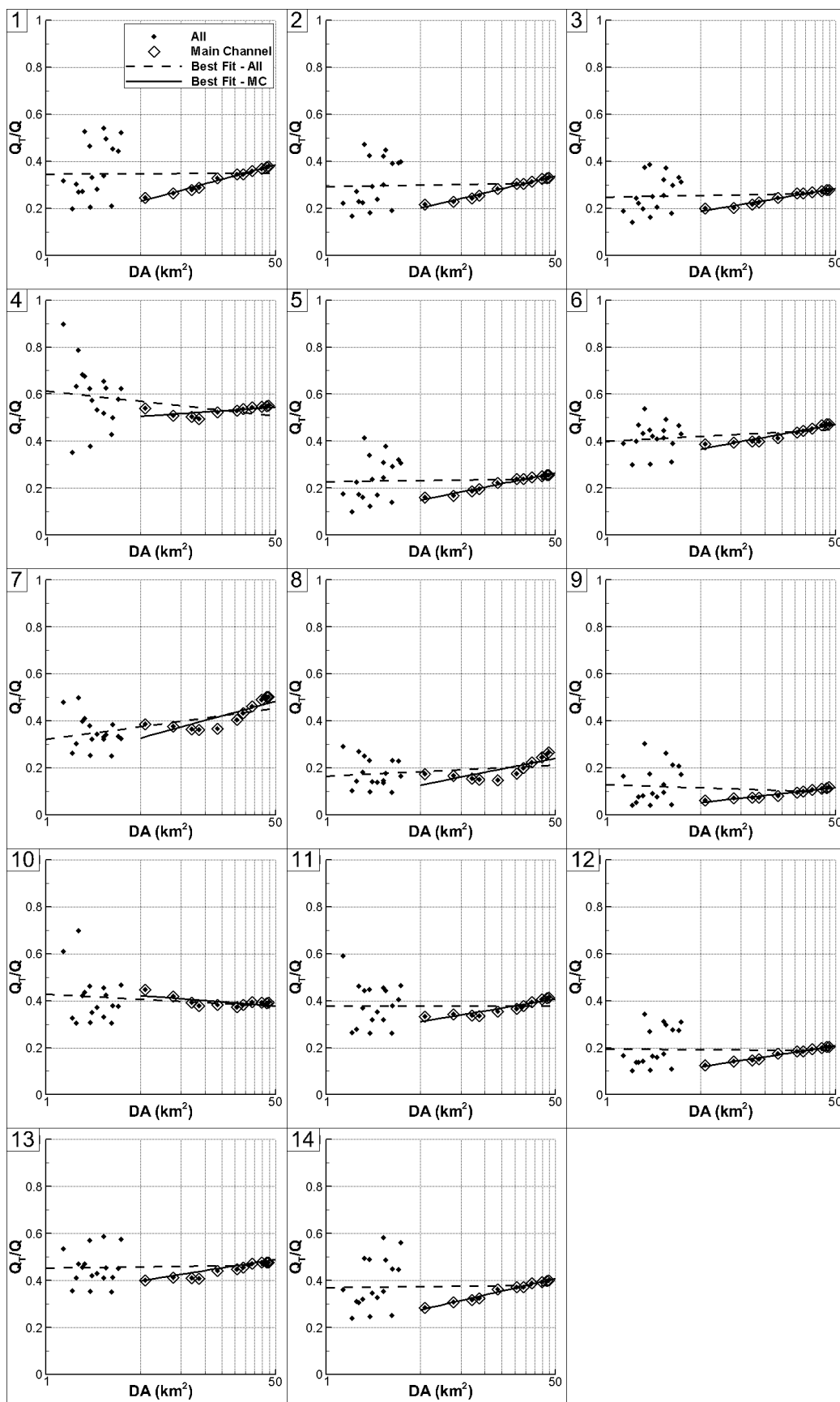
Figure 8.16 Event integrated Q_T/Q at 29 observation points (Fig. 8.6) on a semi-log plot with logarithmic regression lines for all observation points (dashed) and for the observation points identified as MC (solid). The number in the top left corner indicates event number corresponding to Fig. 8.15, Table 8.6, and Table 8.7.

Table 8.7 Event integrated logarithmic regression parameters for MC points. *Denotes p < 0.01.

Name	m	b	R^2
E1	0.16*	0.12	0.98
E2	0.14	0.11	0.98
E3	0.10	0.12	0.97
E4	0.04*	0.48	0.37
E5	0.12	0.07	0.98
E6	0.10	0.29	0.92
E7	0.16*	0.22	0.69
E8	0.11	0.05	0.60
E9	0.06	0.01	0.94
E10	-0.04*	0.45	0.43
E11	0.10	0.24	0.85
E12	0.09	0.06	0.98
E13	0.09	0.34	0.91
E14	0.13	0.18	0.98
Mean	0.10	0.19	0.83

8.2.2.4 Non-event Contribution of Tile Drainage

NE time periods were allocated to the time between specified events, totaling 15 NE periods. NEs averaged 16.8 days long, with the maximum duration NEs occurring at the beginning (NE1) and at the end of the year (NE14) (Fig. 8.17, Table 8.8). NEs totaled to 252 d or 69 % of the year. The variability in L and timing of the NEs was related to the accumulation of P, and subsequent identification of an E period. NE periods were as short as 2.5 days and as long as 65.7 days. NE times were dominated by ET, averaging 19.5 mm, with low average values of P (5.6 mm), Q (4.9 mm), and Q_T (3.0 mm). The low levels of P in NE times produced appreciably different water balance ratios as compared to E periods. Integrating over all NE periods produced Q/P of 0.87, Q_T/Q of 0.61, and

ET/P of 3.5. Q_T/Q was much higher during NEs as compared to Es. Q_T/Q averaged 0.61, with the largest ratios occurring early and late in the year, when ET volumes were low.

Logarithmic best fit lines for the NE periods displayed consistently negative slopes (Table 8.8). Ratios of Q_T/Q at all scales were higher than E time periods. Similar to the other scaling analyses, Q_T/Q was more varied at a DA of less than 3 km^2 (Fig. 8.18). Contribution at small scales ranged from no flow (NE8, NE9) to Q_T/Q ratio of 1.0 (NE2, NE7). Q_T/Q of 0.0 indicated the stream was dry at the given location, these points were removed from regression analysis. Slopes for 10 of the 15 NE were not significantly different from the mean m of NEs. Just as in the E periods the scaling of Q_T/Q with DA was similar across all ET driven NEs. The intercept had a wide range (0.53 to 1.14), which acted to shift the Q_T/Q trend vertically, in the same vein as E periods.

Slopes for NE1, NE5, NE7, NE8, and NE14 were identified as significantly different from the mean of NEs. E1 and E14 occurred during long, atypical NE periods where neither E nor P dominated. E8 transpired when ET was high and ephemeral streams began to dry (Fig. 8.18). E4 and E7 occurred immediately after two major storm events, responding largely from antecedent conditions.
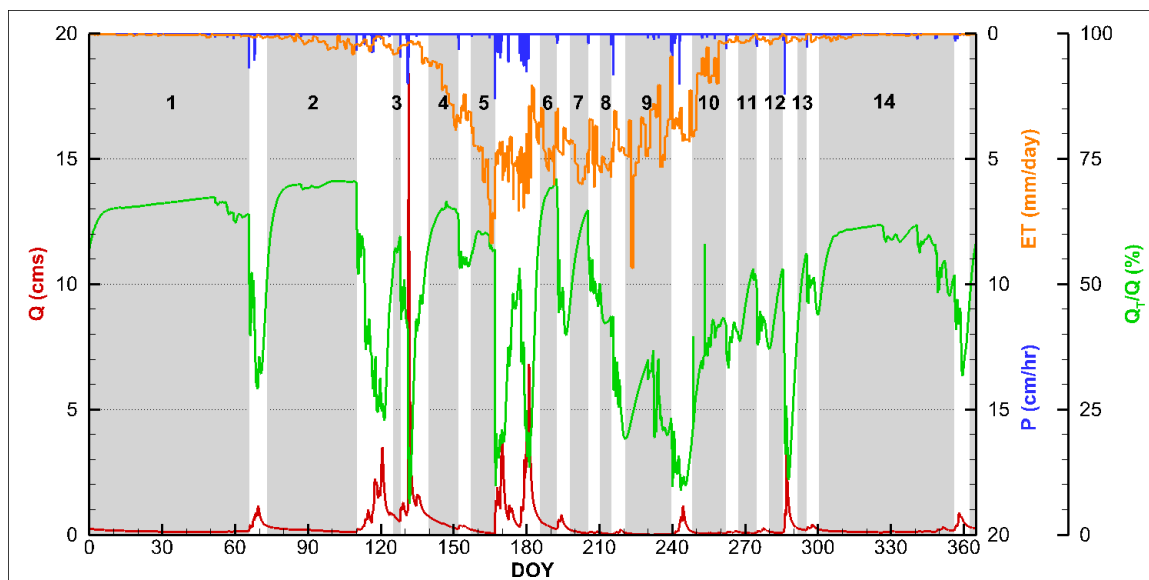
Figure 8.17 Non-event water balance components for the year of 2014. Grey areas denote start and end of individual non-events labeled (1-14) NE15 was not labeled, but represents that final 2.5 days of the year. Components represented - Q (red), P (blue), ET (orange), and Q_T/Q (green).

Table 8.8 Non-event integration of water balance components for 2014.

Name	Start (DOY)	Length (d)	P (mm)	ET (mm)	Q (mm)	Q_T (mm)	Q_T/Q
NE1	0	65.7	8	4	17	11	0.65
NE2	73	36.6	2	11	13	9	0.68
NE3	125	2.6	1	2	3	2	0.57
NE4	140	12.0	3	25	10	7	0.63
NE5	157	9.7	3	53	2	1	0.59
NE6	186	6.4	0	29	4	3	0.68
NE7	198	7.3	0	38	2	1	0.56
NE8	210	4.2	0	22	0	0	0.43
NE9	221	18.8	20	80	1	0	0.23
NE10	248	13.7	16	21	2	1	0.36
NE11	267	7.4	4	2	1	0	0.46
NE12	280	5.5	1	1	1	0	0.44
NE13	292	3.5	0	1	1	1	0.49
NE14	300	55.5	25	4	14	8	0.57
NE15	363	2.5	0	0	1	1	0.54
Mean		16.8	5.6	19.5	4.9	3.0	0.61
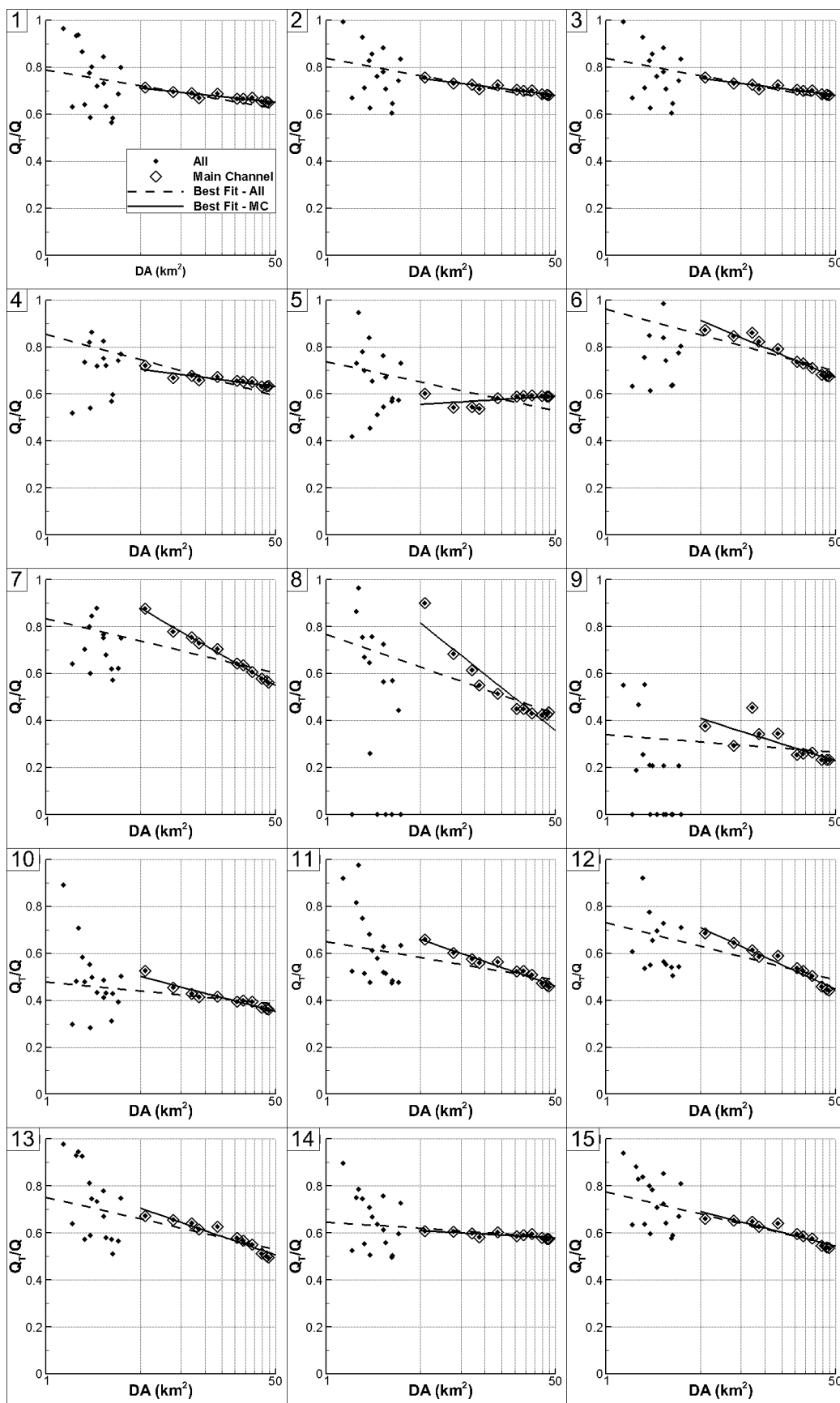
Figure 8.18 Non-event integrated Q_T/Q at 29 observation points (Fig. 8.6) on a semi-log plot with logarithmic regression lines for all observation points (dashed) and for the observation points identified as MC (solid). The number in the top left corner corresponds to event numbers in Fig. 8.17, Table 8.8, and Table 8.9.

Table 8.9 Non-event integrated logarithmic regression parameters for MC points. *Denotes $p < 0.01$.

Name	m	b	R^2
NE1	-0.06*	0.75	0.87
NE2	-0.07	0.80	0.90
NE3	-0.11	0.74	0.94
NE4	-0.07	0.76	0.82
NE5	0.04*	0.53	0.20
NE6	-0.24	1.08	0.94
NE7	-0.33*	1.11	0.99
NE8	-0.46*	1.14	0.89
NE9	-0.18	0.53	0.58
NE10	-0.15	0.60	0.91
NE11	-0.20	0.80	0.96
NE12	-0.26	0.89	0.96
NE13	-0.20	0.84	0.91
NE14	-0.03*	0.63	0.57
NE15	-0.15	0.79	0.87
Mean	-0.17	0.80	0.82

Scale dependency of tile drainage contribution varied when integrated over different time periods. Contributing DA of less than 3 km^2 produced the most variability, with a general pattern of improved trend with increased DA. Logarithmic regression lines for the MC points produced increasing trends in Q_T/Q when integrated over the entire year, each of the four seasons, and all but one of the event time periods. NE period regression lines displayed the opposite trend as DA increased, Q_T/Q decreased. A comparison of all regression lines indicated a significantly lower variability in Q_T/Q ratios at high DAs. The range of Q_T/Q values for all integration periods at the outlet ranged from 0.12 to 0.65. At low DA the range was from 0.0 to 1.0 Q_T/Q.
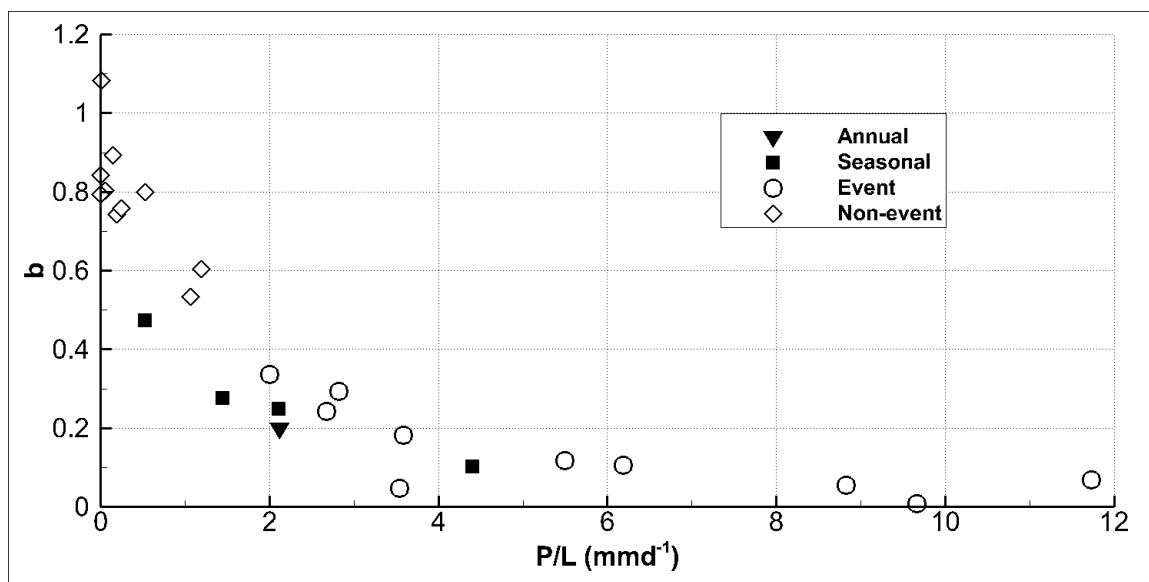
Figure 8.19 Variable logarithmic b (Table 8.3, Table 8.5, Table 8.7, Table 8.9) as explain by precipitation intensity (P/L) over each integration interval. *Intercepts for E, and NE periods having significantly different slopes from the mean were not included.
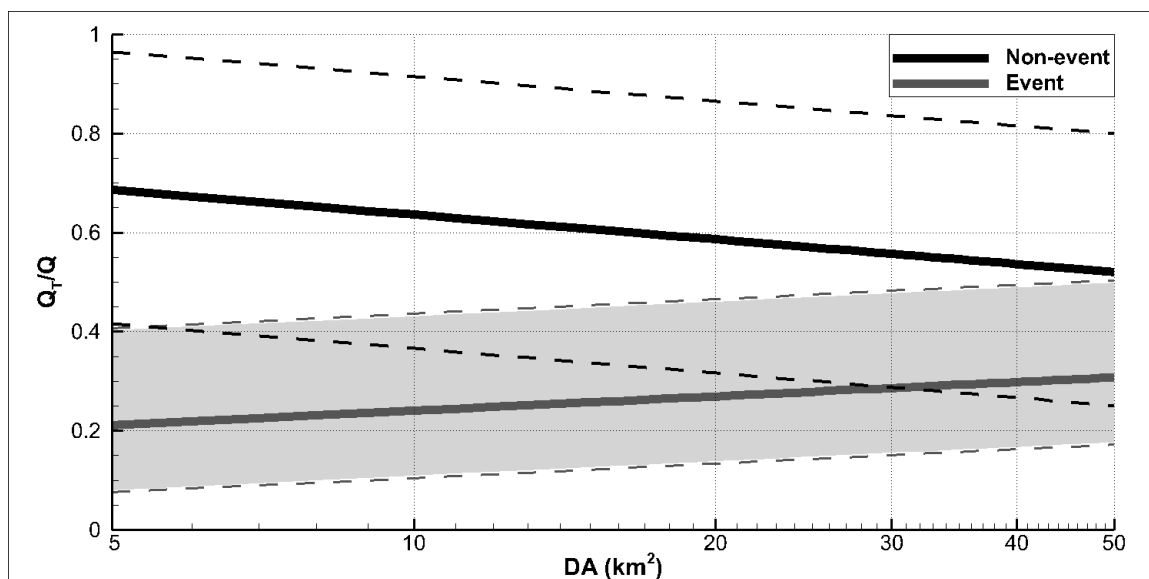
Figure 8.20 Logarithmic regression for E and NE periods. Thick lines indicate the mean m and b for the NE, and E periods, respectively. Narrow lines indicate maximum and minimum b values for each the E and NE periods. Significantly different E and NE trends were removed.

Regression lines for the E and NE periods displayed consistency, positive for E periods, and negative for NE periods. The intercept of regression lines for each of the

integration periods varied predictably with precipitation intensity (P/L). Low

precipitation intensities during NE periods tended towards a high Q_T Q at low DA. High

P/L values diluted Q_T/Q at lower DA, forcing the intercept to asymptotically approach a

Q_T Q value of 0, a heavily surface dominated system. (Fig. 8.19).
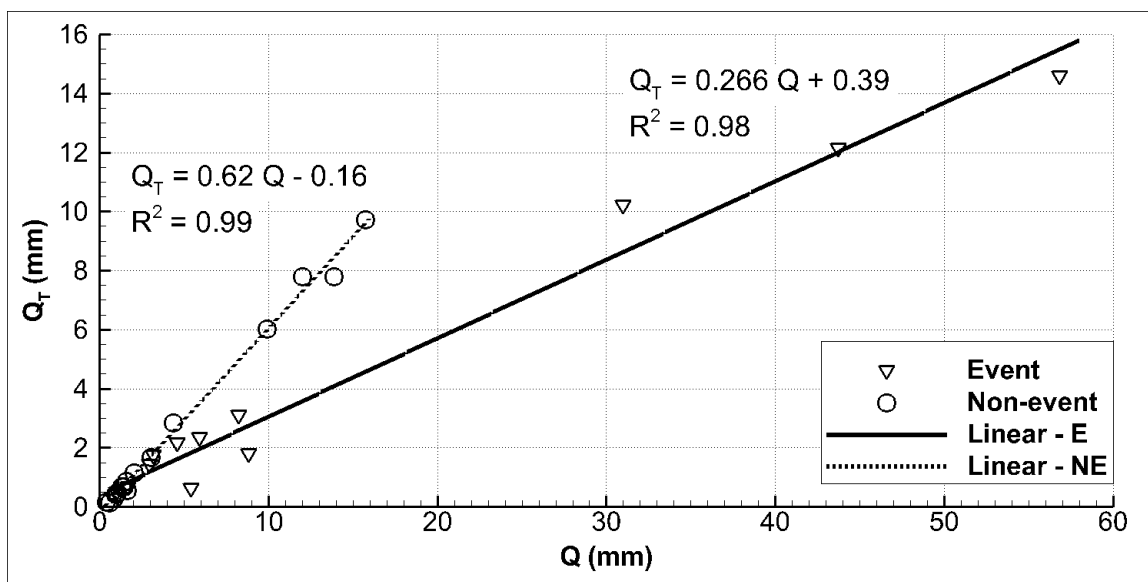
Figure 8.21 Q_T/Q for E and NE periods (Fig. 7.15. Fig 7.17) at the outlet.
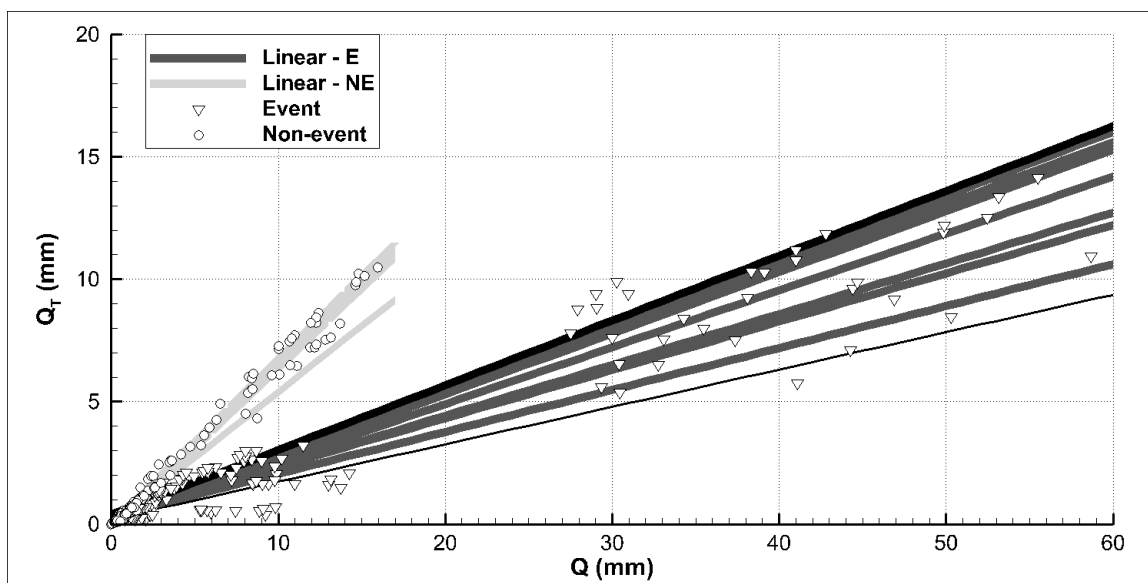
Figure 8.22 Q_T to Q for E and NE periods for each MC point. Best fit for NE (light gray), and E (dark gray) periods. The think black line represents the largest MC DA for E periods, and the thin black line represents the smallest MC DA for E periods.

Q_T was linearly related to Q during E and NE durations. The relationships indicated an increased slope of 0.62 during NE periods, or that 62 % of Q at the outlet was Q_T (Fig. 8.21). As the DA decreased the slope of the NE linear best fit line decreased, representative of a dilution of instream Q_T at smaller DA values (Fig. 8.22). A similar relationship between Q and Q_T at the outlet for events was identified, with a slope of 0.27 and decreasing in slope as DA decreased. The lower event slope was expected due to dilution of stream flow from increased P volumes.

To summarize, Q_T/Q generally exhibits an increasing log-linear trend with increasing DA. This relationship reversed when integrating over NE periods. Logarithmic regression slopes of Q_T/Q to DA for E and NE periods responded in a statistically consistent manner with respect to the mean slope. P/L shifted these trends through dilution, and concentration of Q_T/Q to precipitation water. Trends generally show more Q_T/Q at larger DA for all time periods.

8.3. Discussion

In this study, HGS results from explicit tile drainage simulations provided values to parameterize an equivalent medium representing tile drainage impacts on stream flow. Calibrated simulations at the field scale produced a spatially averaged response in depth to GWT as compared to explicit drainage simulations. The averaged response was produced while remaining consistent with calibration target outflow accumulation. These results were applied to a watershed scale model to investigate spatiotemporal impacts of tile drainage on streamflow for the year of 2014. Results indicated a varied response in Q_T/Q, as P and ET altered hydrologic conditions. A general trend of increasing Q_T/Q as DA increased was observed. Between major events this trend was reversed showing large Q_T/Q at small DA.

8.3.1 Equivalent Medium Hydraulic Conductivity

Calibrated drainage layer hydraulic conductivity in this study ranged from 164 md^{-1} to 530 md^{-1}, representing an increase of three orders of magnitude from those the predominant soil classifications in the BCW (Table 5.1). Equivalent hydraulic conductivity values have previously been manually calibrated, 864 md^{-1} (De Schepper et al. 2015), calibrated automatically 7,570 md^{-1} (Rozemeijer et al. 2010), or theoretically derived (Carlier et al. 2007). Calibrated hydraulic conductivity values for the two above studies were larger than values achieved in this study.

Manual calibration results from De Schepper et al. (2015) closely resemble those from this study. The field scale calibration adopted a similar conceptual modeling approach to De Schepper et al. (2015). The network De Schepper et al. (2015) investigated drained a significantly larger area (3.5 ha), with less relief than the channelized experiment, adapted in this study (Abdul 1985). Increased relief allowed drained water to route more rapidly though the equivalent medium over a shorter distance. An increased slope and shorter flow path produced higher hydraulic gradients requiring less aid, in the form of equivalent hydraulic conductivity, to transport soil water.

PEST calibrated parameters from Rozemeijer et al. (2010) were a factor of 15 higher than those calibrated in this study. Calibration of equivalent parameters for the 38 ha catchment occurred at a single internal groundwater and tile flow measurement location. The equivalent tile drainage medium was applied as a boundary condition for an internal explicit tile drainage investigation. The equivalent medium in this study was introduced to incorporate the effects of combined tile drainage and open ditches (Rozemeijer 2015). Open ditch drainage was not incorporated into the current study producing a lower resultant hydraulic conductivity. The results of Section 8.2.1 align well with De Schepper et al. (2015) and represent the field scale application well. Providing an applicable range of tile drainage conductivity values for watershed scale simulations.

8.3.2 Annual Tile Drainage Contribution to Watershed

Hydrology

P over the study period totaled 774 mm, and was less than the 30 year annual average of 886 mm (IFC 2014). Of the P, 32 % was lost through Q, and 67 % was lost through ET. The Q/P values fall within the range (10 % to 40 %) of values identified over 28 yearlong study in central Iowa by Schilling and Zhang (2004). On average Q represented 26 % of the P (Schilling and Zhang 2004). Tomer et al. (2003) that as drainage area increased the response of individual basins was dampened in a paired watershed study. Researchers noted an increased Q/P ratio at the field scale when compared to downstream measurements. This result was further established by King et al. (2014) reporting a Q/P ratio for basins less than 3 km^2 of 0.44 to 0.61.

At the outlet Q_T contributed 97 mm to stream outflow, representing 13 % of P and 39 % of Q. These values compare well with those reported in literature. Annual accounting of precipitation partitioning to tile flow ranged from 6 % to 64 %, on field scale plots of less than 45 ha (Algoazany et al. 2007; Bakhsh et al. 2004; Hirt et al. 2011; Kladivko et al. 1991; Logan et al. 1980; van der Velde et al. 2010). In larger catchments (2 km^2 to 50 km^2) tile flow was reported as a function of stream discharge (Q_T/Q), with annual contributions of 30 % to 61 % (Culley and Bolton 1983; King et al. 2014; Macrae et al. 2007). Significant variability in these studies was incurred due to subsurface heterogeneity (Eastman et al. 2010; Macrae et al. 2007; van der Velde et al. 2010), land use (King et al. 2014), drainage area (King et al. 2014), and precipitation depth (King et al. 2014; Macrae et al. 2007).

In this study, the effects of DA on Q_T/Q were analyzed for all 29 observation points, and then those points which represented only the main channel of Beaver Creek (MC). Significant variability was seen with decreasing scale, specifically when investigating tributary observations. Variability at drainage areas of less than 3 km^2 were in part attributed to the capacity of the numerical model to incorporate field scale

response with a mean element size of 0.18 ha. This issue was sought to be addressed by requiring observation locations to have 1 km^2 of upstream drainage area, and drain more than 100 elements, but the variability persisted. Spatial variability of subsurface properties (King et al. 2014; Macrae et al. 2007; van der Velde et al. 2010), upstream land use (Hirt et al. 2011), and upstream slope could impact results. As drainage areas aggregated the variability in stream flow response stabilized (Ayalew et al. 2015; Macrae et al. 2007). Logarithmic best fit lines for each the main channel points, and all observation points were analyzed simultaneously.

King et al. (2014) and van der Velde et al. (2010) concluded that tile discharge was strongly correlated to the size of the contributing area. van der Velde et al. (2010) estimated a decreased Q_T/Q with increased DA. In this study, as DA increased, so did Q_T/Q over the entire year. Q_T/Q ranged from 0.21 to 0.50 through all observation points, and in the MC from 0.29 to 0.39. These values of Q_T/Q reported here were within the range of 0.30 to 0.61 over a 6 year period at 3 km^2 noted by King et al. (2014).

<div align="center">

8.3.3 Seasonal Tile Drainage Contribution to Watershed

Hydrology

</div>

Water balance components (P, ET, Q, and Q_T) varied with season. Q was the largest in S2, where P was the highest and the ET was subdued, as the simulation had yet to enter the growing season. ET (314 mm) was the driving force in S3, representing 1.62 times P. The increased ET removed water from the near surface soils, drying the tile and near tile areas reducing Q_T/Q to 0.36 at the basin outlet. Q_T had the largest magnitude in S2 of 44 mm, but was diluted by a large P (400 mm) in turn producing elevated Q (136 mm), and the lowest seasonal Q_T/Q of 0.34. Q_T/Q was the greatest during S1 and S4 where Q_T/Q averaged 0.51.

Q_T and Q_T/Q reached its maximum during S1, S2, and S4, where ET was muted, this result was consistent with literature (Eastman et al. 2010; King et al. 2014; Kladivko

et al. 2004; Macrae et al. 2007). Monitored tiled fields in Quebec Canada indicated a consistent reduction in both Q and Q_T during the growing season (Eastman et al. 2010). Each author identified a similar trend in tile drainage contribution, reproduced in this study.

Seasonally, the slope of MC logarithmic regression lines indicated an increasing trend in Q_T/Q with increasing DA. Calculated m values were similar in S1, S2, and S4 for the MC points (Fig. 8.15, Table 8.5). The P dominated S2 displayed the steepest slope (m). S2 had 400 mm of P, and the highest P/L of all the seasons. The increased P/L saturated soils, and increased both Q and Q_T. The increased P/L forced the entire hydrologic system to respond in a similar manner as events. Fig. 8.13 corroborated this description, as over a majority of S2, Q was at an elevated level.

<center>8.3.4 Precipitation Dependency of Tile Drainage</center>

<center>Contribution to Stream Flow</center>

The simulated time series was split between E and NE time periods though a requisite P accumulation. During E delimited time periods P dominated the meteorological forcing and during NEs, ET served as the driver. During the accumulated E time periods 91% of the P, 44% of ET, 71% of Q, and 54% of QT occurred over 114 days of the year. Large P saturated the soil, increased surface runoff, and QT. Due to the large quantities of Q, Q_T was diluted, producing a lower Q_T/Q. Over half of the Q_T volume occurred during the events with an average Q_T/Q of 0.30. In NE periods Q_T/Q averaged 0.59.

At the watershed outlet Q_T/Q ranged from 0.11 to 0.65, and for the entire DA range, from 0.0 to 1.0. King et al. (2014) indicated a similar response of tile, which contributed 30 % to 61 % of Q at the outlet. Macrae et al. (2007) measured a range from 0 % to 90 %. Logan et al. (1980) reported a range of precipitation recovery (QT/P) of 0 %

to 66 %. Flow contributions throughout the year from this study were consistent with those from other field studies.

Ephemeral stream locations measuring tile drainage contribution became dry during NE8 and NE9. Tile systems often cease flowing during approximately 25% of the year. These no flow periods occurred in the summer due to intense growing season ET, and over the winter in the northern climates due to freeze (Kladivko et al. 2004; Logan et al. 1980; Macrae et al. 2007). The numerical simulation in this model did not incorporate the freeze thaw cycle or snow accumulation and melting, but was able to capture summer dry periods.

E periods (Fig. 8.17) responded in a similar scaling with DA trend as S2, both of which incurred large P depths. As DA increased, Q_T/Q increased at a similar rate (m) for all events but E1, E4, E7, and E10. Each display approximately the same slope with a changing intercept. The uniformity of response was evident from the consistent slopes over a range of events, and better fits (R^2) for the highest precipitation events (E2, E5, E9, and E12).

NE periods displayed a decreasing trend in Q_T/Q with increasing DA, an outcome which was expected by van der Velde et al. (2010). NE periods displayed more variability in the regression slope, with 10 of the 15 events retaining consistency. van der Velde et al. (2010) applied a linear mixing model to estimate tile drainage contribution to stream flow beyond the field scale. The assumption was that Q_T scaled with a ratio of tile drained area to total contributing area. In this study, the ratio of tile drained area to all contributing area was unity, as the tile drains were uniformly distributed across the system. This allowed for a simplified examination without variability in tile contribution due to spatial heterogeneity in tile density. van der Velde et al. (2010) over all time periods estimated a decreasing trend of Q_T/Q, as DA increased was explained by a reduction in upstream area drained by tile with increasing DA.

BCW is an elongated basin 3.5 km wide and 14.8 km long, flowing from north to south. Magnifying the impact of the elongated basin was the increased slope of the southern portion of the basin. The southern half of BCW contributed surface and subsurface water to the outlet at a faster rate than upstream areas. Single storm events flowing through the system often produce a bimodal stream flow response at the outlet. In the lower half of BCW, surface water and tile water arrived at the outlet quickly during rainfall periods. Surface runoff and near surface lateral flow dominate the total proportion of stream flow in events. Water must travel vertically one meter into the subsurface to reach the tile, reducing and delaying the tile response. In steep conditions tile flow responds fast enough to reach the outlet within the 5 d minimum event length. This tile water increased total tile contribution during E periods. During NEs, tile water from the previous event in the upper half of BCW contributed to the outlet, diluted by lower half of BCW groundwater flow. The combined effect of increased slope and lateral groundwater flow near the outlet can explain the reduced Q_T/Q as DA increased (Fig. 8.22).

The major deviations in S, E, and NE logarithmic regression fits occurred in the intercept. Each time period displayed statistically similar slopes, with a widely changing intercept. An increase in P/L diluted instream Q_T, and decreased the intercept (Fig. 8.19). As P increased the basin became more saturated, and dependent upon its own hydraulic capacity of the tile system to transport water. A lack of P tended to concentrated Q_T/Q.

Macrae et al. (2007) found that the highest 17% of Q correlated very well with Q_T. In this case Q_T was positively correlated to Q with a linear regression slope of 0.60. Macrae et al. (2007) further noted extreme variability for the intermediate 13% of flows, the remaining measurements were dry or displayed relatively little contribution. King et al. (2014) found a linear relationship between Q and Q_T with a slope of 0.47 over the entire range of measured Q and Q_T values. Fig.7.21 displayed a similar linear pattern, but was split between E and NE periods. Each displayed high correlation, with linear slopes

of 0.59 (NE) and 0.26 (E) at the outlet. A NE intercept of -0.011 indicated that under extremely low Q conditions, Q_T was not expected to contribute to streamflow. Overlap between E and NE periods from 5 mm to 15 mm of Q corresponded to the unpredictability of Q_T at moderate stream flows noted by Macrae et al. (2007). Fig. 8.21 indicated that varied processes occurred in E, NE, and S periods. The rapid wetting and transport of runoff to streams, diluted tile drainage response shifting b downward. NEs were representative of baseflow and intermittent P periods, where tile drainage interplay with near surface flow impacted hydrologic response.

8.3.5 Challenges

The field scale simulation was completed as a numerical test, and was not representative of a real drainage system. To improve this experiment, field scale measurements of tile flow, surface flow, and groundwater variability, would offer calibration and validation targets to PEST. The response of the field scale model was tested in a pure drainage scenario (without P or ET). The addition of rapid wetting and drying through precipitation could alter the calibration results. In addition the equivalent medium was calibrated to a flow volume accumulation after 10 days of drainage. Additional calibration targets of volume or instantaneous discharge could offer improved results.

Tile drainage at the watershed scale was assumed uniform in spacing and application throughout the watershed, an incorrect assumption. The addition of spatially variable equivalent medium parameters could advance the findings incorporating spatial heterogeneity of tile response. Coupling of the tile drainage system under the stream by increasing the hydraulic conductivity of the stream bed, was a non-physical representation of reality. This could impact low stream flows and exchange into the subsurface at the stream location. Macropores have been noted as important in conveying fast flowing water into drains quickly (Hirt et al. 2011). Preferential flow was

incorporated by increasing the vertical hydraulic conductivity of subsurface soils. This was a simplification to the physical process occurring in macropore flow.

8.4 Summary of findings

This study advanced the watershed scale tile investigation beyond dendritic tile drainage systems (Schilling et al. 2012), to uniform drainage patterns in more recently glaciated regions of the Central U.S. A field scale numerical experiment was constructed to investigate explicit tile drainage simulations. It provided calibration targets for an equivalent medium representing a tile drainage layer. A comparison of calibration results at the field scale indicated that the equivalent system produced a spatially averaged solution relative to explicit results. Calibrated equivalent properties for a range of tile densities at the field scale produced a viable option for hydrologic model application of equivalent tile drainage at the watershed scale.

These results were applied to an annual simulation of the BCW to investigate spatiotemporal impacts of tile drainage on streamflow. Results indicated a significant response in Q_T/Q as climatic forcing (P and ET) altered hydrologic conditions. Results showed that Q_T/Q responded logarithmically with DA. An increase in DA produced an increase in Q_T/Q. Only during NE periods would this trend reverse. The response reversal denoted an important shift, precipitating the investigation of E and NE periods. Tile drainage systems respond at a slower time scale than surface and near surface flows, heavily impacting post event hydrologic processes. Logarithmic regression coefficients for E and NE periods responded similarly. Q_T/Q trends with DA were retained for a majority of E and NE periods, independently. The magnitude of Q_T/Q was found to be related to the precipitation intensity.

During events tile drainage contributed averaged 27 % of the total stream flow at the outlet, and 15 % in the headwaters. Over non-event periods, tile drainage contributed 62 % of total stream flow at the outlet, and 54 % in the headwaters. The consistent

increase in contribution with increasing DA was due to precipitation dilution, the physical basin shape, and topography.

The addition of sampling frequency in time and space benefit from this work. Most studies investigate tile impacts at the field scale, as catchment wide measurements of tile flow would be unfeasible. This study was able to represent the same temporal patterns observed in literature, while expanding the understanding of metrological forcing on tile flow contribution to stream flow. This work offers insight into the spatiotemporal processes of Q_T/Q. It takes an aged approach of tracer analysis and incorporated it numerically to achieve a further understanding into tile drainage.

9.0 TERRACES

Land use and land management practices in the agriculturally dominated central U.S. have adversely affected flow and quality of the regions water bodies (Bracmort et al. 2006; Eidem et al. 1999; Hutchinson et al. 2013; Karlen et al. 1999; Peterson et al. 2013; Schilling et al. 2008; Secchi et al. 2007; Squillace et al. 1996; Tomer et al. 2005; Villarini and Strong 2014). Non-point source (NPS) pollution from cultivated landscapes has been linked to increased nutrients in streams, reduced water quality, and hypoxia (IDALS 2013; Mitsch et al. 2008; Shen et al. 2011; Tuppad et al. 2010; Vache et al. 2002; Yang et al. 2009). Overland sediment movement in predominantly till-derived soils of North Central Iowa, have been documented to increase erosion and subsequent loss of agrochemicals (Fenton et al. 2005; Karlen et al. 1999). Reducing soil erosion is recognized as critical to minimizing NPS nutrient loads (Nearing et al. 2011; Vellidis et al. 2003).

NRCS Best Management Practices (BMPs) to reduce soil erosion include terraces amongst other approaches (Baker et al 2006). Terraces are earthen embankments built across moderate to steep slopes, often in groupings of more than one at regular intervals. They shorten unimpeded flow lengths to reduce rill and gully erosion, trap sediment, retain runoff, reduce flood peaks, and increase groundwater resources through infiltration (Baryla and Pierzgalski 2008; Cammeraat 2004; Kramer et al. 1999; Strauch et al. 2013; Tomer et al. 2005; Yang et al. 2009). Terraces became popular in the Central U.S. in the 1960's (NRCS 650), with nearly 118,000 km of terraces scattered across Iowa (Hultquist and Best 2001).

Terrace systems are commonly investigated at the field (Bracmort et al. 2006; Cammeraat 2004; Gallart et al. 1994; Gatot et al. 2001; Karlen et al. 1999; Kramer et al. 1999; Onstad and Jamieson 1970; Tomer et al. 2005), and watershed scale (Arabi et al. 2008; Cammeraat 2004; Gatot et al. 2001; Secchi et al. 2007; Strauch et al. 2013; Tuppad

et al. 2010; Vache et al. 2002). Empirical and deterministic approaches have been followed thus far to include terrace systems into numerical simulations. Most studies have simulated terrace incorporation with lumped conceptual numerical models, which simplify infiltration mechanisms to partition rainfall over sub-basin areas (Arabi et al. 2008). Conceptual lumped models limit the interaction between surface and subsurface components, negating their ability to represent more complex spatial patterns of surface-subsurface soil water transfer (Opolot et al. 2014; Verbist et al. 2012). There is no current standard practice for incorporating terraces into numerical models, potentially producing inconsistent results subject to modeler judgement (Arabi et al. 2008). Often terraces are accounted for in conceptual lumped models, where a few nonphysical parameters are altered to account for the change of flow path (Arabi et al. 2008; Bracmort et al. 2006; Secchi et al. 2007; Strauch et al. 2013; Vache et al. 2002; Yang et al. 2009). Aggregated temporal accounting of terrace impacts, often occur at daily increments (Arabi et al. 2008; Bracmort et al. 2006; Secchi et al. 2007; Strauch et al. 2013; Yang et al. 2009). Daily accounting has been noted as too coarse. Important topographic features alter travel times and runoff generating processes, impacting a basins immediate response as reviewed by Frei and Fleckenstein (2014).

Lumped descriptions of hydrologic processes can be avoided by the use of physically based coupled models. Distributed models are able to take into account the spatial heterogeneity of watershed processes (Zhang et al. 2008). The impact of a terrace system has yet to be investigated with this modeling format. Regularly spaced rainwater harvesting trenches have been investigated with a coupled surface-subsurface hydrologic model (Opolot et al. 2014; Verbist et al. 2012). These practices exhibit similar runoff altering mechanisms as terrace systems. Authors noted the impact of the built structures reducing surface water runoff by 68%, and increased deep infiltration by 37% to 43% annually.

The recommended spacing of terraces are too narrow to be explicitly represented in basin scale simulations. Frei and Fleckenstein (2014) conceptualized an approach to upscale micro-topography to coarse grid elements. Storage thresholds were applied to large scale grid elements, representing the impact of depression storage on hydrologic controls. Timing of runoff generation, infiltration, and exfiltration were able to be adequately accounted for through calibration of depression storage.

The goal of this study was to incorporate terraces into a watershed scale coupled surface-subsurface hydrologic model. Regularly spaced terraces were conceptualized as an increased overland roughness. An increased roughness was estimated through PEST at the field scale. Terraces have been noted to delay and reduce peak flows, and increase infiltration. These claims were investigated by scaling up field based effective roughness values to watershed scale.

9.1 Study Methodology

The impact of terrace systems were evaluated at the field scale and applied at the watershed scale. A terrace system refers to multiple continuous earthen embankments constructed across a field to reduce runoff and erosion (NRCS 2011). Terrace systems consist of either storage or gradient terrace designs. Storage terraces collect and store water until infiltration, evaporation, or flow from a controlled underground outlet removes the accumulated runoff. Gradient terraces are designed as mild sloping channels facilitating continuous water movement towards a stable outlet (NCRS 2001).

This study investigated gradient terraces, as HGS modeling capabilities prohibit simulation of storage terraces, see Section 9.3.1. Multiple gradient terrace densities were explicitly incorporated at the field scale by altering the topography (Fig. 9.1a, Fig. 9.2). The terrace systems were conceptualized as an effective roughness over the area draining to the most downstream terrace. Through a PEST calibration of surface effective roughness, a relationship between density of terraces (length of terraces/drainage area)

and effective roughness was produced. The field scale relationship was applied to watershed scale analysis as a function of grid element slope (Fig. 9.1a).
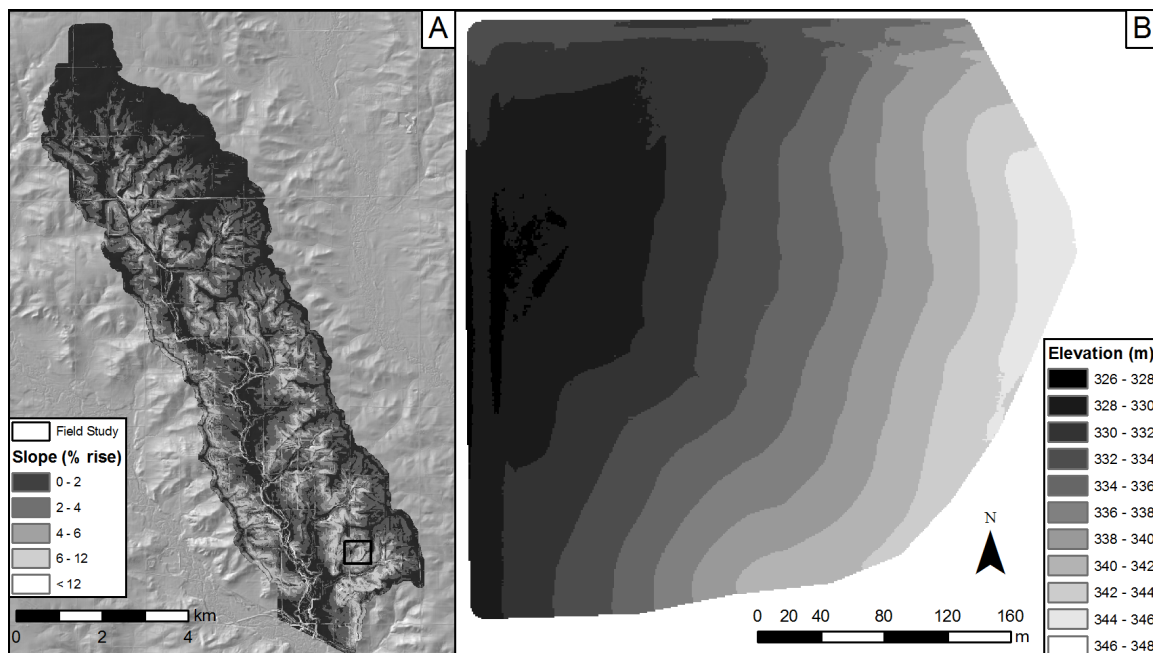
Figure 9.1 a) Field study calibration location within BCW b) Calibration study location topography prior to terrace investigation.

9.1.1 Field Scale Parameter Estimation

Coupled surface-subsurface modeling at large scales requires simplifications to the mesh, coarsening elements to increase efficiency. Coarse element sizes required sub-grid scale roughness to incorporate the impact of terraces. Frei and Fleckenstein (2014) adequately replicated surface and subsurface flow patterns through incorporation of sub grid scale roughness at the plot scale. A similar method was investigated in this study. The incorporation of terraces into larger scale simulations was completed with HGS, a coupled surface-subsurface hydrologic modeling software described in Section 3.0.

Flow in HGS is assumed to occur over a flat plane, with only frictional roughness impacting flow acceleration. An increased effective frictional roughness was used as a surrogate to replicate the runoff response of an explicitly incorporated terrace system.

Gradient terraces alter flow patterns by delaying and reducing the runoff peak produced from a rainfall event. An increase in friction roughness would effectively delay surface flow. Frictional roughness was estimated to replicate the flow of gradient terraces.

The surface hydrology of an explicit terrace system was studied on a 1.12 ha abstraction from the greater BCW area (Fig. 9.1a). The field site was located in the southern portion of BCW, defined by steeper slopes, increasing the potential benefits of terraces. The dominant flow paths of the field study was sloped at 6.6% over row crop agriculture.

A 2-D unstructured finite element mesh was created using Gridgen V15. Gridgen requires mesh generation boundaries to produce an irregular grid though Delaunay Triangulation (Fig 9.2). The field boundary was delimited by relative topographic high points, with the encompassing area draining to a single outlet point. Potential terrace locations were identified through the Terrace Practice Standard 650 (NRCS 2002), requiring a minimum spacing based on a given slope. Required terrace spacing ranged from 27 m to 45 m. The spacing minimum requirements were dependent upon the rainfall erosion factors which vary based on location (NRCS 2015).

A 40 m spacing was selected for explicit terrace inclusion, representing the mean variability across Iowa. Terrace spacing specific to this study is discussed in Section 9.1.2. A field scale mesh was the product of, the field boundary and locations of 5 contour type terraces at 40 m increments through the same methodology applied at the watershed scale (Fig. 9.2) (Section 5.2). Herein each explicit terrace is referred to by numeric label, from most downstream (terrace 1) to most upstream (terrace 5) (Fig. 9.2). Multiple terraces incorporated into the same simulation are herein referred to by a number identifying which terraces were simulated (i.e. a terrace simulation with terrace 1 and 3 is referred to as arrangement 13).

The product of mesh generation was a 1,931 node, 3,717 element mesh with an average element area of 30 m^2. A 2-D mesh was needed as only the surficial impacts of

terraces were calibrated. The 2-D mesh was then projected onto the one meter resolution LiDAR derived DEM. This version of the topography represents the control condition. The field contains a single sloped hillslope draining from East to West. The field drains into an established stream flowing across the Northwest of the domain, exiting the outlet on the Western boundary (Fig. 9.2). Water was only allowed to exit the system through the stream channel outlet on the Western boundary. Surface properties were derived from Table 5.2 for an agricultural land classification.
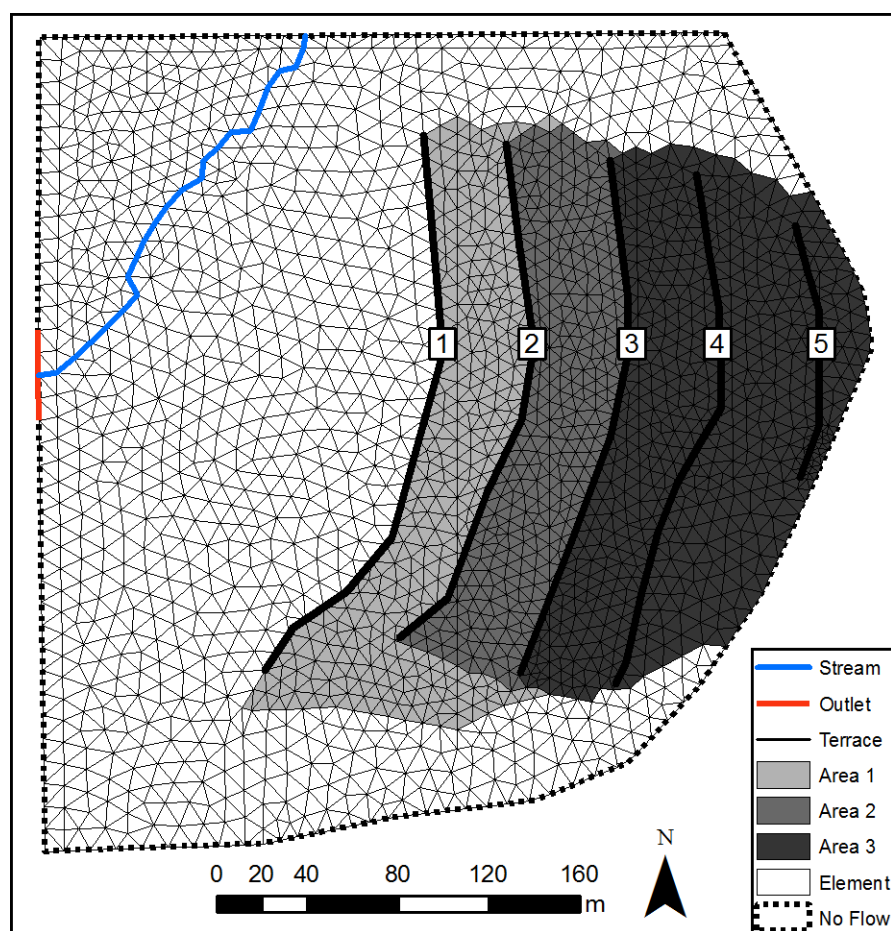
Figure 9.2 Field scale numerical mesh for terrace calibration abstracted from the BCW (Fig. 9.1). Boxed numbers represent names for each terrace. Area 1, Area 2, and Area 3 refer to calibration areas upstream of terrace 1, terrace 2, and terrace 3, respectively.

Simulations were ran on the numerical grid described above, with 29 different terrace arrangements. The terrace arrangements incorporated 1, 2, 3, 4, or all 5 terraces. They were completed such that terrace 1, terrace 2, terrace 3, or all three were explicitly included in model simulations. Terraces were incorporated by increasing the elevation at a single line of nodes along the hillslope contour. The mesh was constructed with grid lines running along the contours to adequately reproduce lateral terrace flow. Terrace elevations were held constant along the contour, at 0.7 m above the original land elevation. The added elevation forces concentrated flow to the outer portions of the domain, reducing and delaying runoff peaks at the field outlet.

Precipitation was applied uniformly over the entire domain at 50 mmhr^{-1} for one hour. The simulation was initialized without any surface water. Simulations were run for six hours. A time series of runoff data was recorded as calibration targets for parameter estimation.

Calibration of the field scale effective roughness was completed for each of the 29 terrace arrangements. The effective roughness was only calibrated on the area upstream of the most downstream terrace incorporated in a given model run. For configurations including terrace 1, roughness was calibrated for Area 1. Similarly, for configurations not including terrace 1, instead terrace 2 represents the most downstream terrace, and roughness was calibrated for Area 2 (Fig 9.2).

PEST a parameter estimation software was utilized to calibrate effective roughness values to calibration targets provided by the explicit terrace simulations. PEST was described in detail in Section 7.1. Instantaneous surface outflow values were used as calibration targets every 500 s (500 s, 1000 s, 1500 s, etc.). One additional target at the end of precipitation was added (3600 s). In a small drainage areas, the end of precipitation often coinciding with the time of peak discharge (Fig. 9.3). Calibration targets (44 total) were weighted more heavily during the rising limb of the hydrograph and most heavily at the peak (Fig. 9.3), ensuring calibrated parameters best fit during

high flow periods (Fig. 9.3). Effective roughness was assigned uniformly to areas upstream of the most downstream terrace (Fig. 9.2). Effective roughness values for PEST simulations were bounded between 0.07 sm$^{-1/3}$ and 5.0 sm$^{-1/3}$. Results from field scale PEST calibrations produced a relationship of effective roughness to represent a specific terrace density. The relationship was built for application to the watershed scale study.
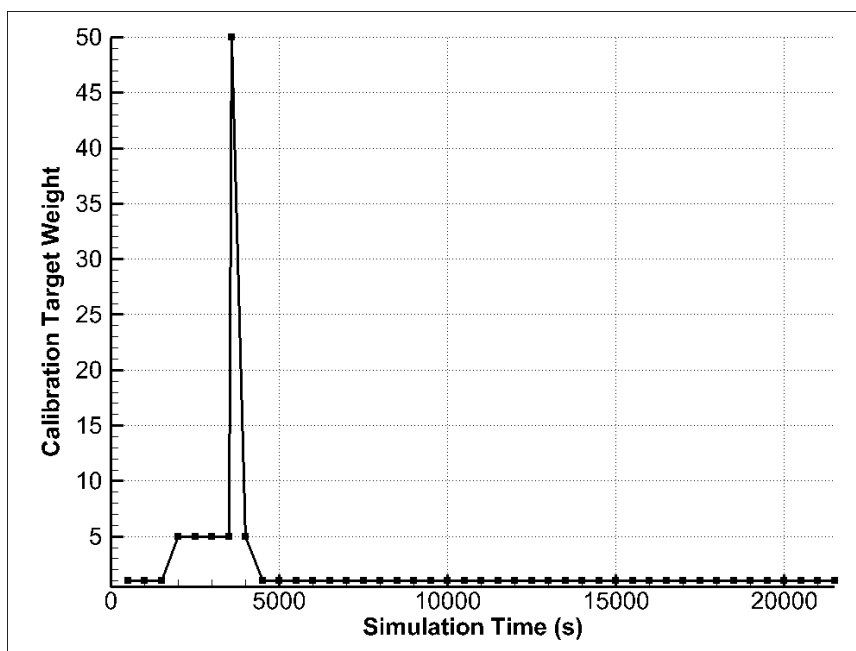
Figure 9.3 PEST calibration target weights for terrace simulations.

9.1.2 Watershed Scale Implementation

The focus of this study was on the watershed scale implementation of terraces in the BCW. Soil erosion is a significant issue in agricultural soils (Fenton et al. 2005; Tomer et al. 2005; Yang et al. 2009), increasing with severity as fields become steeper (Yang et al. 2009), and unimpeded flow paths become longer (NRCS 2014; Wischmeier and Smith 1978; Yang et al. 2009). As stated earlier terraces divide flow paths and reduce the effective slope at application sites. BCW is dominated by row crop agriculture (> 70 %) (Fig. 9.4), and has increasingly sloped land in the southern half of the catchment (Fig.

9.1). BCW currently contains 7.5 km of terraces, located primarily in the south (Fig 9.4). In watershed wide terraced simulations the current locations of terraces were not directly incorporated. Terraces were implemented across the catchment with densities varying by land slope.
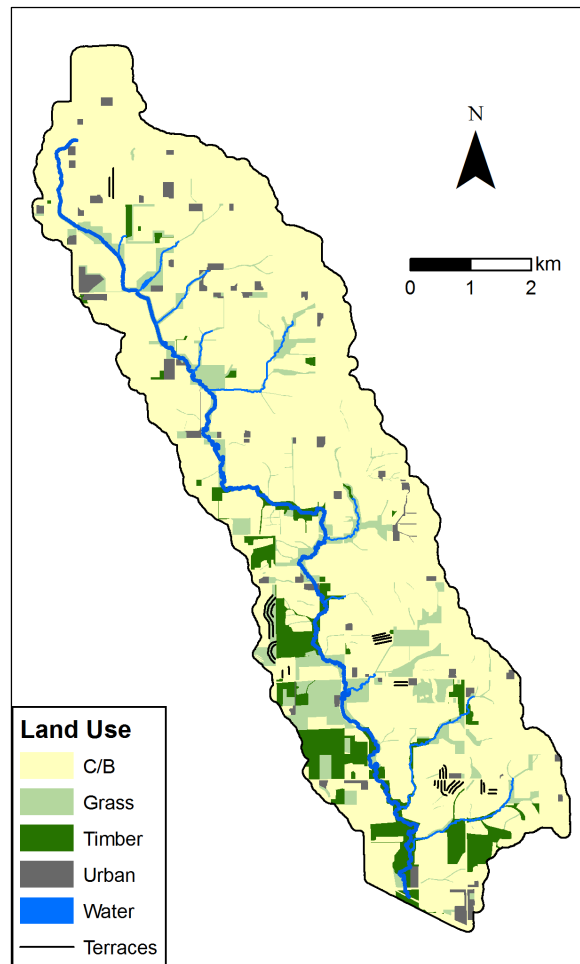
Figure 9.4 Current terrace locations in BCW.

To investigate terraces at the watershed scale, HGS was applied to the 16 layer, 212,993 node, and 371,460 element 3-D grid, discussed in Section 5.2. Basin characterization, parameter identification, and boundary conditions were described in Section 5.0. The initial condition was the product of three years of iterative atmospheric forcing described in Section 6.1.

Surface elements in the watershed scale model averaged 0.18 ha, making them too large to explicitly incorporate terraces. To preserve efficient computational times elements could not be exhaustively distributed. Surface roughness was adjusted to incorporate terraces into larger watershed scale elements.

Narrow based terraces were selected for design purposes, as they retain the largest amount land in crop rotation. Terrace spacing was estimated through the Universal Soil Loss Equation (USLE) (NRCS 2002), as required by NRCS code 600 (NRCS 2014). A brief description of the procedure to estimate terrace spacing based on erosion control is provided below, for a detailed review refer to (NRCS 2011; NRCS 2014; Wischmeier and Smith 1978).

$$A = RKLSCP \hspace{4cm} [9.1]$$

Where A is the computed soil loss per unit area (ton acre^{-1} yr^{-1}), R is the rainfall runoff factor for an average year of rainfall, typical values range from 150 to 175 in Iowa, K is the soil-erodibility factor indicating the soil lost from a unit standardized plot (slope, length, and ground cover), L is the length factor as compared to the standardized plot, S is the slope gradient factor as compared to the standardized plot, C is the land cover and management factor, and P is the support practice factor representing the effects of various erosion reduction practices.

The USLE was solved for slopes ranging from 4 % to 12 % depicted by Fig. 9.5b, assuming that A = T, where T is a threshold value for sediment loss. Rearranging Eq. [9.1] to solve for L, provided Eq. [9.2]. Eq. [9.2] was solved with values from Table 9.1 representing an averaged condition within the BCW. Results of USLE produce a maximum terrace spacing based on slope, ranging from 20 m to 90 m. An additional 7.6 m was added to the USLE derived spacing to account for the non-farmable front and back slope of the terrace structure. These values fit within the minimum (27 m) and maximum

spacing (152 m) for the BCW (NRCS 2002). Spacing values are depicted spatially in Fig. 9.5b, and over the range of slopes in Fig. 9.6.

$$L = \frac{T}{RKSCP} \qquad\qquad [8.2]$$

Table 9.1 USLE erosion estimation factors to compute terrace spacing.

Parameter	Value	Explanation	Source
R	160.0	Values for Floyd and Chickasaw counties containing BCW	(NRCS 2015)
K	0.37	Area weighted average of reported K values	(SURGGO)
C	0.31	Annual average continuous corn	(USDA 1978)
P	0.50	Gradient terraces with closed outlet	(NRCS 2002)
P	0.40	Contour farming with moderate ridge height, Contour terraces force contour farming	(NRCS 2002)
T	5.0	Area weighted average of reported T values	(SURGGO, USDA 1978)
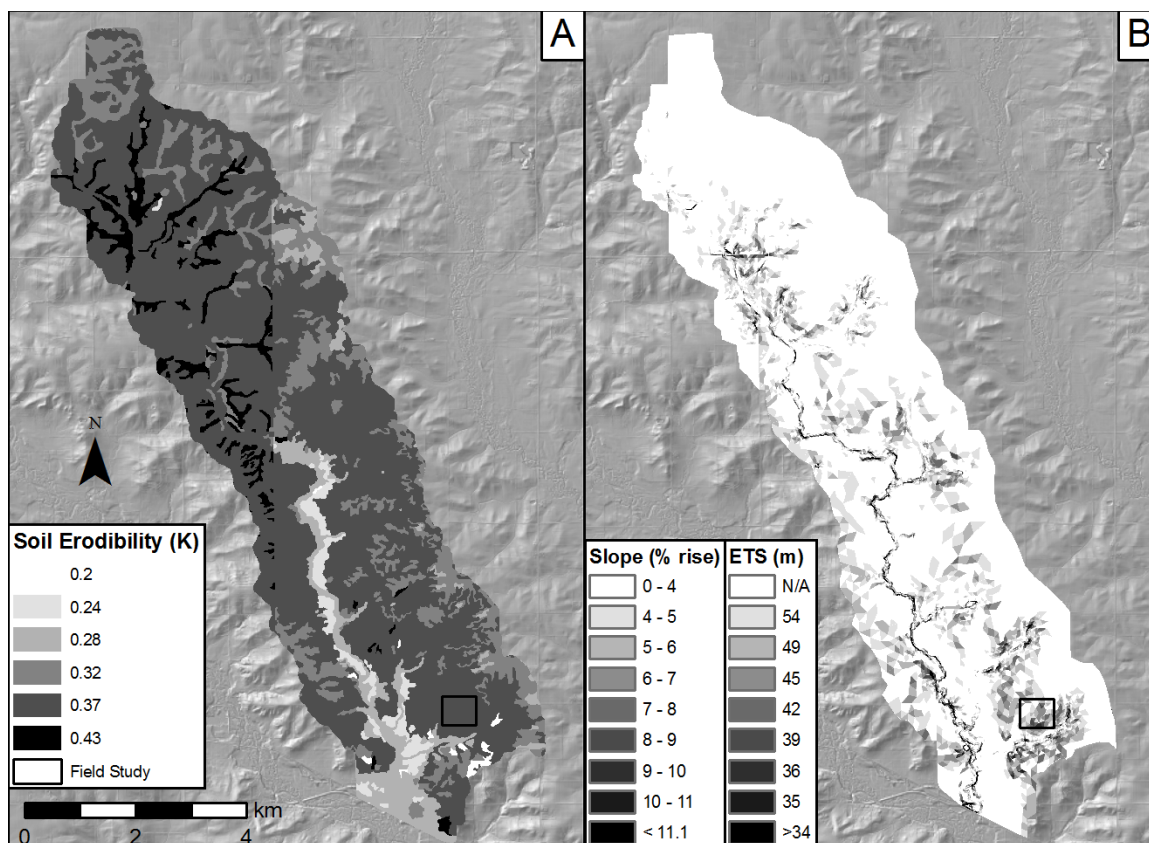
Figure 9.5 a) BCW spatially variable soil erodibility factor (K) for USLE calculation (NRCS 2014) b) Slope of BCW elements, for incorporation of effective roughness and Estimated Terrace Spacing (ETS), provided by USLE erosion calculations.
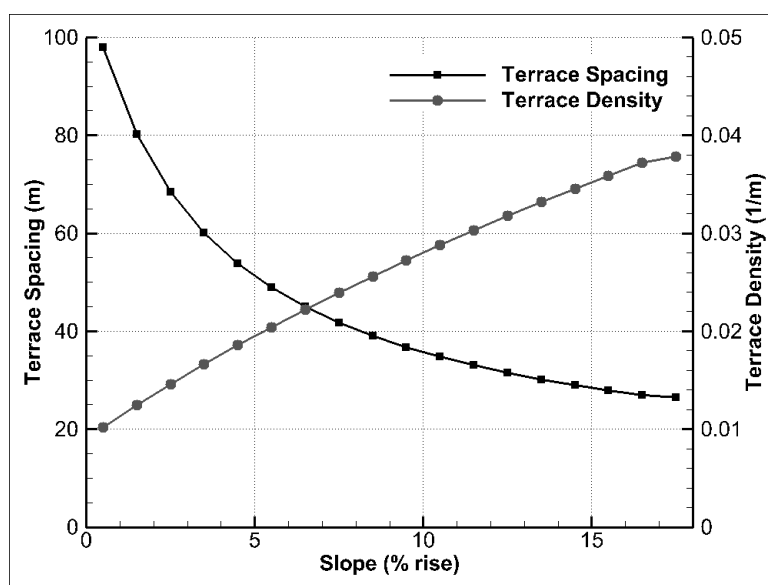
Figure 9.6 Terrace spacing for a given slope, based on USLE calculations.
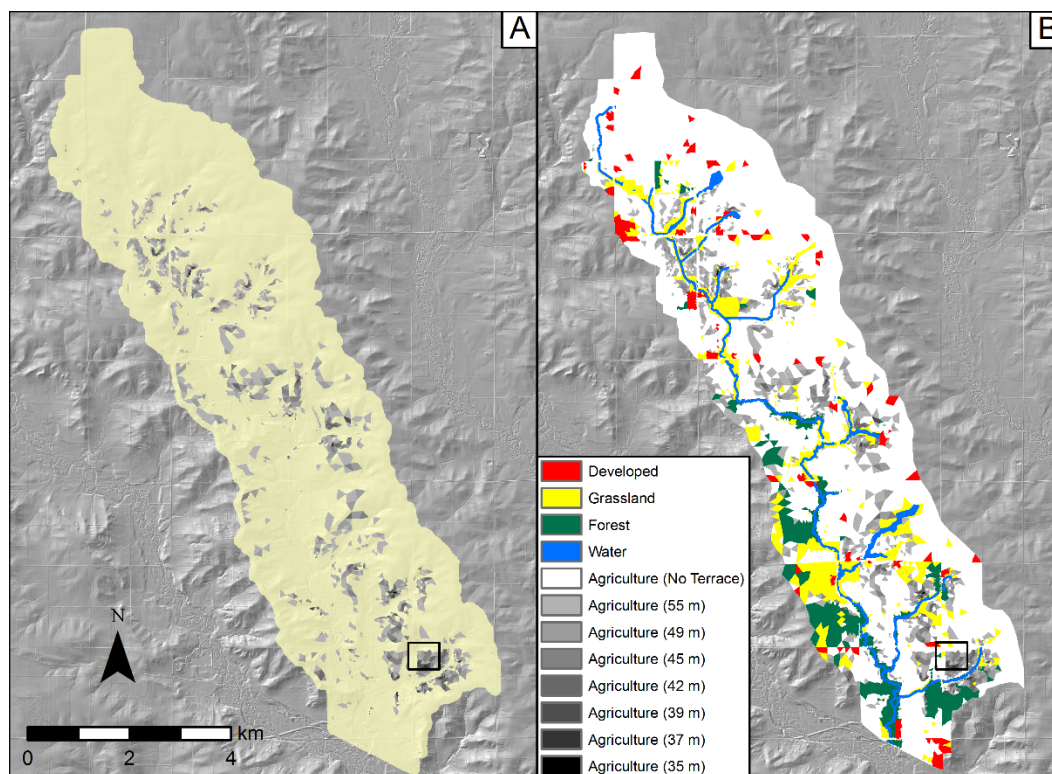
Figure 9.7 a) BCW included terrace locations and expected terrace spacing b) All land use classifications including terraces.

Terraces were only installed in agricultural land uses of 4% slope or greater, and were not installed near potential project locations described in Section 6.0. Land use classifications described in Section 5.3.4, were further separated to incorporate variable terrace implementations. Fig. 9.7a depicts the resulting alterations to include terraces. The total altered land area due to terrace implementation is 5.53 km^2, averaging a density of 0.02 m^{-1} over the whole catchment, totaling 109 km of terraces. USLE and land slopes identified terrace installation at sites where they currently exist (Fig. 9.4 and 9.7), providing evidence of an appropriate distribution. All land use classification are depicted in Fig. 9.7b.

Section 9.1.1 described the process to calculate an effective roughness based on a given terrace density. The resulting relationship between slope and effective roughness from Section 9.1.1 was applied to elements identified in Fig 9.7a based on the slope rate

given in Fig. 9.6. Simulations were run with the initial condition described in Section 5.5 for the year of 2014. Deviations in hydrologic conditions when comparing with and without terraces are described in Section 9.2.2.

9.1.3 Watershed and Nested Subcatchment Water Balance Investigation

BCW wide investigations were completed in parallel with those of nested subcatchments (SC) with a drainage areas (DA) of 2.8 km^2 and 1.9 km^2 (Table 9.2, Fig. 9.8). A high USLE recommended terrace density in the selected SCs of 0.0051 m^{-1} and 0.0055 m^{-1}, made for an ideal comparison to a lower density at the outlet 0.0024 m^{-1}. Peak flow rates and volumetric water balance components were studied at the outlet of BCW and of the densely terraced SCs. The terraced impact on peak flows and the volumetric water balance were expected to be significantly different at the three scales. Events were isolated from the annual simulation, as terraces were expected to impact the events and receding portion of the hydrograph. The relative difference in peak flows Eq. [9.3], and spatially normalized outflow volumes were the key metrics for comparison.

$$\varepsilon = \left[\frac{Q_T - Q_{NT}}{Q_{NT}} \right] 100 \qquad\qquad [9.3]$$

Where ε is the relative difference (%), QT (cms) is the surface flow from the terraced simulation, QNT (cms) is the surface flow from the non-terraced simulation.

Table 9.2 Physical characteristics of the nested SCs.

Location	DA (km^2)	Terrace Density (m^{-1})	slope (%)	Ag - LU (%)
0	44.4	0.0024	2.8	78
1	2.8	0.0051	3.8	80
2	1.9	0.0055	3.6	83
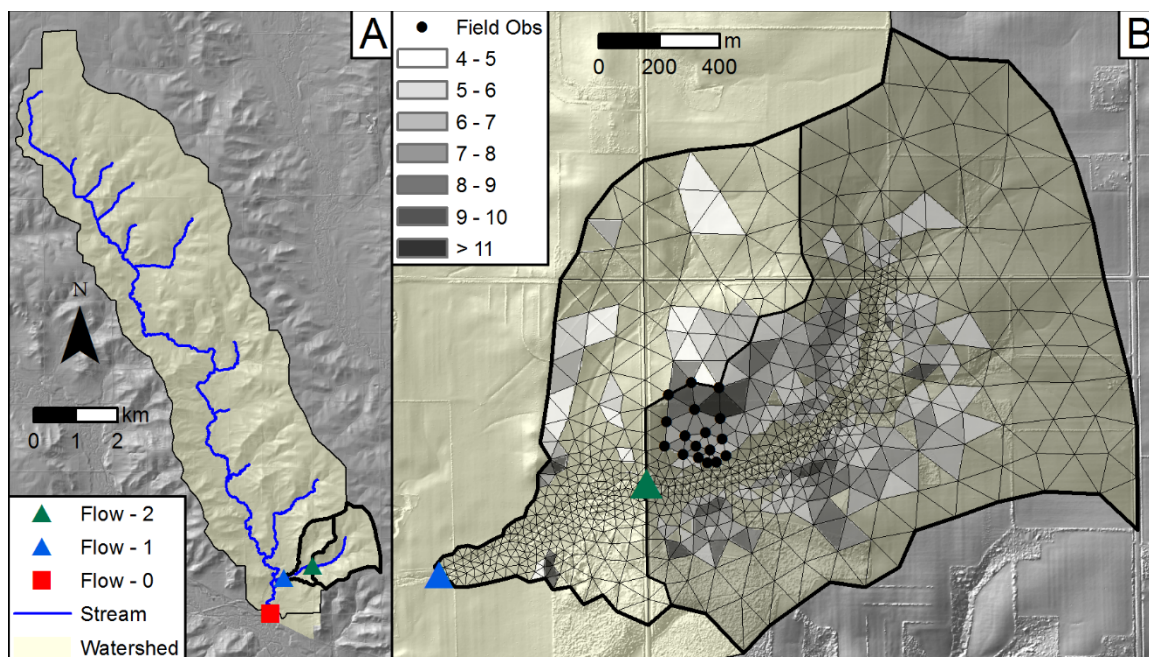
Figure 9.8 Nested watershed scale catchments for terrace investigation, a) BCW SC flow observation points for integrated water balance component and peak flow comparison, b) Selected SC slope distribution including field scale observation point location for infiltration comparison.

9.1.4 Field Scale Exchange Flux Monitoring

Infiltration capacity was investigated at the field scale through monitoring of surface subsurface coupling variables at high spatial and temporal resolutions. The exchange flux between the surface and subsurface was post processed external to model iteration.

A heavily terraced field was isolated to compute exchange fluxes. Within SC2 identified for parallel water balance comparisons. The field consisted of 20 elements, and 17 nodes draining 5.64 ha. Element slope ranged from 4 % to 10 %, resulting in an averaged terrace density over the field of 0.024 m^{-1}. Each of the 17 nodes were numerically monitored to output S, h, and h$_o$. The exchange flux was calculated based on the surface subsurface coupling described in Section 3.2. Exchange fluxes were calculated with Eq. [3.6], repeated here as Eq. [9.4]

$$d\Gamma = \frac{k_r K_{zz}}{l_{exch}} (h - h_o)$$ [9.4]

Where the subsurface water head is h (m), and h_o (m) is the surface water head. The relative permeability for the exchange flux is represented by k_r, K_{zz} (ms^{-1}) is the vertical saturated hydraulic conductivity of the porous medium, and l_{exch} (m) is the coupling length.

For a negative flux or exfiltration from the subsurface into the surface domain k_r is described by the constitutive relationship governing groundwater flow, Eq. [9.5].

$$k_{rw} = S_e^{\frac{1}{2}} \left[1 - \left(1 - S_e^{\frac{1}{\nu}} \right)^\nu \right]^2$$ [9.5]

$$S_e = \frac{S_w - S_{wr}}{1 - S_{wr}} = \frac{1}{[1 + (\alpha\psi)^\beta]^\nu} \qquad \text{for } \psi < 0$$ [9.6]

$$S_e = 1 \qquad\qquad\qquad \text{for } \psi \geq 0$$

Where S_e (-) is the effective saturation, and S_{wr} (m^{3}m^{-3}) is the residual saturation. The relationship between ν and β is $\nu = 1 - 1/\beta$. The parameters α (m^{-1}) and β (-) are empirically derived parameters for the moisture retention and relative permeability functions. α and β are typically obtained through laboratory measurements, soil type identification, or soil database analysis.

For a positive flux or infiltration into the subsurface, k_r is represented by Eq. [9.7]. Where H_s (m) is the total obstruction height defined by the combination of depression storage height, and obstruction storage height. Exchange fluxes were calculated for no terrace, recommended terrace density, and maximum terrace density simulations.

$$k_r = \begin{cases} S_{exch}^{\,2(1-S_{exch})} & \text{when } d_o < H_s \\ 1 & \text{when } d_o > H_s \end{cases}$$ [9.7]

Where $S_{exch} = \frac{d_o}{H_s}$

The objectives of this study were to evaluate the impact of an equivalent gradient terrace representation on surface flow at the field scale. Surface flow delay and reduction in hydrograph peak were incorporated though an effective roughness. The effective frictional roughness was calibrated to instantaneous outflow for varied terrace densities. Effective roughness values were applied to watershed scale simulations through USLE recommendations. Stream flow response and infiltration capacity were investigated at catchment and field scales, respectively.

9.2 Results

The proceeding section describes the simulation results from field scale calibration, and watershed scale application of equivalent terraces.

9.2.1 Numerical Calibration at the Field Scale

Field scale terrace arrangements were calibrated to simulated explicit terrace surface outflow. Each terrace arrangement (29 total) was calibrated with PEST, running in parameter estimation mode. PEST required between 26, and 41 HGS runs to converge on an effective roughness. For each terrace arrangement a precipitation event totaling 50 mm in depth over a 1 hour duration was applied uniformly to field scale simulations. Volumetric outflow rates at 44 instances were extracted for use as calibration targets.

The field scale simulation without terraces (control) responded rapidly to precipitation, reaching a state where inflow equaled outflow in 0.8 hr (Fig. 9.9). Incoming precipitation was routed into hillside gullies, conveying water into the perennial stream. The stream centerline was the domain low point, accumulating the largest water depths (Fig. 9.10a). After the precipitation event, simulated outflow recessed to less than 10% of the peak flow rate of 1.5 cms in 0.7 hr.

The terrace arrangement 12345 was used as a case study. In this arrangement all 5 terraces were explicitly incorporated, equating to a terrace density of 0.24 m^{-1} (Fig. 9.10b). Simulations with terraces responded slowly to rainfall as compared to the control, with outflow never equal to the inflow (Fig. 9.9). Peak flows occurred at the same time in the control and explicit terrace simulations, corresponding to the end of precipitation. Including terraces at an arrangement of 12345 reduced the peak flow rate reduced in magnitude by 5 %. Terraces forced an accumulation of water immediately upstream of the respective embankment, conveying flow laterally, along the contour around the terraces. Surface water from the terraced simulations accumulated behind the hillside terraces to a depth greater than 10 cm (Fig. 9.10b). A larger volume of water was accumulated on the surface in terraced simulations as compared to the control (Fig. 9.10b). Stream flow after the event peak was increased, reducing to less than 10 % of the peak flow in 1.15 hr.

Explicit terraces were removed from field scale simulations and replaced by an equivalent approach. Manning's roughness for the area draining the furthest downstream terrace was calibrated to incorporate a delayed surface flow response. Terrace arrangement 12345 had 5 terraces, the most downstream of which was terrace 1. The effective roughness was calibrated to a value of 0.64 uniformly distributed over the 44,700 m^2 area draining to terrace 1. The calibrated roughness represented a factor of 9 increase from the control (Table 9.3). The equivalent terrace approach mimicked the explicit scenario well. The hydrograph peak was reduced by 5 %, the rising limb was slowed, and the receding limb of the hydrograph was increased. The largest deviation from the explicit model occurred after the rainfall peak, during hydrograph recession as an overestimation. A larger quantity of precipitation was stored on the surface as compared to the control case. The surface storage was well distributed across the field, differing from the high depths along the contours in the explicit model. A notable

reduction in depth was displayed just below the last terrace location, where the effective

roughness decreased back to the original parameter values (Fig. 9.10c).
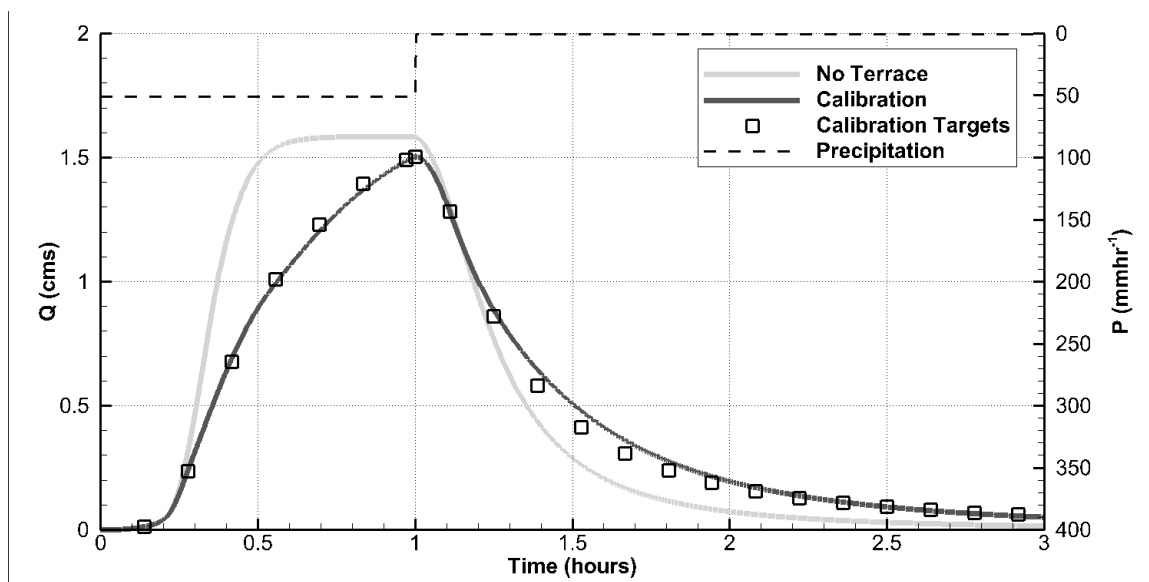
Figure 9.9 PEST calibration results for terrace arrangement 12345 (Table 9.2). Calibration targets (44) were extracted from explicit terrace simulations of the same terrace arrangement.
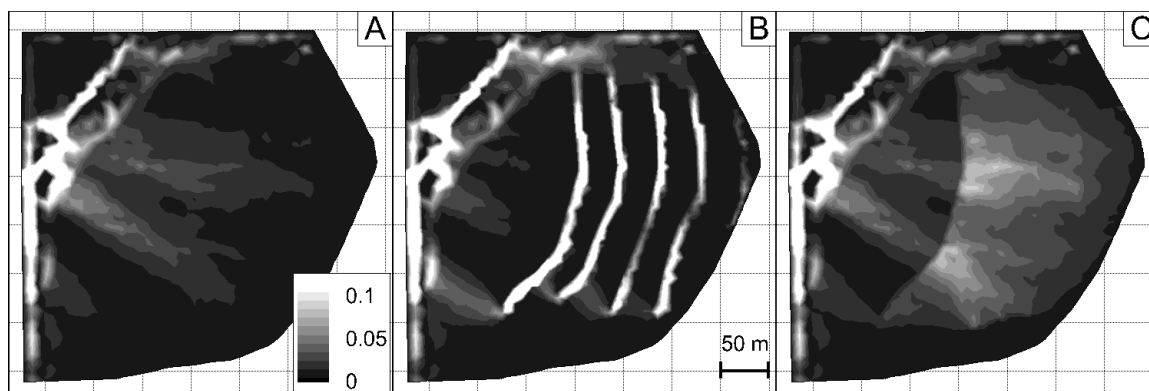
Figure 9.10 Surface water accumulation (m) at t = 1 hr for, a) No terrace simulation, b) Explicit terrace incorporation for terrace arrangement 12345, c) Equivalent terrace incorporation for a terrace density of 0.024 m^{-1}, or an effective roughness of 0.64 (Table 9.2).

Table 9.3 Field scale terrace calibration results. Terrace arrangements indicated which terraces were incorporated into each model simulation (Fig. 9.2). Terrace density reflects the length of terraces over the upstream drainage area, and the calibrated roughness value is n_{eff}.

Terrace Arrangement	Terrace Density (m^{-1})	n_{eff} ($sm^{-1/3}$)
1	0.006	0.29
12	0.011	0.45
13	0.011	0.39
14	0.011	0.41
15	0.008	0.30
123	0.016	0.56
124	0.016	0.57
125	0.016	0.47
134	0.016	0.51
135	0.014	0.40
145	0.014	0.44
1234	0.022	0.62
1235	0.019	0.57
1245	0.019	0.59
1345	0.019	0.53
12345	0.024	0.64
2	0.007	0.25
23	0.014	0.41
24	0.014	0.43
25	0.011	0.27
234	0.022	0.57
235	0.018	0.43
245	0.018	0.46
2345	0.025	0.61
3	0.011	0.36
34	0.021	0.63
35	0.016	0.35
345	0.027	0.69
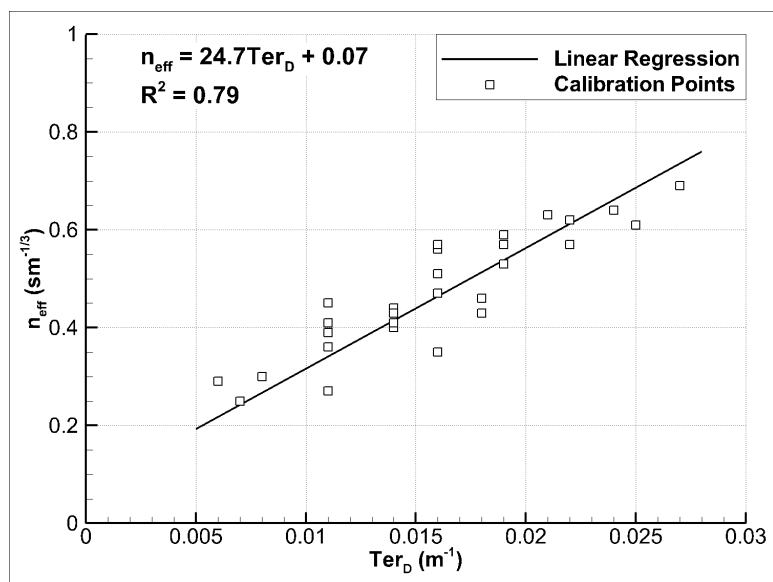
Figure 9.11 Field scale calibrated equivalent roughness (n_{eff}) as explained by terrace density (Ter_D).
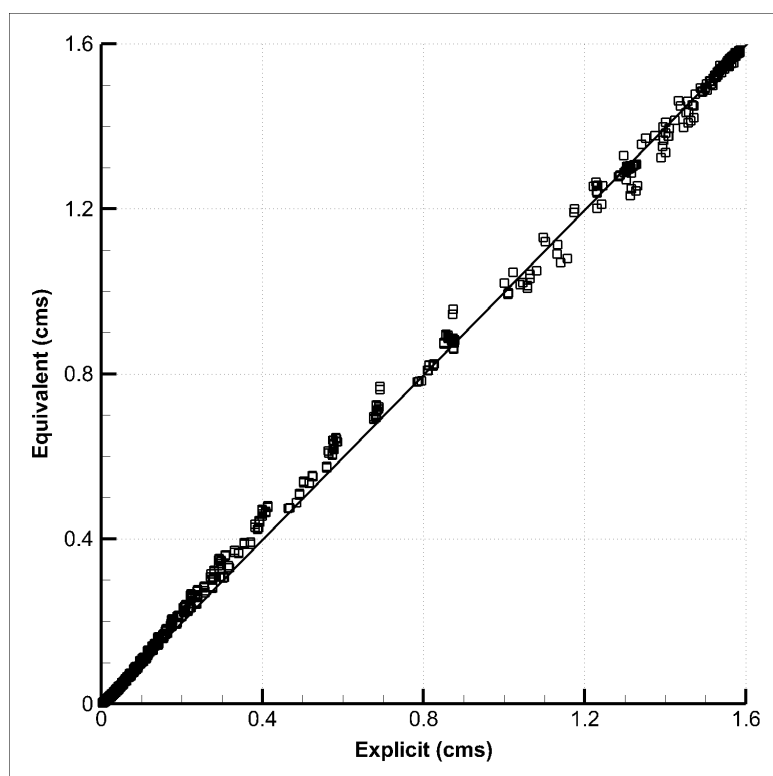
Figure 9.12 Comparison of calibration targets to equivalent results for 44 target calibration points and each of the 29 terrace arrangements.

Ordinary least squares (OLS) regression of terrace density to effective roughness produced a high correlation ($R^2 = 0.79$). The intercept was fixed at 0.07, equal to the control roughness. Effective roughness values were interpolated from the linear trend for watershed scale simulations. Results for each of the 29 calibration runs were presented in Table 9.3 and Fig. 9.11. Optimized roughness values represented a factor of 3 to 10 increase from the control value.

Calibrated simulation results fit the calibration targets well (Fig. 9.12). The largest deviations occurred as overestimates of midrange flows of 0.2 cms to 0.8 cms. The equivalent approach tended to have a higher falling hydrograph limb as compared the explicit incorporation of terraces.

9.2.2 Watershed Scale

Field scale calibration results were applied to watershed scale annual model simulations. Element slopes across the watershed from Section 9.1.2 were binned into whole number values from 4 % to 12 % slope (Table 9.4). A relationship based on USLE analysis performed in Section 9.1.2 (Fig. 9.6) related land slope to terrace spacing. The mean terrace spacing of each 1 % slope bin was converted into an effective Manning's roughness value, through OLS regression (Fig. 9.11). The results of this conversion are displayed in Table 9.3. Effective roughness was allocated to elements based on slope and land use (Fig. 9.7).

A second terrace implementation was simulated, as an upper bound for reasonable application. Each element selected in Section 9.1.2 for standard USLE based terrace application was uniformly assigned an effective roughness value equal to the maximum recommended spacing of 27 m (Table 9.5). This simulation highlights the highest plausible terrace density, and expected hydrologic impact. Simulations were run with no terraces (NT), USLE recommended terrace spacing (T), and a maximum terrace density (MT).

Table 9.4 Effective roughness (n_{eff}) aggregated for application at the watershed scale based on USLE spacing recommendations (T).

slope (%)	Terrace Spacing (m)	Terrace Density (m^{-1})	n_{eff} ($sm^{-1/3}$)
4 -5	54.6	0.019	0.53
5 -6	49.0	0.020	0.57
6 -7	45.0	0.022	0.62
7 -8	41.8	0.024	0.66
8 -9	39.1	0.026	0.70
9 -10	36.7	0.027	0.74
10 -11	34.7	0.029	0.78
11 -12	33.0	0.030	0.82

Table 9.5 Effective roughness values indicative of the maximum terrace spacing (MT).

slope (%)	Terrace Spacing (m)	Terrace Density (m^{-1})	n_{eff} ($sm^{-1/3}$)
4 -18	26.9	0.037	0.98

9.2.2.1 Annual Terrace Impacts at the Watershed Scale

Watershed response was accumulated over an annual time period. Each observation was integrated over the catchment area. A NT stream flow at the outlet (Q_0) of 252 mm, represented 32 % of the total precipitation (P) 774 mm, with evapotranspiration (ET) representing the other 67 % of P. Infiltration (I) of 687 mm was 89 % of the total P volume. A comparison of the NT to the T and MT simulations indicated no difference between terraced and non-terraced simulations for an annual watershed integration. Differences in ET, I, and Q_0 were small enough to consider insignificant (Table 9.6).

Table 9.6 Annual integration of volumetric water balance components for each NT, T, and MT simulations.

Name	P (mm)	ET (mm)	I (mm)	Q_0 (mm)
NT	774	522	687	251
T	774	522	686	250
MT	774	521	686	250

9.2.2.2 Event Terrace Impacts at the Watershed Scale

Events (E) were defined in the same manner described in Section 8.2.2.3. The start of an event was defined as any P accumulation in excess or equal to 10 mm over a 3 hour duration. This accumulation of P was chosen such that a response was evident in stream flow at the outlet. The uniformly distributed P applied to the watershed ensured that a response at the outlet would guarantee the same at smaller scales. The end of an event was identified with a lag time of 5 days after that last accumulation of 10 mm of P in 3 hours.

All volumetric measures were integrated over the catchment area, and then over the duration of each event. P, ET, I, and volumetric runoff coefficient (C = Q/P) values were reported for the NT simulation only. Additional investigation indicated no deviations in each of the components for the T and MT cases. E's averaged a length of 8.1 d, and P of 47 mm of which 87 % was infiltrated into the subsurface domain. I ranged from a high of 172 mm to a low of 10 mm and (I/P) of 0.71 to 1.01.

Higher I volumes occurred in response to high P, where the ratio of I/P was higher for low P volume events. Where all of the P was able to be absorbed into the subsurface. High I/P ratios correlated with low C values (Fig. 9.14). As P volumes increased, the infiltration capacity of the watershed was exceeded, subsequently producing larger Q and C values. The maximum C value (0.68) occurred in concert with the lowest I/P (0.71).

T and MT simulations on average did not produce a measurably different Q_0 (Table 9.7). Over each of the E periods, ε ranged from 0.1 % to -0.2 %. Peak flows (Q_P) for NT simulations reached a high at E3 of 18.3 cms, a product of the smallest I/P and largest C. Low volumetric changes were in line with low peak discharge changes for T and MT simulations. An average ε increase of 0.2 % in each the T and MT simulations varied from -0.7% to 1.1 %. Variability in Q_p were similar in NT, T, and MT simulations (Table 9.8).

Table 9.7 Event integration of volumetric water balance components for each the NT, T, and MT simulations at the outlet. Integration measures are displayed for only NT simulations as no notable difference were measured in T and MT simulations.

Name	DOY	L (d)	P_{NT}	ET_{NT}	I_{NT} (I/P)	Q_{NT}	C_{NT}	ε_T / ε_{MT} (%)
E1	66	8	37	1	34 (0.92)	8.3	0.22	0 / 0
E2	110	15	94	6	80 (0.86)	31.2	0.33	0 / 0
E3	128	12	65	7	46 (0.71)	44.0	0.68	0 / 0
E4	152	5	11	17	11 (0.98)	3.2	0.29	0 / 0.1
E5	167	19	208	88	172 (0.83)	57.1	0.28	0 / -0.1
E6	192	6	14	24	13 (0.94)	4.6	0.32	-0.1 / -0.1
E7	205	5	11	24	11 (1.01)	1.0	0.09	-0.1 / -0.2
E8	215	6	21	26	21 (0.97)	1.2	0.06	-0.2 / -0.2
E9	240	9	79	30	76 (0.94)	5.5	0.07	0.1 / -0.1
E10	262	5	16	1	16 (0.99)	1.1	0.07	0 / -0.1
E11	275	5	14	1	14 (0.98)	1.7	0.12	0 / 0
E12	285	6	54	1	49 (0.9)	8.9	0.16	0.1 / 0
E13	295	5	11	1	10 (0.99)	3.0	0.28	0.1 / 0
E14	356	7	23	0	21 (0.93)	5.9	0.26	0 / 0
Mean		8.1	47.0	16.4	41 (0.87)	12.6	0.27	0 / 0
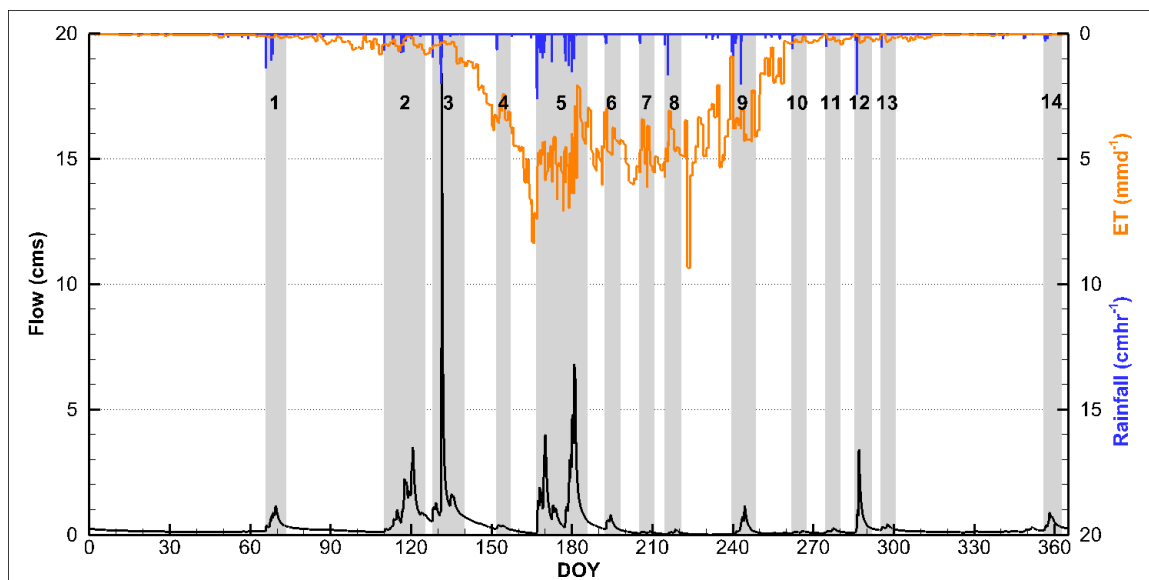
Figure 9.13 Event water balance components for the year of 2014. Grey areas denote individual events labeled (1-14). Components represented - Q (red), P (blue), and ET (orange).
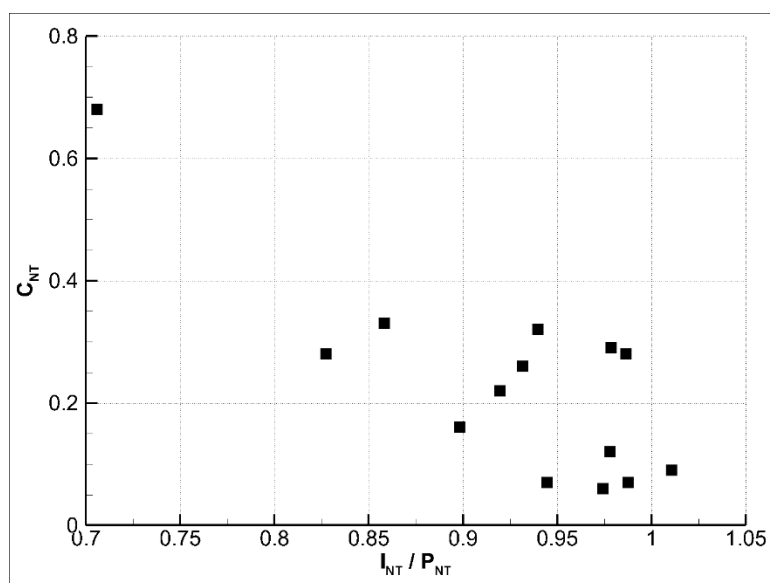
Figure 9.14 Event integrated volumetric infiltration ratio (I/P) as compared to C for NT simulations.

Table 9.8 Q_p at the outlet for each the NT, T, and MT simulations. NT peak flow rates are displayed with relative difference of T and MT scenarios from the NT case.

Name	DOY	Q_{NT} (cms)	$\varepsilon_T / \varepsilon_{MT}$ (%)
E1	66	1.2	0.1 / 0.1
E2	110	3.5	-0.1 / 0.1
E3	128	18.3	0.3 / 0.3
E4	152	0.4	0.1 / 0.2
E5	167	6.8	0.4 / 0.4
E6	192	0.8	0 / 0.3
E7	205	0.1	0 / 0
E8	215	0.2	-0.2 / -0.1
E9	240	1.2	0 / -0.2
E10	262	0.2	-0.7 / 0
E11	275	0.3	-0.7 / -1.1
E12	285	3.5	0.1 / 0
E13	295	0.4	0 / -0.1
E14	356	0.9	0.1 / 0
Mean		2.69	0.2 / 0.2

9.2.3 Nested Subcatchments

In NT, T, and MT simulations outflow was monitored at the BCW outlet, and two densely terraced nested subcatchments (SC1 and SC2) (Table 9.2, Fig. 9.8b). The influence of DA, and terrace density were investigated with respect to Q_p. Model runs were investigated at the annual and event time scale.

The annual catchment averaged flow from SC2 (Q_2) of 215 mm, was less than Q_1 of 219 mm, which was less than Q_0 of 251 mm. Each successively larger catchment produced a higher Q and C. Terraces at the recommended spacing and at the maximum spacing had no impact on total Q at either SC DA (Table 9.9).

Table 9.9 Annual integration of Q in SC1 (Q_1) and SC2 (Q_2) for NT, T and MT simulations.

Name	Q_1 (mm)	Q_2 (mm)
NT	219	215
T	219	215
MT	219	215

Precipitation driven event time periods were separated from the annual time series. At smaller DAs Q responds more rapidly to rainfall. Events as defined for the watershed scale investigation often had multiple independent SC peak flow events. SC events were defined independently of watershed scale events. The start of a SC event (SE) was defined as any P accumulation in excess or equal to 5 mm over a 3 hour duration. This accumulation of P was chosen such that a response was evident in stream flow at the outlet in of each SC. The end of an event was identified with a lag time of 1 day after that last accumulation of 5 mm of P in 3 hours. This methodology produced 23 SC specific events (SE1-23) (Fig. 9.15).

SEs responded at a much faster rate to rainfall as compared to the watershed outlet. Perennial flow occurred at the BCW scale. For a 23 d period beginning DOY 218 there was no surface outflow from SC1 or SC2 (Fig. 9.15). The Q_p's occurred for SE8 of 1.57 cms and 1.06 cms for SC1 and SC2, respectively. This SE had the 4th highest P and 2nd highest Q (Table 9.10 and Table 9.11). The highest Q_p was the product of the highest P intensity. The largest C occurred in SE6 of 0.64 and 0.56 for SC1 and SC2, respectively. The high C values were a product of the highest initial saturation of 0.82. As DA increased the average event and annual C value increased.

Although not depicted in tabular format the flow volumes at the SC scales were unchanged by the inclusion of terraces. Cumulative flow patterns were altered by including terraces, such that the Q_p was reduced, and delayed. The rising and falling limbs of the hydrograph were delayed. Cumulative flow patterns (Fig. 9.16, Fig. 9.17)

showed a reduction in flow by the terraces prior to and during the peak of the event. Any reduction in cumulative flow was regained by an extended falling limb in NT, T, and MT simulations. Changes in cumulative Q were only evident during the two days surrounding an event. MT simulation displayed larger deviations from NT than T simulations in peak and cumulative flow patterns.

SC1 responded to rainfall events with multiple hydrograph peaks, not stemming from temporal variability in rainfall. The two peaks occurred from the two upstream branches. The southern 1.9 km^2 representing SC2, and the northern 0.9 km^2 representing another independent SC. The northern SC had a steeper slope, thus a faster response to P. Each of the branches to SC1 displayed reductions in Q_p, with the north catchment having a lower density of terraces, a smaller reduction was expected. Reduction in Q_p due to terraces occurred in both north and south branches to SC1. Higher terrace density in SC2 produced lower secondary hydrograph peaks at SC1 as compared to the northern branch. SC2 has a single peaked response directly relating directly to variability in rainfall intensity.

The average ε were 10% and 15 % for SC1 and SC2, respectively. ε varied from an increase of 2%, to a reduction of 28%. Each extreme related to a low initial saturation, low P, and subsequent low Q response. Only small ε occurred in very dry periods (SE17-SE21), producing low Q_p. MT simulations always produced higher or equal ε when compared to T simulations. SC2 always had higher ε as compared to SC1.

A relationship between ε, and initial saturation became apparent (Fig. 9.18). The trend lines were included for visualization purposes only. The relationship shifted vertically in response to SC DA, and in slope to terrace density (T vs. MT). An increase in initial saturation reduced the ε. This was true for each SC and terrace density. An increase in DA shifted this trend upward towards a lower ε, while maintaining approximately the same relationship with initial saturation. At each independent DA the

increased terrace density had a larger impact at lower initial saturations, converging as the initial saturation increased.

Additional tests demonstrated that the flow volume at each SC location was negligible for each SE. In the duration of each SE, averaging 1.5 days, the addition of terraces delayed the hydrograph response. Obvious Q_P impacts were achieved in these simulations, but volumetric alterations were only short term.
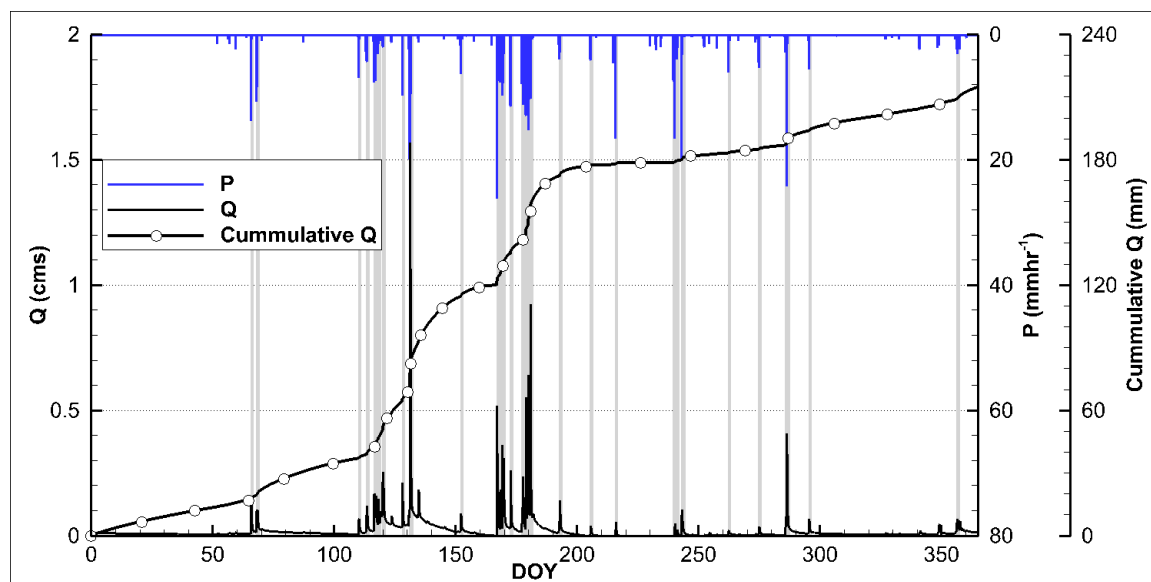
Figure 9.15 Event water balance components for the nested subcatchments SC1 and SC2, for the year of 2014. Grey areas denote individual SC events labeled (1-23).
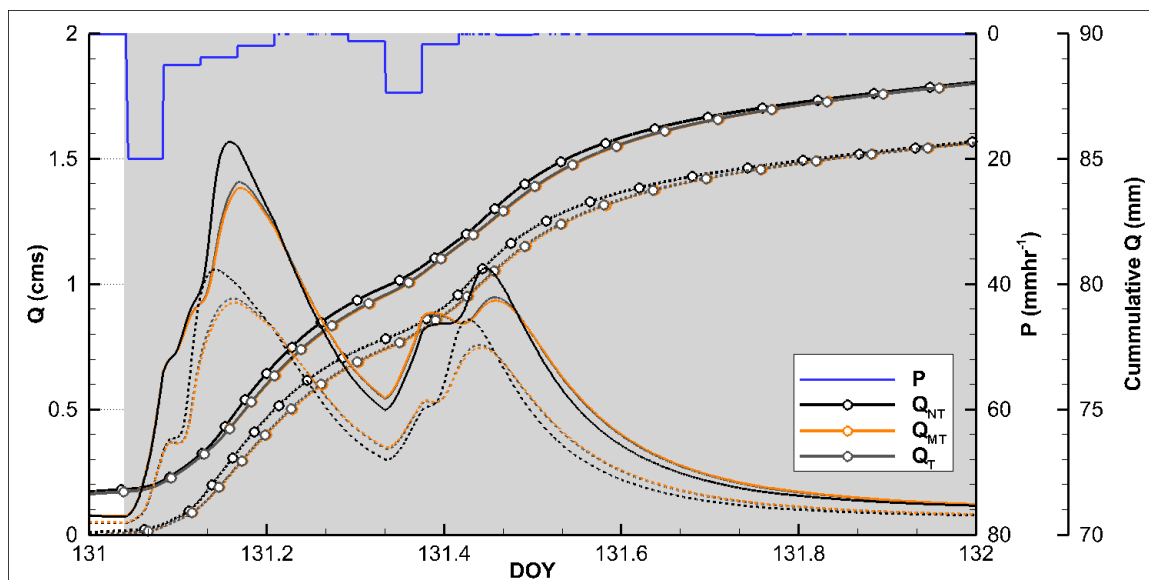
Figure 9.16 SE8 event flow rates and cumulative outflow (lines with circles), for SC1 (broken lines) and SC2 (solid lines).
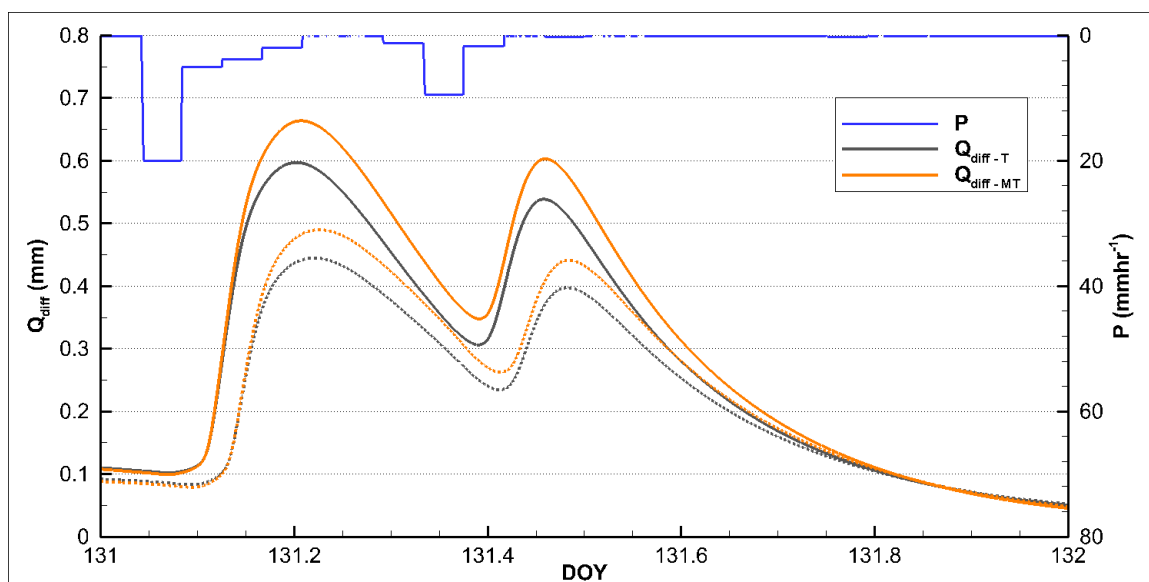
Figure 9.17 SE8 event cumulative flow difference of T and MT scenarios from the NT model simulations, for SC1 (broken lines) and SC2 (solid lines).

Table 9.10 SE integration of volumetric water balance components for each the NT, T, and MT simulations. Where Sat_s represents the initial saturation.

Name	DOY	L (d)	P (mm)	Sat_S (%)	Q_{NT-1} / Q_{NT-2} (mm)	C_{NT-1} / C_{NT-2}
SE1	66	1.0	14	73	1.6 / 1.3	0.11 / 0.09
SE2	68	1.5	19	69	2.6 / 2.2	0.14 / 0.12
SE3	110	1.0	8	72	1.1 / 0.9	0.13 / 0.11
SE4	113	1.0	10	75	2 / 1.6	0.2 / 0.17
SE5	116	2.8	40	73	7.9 / 6.7	0.2 / 0.17
SE6	120	1.0	7	82	4.6 / 4	0.64 / 0.56
SE7	128	1.0	9	73	2.8 / 2.5	0.3 / 0.27
SE8	131	1.3	44	75	17.4 / 16.7	0.4 / 0.38
SE9	152	1.0	8	70	1.4 / 1.3	0.17 / 0.17
SE10	167	3.8	112	56	15.2 / 13.1	0.14 / 0.12
SE11	173	1.1	13	70	3 / 2.7	0.23 / 0.21
SE12	177	1.4	19	72	3.7 / 3.3	0.19 / 0.17
SE13	179	3.0	61	70	18.8 / 17	0.31 / 0.28
SE14	193	1.2	10	71	2.1 / 1.8	0.21 / 0.18
SE15	205	1.0	5	63	0.5 / 0.6	0.09 / 0.11
SE16	216	1.0	17	52	0.5 / 0.7	0.03 / 0.04
SE17	240	2.4	43	48	0.8 / 1	0.02 / 0.02
SE18	243	1.4	32	67	1.6 / 1.5	0.05 / 0.05
SE19	262	1.1	14	60	0.4 / 0.4	0.03 / 0.03
SE20	275	1.1	11	69	0.6 / 0.6	0.05 / 0.05
SE21	286	1.8	50	71	4.6 / 3.6	0.09 / 0.07
SE22	295	1.1	7	72	1.1 / 0.9	0.16 / 0.14
SE23	356	1.4	16	75	1.8 / 1.6	0.12 / 0.1
Mean		1.5	25	69	4.2 / 3.7	0.17 / 0.15

Table 9.11 Peak flow rate at the outlet of SC1 and SC2 and relative difference (ε) of the T and MT cases as compared to the NT simulations.

Name	DOY	Q_{NT-1} / Q_{NT-2} (cms)	ε_{T-1} / ε_{T-2} (%)	ε_{MT-1} / ε_{MT-2} (%)
SE1	66	0.14 / 0.1	-1 / -14	-1 / -16
SE2	68	0.1 / 0.07	1 / -14	2 / -15
SE3	110	0.07 / 0.05	-5 / -13	-4 / -14
SE4	113	0.12 / 0.07	-2 / -10	-2 / -11
SE5	116	0.17 / 0.11	-3 / -8	-3 / -8
SE6	120	0.25 / 0.15	-5 / -6	-5 / -6
SE7	128	0.21 / 0.14	-13 / -18	-14 / -20
SE8	131	1.57 / 1.06	-10 / -11	-12 / -12
SE9	152	0.09 / 0.06	-10 / -12	-11 / -14
SE10	167	0.52 / 0.41	-15 / -20	-16 / -22
SE11	173	0.26 / 0.17	-12 / -18	-13 / -20
SE12	177	0.24 / 0.16	-11 / -17	-12 / -18
SE13	179	0.92 / 0.7	-14 / -16	-16 / -19
SE14	193	0.14 / 0.09	-8 / -12	-8 / -14
SE15	205	0.04 / 0.04	-14 / -16	-15 / -18
SE16	216	0.05 / 0.06	-22 / -25	-24 / -28
SE17	240	0.05 / 0.05	1 / 0	1 / 0
SE18	243	0.1 / 0.09	0 / -2	-1 / -1
SE19	262	0.02 / 0.02	0 / 0	0 / 0
SE20	275	0.03 / 0.03	0 / 0	0 / 0
SE21	286	0.41 / 0.23	0 / -13	0 / -14
SE22	295	0.07 / 0.05	-2 / -11	-2 / -13
SE23	356	0.07 / 0.04	0 / -7	0 / -8
Mean		0.24 / 0.17	-9 / -13	-10 / -15
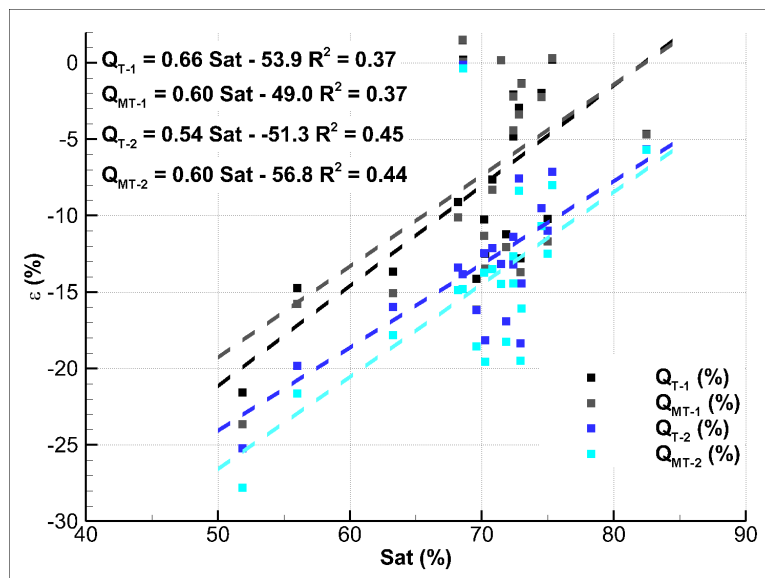
Figure 9.18 ε in the T and MT simulations as compared the NT case for SC1 and SC2 as described by the surface initial saturation at the field scale location (Fig. 9.8). SE19 and SE20 were removed from plot. Each P total met the SE criteria, but the flow at SC1 and SC2 was not significantly different from low flow levels.

9.2.4 Field Scale Infiltration

Infiltration variability imposed by terraces at the field scale was investigated within watershed wide simulations. 17 observation points were placed at a densely terraced location, reporting h, h_o, and S values for the first subsurface nodes (Fig. 9.8). The exchange flux was calculated based on simulation values at each of the 17 points by the methodology posed in Section 9.1.4.

In watershed wide integration of infiltration, NT, T, and MT simulations were approximately the same for annual and event time scales. P depicted in Fig. 9.19 had the canopy evaporation removed, displaying only the P landing on the surface, capable of infiltrating. I for each of the NT, T and MT simulations was 732 mm and P totaled 741 mm. At the field scale 99 % of the precipitation was infiltrated. This was consistent across all terrace densities. The impact of terrace density was investigated at each of the 17 observation locations over each of the SEs described in 9.2.2 (not shown here). Small deviations in exchange flux occurred between observation nodes, and terrace densities.

The small deviations were a product of variable time steps among the simulations, and temporal interpolation. Any impact the terraces had on the infiltration capacity was immeasurable in this analysis.
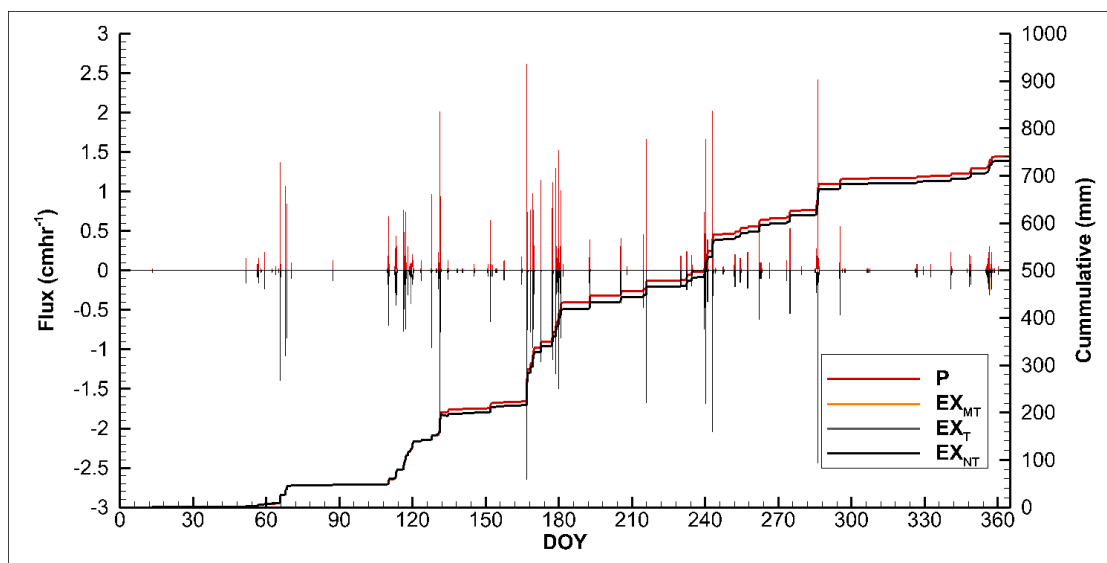
Figure 9.19 Annual P and calculated exchange flux averaged for each of the 17 observation points for each NT, T and MT simulations. Cumulative P and exchange flux were represented by thick lines.
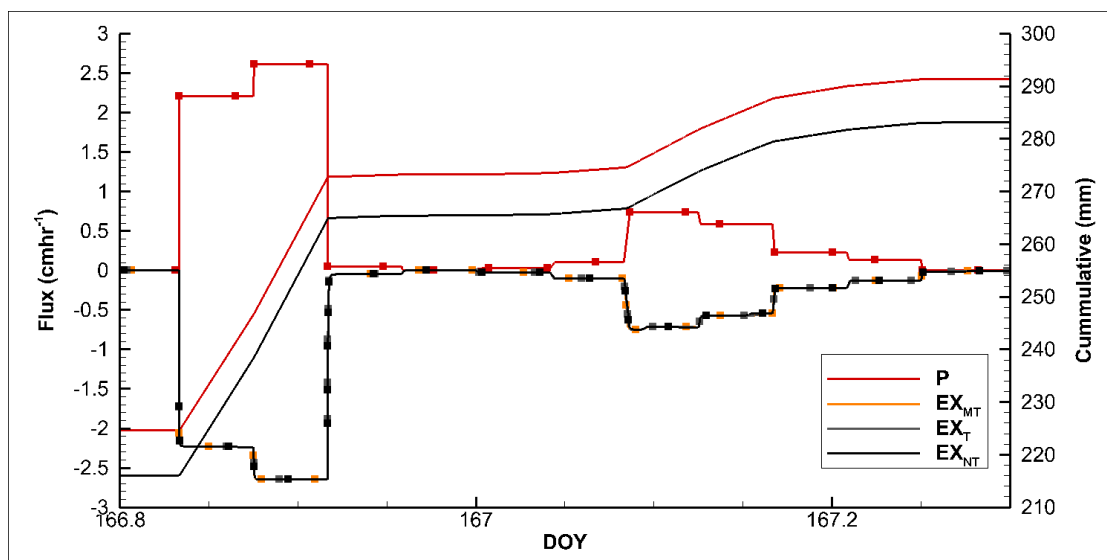
Figure 9.20 A single event (DOY 166.8) precipitation and calculated exchange flux averaged for each of the 17 observation points for each NT, T and MT simulations. Fluxes are lines with circles.

9.3 Discussion

In summary, the incorporation of two terrace densities at the catchment scale had no observable impact on catchment wide flow volumes, peaks, or other water balance components. Within the nested SCs, Q_p was reduced and delayed, followed by an increase in the receding limb of the hydrograph. At the SC outlets, annual integration of Q was not altered by terraces. ε by including terraces, decreased with increasing saturation. At the field scale, terraces had no measureable effect on the exchange of water between the surface and subsurface.

Terraces are commonly applied agricultural practices, built to reduce unimpeded flow path lengths prone to erosion. Currently, there are no standard procedures to incorporate these structures into a modeling environment to test their efficacy under varying climate and conservation scenarios (Arabi et al. 2008; Bracmort et al. 2006). Gradient terraces were chosen for investigation as the HGS numerical platform was not able to simulate the required features to represent storage terraces. Storage type terraces are more common to reduce erosion in Iowa. Storage terraces act as small reservoirs, impounding water behind an earthen embankment, and released it through a surface intake into a nearby waterway. A surface inlet into a subsurface tile drainage pipe, acts as the primary control structure. Explicit tile drainage components can only be incorporated into the subsurface domain, and currently have limited surface interaction capabilities in HGS. 1-D elements can only interact with one domain, and are currently not able to be coupled between the surface and subsurface domains, severely limiting the ability to simulate these structures. As a result the equivalent terrace implementation approach was calibrated and applied to gradient style terraces. These terraces are built to route water laterally along the hillslope contour to a stable outlet. Without the capability to simulated coupled 1-D elements, gradient terraces were investigated.

This study was a first attempt to incorporate terraces into a coupled hydrologic model in an equivalent approach. In the absence of standard practice for incorporating

this common engineering conservation practice into hydrologic models, a twostep approach was applied (Arabi et al. 2008). An effective surface roughness was calibrated to represent subsurface flow from a variety of terrace arrangements. The effective roughness was applied at the watershed scale delaying surface water, increasing depth, and altering infiltration characteristics.

9.3.1 Analyzing the Conceptual Field Scale Approach

Few studies have applied a physics based coupled model to water conservation practices (Opolot et al. 2014; Verbist et al. 2012), and none at the watershed scale. Opolot et al. (2014) and Verbist et al. (2012) pioneered work in simulating rainwater harvesting trenches to reduce runoff and force infiltration during peak rainfall events. These practices accumulated surface flow in trenches set below the land surface improving infiltration capacity of the hillslope. The conceptual impact of these measures are different from gradient terraces. Gradient terraces increase the travel time to the outlet by rerouting water over the surface. Infiltration trenches impound water up to a given capacity, while the remaining water is routed to the outlet without effect.

In this study, gradient terraces were incorporated through an increased Manning's roughness over the area upstream of explicit terrace implementation. Field scale calibrations reproduced a very good fit to surface flow calibration targets. Although not tested, gradient terraces were expected to increase infiltration, as water was retained on the surface longer. Similarly, the effective roughness approach was also expected to increase infiltration. Surface water velocity decreased with increased roughness, increasing the flow depth, and the duration of flow on a terraced element. Gradient terraces don't impound rainfall, they increase the surface travel time. Terraces were incorporated in an effective manner to mimic the increased flow path length water would encounter under an explicit terraced scenario.

In Frei and Fleckenstein (2014), the depression storage parameter was superimposed onto a planar grid, accounting for micro-topographic relief. Depression storage retains water without surface conductance until the attributed depth threshold is met. Spatially variable subsurface and surface flow patterns were a product of variable application of depression storage heights. Depression storage height is included in the calculation of the exchange flux, directly impacting infiltration. Depression storage impedes flow, which is conceptually different from the effect of gradient terraces. Alternatively, depression storage could represent infiltration trenches well for an equivalent approach at the watershed scale (Opolot et al. 2014; Verbist et al. 2012).

29 explicit terrace arrangements were simulated at the field scale to calibrate a distributed effective roughness at various terrace densities. Calibrated effective roughness values were distributed across the watershed scale model based on land use and element slope. Investigation of infiltration was approached by a detailed field scale analysis of each node allocated to a densely terraced hillslope. Nodal exchange fluxes were post-processed, calculating the infiltration capacity and related variables. Simulations utilized an adaptive time stepping scheme, varying time steps based on internal flow variables and numerical convergence criteria. The time steps in each NT, T, and MT, simulations were not the same. Exchange flux calculations were interpolated onto a 5 second uniform grid allowing for direct comparison between results. This level of temporal resolution was enough to capture the flux variability at the initiation of wetting.

Reviewing Eq. [9.4], infiltration is dependent on two variables, h and h_o, where $k_r = f(h_o)$. For surface flow to occur the water depth (d_o) must be greater than the depression storage (H_s) of 0.0002 m. Upon initiation of surface flow, the effective frictional roughness decreases flow conductance. When $d_o > H_s$ $k_r = 1$, and no longer limits surface subsurface exchange. Most frequently surface flow did not occur, $d_o < H_s$, and the exchange flux was dependent upon h_o and h. When $d_o < H_s$, h_o and h are the same for each of the terrace scenarios (NT, T, and MT). As discussed in Section 9.2.1 at the field

scale, Q_p occurred at the end of a precipitation event for terraced and non-terraced simulations. Overland flow and surface depths rapidly decayed. Without significant increases in water depth and delay of flow over dry time periods, infiltration capacity remained unaffected.

To further this study, a coupled surface subsurface PEST calibration must be performed. The effective parameters would be required to alter the surface conductance and infiltration capacity over a distributed area. Suitable parameters to increase infiltration include the vertical hydraulic conductivity, and the coupling length. Calibration runs must be tested over multiple initial soil wetness values to ensure proper parameter identification under variable conditions.

9.3.2 Impact at the Watershed Scale

Terraced simulations did not alter flow volumes or peak flows at the watershed outlet, over annual or event time periods. At the SC scale peak flows were reduced in an expected manner, as terrace density increased, ε was increased. Similarly as, the DA increased, and the terrace density decrease, the ε decreased. Indications of this nature give prudence to the approach taken to investigate gradient terraces. A combination of subsurface flow dominated large drainage areas and low terrace densities, attenuated the terrace effects at increasing DAs.

Other studies have numerically investigated terraced systems at the watershed scale with process based models such as SWAT (Arabi et al. 2008; Bracmort et al. 2006; Secchi et al. 2007; Strauch et al. 2013; Tuppad et al. 2010; Tuppad et al. 2009; Vache et al. 2002; Yang et al. 2009; Zhou et al. 2009). These studies typically focus on the water quality component, noting that terraces reduce sediment loads by 28% to 88% (Secchi et al. 2007; Strauch et al. 2013; Tuppad et al. 2010). To impact rainfall partitioning terraces have been incorporated into watershed scale SWAT models through a reduction in the SCS CN by 5 or 6 units (Arabi et al. 2008; Bracmort et al. 2006; Strauch et al. 2013;

Tuppad et al. 2010; Tuppad et al. 2009; Yang et al. 2009). A reduction in CN decreased the surface runoff volume, assuming soil or atmospheric losses. These methods of rainfall runoff modeling have often been critiqued for their extrapolation of the SCS CN method beyond the original study bounds (Ponce and Hawkins 1996). SCS CN method has been recommended for use in event based simulations only (Ponce and Hawkins 1996), but has been expanded to continuous simulations with CN regeneration schemes (Sahu et al. 2007). Better methods to incorporate runoff and infiltration dynamics are available (Singh and Woolhiser 2002), but come at a higher computation cost (Kollet et al. 2010).

Terraces are known to intercept surface runoff, encourage infiltration, and evaporate or divert water to stable outlets (NRCS 2011). Field measurements and model simulations reciprocate these terrace impacts on flow (Chow et al. 2010; Chow et al. 1999; Dumbrovsky et al. 2014; Tuppad et al. 2009; Yang et al. 2009). Measured seasonal runoff in a paired watershed study indicated that terraces combined with grassed waterways reduced runoff by 78 %, increased the time of concentration, and reduced Q_p (Chow et al. 1999). Extending the previous work, Chow et al. (2010) found a 87% reduction in seasonal runoff over a longer duration. For a 100 year annual exceedance flow, variable terrace densities produced a reduction in Q_p capacity by 4 % to 21 % in small steep tributaries (Dumbrovsky et al. 2014). Tuppad et al. (2009) studied a range of BMPS indicating that terraces reduced runoff by up to 32 %. Flow diversion terraces commonly applied in Canadian agricultural practice achieved an annual reduction in water yield ranging from 9 % to 37 % (Yang et al. 2009). Many of these studies taking place at small Das were more likely to achieve a response in ε. A reduction in Q_p was achieved in this study at small Das as well.

Studies have also shown variability in the impact of terracing. Indicating terraces retain too much water leading to saturation and consequently increased storm runoff (Gallart et al. 1994). Terraces implemented at variable densities across all agricultural land achieved a low level of annual ε (0.6 %) (Strauch et al. 2013). Terraces have been

noted to reduce Q_p, but not over all annual volumes (Kramer et al. 1999; Onstad and Jamieson 1970; Tomer et al. 2005). In this study, Q_p were reduced at the SC scale by up to 28 % with terraces. Terrace impacts attenuated with increasing DA. During events, Q_p were delayed and reduced, shifting the hydrograph later, and increasing the receding limb (Fig. 9.16). Changes in the cumulative Q when comparing with and without terrace simulations occurred only during event periods. NT simulations responded to peaks faster, in the rising and falling limb of the hydrograph for each event period. As compared to the calibration simulations, nested SCs simulation responded in the same manner. The terrace impact on Q_p, but not cumulative Q aligns well with the studies of (Kramer et al. 1999; Tomer et al. 2005).

Terraces are the most successful in locations with increased overland flows (Rittenburg et al. 2015). Prior to incorporating terraces at the watershed scale, the NT model had high I volumes over the year, and events. In all but three watershed scale events I/P > 0.9. In these scenarios stream and near stream rainfall produced Q_p response, as P was likely infiltrated in overland areas (Meyles et al. 2003). Event based responses not originating from the upland terraces areas, cannot be impacted by the structures. Rainfall intensity is an important factor in production of broad scale events (Cammeraat 2004). In this study, increased rainfall intensity forced larger areas to respond to the event, producing higher overland runoff. Counteracting the effects of rainfall intensity was the vertical hydraulic conductivity which incorporated macro porosity (Section 5.3.1), and the addition of a tile drainage layer. These attributes route water into and though the subsurface, out of the terraced pathways, and reducing their effectiveness.

ε was shown to vary with terrace density, DA, and initial soil moisture (Fig. 9.18). The R^2 in each of the four least squares regression lines was not indicative of a good fit, but indicated a pattern. Generally as the initial wetness increased, ε decreased. This result was reciprocated by Gallart et al. (1994). As DA increased, ε were lowered. As the

terrace density increased ε also increased (Dumbrovsky et al. 2014; Tuppad et al. 2009), and lessened as the initial soil water content increased.

9.3.3 Challenges and Future Work

The most significant obstacle to overcome in this study was to incorporate the appropriate style of terraces in Iowa. Common terrace practice in Iowa uses storage terraces most frequently, with a lesser application of gradient terraces. Storage terraces are designed as small reservoirs, impounding water, and releasing it through a tile drain control structure. Limitations in the selected simulation platform currently did not allow the incorporation of explicit 1-D elements to directly and dynamically interact with the surface and subsurface domains. If this limitation was broached, the two phased framework at field and watershed scale would not change. The calibration procedure would be reconfigured to include a 3-D system, incorporating a subsurface tile drain which would outlets into the nearby stream. In an effort to test this framework, gradient style terraces were implemented.

A need for incorporation of infiltration into the calibration procedure is prudent to achieve watershed scale reciprocation of local response. Gradient terraces were conceptualized to increase travel in steep agricultural hillslopes. This was achieved as noted by the peak flow delay and reduction in field scale calibrations, mimicked at the SC scale. Watershed scale and long term investigation indicated only brief alterations to flow. Without an increased infiltration capacity at the field scale to incorporate the slower subsurface pathways, lasting change was not achieved. Applying PEST to a coupled surface-subsurface simulation, with infiltration as a calibration target works to achieve this goal.

This was a numerical experiment, a first attempt to incorporate terraces as a distributed effective roughness. This work could be improved through additional numerical capabilities and attention to infiltration. Without the capability to alter the

numerical model, incorporation of the increased infiltration capacity needs to be a priority. Coupled 3-D calibration scenarios with infiltration and surface flows as targets offers a further direction for this work to proceed.

9.4 Summary and Findings

Terraces are commonly applied agricultural practices, built to reduce erosion by dividing unimpeded flow path lengths. Currently, there are no standard procedures to incorporate these structures into a modeling environment, testing their efficacy under varying climate and conservation scenarios (Arabi et al. 2008).

This study was the first attempt to investigate distributed equivalent terrace incorporation into a coupled physics based model. PEST estimated effective surface roughness values for 29 terrace arrangements. Equivalent roughness hydrographs matched the explicit incorporation of terraces well. These results were applied to watershed scale simulations based on land use and slope. Annual, and event based Q_p and cumulative Q were investigated at the BCW outlet and the outlets of a set of densely terraced nested SC. Infiltration was investigated on a heavily terraced hillslope.

The results indicated that terraces reduced and delayed Q_p at each of the SCs over event durations, by an average of 10 % and 15 % for T and MT simulations, respectively. Hydrographs were shifted responding to rainfall later than NT scenarios. Cumulative flow volumes varied between terrace arrangements within an event but returned to equilibrium within 2 days. ε reductions were shown to vary with event antecedent moisture, DA, and terrace density. In an annual time integration water balance components for the SCs and over the total catchment area did not differ between T and NT scenarios. Similarly, at the field scale, infiltration was not impacted by the terraces. This unchanged watershed integrated response was likely due to the lack of infiltration at the field scale.

SC scale results reciprocated the calibration scenarios well, reducing and delaying the hydrograph. To achieve catchment wide impacts an alteration to the infiltration capability at the field scale was required. The effects of SC results were dampened by a subsurface driven system, with a high a priori infiltration capacity. Future work would do well to incorporate infiltration as a PEST calibration target. Model limitations in incorporation of required storage terrace features forced an alternative, implementation of gradient terraces.

Although the exact simulation response was not achieved, this work encouraged a deeper understanding of the coupled surface-subsurface exchange processes. It further assembled a framework to analyze a system at the field scale for implementation at the watershed scale. It showed large scale simulations reproduce field scale results well. This procedure can be reasonably extrapolated to another terrace scenario, or distributed water conservation practice.

10.0 A FUTURE DIRECTION OF MODEL CALIBRATION AND VALIDATION

As noted by Singh and Woolhiser (2002) the amount of data available often dictates the style of model applied to a problem. Well instrumented areas are suited to physics based models. However, integrating large amounts of data with the simulation capabilities of physics based models is challenging. These challenges lead to difficulty in attributing, calibrating, and validating a model appropriately.

Conventional strategies for watershed model calibration and validation often rely on comparisons between modeled and measured stream flows at a basin outlet. Utilizing a single point of calibration is an approach deemed inappropriate when investigating a distributed hydrologic model (De Schepper et al. 2015; King et al. 2014; Rosso 1994).

The predictive capabilities of the models is predicated on the appropriate assignment of soil hydraulic properties (Vrugt et al. 2004). Soil texture and hydraulic properties are critical to modeling vadose zone water movement that includes infiltration, runoff, and evapotranspiration. Spatial heterogeneity in soil hydraulic properties result in large variability of input parameters. Available measured hydrologic data over time offers the capability to calibrate vadose zone properties. In-situ soil moisture sensors (Mertens et al. 2006; Pfletschinger et al. 2014; Verbist et al. 2012), satellite soil moisture (Santanello et al. 2007), subsurface drainage (Mertens et al. 2006; Rasoulzadeh and Yaghoubi 2014; Vrugt et al. 2004), and surface runoff (Verbist et al. 2012; Vrugt et al. 2004) have been applied as calibration targets for automated hydraulic parameter calibration or inverse modeling within the vadose zone. Over parameterization through inverse modeling of soil hydraulic properties presents itself through solution non-uniqueness. Reducing the quantity of adjustable parameters through evaluation of parameter correlation often alleviates solution non-uniqueness (Laloy and Bielders 2009).

In the glaciated central United States, silty clay loam, silt loam, and loam type soil texture classes make up the majority of soil classifications, and in Iowa, these textures comprise more than 80% of Iowa's surficial soils (NRCS 2014). Some hydraulic characteristics of these soils can be found in The Soil Survey Geographic (SSURGO) database and the State Soil Geographic (STATSGO) database. Further work has been completed to estimate soil hydraulic parameters with hierarchical pedotransfer functions in the form of ROSSETTA (Schaap and Leij 1998; Schaap and Leij 1998; Schaap and Leij 2000; Schaap et al. 1998; Schaap et al. 2001). Through a combination of the SSURGO database and ROSSETTA, estimated soil hydraulic property data can be attributed to land areas across the central U.S. However, the soil hydraulic data comes with a large variance, as hydraulic property measurements originate from across the US and Europe.

The objectives of this section were to, utilize field measured rainfall and soil water content data from the most common soils of agricultural Iowa to estimate soil hydraulic property values, validate the estimated hydraulic properties to soil water content data, and investigate the error associated with numerical discretization, and calibrated soil properties. To accomplish these objectives, a coupled surface-subsurface hydrologic model, together with a parameter estimation software were applied to calibrate and validate soil column experiments for application at the watershed scale.

10.1 Study Methodology

This section describes the parameter estimation locations, the numerical soil column experiment, and the calibration approach.

10.1.1 Site Description

This study evaluated continuous data collected at three RGSM platforms in Iowa (Fig. 10.1). RGSM platforms were a part of a monitoring plan, to measure hydrologic processes deemed important in flood producing events. The stations were installed in

watersheds selected for detailed hydrologic modeling and project implementation as part

of the IWP. The soil textures of these sites represent more than 80% of Iowa's surficial

soil texture classes, silty clay loam (35.2%) station 1, silt loam (28.5%) station 3, and

loam (19.7%) station 2 (Fig. 10.1). Station 2 represents the BCW, sensor RGS0040 from

Fig. 4.2. However, there are no measured hydraulic properties available for the rain

RGSM sites. The SSURGO soils database contains soil texture information and physical

hydraulic property information for varying soil horizons measured at these point

locations. Hydraulic data for the soil types found at each site is often generalized to large

representative regions with wide ranges in variability. The USDA offers class averaged

hydraulic parameters for each of the twelve identified soil texture classification,

representing the first hierarchical sequence of the ROSSETTA pedotransfer function

(Schaap and Leij 1998; Schaap et al. 2001) (Table 10.1).
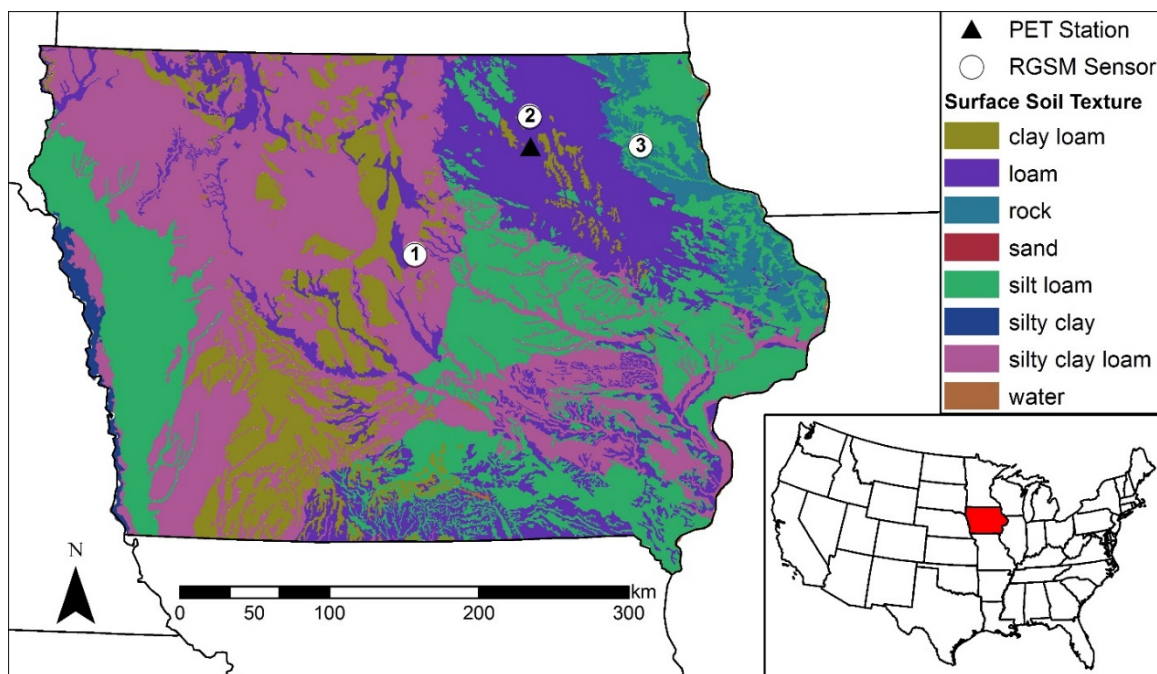
Figure 10.1 Iowa surficial soil textures from gSSURGO (NRCS 2014) database. RGSM platforms located in one of the three dominant soil textures. (1) silty clay loam, (2) loam, (3) silt loam. The triangle identifies the Nashua weather station.

Table 10.1 Soil hydraulic properties abstracted from Table 5.1, for the three dominant soil types in Iowa. Values in the table are formatted as, "mean (-1 standard deviation, +1 standard deviation)," based on the first model of the hierarchical sequence of the pedotransfer function ROSSETTA (Schaap and Leij 1998; Schaap et al. 2001).

Texture Class	θ_r (m^3/m^3)	θ_s (m^3/m^3)	α (m^{-1})	β (-)	K_{sat} (cmd^{-1})
Silty Clay Loam	0.09 (0.01, 0.17)	0.44 (0.35, 0.53)	0.84 (0.22, 3.3)	1.52 (1.13, 0.13)	18.2 (0.6, 550)
Loam	0.06 (0, 0.13)	0.4 (0.3, 0.5)	1.11 (0.21, 6)	1.47 (1.09, 0.13)	12.1 (0.17, 830)
Silt Loam	0.07 (0, 0.14)	0.48 (0.35, 0.53)	0.51 (0.14, 1.9)	1.66 (1.21, 0.14)	11.1 (0.34, 370)

10.1.2 Model Setup

This study investigated coupled surface-subsurface hydrologic flow in a representative soil column containing the RGSM platforms at each site. A single four node, finite element surface grid was projected downwards generating elements to a depth of 80 cm. Vertical nodes were allocated to each soil water content measurement location, at 5 cm, 10 cm, 20 cm, and 50 cm allowing for exact comparison between measured and simulated soil moisture. A numerical layer was added between each sensor location to ensure the solutions are numerically independent producing a total of 10 vertical layers (Fig. 10.2), a further discussion of grid sensitivity is found in Section 10.2.1.

Cornelissen et al. (2013) identified that using vertically uniform surficial soil properties makes simulation of soil moisture dynamics inaccurate. Near surface soils were noted to be highly permeable and highly porous in a forested catchment (Sciuto and Diekkruger 2010), while Azevedo et al. (1998) and Mohanty et al. (1996) indicated a reduction in infiltration in cultivated settings. Without prior knowledge of near surface stratigraphy, a vertical representation of the soil hydraulic profile was not assumed. In this study, two different sets of parameters were used to characterize the top 80 cm of the

soil column. One representing the top 5 cm of the soil column, above the soil moisture measurement devices, and a second for the remaining 75 cm of soil column.

Based on observed data it was assumed that the position of the water table was outside of the model domain. Capillary fringe effects from a shallow water table position have yet to be studied for these sites and could impact results. Surface topography was assumed negligible and was modeled as a flat one square meter surface. Evapotranspiration parameters were described in Table 5.2 and Table 5.3. Each RGSM sensor was located in cool season turf grass, thus altering LAI (1.0) and root depth values (0.3 m) (Beard 2001).

Rainfall was applied as a flux at 15 minute intervals to the surface of the modeling domain, where precipitation was stored up to a rill storage height of 0.002 m (Perez et al. 2011), infiltrated into the subsurface governed by a coupling length of 0.01 m (Perez et al. 2011), or allowed to run off from all surface edges through a critical depth boundary condition. Once in the subsurface water can move vertically downwards, exiting through a free drainage boundary condition at 80 cm below the land surface. Two additional highly resolved numerical layers were placed in the lowest one cm of the column to reduce numerical error at the free drainage lower boundary. All remaining subsurface boundaries were considered no flow. Evapotranspiration can remove water from the domain via the surface or subsurface up to defined evaporation and transpiration depths and through a cubic decay function.
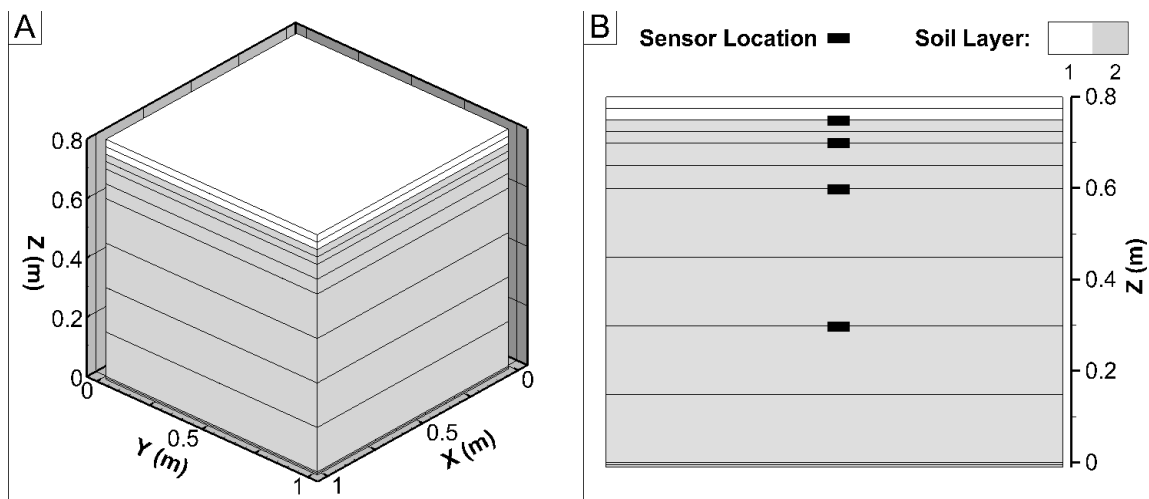
Figure 10.2 a) Isometric view of numerical soil column with soil calibration layers. b) X-Z depiction of the soil column with soil layering and sensor locations.

10.1.3 Parameter Estimation

Subsurface unsaturated flow parameters were calibrated using Parameter Estimation (PEST) software (Doherty 2010). Parameters deemed insensitive to soil water variation by Verbist et al. (2012) were not included in the study. PEST was linked with HGS through porous media input files. Hydraulic parameters in the porous media input files were assigned based on deviations from observed data at each observation depth. PEST communicates through a models' raw ASCII output files and alters input properties in an interactive fashion until termination criteria are met.

In this study, PEST was used to calibrate α, β, and the saturated hydraulic conductivity for two soil layers (Fig. 10.2). Unsaturated flow properties α and β were assigned a parameter range equal to one standard deviation above and below the mean value (Table 10.1). The saturated hydraulic conductivity was assigned a range of two standard deviations above and below the mean measured value (Table 10.1). Hydraulic conductivity varies significantly with depth and location (Azevedo et al. 1998; Ebel et al. 2009; Mohanty et al. 1996; Sciuto and Diekkruger 2010; Verbist et al. 2012) . Soils nearest to the surface are often not described by SSURGO. The topsoil can be impacted

by surficial land uses (Chen et al. 2014), and can fall outside the measure range for a given soil texture. Without knowledge of subsurface layering or calibration data below 50 cm, the remaining soil column below 50 cm was assumed have the same hydraulic properties as layer 2.

Residual saturation values in both subsurface layers were held constant at zero. Numerical error increased as a function of increasing residual saturation, a product of suction head values exceeding 100 m. The ROSSETTA first hierarchical approximation of a mean and standard deviation of residual saturation includes a residual saturation value of zero. Residual saturation was not identified as significantly different from zero (Verbist et al. 2012), resulting from low sensitivities to water content variations and runoff production. A residual saturation close to zero best approximates exceedingly dry periods better, producing more appropriate hydraulic parameter estimates (Pfletschinger et al. 2014).

Porosity was assigned the maximum water content measured at the 10 cm observation depth, and was assumed constant for the entire column for each soil texture at 0.42 m^3m^{-3}, 0.40 m^3m^{-3}, and 0.43 m^3m^{-3} for the silty clay loam, loam, and silt loam soil types respectively. The maximum water content indicates that all of the pore space is filled with water. Porosity values for each of the soil types were within one standard deviation of the mean value for each soil texture class from the ROSSETTA first order analysis (Table 10.1). The remaining soil, evapotranspiration, and overland flow properties were held constant throughout the analysis.

Soil properties were calibrated to a precipitation event occurring on October 13, 2014. The rainfall initiated a similar soil water response at each of the RGSM locations. The time window selected encompassed a rise and fall in soil water content, at all observation depths. The silty clay loam soil type received a precipitation depth of 36.8 mm, with a peak rainfall intensity of 1.15 mm·15 min^{-1}. The loam soil type received a precipitation depth of 28.4 mm, and a peak rainfall intensity of 0.51 mm·15 min^{-1}. The

silty loam soil type received a precipitation depth of 71.3 mm, and a peak rainfall intensity of 1.71 mm·15 min^{-1}. Although the time window was not during the peak summer months, PET was nontrivial and estimated to average of 2.35 mmd[-1]. Calibration simulations were run for a 24 day time period, beginning September 29, 2014. The first 7 days of this time period were utilized as initialization, enabling model results to be independent of the initial conditions. The final 17 days of measured data beginning October 6, 2014, were utilized as calibration targets.

The calibrated parameters were validated to intermittent precipitation occurring between August 22, 2014 and October 23, 2014. Precipitation events totaled 187.5 mm, 171.8 mm, and 150.9 mm on the silty clay loam, loam, and silt loam soil types respectively. The precipitation initiated a wide ranging response in water content at the four measurement depths and at each of the three RGSM locations. The September intermittent rainfall produced a differing soil water content response, with a series of increased intensity events occurring during a time period with larger PET (average 3.0 mmd[-1]) than the calibration window. The combination of the increased intensity of precipitation and PET produced rapid responses in water content variability. Validation simulations were run for a 53 day time period, with a 13 day initialization period prior to August 22, 2014. The final 17 days of the validation time period overlapped with the calibration time window. Common practice considers validating over the calibration periods to be inappropriate, biasing the results. Soil moisture dynamics were highly dependent upon the initial condition. Thus, validation in this scenario permitted evaluation of the spin up period prior to the calibration time period.

10.2 Results

Grid independence, calibration, and validation computations were carried out for a one dimensional vertical, 80 cm soil column. Grid independence and calibration were

analyzed from October 6, 2014 to October 23, 2014, and validation was performed for the August 22, 2014 to October 23, 2014 time period.

10.2.1 Grid Independence Study

To verify that the HGS solution was independent of grid size, a grid independence study was performed through a systematic vertical mesh refinement. This method makes it possible to determine the numerical error originating from a chosen mesh resolution. The coarsest vertical resolution contained five layers (six nodes). One node was allocated to each measurement depth, similar to Verbist et al. (2012). Numerical elements were systematically added by a factor of two, from five layers up to 640 layers.

The grid sensitivity analysis was completed by investigating the variation in soil water content due to vertical mesh resolution. The time period from October 13, 2014 to October 23, 2014 was run with a one week spin up period, and mean hydraulic properties for the entire soil column. The relative difference in modeled water content between 320 vertical layers and 640 layers was consistently less than 0.2%. Numerical convergence was assumed at 640 vertical layers. Each lower resolution grid was compared to the 640 layer grid. For the remainder of this section the relative difference in modeled water content between each refinement level and the 640 layer model is referred to as error.

The largest deviation from the 640 layer grid was observed in the five layer model, the maximum error at each depth coincided with the respective maximum water content change. An overestimate of 4.5% at a 10 cm depth below the surface represented the largest error (Fig. 10.3). Increasing the numerical resolution generated a more rapid response to wetting and drying of the soil column. The maximum error reduced to 0.2% when the vertical resolution was increased to 320 layers. Each grid refinement simulation exhibited a similar behavior. The largest cumulative error occurred under dry conditions (Fig. 10.3b, Oct. 6 to Oct. 13). The maximum error occurred in response to rapid soil wetting (Fig. 10.3, Oct. 14). The highest mean error, time averaged, of 1.76% occurred in

the coarsest model, at the 5 cm depth. The lowest mean error occurred in the most refined 320 layer model at 0.02%. Table 10.2 depicts an asymptotic trend in mean error percent from over 1.76% at the coarsest mesh that approaches zero in the most refined.

Each of the refinement levels display relatively low error levels. High mesh resolutions described soil water dynamics better during wetting events. A good agreement was achieved at refinement levels higher than five numerical layers. Considering the large number of model runs required to iteratively calibrate parameters through PEST, and the motivation to upscale the calibrated parameters to computationally expensive large scale models, a coarser grid refinement was chosen. The 10 layer grid was chosen to complete parameter estimation as a balance between computational efficiency and grid refinement induced error.
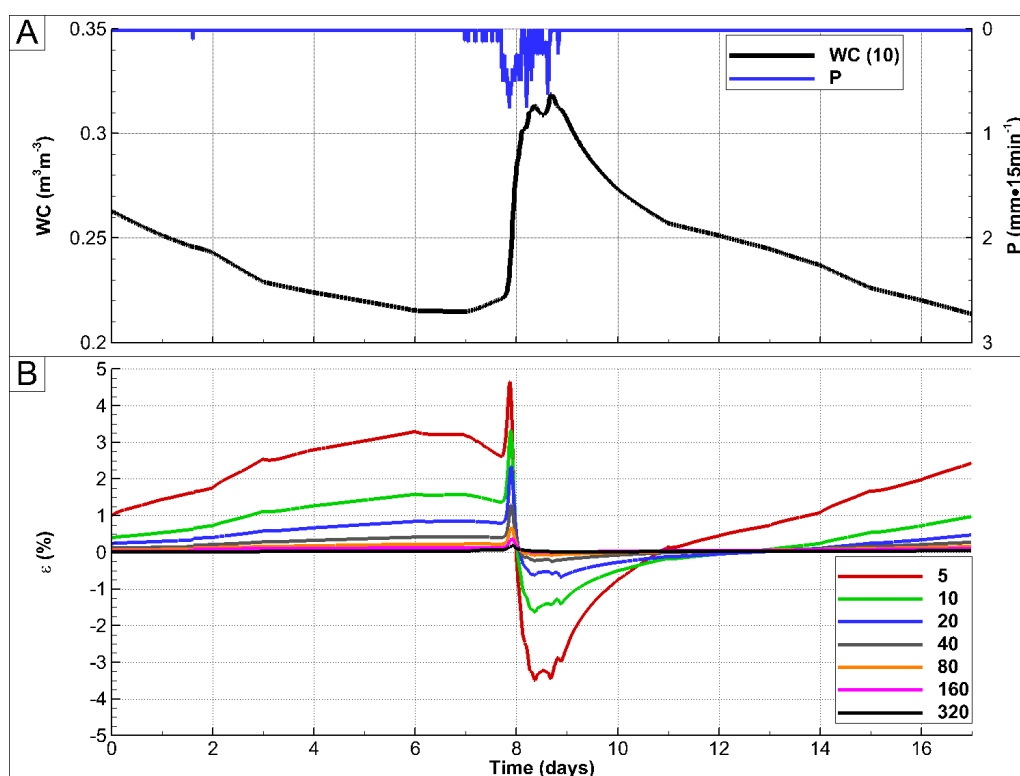
Figure 10.3 Grid Sensitivity. a) Simulated water content at 10 cm depth and rainfall flux from October 6, 2014 to October 23, 2014, for the 640 numerical layer grid. b) ε, Eq. [10.1] at each grid resolution (i.e. 5, 10, 20, 40, 80, 160, or 320 layers) when compared to the 640 numerical layer grid.

Table 10.2 Summary of the grid refinement study. Values are depicted as "Mean ε (maximum ε)" Eq. [10.1], when comparing each grid resolution to the 640 layer grid for the 5 cm, 10 cm, 20 cm, and 50 cm observation depths.

Observation Depth (cm)	Numerical Layers						
	5	10	20	40	80	160	320
5	1.8 (3.9)	0.78 (2.4)	0.42 (1.6)	0.2 (0.8)	0.11 (0.5)	0.07 (0.3)	0.03 (0.2)
10	1.7 (4.6)	0.77 (3.3)	0.42 (2.3)	0.21 (1.3)	0.12 (0.7)	0.07 (0.4)	0.03 (0.2)
20	1.2 (3.2)	0.53 (1.8)	0.31 (1.4)	0.17 (1)	0.1 (0.6)	0.06 (0.4)	0.03 (0.2)
50	0.4 (2.7)	0.27 (1.7)	0.2 (1.1)	0.12 (0.6)	0.07 (0.3)	0.04 (0.2)	0.02 (0.1)

10.2.2 Model Calibration

The automated parameter estimation software PEST required 214, 215, and 412 HGS simulation runs to converge on a suite of parameter estimates for the silty clay loam, loam, and silt loam soil textures, respectively. Calibrated and ROSSETTA based parameters are depicted in Table 10.3 for a direct comparison.

Calibrating the water retention parameters α and β altered the soils capacity to transport water under unsaturated conditions. An increased α enabled the soil to shift from a saturated state to an unsaturated state at a lower suction head. An increased β value allowed less water to be retained in the soil under field capacity. Increasing the saturated hydraulic conductivity increased the potential soil transport rate. Silty clay loam, loam, and silt loam calibrated unsaturated properties in Layer 2 reduced water movement in less than saturated conditions and increased the potential vertical water movement at saturation (Fig. 10.12, Table 10.3). The calibrated parameters significantly impacted the soil response to rainfall, which agreed well when compared to observed data.

Graphic and statistic measures were applied to each of the soil texture calibration results, describing the quality of fit at each observation depth. Time series plots for each observation depth of observed and simulated water contents (Fig. 10.4), ε (Fig. 10.5) Eq. [10.1], d (Fig. 10.7) Eq. [10.2], and plotting observed vs. simulated water contents (Fig. 10.6) graphically depicted error trends. An estimate of the volume of water in the soil column was produced by assuming each observation location is valid for half of the depth between the next observation location above and below a given sensor (i.e. the 10 cm sensor is valid from 7.5 cm to 15 cm deep) (Fig. 10.7) Eq. [10.2]. Statistical measures and associated performance ratings were recommended by Moriasi et al. (2007), and included the Nash-Sutcliffe Efficiency (NSE) Eq. [10.3], Root Mean Square Error Ratio to the standard deviation of the observations (RSR) Eq. [10.4], and the Percent Bias (PBIAS) Eq. [10.5] (Table 10.4, Table 10.5).

$$\varepsilon = \left[\frac{\theta_{obs} - \theta_{sim}}{\theta_{obs}}\right] 100 \qquad [10.1]$$

$$d = [(0.075)\theta_{5cm} + (0.75)\theta_{10cm} + (0.20)\theta_{20cm} + (0.45)\theta_{50cm}]\theta_s \qquad [10.2]$$

$$NSE = 1 - \left[\frac{\sum_{i=1}^{n}\left(\theta_i^{obs} - \theta_i^{sim}\right)^2}{\sum_{i=1}^{n}\left(\theta_i^{obs} - \bar{\theta}\right)^2}\right] \qquad [10.3]$$

$$PBIAS = \left[\frac{\sum_{i=1}^{n}\left(\theta_i^{obs} - \theta_i^{sim}\right)100}{\sum_{i=1}^{n}\left(\theta_i^{obs}\right)}\right] \qquad [10.4]$$

$$RSR = \frac{RMSE}{STDEV_{obs}} = \frac{\left[\sqrt{\sum_{i=1}^{n}\left(\theta_i^{obs} - \theta_i^{sim}\right)^2}\right]}{\left[\sqrt{\sum_{i=1}^{n}\left(\theta_i^{obs} - \bar{\theta}\right)^2}\right]} \qquad [10.5]$$

Where ε (%) is the relative error, θ_{obs} (m³m⁻³) is the observed water, and θ_{sim} (m³m⁻³) is the simulated water content. The estimated storage depth is d (m), θ_{5cm} (m³m⁻³)

is the water content at 5 cm, θ_{10cm} (m^3m^{-3}) is the water content at 10 cm, θ_{20cm} (m^3m^{-3}) is the water content at 20 cm, θ_{50cm} (m^3m^{-3}) is the water content at 50 cm, θ_s (m^3m^{-3}) is the porosity of the given soil texture, and $\bar{\theta}$ (m^3m^{-3}) is the mean observed water content.

10.2.2.1 Silty Clay Loam

The silty clay loam soil texture calibration simulation captured soil water content variability with a high level of accuracy at all water depths (Fig. 10.4). This was further corroborated by a consistently less than 10% in ε for all measurement depths, except during the precipitation event (Fig. 10.5). The calibrated water content responded late to the initial wetting front by 0.50 hours, 1.25 hours, 1.75 hours, and 21.75 hours for the 5 cm, 10 cm, 20 cm, and 50 cm observation depths, respectively. A tight grouping of observed to simulated water content values (Fig. 10.5), and a RSR of less than 10% indicated a low deviation from observed data and a good to very good agreement (Table 10.4, Table 10.5). A very good agreement was achieved for the silty clay loam soil type with the largest difference occurring as an underestimation of soil water during the maximum wetting period. The largest PBIAS occurred at the 10 cm depth with and underestimation of 5.19%, which indicated a very good agreement (Table 10.4, Table 10.5).

10.2.2.2 Loam

The loam type soil texture showed good agreement at the 10 cm and 20 cm depths with a RSR value of less than 0.5, NSE of greater than 0.4 and less than 10% PBIAS (Table 10.4, Table 10.5). The calibrated water content responded late to the initial wetting front by 0.50 hours, 0.61 hours, 3.00 hours, and 22.63 hours for the 5 cm, 10 cm, 20 cm, and 50 cm observation depths, respectively. The 5 cm observation depth showed a consistent overestimation for the calibration period (largest PBIAS -8.43%) (Fig. 10.4, Fig. 10.5). The 5 cm depth overestimation worsened during dry periods (Fig. 10.5). ε at 50 cm steadily increased as the simulation progressed, as water was lost through the free

drainage boundary condition, but was not replenished through precipitation (Fig. 10.5). The 50 cm observation depth was assigned a 56.3% weight as this observation depth is representative of the soil column from 35 cm deep to 80 cm deep. The added weight to the 50 cm depth and the associated increase ε (Fig. 10.5), skewed d towards under estimation (Fig. 10.7). Trends at each observation depth are followed well at each observation depth, with the 5 cm, 10 cm, and 20 cm, achieving a high level of agreement with measured data.

10.2.2.3 Silt Loam

A large water content response occurred at all observation depths for the silt loam type soil texture, with NSE greater than 0.8 for all but the 50 cm observation depth indicating a very good agreement (Fig. 10.4, Table 10.4, Table 10.5). A consistent deviation from measured values occurred during the advancement of the wetting front at each observation depth, depicting ε greater than 20% (Fig. 10.5), and below 10% for the remainder of the time series. The water content response to precipitation arrived early by 1.9 hours, 4.0 hours, 10.9 hours, and late by 3 hours at 5 cm, 10 cm, 20 cm, and 50 cm, respectively. Model results consistently depicted water content trends well at the 20 cm and 50 cm observation depths with slight over (PBIAS -4.71%) and under (PBIAS 6.82%) estimates at each depth, respectively (Fig. 10.5, Fig. 10.6). The underestimate of soil water content at the 50 cm depth is depicted in Fig. 10.7, as the d was heavily weighted on the deepest observation, still maintaining an adequate, but shifted response consistent with data.

Each soil texture simulation offered the least reliability at the beginning of the rising limb of the water content time series, as ε exceeded 10% at all depths. Simulated soil water contents were underestimated prior to an event and overestimated after the event in all soil textures (Fig. 10.5). Error estimators indicated a good calibration of soil parameters for each of the three soil types, at each depth except the 50 cm depth for the

loam type soil. Statistical deviations from a good agreement were in large part due to a shift in water content response, with an observation depth consistently over or under estimating the water content. Temporal patterns of soil moisture were retained throughout each of the calibrations.

Table 10.3 Final calibrated parameters for October 6, 2014 to October 23, 2014 time period. Calibration layer 1 (L2) and layer 2 (L2) represent the top 5 cm of soil column, and from 5 cm to 80 cm deep, respectively. Where μ is the mean textural parameter from the USDA SSURGO soil database (Table 10.1).

Texture Class	α (m^{-1})			β (-)			K_{sat} (cmd^{-1})		
	L1	L2	μ	L1	L2	μ	L1	L2	μ
Silty Clay Loam	0.89	4.25	0.84	1.39	1.14	1.52	9.7	148.4	11.1
Loam	0.89	1.25	1.11	1.10	1.15	1.47	69.1	17.3	12.1
Silt Loam	0.06	1.35	0.51	3.16	1.24	1.66	83.0	8.7	18.2
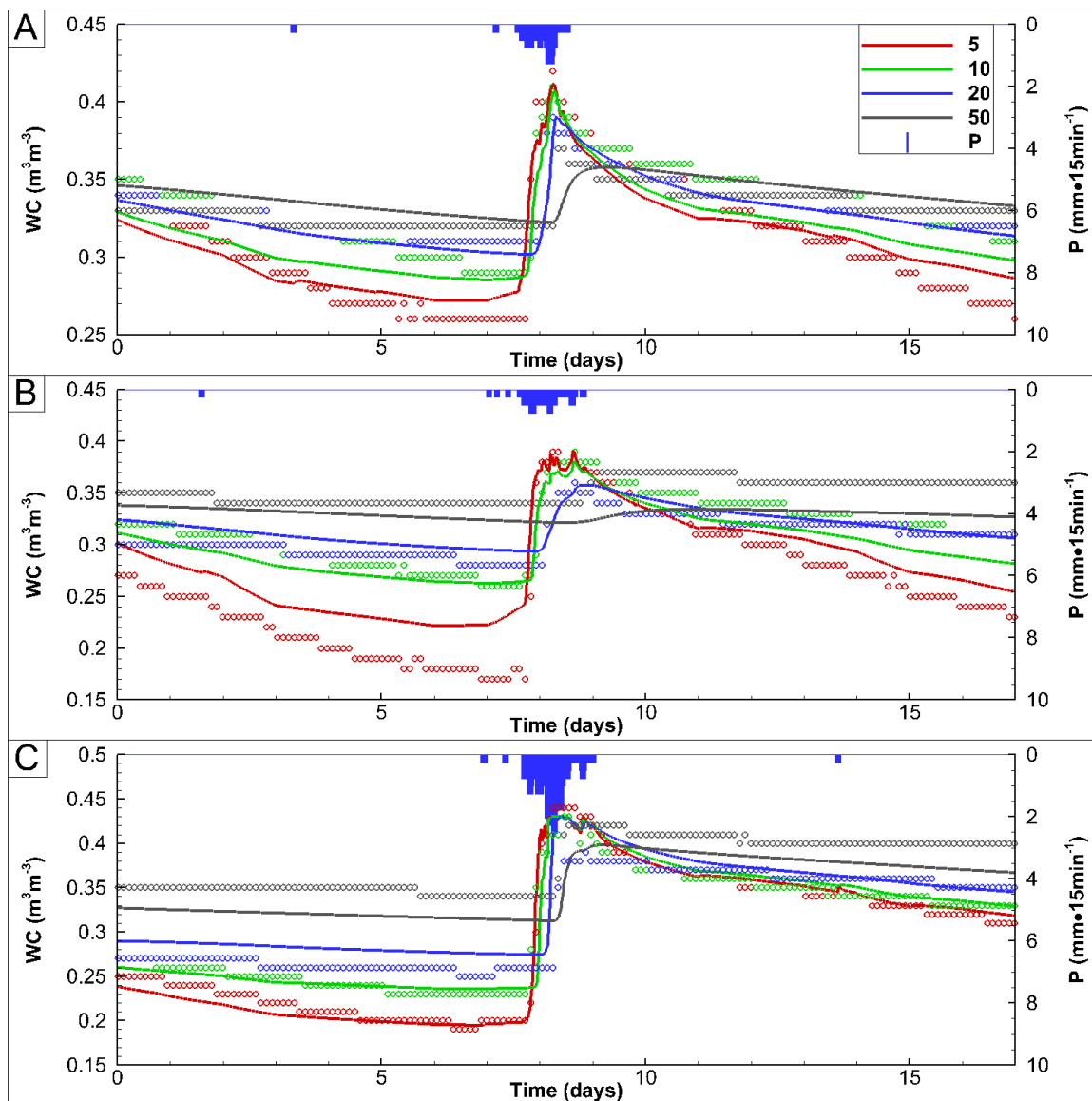
Figure 10.4 Calibration period observed (circles) and simulated (lines) soil water contents for the time period of October 6, 2014 to October 23, 2014. a) Silty Clay Loam. b) Loam. c) Silt Loam. Note that only 10 % of all observed data were displayed, to reduce clutter.
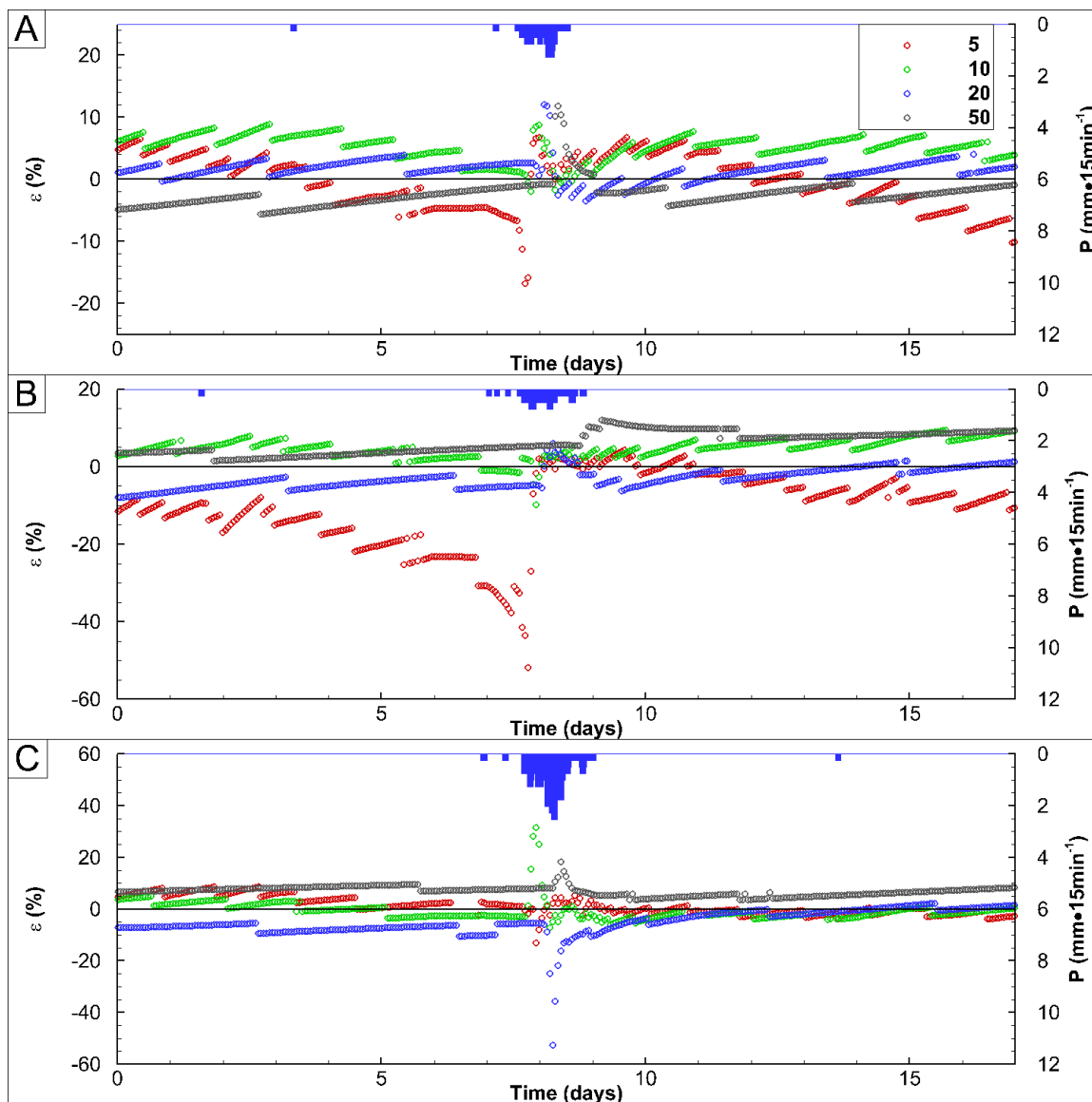
Figure 10.5 Calibration period ε, Eq. [10.1], between observed (circles) and simulated (lines) soil water contents for the time period of October 6, 2014 to October 23, 2014. a) Silty Clay Loam. b) Loam. c) Silt Loam. Note that only 20 % of all observed data were displayed, to reduce clutter.
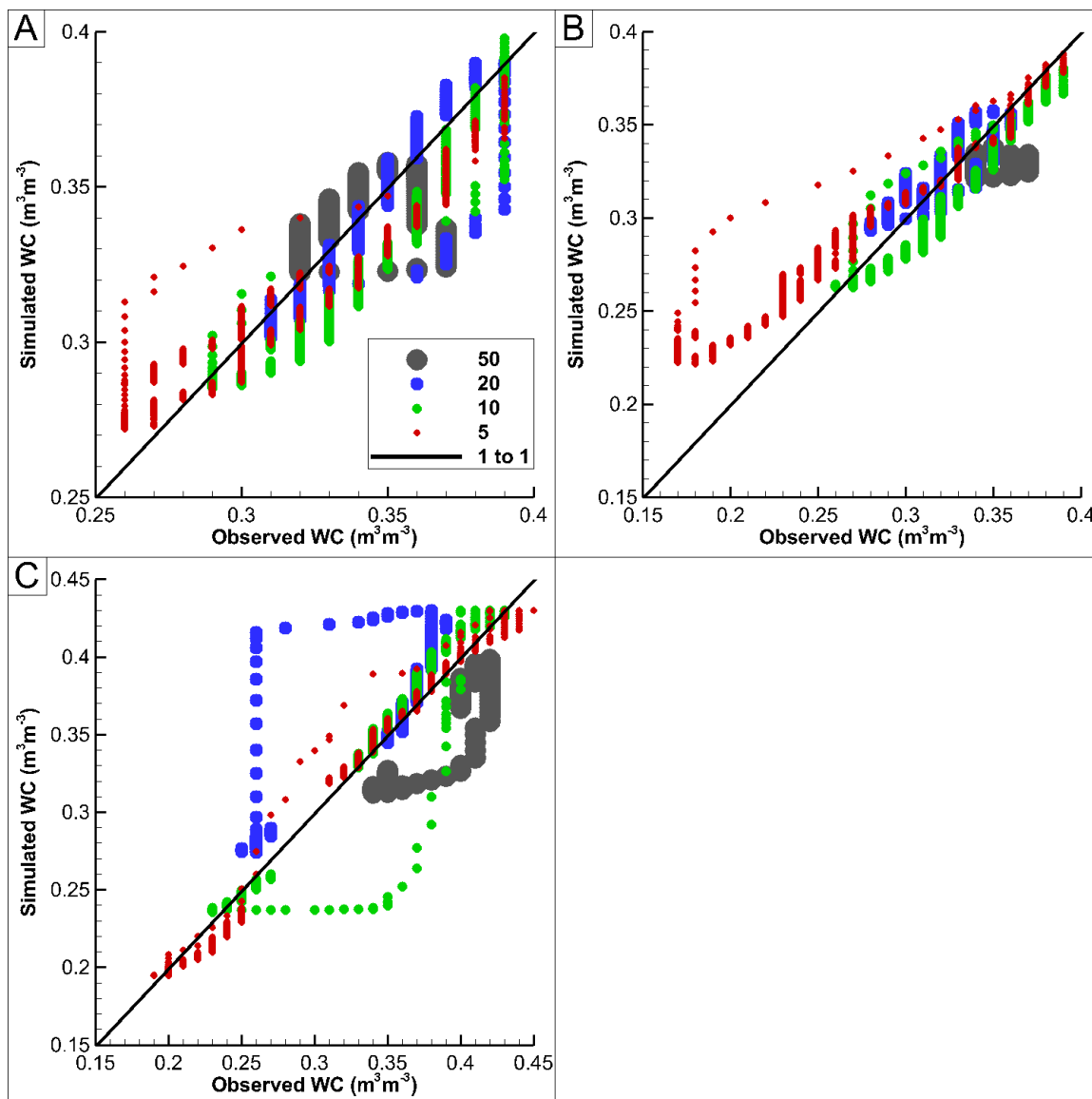
Figure 10.6 Calibration period scatter plot of observed vs. simulated soil water contents for the time period of October 6, 2014 to October 23, 2014. a) Silty Clay Loam. b) Loam. c) Silt Loam.
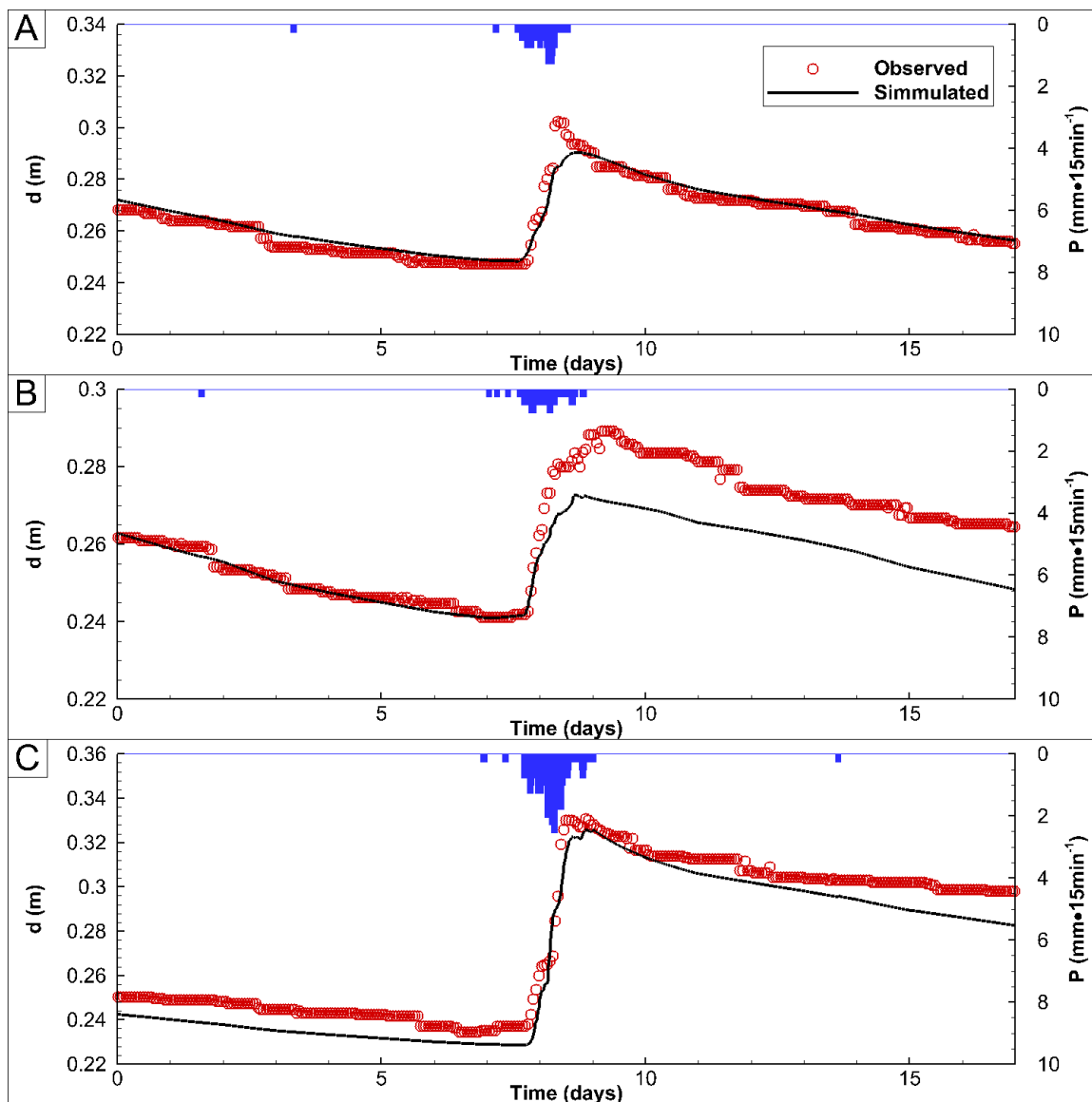
Figure 10.7 Calibration period observed (circles) and simulated (lines) *d,* Eq. [10.2], for the time period of October 6, 2014 to October 23, 2014. a) Silty Clay Loam. b) Loam. c) Silt Loam. Note that only 20 % of all observed data were displayed, to reduce clutter.

10.2.3 Model Validation

Validation of calibrated soil hydraulic parameters was performed for a 53 day duration, encompassing large variations in water content responses at each observation depth. The same statistic and graphic metrics discussed in Section 10.2.2 were applied for

the validation case. Application of the same metrics produced a direct comparison of quality between calibrated and validated simulation windows.

10.2.3.1 Silty Clay Loam

The silty clay loam validation (Fig. 10.8, Fig. 10.9) showed very good agreement at all observation depths. The largest deviations occurred in the first 10 days at the 50 cm depth. The 50 cm observation depth responded slowly from a dry state to near saturation over the first 10 days of the simulation. Fig. 10.11 shows an overestimation of water storage from days 6 to 20 and 30 to 40. This overestimation in the subsurface storage was likely due to the slight overestimation of water content at the 5 cm, 10 cm, and 50 cm depths (Table 10.4, PBIAS). A high NSE of 0.4 or greater at the 5 cm, 10 cm, and 20 cm, depths indicated a good fit, with exception to the 50 cm (NSE -0.07). Poor fit at the 50 cm depth was likely due to the underestimation of water content at the onset of the validation window.

10.2.3.2 Loam

Fig. 10.8 and Fig. 10.9 for the loam soil texture showed an increasing level of agreement as the validation period progressed. The 50 cm observation contained the largest ε, which occurred at the beginning of the validation period in the same manner as the silty clay loam texture class (Fig. 10.9). The 10 cm simulated depth underestimate water content (PBIAS 5.55%), while the 20 cm overestimated water content (PBIAS -3.88%) (Fig. 10.10). The 50 cm simulated depth was unresponsive to precipitation events, with a consistent underestimation (Fig. 10.8). NSE indicated poor agreement at the 20 cm and 50 cm observation depths with values of less than zero (Table 10.4).

10.2.3.3 Silt Loam

The silt loam validation showed good agreement at the 5 cm and 10 cm depths, but consistently underestimated water content at 50 cm, and over estimated at 20 cm (Fig.

10.8, Fig. 10.9). The largest ε occurred at the onset of precipitation and represent the largest peak relative errors for any of the calibration or validation results (Fig. 10.9). The validation underestimated water contents at the 50 cm depth (Fig. 10.10), depicted by the consistent under prediction of soil water storage (Fig. 10.11). NSE values of 0.80, 0.88, and 0.78 at 5 cm 10 cm and 20 cm observations depths indicated good agreement for the top 20 cm of the soil column, and poor agreement at a 50 cm depth (NSE -5.043). A PBIAS of 14.15% represented the highest bias in the calibration or validation results, which indicated a consistent underestimation of water content at 50 cm. The remaining 5 cm, 10 cm, and 20 cm depths all had a PBIAS of less than 2% indicating a very good agreement (Table 10.4, Table 10.5).

Validation simulations generally depicted similar tendencies as the calibration simulations. The expanded water content range in the validation window produced larger simulated deviations from observed data. Trends in water content variation were well maintained thought the validation simulations.
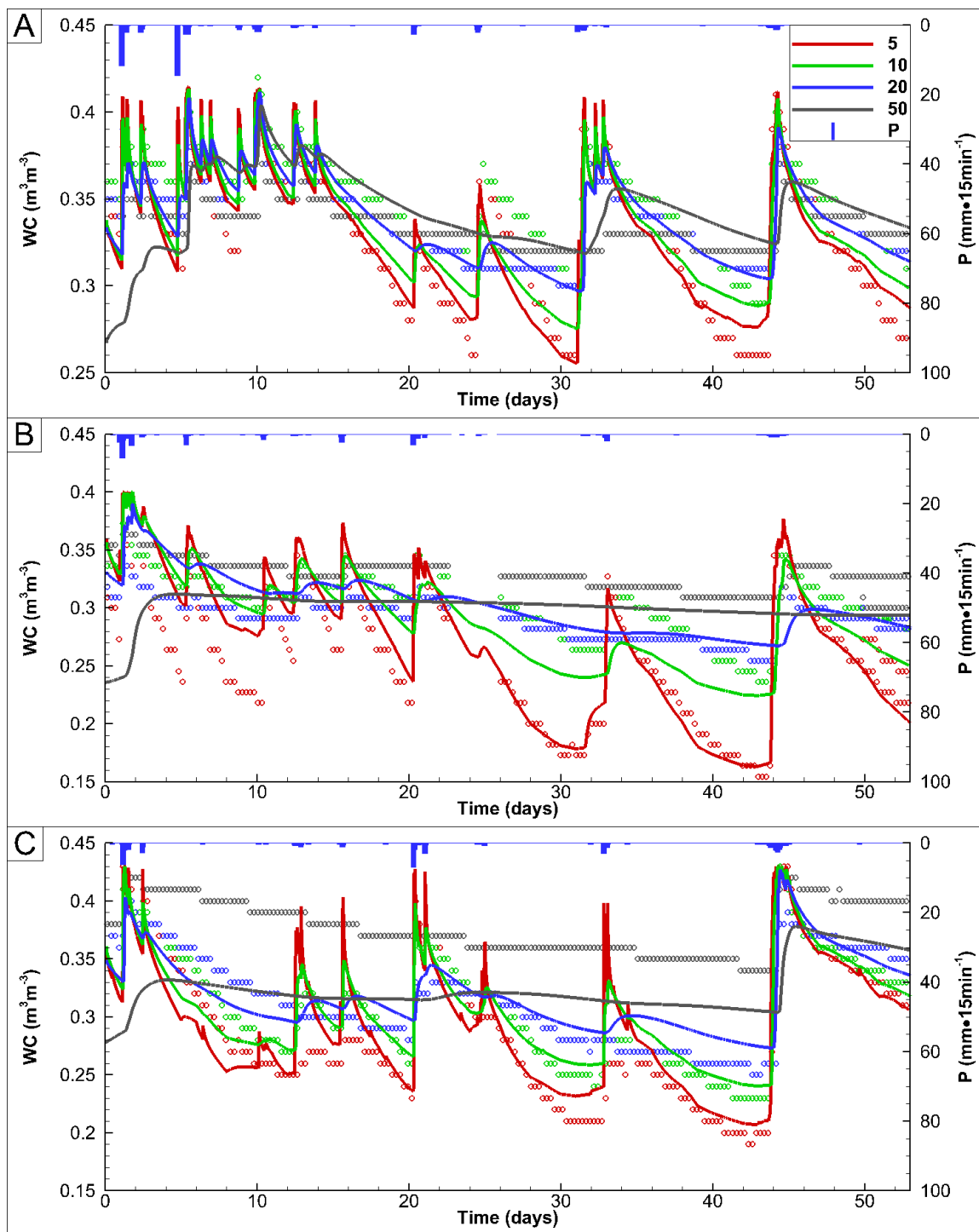
Figure 10.8 Validation period observed (circles) and simulated (lines) soil water contents for the time period of August 22, 2014 to October 23, 2014. a) Silty Clay Loam. b) Loam. c) Silt Loam. Note that only 4 % of all observed data were displayed, to reduce clutter. Note a data gap in plot B from day 22 to day 25.
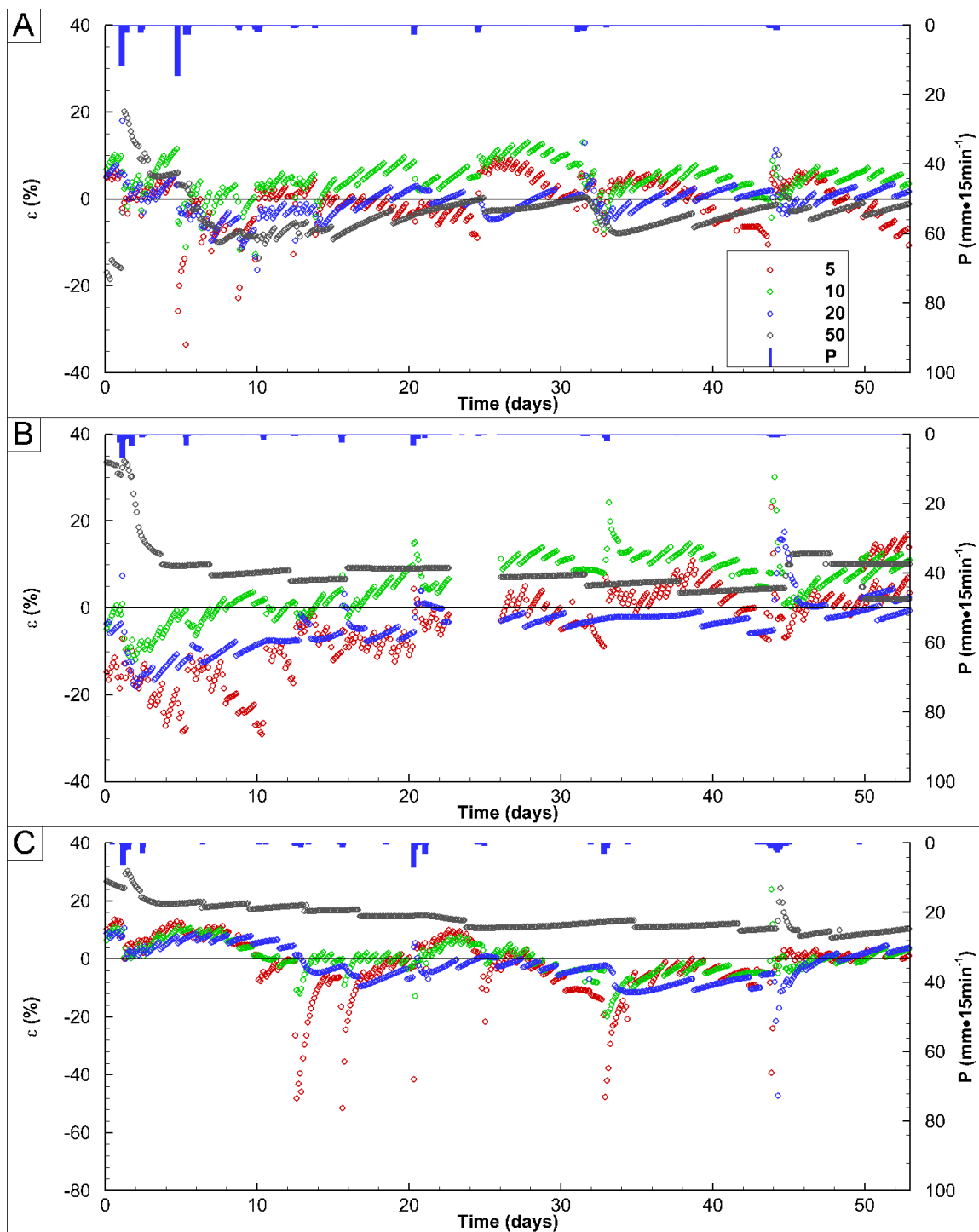
Figure 10.9 Validation period ε, Eq. [10.1], between observed (circles) and simulated (lines) soil water contents for the time period of August 22, 2014 to October 23, 2014. a) Silty Clay Loam. b) Loam. c) Silt Loam. Note that only 10 % of all observed data were displayed, to reduce clutter. Note a data gap in plot b from day 22 to day 25.
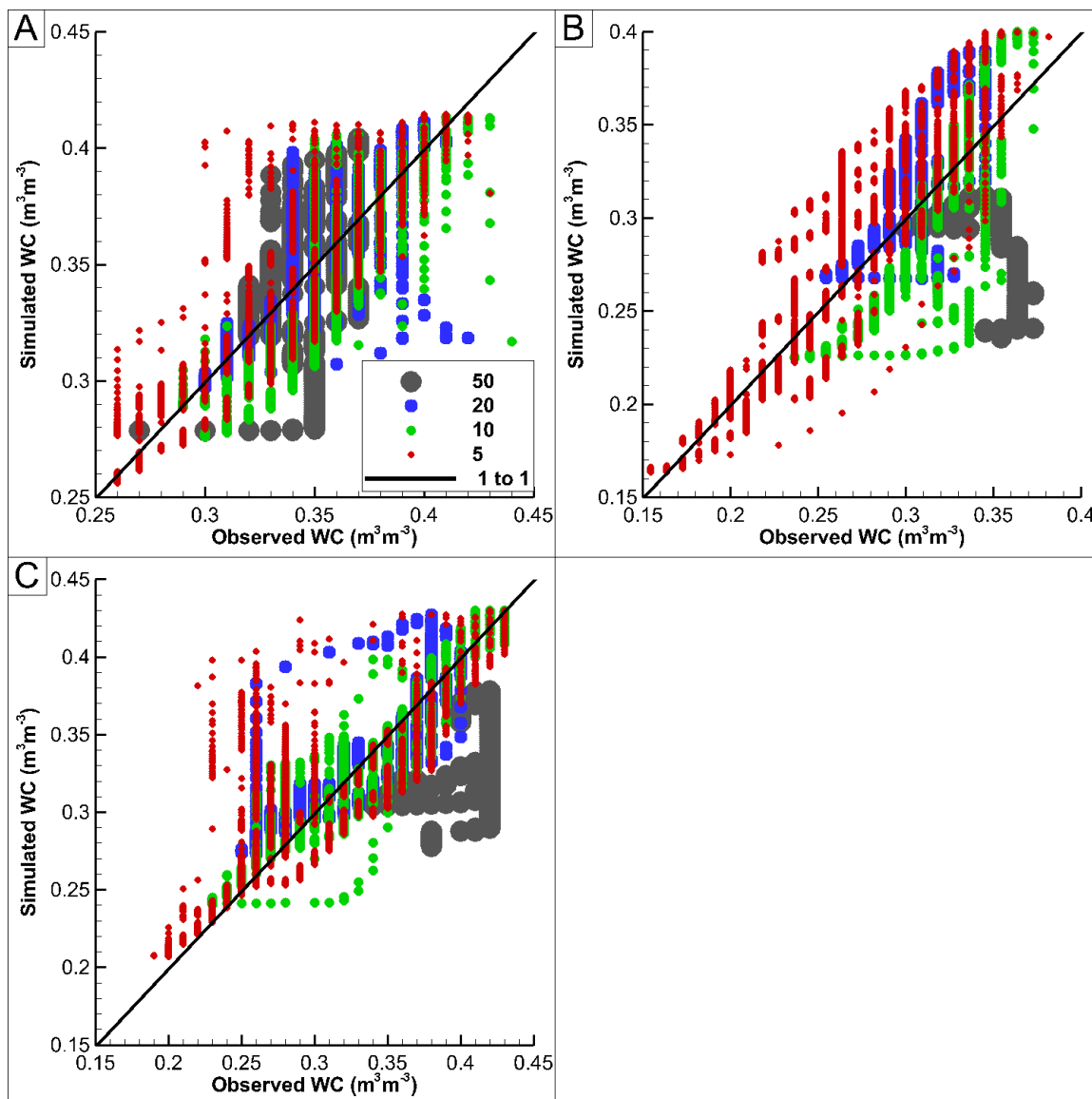
Figure 10.10 Validation period scatter plot of observed vs. simulated soil water contents for the time period of August 22, 2014 to October 23, 2014. a) Silty Clay Loam. b) Loam. c) Silt Loam.
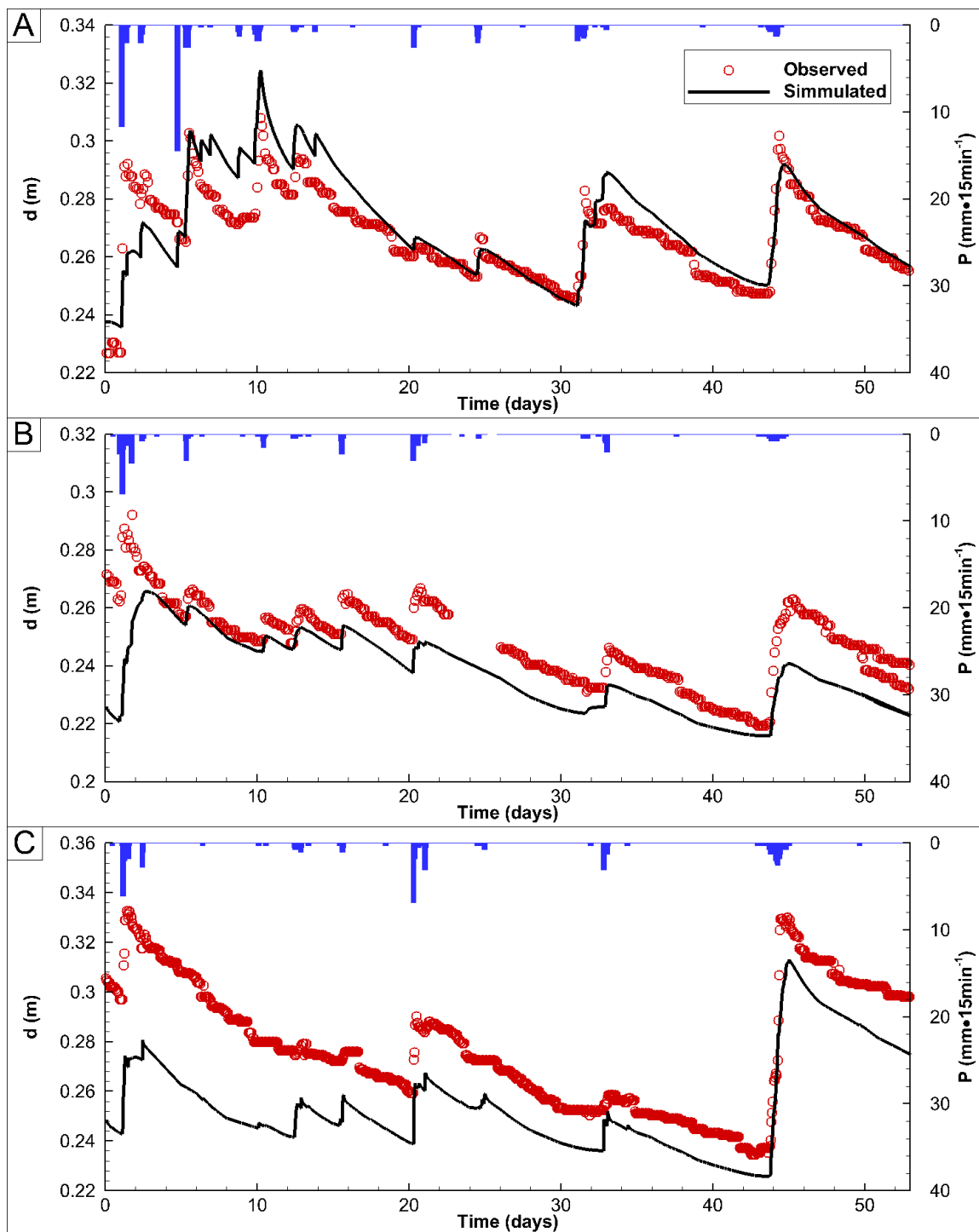
Figure 10.11 Validation period observed (circles) and simulated (lines) *d*, Eq. [10.2] for the time period of August 22, 2014 to October 23, 2014. a) Silty Clay Loam b) Loam c) Silt Loam. Note that only 10 % of all observed data were displayed, to reduce clutter. Note a data gap in plot B from day 22 to day 25.
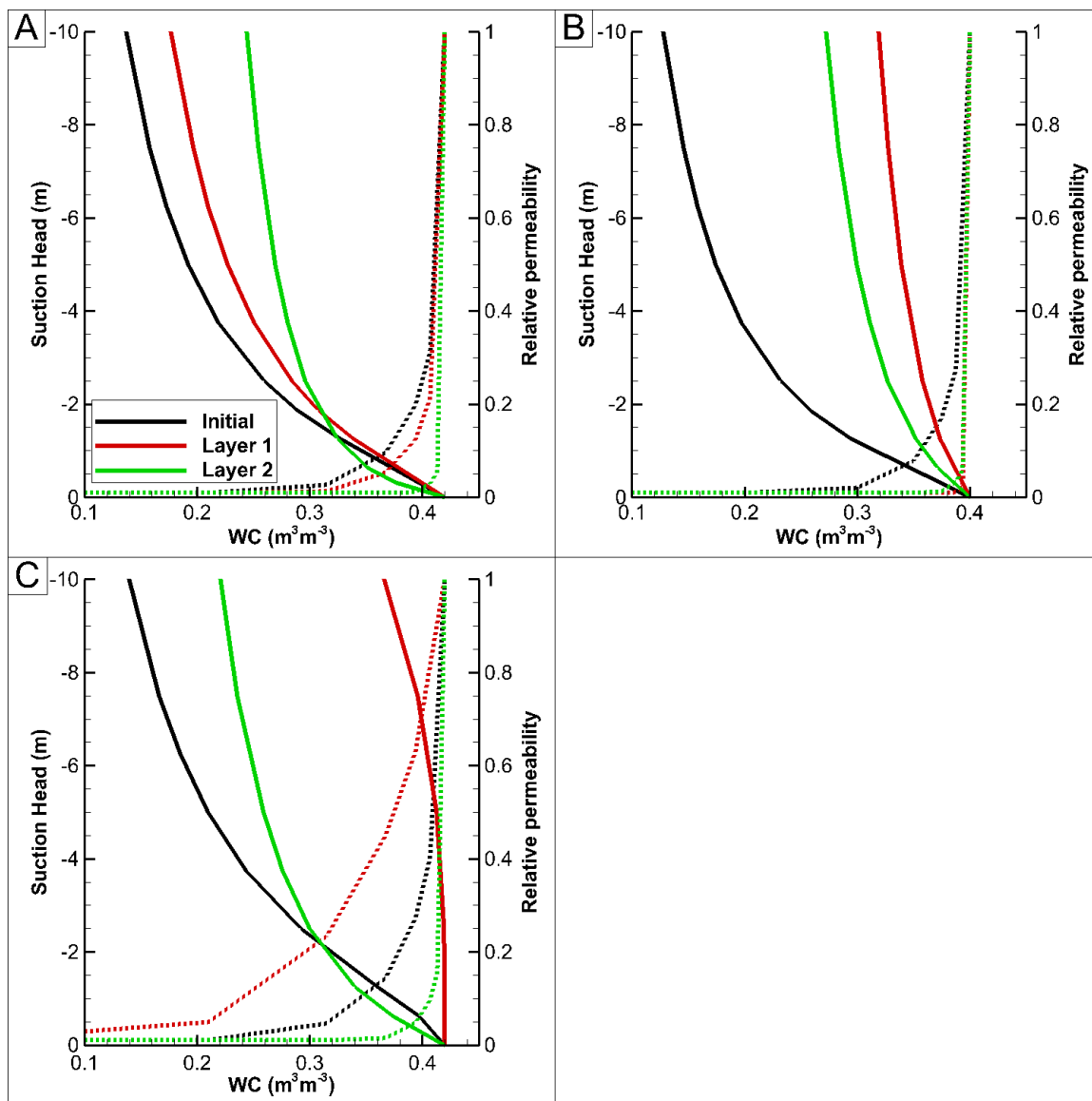
Figure 10.12 Constitutive unsaturated relationships, Eq. [3.2] and Eq. [3.3], water content vs. suction head (solid), water content vs. relative permeability (broken). a) Silty Clay Loam. b) Loam. c) Silt Loam.

Table 10.4 Statistic model evaluation through NSE Eq. [10.3], RSR Eq. [10.4], and PBIAS, Eq. [10.5] for each soil texture class at each measurement depth (5 cm, 10 cm, 20 cm, and 50 cm), and *d*, Eq. [10.2]. Results are depicted as "Calibration (Validation)" for each statistical measure.

| Soil Texture Class	Sensor Depth (cm)	NSE	RSR	PBIAS
Silty Clay Loam	5	0.89 (0.82)	0.34 (0.43)	0.1 (-0.3)
	10	0.47 (0.4)	0.73 (0.78)	5.2 (4.6)
	20	0.78 (0.69)	0.47 (0.56)	1.5 (-0.5)
	50	0.13 (-0.07)	0.93 (1.04)	-2.4 (-3.2)
	d	0.94 (0.54)	0.25 (0.68)	-0.5 (-1.5)
Loam	5	0.78 (0.71)	0.47 (0.54)	-8.4 (-4.2)
	10	0.72 (0.11)	0.53 (0.94)	4.8 (5.6)
	20	0.6 (-0.33)	0.64 (1.15)	-2.9 (-3.9)
	50	-3.68 (-5)	2.16 (2.45)	6.3 (8.7)
	d	0.49 (0.01)	0.72 (1)	2.9 (4.5)
Silt Loam	5	0.98 (0.79)	0.12 (0.45)	0.7 (-1.2)
	10	0.95 (0.88)	0.22 (0.34)	-0.8 (0.5)
	20	0.83 (0.78)	0.41 (0.47)	-4.7 (-1.3)
	50	0.22 (-5.04)	0.88 (2.46)	6.8 (14.1)
	d	0.92 (-0.1)	0.28 (1.05)	3.1 (8.3)

Table 10.5 Statistical model evaluation performance ratings (Moriasi et al. 2007) for NSE Eq. [10.3], RSR Eq. [10.4], and PBIAS Eq. [10.5].

Performance Rating	NSE	RSR	PBIAS
Very Good	> 0.75	< 0.5	< ±10
Good	> 0.65	< 10	< ±15
Satisfactory	> 0.5	< 20	< ±25

<u>10.3 Discussion</u>

In this study, measured rainfall and water content data from the most common agricultural soils were utilized to calibrate and validate soil hydraulic properties in a coupled surface subsurface model. Validation period simulated soil water contents largely resembled the calibration results. The largest errors were magnified over the longer simulation, enabling a better description of parameter adequacy. The silty clay loam calibration produced the best fit, with reasonable results produced for the loam and silt loam type soils. Calibration results generally achieve very good graphical and statistical agreement with observed data, while validated water contents tend towards satisfactory results (Moriasi et al. 2007).

<u>10.3.1 Evaluating the Initial Condition</u>

A better calibration and validation was achieved under wetter conditions, where the soils produced an adequate water content response to rainfall. Validation simulations began at very low water content states, while calibration simulations began at a wetter state. Unsaturated water retention properties were calibrated to allow significantly less water movement when the soil matrix is at less than full saturation (Fig. 10.12). In this study the best simulated results were achieved through a spin up period including at least one significant rainfall event. Fig. 10.8 shows a poor representation of observed water contents in each soil texture over the first five to 15 days, and an improved representation near the end of the evaluated time period. Initialization periods range from days to years (Ajami et al. 2014; De Schepper et al. 2015; Li et al. 2008; Sciuto and Diekkruger 2010), and depend on the stability of subsurface storages. A longer spin up in this situation could yield a closer representation of soil water variability, but would require additional measured data. Initial conditions were not addressed in the study, due to a limited rainfall soil moisture time series, but may offer relief to severe initial errors in drier validation simulations.

10.3.2 Vertical Soil Moisture Movement

The best water content calibrated results consistently occurred at the 5 cm observation depth, with a reduction in fit quality with depth. Simulated water content in calibration and validation results showed the worst performance at the 50 cm depth, noted by NSE values of less than 0.25 for all soil textures. Cornelissen et al. (2013) indicated a similar inability to match short-term soil moisture dynamics at a 50 cm depth, agreeing well with 20 cm, and overestimating 5 cm observations. The two layer approach used in this study, and recommend by Cornelissen et al. (2013), enabled simulations to reproduce surficial soil dynamics. Previous studies have documented the effect of land use on surficial soil properties (Chen et al. 2014). Discrepancies between measured and simulated water contents, particularly at 50 cm, indicated the need to include fast flow effects in simulations (Verbist et al. 2012). Calibration of the silty clay loam soil texture offered the best statistic and graphic agreement to observed data. Through calibration the saturated hydraulic conductivity of layer 2 was increased by more than an order of magnitude. The additional vertical water movement capability produced the best agreement. Calibrated parameters for all soil types offered an ability to capture trends in deeper soil water content variability, but were unable to capture short term fluxes.

10.3.3 Timing of Water Content Response

The results indicated that the timing of soil water content responses were frequently well represented by simulated soil water dynamics. A significant amount of error still occurred in response to rainfall events (Fig. 10.9). Maximums in the relative error (Fig. 10.5) were a function of shifted timing, either a delaying or expediting the vertical movement of simulated soil water. The silty clay loam and loam texture calibrations responded increasingly late to the initial wetting front as observation depth increased. Section 10.2.1 showed an increased ε in coarser resolution models immediately before and after the rainfall event. While some amount of error in calibration

and validation results can be attributed to grid refinement errors, the grid independence study produced a maximum error in the 10 layer model of 3.34%. The tendency was for coarser models to respond more slowly to water content dynamics, similar to the calibrated water contents when compared to simulated results.

Silty clay loam and loam calibrated unsaturated soil parameters tended to reduce vertical movement under less than saturated conditions, as indicated by the saturation relative permeability curve (Fig. 10.12). The slowing effects of calibrated subsurface unsaturated properties increased with depth, and were apparent from the increased time delays reported with depth. Silt loam water content response to precipitation occurred increasingly early with observation depth, up to 50 cm, where it arrived late. The top 5 cm of the silt loam soil texture was calibrated to move water vertically at a more rapid rate under less than saturated conditions, and retain soil water longer (Fig. 10.12). A larger rainfall depth at the silt loam site (71.3 mm) forced the soil column to reach saturation at the 5 cm, 10 cm, and 20 cm depths, a feat the silty clay loam, and loam calibration simulations did not achieve. A relatively steep drop in soil permeability as water content decreased, immobilized water at values less than saturation (Fig. 10.12). The decrease in relative permeability produced a late response by the silty clay loam, and loam calibration simulations. At 50 cm the silt loam soil column did not reach saturation resulting in a delay in peak water content, a similar result to the silty clay loam and loam calibrated responses at each observation depth.

10.3.4 Challenges

HGS calibration and validation performance measures indicated a decrease in the goodness of simulated results with depth, both in absolute soil water content and in timing of response. Added soil stratigraphy could offer better calibrated results, but the additional calibration parameters increase the potential to over parameterize the model

(Verbist et al. 2012). Additional soil sampling to obtain site specific stratigraphic details and appropriate parameter ranges would simplify the parameter estimation procedure.

Fast flow pathways were apparent in observed data via a rapid response to rainfall at the 20 cm and 50 cm observation depths. Preferential flow paths created by vegetation or soil cracking offer a vertical pathway that allows water to enter the subsurface bypassing the soil matrix (Chen et al. 2014; Cornelissen et al. 2013; Verbist et al. 2012; Vrugt et al. 2004). The effects of macropores were not directly taken into account in these simulations. Cornelissen et al. (2013) indicated the inability to simulate deeper observations, as vegetation offered flow routes bypassing the soil column, allowing a more rapid response to precipitation. Measured suction head (Chen et al. 2014), or near surface groundwater variability to rainfall events offer additional calibration targets to better estimate a soil's fast flow response to precipitation. Preferential flow paths were more appropriately described by a dual continuum (Gerke and Vangenuchten 1993). Dual continuum models often become numerically and computationally cumbersome. This resulting calibration produced effective parameters, which attempt to indirectly incorporate the fast flow effects, but without added subsurface information below 50 cm (Verbist et al. 2012), the problem becomes ill posed.

The calibration time period was selected during a relatively low PET period, after the growing season, to avoid potential variability in vegetation parameters. Validation overlapped with the end of the growing season, where PET increased, and the actual evapotranspiration was expected to significantly increase. Vegetation parameter variability was not incorporated in this study, and the lack of transpiration variability may affect water content simulations (Chen et al. 2014). Additional investigation into vegetation parameter and PET variability both daily and seasonally could prove valuable in describing model sinks appropriately.

This study utilized limited input data for the ROSSETTA pedotransfer function to estimate initial water retention parameters. Schaap et al. (2001) showed that as input data

was extended to include bulk density, along with water retention points, the error in associated water retention curves significantly reduce. Additional SURRGO near surface stratigraphic inputs, along with site specific measured hydraulic parameters could yield better PEST initial estimated parameters, bounds on parameters, and identify insensitive soil retention parameters.

10.3.5 Future Direction

Results from the calibration and validation of the three most common soil types in an agriculture dominated landscape agree well with previously studies (Chen et al. 2014; Cornelissen et al. 2013; Pfletschinger et al. 2014; Verbist et al. 2012). In recent years the addition of vadose zone water content dynamics to surface hydrologic modeling has become more common (Cornelissen et al. 2013; De Schepper et al. 2015; Goderniaux et al. 2011; Jones et al. 2008; Kollet et al. 2010; Pfletschinger et al. 2014; Rozemeijer et al. 2010; Sciuto and Diekkruger 2010). Application of calibrated properties, from this study, can readily be applied to large scale surface subsurface hydrologic simulations. This study offers additional information on the amount and timing of error incurred numerically and via parameter estimates. Future work is focused on expanding the network of RGSM platforms and collocated shallow groundwater wells across Iowa to increase knowledge of vadose zone dynamics across the state. The increase in information will allow researchers to further study column, field, and watershed scale soil moisture dynamics.

10.4 Summary of Findings

In this study, input soil hydraulic parameters for a coupled surface-subsurface hydrologic one-dimensional model were calibrated and validated with an automated parameter estimation software. Measured soil water content and rainfall events in late 2014 were used to calibrate a single event and validate over a series of events. Calibrated results produced good agreement for each soil texture, though statistic and graphic

measures (Moriasi et al. 2007). Near surface soil water dynamics were better represented than deeper soil water movement. Validation results mimicked the tendencies of the calibration results, reproducing near surface soil water variability very well and worsening with depth. Dry initial conditions, preferential flow, soil stratigraphy, and transpiration parameter variability offer future directions for this column study. The promising calibrated parameters are able to be applied to larger scale simulations to investigate spring and late fall flooding, while more investigation on summer month dynamics are needed. This work offers a direction for additional research into coupled near surface dynamics, while identifying immediately applicable soil water retention parameters and associated errors for the most common central U.S. soil textures.

11.0 SUMMARY AND CONCULSIONS

Heavy precipitation and subsequent flooding in the summer of 2008 brought economic, social, and environmental impacts to the people and communities of Iowa. In the wake the 2008 event, the IWP was funded. Its objective was to plan, implement, and evaluate distributed flood mitigation strategies to lessen the severity and frequency of flooding in Iowa. This research included and expanded on Phase II of the IWP project, discussed in Section 1.1.

A coupled surface-subsurface hydrologic model was constructed to investigate the impacts of flood mitigation projects through the HGS numerical platform. A 3-D numerical mesh was the product of relevant surface flow features, surface-subsurface coupling requirements, tile drainage incorporation, and production of baseflow. The surface and subsurface numerical elements were populated with the most relevant spatially variable parameters, sufficiently representing the BCW. The constructed hydrologic model was validated for water balance components over an annual integration, adequately reflecting published data.

This research systematically analyzed the influence of antecedent soil wetness, rainfall depth, and the subsequent impact on peak flows. Peak flows increased with increasing antecedent wetness and rainfall depth, with the highest peak flows occurring under intense precipitation on wet soils. Flood mitigation structures were included and investigated under full and empty initial storage conditions. Peak flows were reduced at the outlet of BCW by 3 % to 17 %. The highest peak flow reductions occurred in scenarios with dry soil, empty project storage, and low rainfall depths. Peak flows were identified to follow a power law scale invariance, fit through log-log least squares regression. The results of this analysis extended the reductions in peak flow beyond the drainage area associated with the BCW. Typically, peak flows were no longer impacted at a drainage area greater than 200 km^2, or roughly 2 km downstream of the BCW outlet.

Peak flow reductions varied with the area upstream of a project, with increased area upstream of a project producing higher peak discharge reductions. Peak flow reductions were scaled to the Upper Cedar River watershed. This study assumed the BCW was representative of projects design, drainage area, and cost. The Upper Cedar River watershed would require approximately 1,000 projects at a cost of greater than $200 million to achieve a similar level of peak flow reductions to that of the BCW.

The construction of a detailed hydrologic model in the BCW offered the capability to investigate a number of other features unique to agricultural systems. A similar methodology was applied to investigate pattern tile drainage, and variable density terraces. These practices were unable to be explicitly represented at the watershed scale as they require a significant increase in numerical resolution to adequately simulate. Instead, a conceptual representation of each physical system was represented in numerical simulations through a parameter adjustment. Tile drainage was represented as an increased conductivity porous medium layer under the entire watershed subsurface. Terraces were represented as an increased surface roughness, varying based on the density of the terrace system. In each case, PEST was applied at the field scale calibrating the representative equivalent parameters. This resulted in an explicit representation of each practice, applicable to watershed scale simulations.

The tile drainage contribution to stream flow (Q_T/Q) was derived from a tracer driven analysis of instream surface water. Q_T/Q varied instantaneously from 6% to 71 % at the basin outlet, with tile flow correlating linearly with total stream flow. In low precipitation periods 62 % of stream flow traveled through the tile system. In heavy precipitation periods a dilution effect shifted Q_T/Q to 27 %. Precipitation driven events produced a strong positive logarithmic correlation between Q_T/Q and drainage area. The addition of precipitation into the system saturated near surface soils, increased lateral soil water movement, and diluted the relatively stable instream tile flow. A negative logarithmic trend in Q_T/Q to drainage area persisted in non-event durations. Larger

groundwater (non-tile) contribution to stream flow at the outlet diluted instream tile flow at increased drainage areas. Logarithmic regression slopes were consistent for event and non-event periods, respectively. While, the intercept responded in a predicable manner to precipitation intensity. This study, indicates a strong systematic response of Q_T/Q to meteorological forcing, drainage area over a single year.

The stream flow and infiltration variability due to terrace implementation was numerically investigated in nested catchments. Terraces reduced and delayed peak flows in each of the less than 3 km^2 subcatchments. Event hydrographs were shifted in time, responding to rainfall later than non-terraced scenarios, while retaining the total volumetric outflow over longer time periods. Subcatchment scale results reciprocated the calibration scenarios well, reducing and delaying the hydrograph. To achieve watershed wide impacts an alteration to the infiltration capability at the field scale was required, but not achieved. The effects of subcatchment results were dampened by a subsurface driven system, with a high a priori infiltration capacity. Future work would do well to incorporate infiltration as a PEST calibration target.

This work benefited from highly distributed models offering significantly increased sampling frequency in time and space. Most studies investigate tile impacts at the field scale, or terrace and flood mitigation projects though watershed wide conceptual simulations. This study was able to represent the same temporal patterns observed in literature. It expanded the understanding of metrological forcing on various agricultural practices, and the subsequent impacts on stream flow and near surface processes. It further assembled a framework to analyze a system at the field scale for implementation at the watershed scale. It showed large scale simulations reproduce field scale results well. This procedure can be reasonably extrapolated to other distributed water conservation practices.

As a direction of future work, this research introduced the idea of calibration and validation of watershed scale models to numerical column experiments. Where field

measured rainfall and soil water content data were utilized to estimate soil hydraulic property values. The soil properties were validated to measured data, reasonably representing water content dynamics visually and statistically. The calibration software PEST and HGS were applied to calibrate and validate soil column experiments for application at the watershed scale.

The BCW and this modeling platform was idealized as a numerical experiment to investigate flood mitigation, and agricultural practices in Iowa. This was realized through each chapter, and the associated accumulation of future research directions. Through the IWP and this research the state of Iowa, its decision makers, and its people have a better understanding of the impacts of various structural measures commonly implemented across Iowan landscapes. Further, the knowledge of flooding, and the costs of flood mitigation were thoroughly investigated. The IWP built $5.1 million in practices across the state, although this is a fraction of the investment required to properly protect the states people and infrastructure. This project holds as a pilot, the first of its kind, influencing not only the people of Iowa, but the direction of flood mitigation and investigation throughout the US.

REFERENCES

Abdul, A. S. (1985). "Experimental and Numerical studies of the effect of the capillary fringe on streamflow generation." Ph. D., University of Waterloo, Waterloo, Canada.

Ajami, H., Evans, J. P., McCabe, G. J., and Stisen, S. (2014). "Technical Note: Reducing the spin-up time of integrated surface water–groundwater models." *Hydrol Earth Syst Sc*, 18.

Ajami, H., McCabe, M. F., and Evans, J. P. (2015). "Impacts of model initialization on an integrated surface water–groundwater model." *Hydrol Process*.

Ajami, H., McCabe, M. F., Evans, J. P., and Stisen, S. (2014). "Assessing the impact of model spin-up on surface water-groundwater interactions using an integrated hydrologic model." *Water Resour Res*, 50(3), 2636-2656.

Ala-Aho, P., Rossi, P. M., Isokangas, E., and Klove, B. (2015). "Fully integrated surface-subsurface flow modelling of groundwater-lake interaction in an esker aquifer: Model verification with stable isotopes and airborne thermal imaging." *J Hydrol*, 522, 391-406.

Algoazany, A. S., Kalita, P. K., Czapar, G. F., and Mitchell, J. K. (2007). "Phosphorus transport through subsurface drainage and surface runoff from a flat watershed in east central Illinois, USA." *J Environ Qual*, 36(3), 681-693.

Allen, R. G., Smith, M., Perrier, A., and Pereira, L. S. (1998). "Crop Evapotranspiration—Guidelines for Computing Crop Water Requirements." *Irrigation and Drainage Paper no. 56*, FAO, Rome, Italy.

Andoh, R. Y. G., and Declerck, C. (1997). "A cost effective approach to stormwater management? Source control and distributed storage." *Water Sci Technol*, 36(8-9), 307-311.

Arabi, M., Frankenberger, J. R., Enge, B. A., and Arnold, J. G. (2008). "Representation of agricultural conservation practices with SWAT." *Hydrol Process*, 22(16), 3042-3055.

Ayalew, T. B., Krajewski, W. F., and Mantilla, R. (2013). "Exploring the Effect of Reservoir Storage on Peak Discharge Frequency." *J Hydrol Eng*, 18(12), 1697-1708.

Ayalew, T. B., Krajewski, W. F., and Mantilla, R. (2014). "Connecting the power-law scaling structure of peak-discharges to spatially variable rainfall and catchment physical properties." *Adv Water Resour*, 71, 32-43.

Ayalew, T. B., Krajewski, W. F., and Mantilla, R. (2015). "Analyzing the effects of excess rainfall properties on the scaling structure of peak discharges: Insights from a mesoscale river basin." *Water Resour Res*, 51(6), 3900-3921.

Ayalew, T. B., Krajewski, W. F., Mantilla, R., and Small, S. J. (2014). "Exploring the effects of hillslope-channel link dynamics and excess rainfall properties on the scaling structure of peak-discharge." *Adv Water Resour*, 64, 9-20.

Azevedo, A. S., Kanwar, R. S., and Horton, R. (1998). "Effect of cultivation on hydraulic properties of an Iowa soil using tension infiltrometers." *Soil Sci*, 163(1), 22-29.

Babbar-Sebens, M., Barr, R. C., Tedesco, L. P., and Anderson, M. (2013). "Spatial identification and optimization of upland wetlands in agricultural watersheds." *Ecol Eng*, 52, 130-142.

Bakhsh, A., Hatfield, J. L., Kanwar, R. S., Ma, L., and Ahuja, L. R. (2004). "Simulating nitrate drainage losses from a Walnut Creek watershed field." *J Environ Qual*, 33(1), 114-123.

Baryla, A., and Pierzgalski, E. (2008). "Ridged terraces - Functions, construction and use." *J Environ Eng Landsc*, 16(2).

Beard, J. B. (2001). "Turfgrass Root Basics." *TURFAX*, 9(3), 5-7.

Berthet, L., Andreassian, V., Perrin, C., and Javelle, P. (2009). "How crucial is it to account for the antecedent moisture conditions in flood forecasting? Comparison of event-based and continuous approaches on 178 catchments." *Hydrol Earth Syst Sc*, 13(6), 819-831.

Blann, K. L., Anderson, J. L., Sands, G. R., and Vondracek, B. (2009). "Effects of Agricultural Drainage on Aquatic Ecosystems: A Review." *Crit Rev Env Sci Tec*, 39(11), 909-1001.

Blessent, D., Jorgensen, P. R., and Therrien, R. (2014). "Comparing Discrete Fracture and Continuum Models to Predict Contaminant Transport in Fractured Porous Media." *Ground Water*, 52(1), 84-95.

Bracmort, K. S., Arabi, M., Frankenberger, J. R., Engel, B. A., and Arnold, J. G. (2006). "Modeling long-term water quality impact of structural BMPs." *T Asabe*, 49(2), 367-374.

Bradley, A. A. (2014). "Potential Evapotranspiration at Charles City." N. W. Thomas, ed.

Bradley, A. A., and Potter, K. W. (1992). "Flood Frequency-Analysis of Simulated Flows." *Water Resour Res*, 28(9), 2375-2385.

Breuer, L., Eckhardt, K., and Frede, H. G. (2003). "Plant parameter values for models in temperate climates." *Ecol Model*, 169(2-3), 237-293.

Brocca, L., Melone, F., and Moramarco, T. (2008). "On the estimation of antecedent wetness conditions in rainfall-runoff modelling." *Hydrol Process*, 22(5), 629-642.

Bronstert, A., and Bardossy, A. (1999). "The role of spatial variability of soil moisture for modelling surface runoff generation at the small catchment scale." *Hydrol Earth Syst Sc*, 3(4), 505-516.

Brookfield, A. E., Sudicky, E. A., Park, Y. J., and Conant, B. (2009). "Thermal transport modelling in a fully integrated surface/subsurface framework." *Hydrol Process*, 23(15), 2150-2164.

Camici, S., Tarpanelli, A., Brocca, L., Melone, F., and Moramarco, T. (2011). "Design soil moisture estimation by comparing continuous and storm-based rainfall-runoff modeling." *Water Resour Res*, 47.

Cammeraat, E. L. H. (2004). "Scale dependent thresholds in hydrological and erosion response of a semi-arid catchment in southeast Spain." *Agr Ecosyst Environ*, 104(2), 317-332.

Carlier, J. P., Kao, C., and Ginzburg, I. (2007). "Field-scale modeling of subsurface tile-drained soils using an equivalent-medium approach." *J Hydrol*, 341(1-2), 105-115.

Carluer, N., and De Marsily, G. (2004). "Assessment and modelling of the influence of man-made networks on the hydrology of a small watershed: implications for fast flow components, water quality and landscape management." *J Hydrol*, 285(1-4), 76-95.

Castillo, V. M., Gomez-Plaza, A., and Martinez-Mena, M. (2003). "The role of antecedent soil water content in the runoff response of semiarid catchments: a simulation approach." *J Hydrol*, 284(1-4), 114-130.

Chen, M., Willgoose, G. R., and Saco, P. M. (2014). "Spatial prediction of temporal soil moisture dynamics using HYDRUS-1D." *Hydrol Process*, 28(2), 171-185.

Chow, L., Rees, H., and Xing, Z. (2010). "Impacts of long-term intensive potato production and conservation terraces/grassed waterway on runoff hydrology and soil quality." *2010 19th World Congress of Soil Science, Soil Solutions for a Changing World* Brisbane, Australia.

Chow, T. L., Rees, H. W., and Daigle, J. L. (1999). "Effectiveness of terraces/grassed waterway systems for soil and water conservation: A field evaluation." *J Soil Water Conserv*, 54(3), 577-583.

Chow, V. T. (1959). *Open-channel hydraulics*, McGraw-Hill, New York.

Cornelissen, T., Diekkruger, B., and Bogena, H. (2013). "Using HydroGeoSphere in a forested catchment: How does spatial resolution influence the simulation of spatio-temporal soil moisture variability?" *Procedia Environ Sci*, 19, 198-207.

Culley, J. L. B., and Bolton, E. F. (1983). "Suspended-Solids and Phosphorus Loads from a Clay Soil .2. Watershed Study." *J Environ Qual*, 12(4), 498-503.

De Michele, C., and Salvadori, G. (2002). "On the derived flood frequency distribution: analytical formulation and the influence of antecedent soil moisture condition." *J Hydrol*, 262(1-4), 245-258.

De Schepper, G., Therrien, R., Refsgaard, J. C., and Hansen, A. L. (2015). "Simulating coupled surface and subsurface water flow in a tile-drained agricultural catchment." *J Hydrol*, 521, 374-388.

Del Giudice, G., Rasulo, G., Siciliano, D., and Padulano, R. (2014). "Combined Effects of Parallel and Series Detention Basins for Flood Peak Reduction." *Water Resour Manag*, 28(10), 3193-3205.

Descroix, L., Nouvelot, J. F., and Vauclin, M. (2002). "Evaluation of an antecedent precipitation index to model runoff yield in the western Sierra Madre (North-west Mexico)." *J Hydrol*, 263(1-4), 114-130.

Doherty, J. (2010). *PEST: Model-Independent Parameter Estimation*, Watermark Numerical Computing, Brisbane, Australia.

Downer, C. W., and Ogden, F. L. (2004). "Appropriate vertical discretization of Richards' equation for two-dimensional watershed-scale modelling." *Hydrol Process*, 18(1), 1-22.

Dueri, S., and Therrien, R. (2003). "Factors controlling contaminant transport through the flood sediments of the Saguenay Fjord: Numerical sensitivity analysis." *Am Soc Test Mater*, 1442, 167-182.

Dumbrovsky, M., Sobotkova, V., Sarapatka, B., Chlubna, L., and Vachalova, R. (2014). "Cost-effectiveness evaluation of model design variants of broad-base terrace in soil erosion control." *Ecol Eng*, 68, 260-269.

Dunne, T., and Black, R. D. (1970). "An Experimental Investigation of Runoff Production in Permeable Soils." *Water Resour Res*, 6(2), 478-&.

Eash, D. A., Barnes, K. K., and Veilleux, A. G. (2013). "Methods for Estimating Annual Exceedance-Probability Discharges for Streams in Iowa, Based on Data through Water Year 2010." USGS, ed.

Eastman, M., Gollamudi, A., Stampfli, N., Madramootoo, C. A., and Sarangi, A. (2010). "Comparative evaluation of phosphorus losses from subsurface and naturally drained agricultural fields in the Pike River watershed of Quebec, Canada." *Agr Water Manage*, 97(5), 596-604.

Ebel, B. A., and Loague, K. (2006). "Physics-based hydrologic-response simulation: Seeing through the fog of equifinality." *Hydrol Process*, 20(13), 2887-2900.

Ebel, B. A., Mirus, B. B., Heppner, C. S., VanderKwaak, J. E., and Loague, K. (2009). "First-order exchange coefficient coupling for simulating surface water-groundwater interactions: parameter sensitivity and consistency with a physics-based approach." *Hydrol Process*, 23(13), 1949-1959.

Eidem, J. M., Simpkins, W. W., and Burkart, M. R. (1999). "Geology, groundwater flow, and water quality in the Walnut Creek watershed." *J Environ Qual*, 28(1), 60-69.

Emerson, C. H., and Traver, R. G. (2008). "Multiyear and seasonal variation of infiltration from storm-water best management practices." *J Irrig Drain E-Asce*, 134(5), 598-605.

Emerson, C. H., Welty, C., and Traver, R. G. (2005). "Watershed-scale evaluation of a system of storm water detention basins." *J Hydrol Eng*, 10(3), 237-242.

Fang, H. L., Liang, S. L., Townshend, J. R., and Dickinson, R. E. (2008). "Spatially and temporally continuous LAI data sets based on an integrated filtering method: Examples from North America." *Remote Sens Environ*, 112(1), 75-93.

Fenton, T. E., Kazemi, M., and Lauterbach-Barrett, M. A. (2005). "Erosional impact on organic matter content and productivity of selected Iowa soils." *Soil Till Res*, 81(2), 163-171.

Freeze, R. A., and Harlan, R. L. (1969). "Blueprint for a physically-based digitally simulated, hydrologic response model." *Journal of Hydrology*, 9, 237-258.

Frei, S., and Fleckenstein, J. H. (2014). "Representing effects of micro-topography on runoff generation and sub-surface flow patterns by using superficial rill/depression storage height variations." *Environ Modell Softw*, 52, 5-18.

FSA, F. S. A. (2013). "Common Land Unit." U. S. D. o. A. USDA, ed., Natural Resources Geographic Information Systems Library.

Furey, P. R., and Gupta, V. K. (2005). "Effects of excess rainfall on the temporal variability of observed peak-discharge power laws." *Adv Water Resour*, 28(11), 1240-1253.

Furey, P. R., and Gupta, V. K. (2007). "Diagnosing peak-discharge power laws observed in rainfall-runoff events in Goodwin Creek experimental watershed." *Adv Water Resour*, 30(11), 2387-2399.

Gallart, F., Llorens, P., and Latron, J. (1994). "Studying the Role of Old Agricultural Terraces on Runoff Generation in a Small Mediterranean Mountainous Basin." *J Hydrol*, 159(1-4), 291-303.

Gatot, I., Perez, P., and Duchesne, J. (2001). "Modelling the influence of irrigated terraces on the hydrological response of a small basin." *Environ Modell Softw*, 16(1), 31-36.

Gerke, H. H., and Vangenuchten, M. T. (1993). "A Dual-Porosity Model for Simulating the Preferential Movement of Water and Solutes in Structured Porous-Media." *Water Resour Res*, 29(2), 305-319.

Goderniaux, P., Brouyere, S., Blenkinsop, S., Burton, A., Fowler, H. J., Orban, P., and Dassargues, A. (2011). "Modeling climate change impacts on groundwater resources using transient stochastic climatic scenarios." *Water Resour Res*, 47.

Goderniaux, P., Brouyere, S., Fowler, H. J., Blenkinsop, S., Therrien, R., Orban, P., and Dassargues, A. (2009). "Large scale surface-subsurface hydrological model to assess climate change impacts on groundwater reserves." *J Hydrol*, 373(1-2), 122-138.

Graf, T., and Boufadel, M. C. (2011). "Effect of viscosity, capillarity and grid spacing on thermal variable-density flow." *J Hydrol*, 400(1-2), 41-57.

Graf, T., and Simmons, C. T. (2009). "Variable-density groundwater flow and solute transport in fractured rock: Applicability of the Tang et al. [1981] analytical solution." *Water Resour Res*, 45.

Graf, T., and Therrien, R. (2007). "Variable-density groundwater flow and solute transport in irregular 2D fracture networks." *Adv Water Resour*, 30(3), 455-468.

Graf, T., and Therrien, R. (2008). "Coupled thermohaline groundwater flow and single-species reactive solute transport in fractured porous media (vol 30, pg 742, 2007)." *Adv Water Resour*, 31(12), 1765-1765.

Graf, T., and Therrien, R. (2008). "A test case for the simulation of three-dimensional variable-density flow and solute transport in discretely-fractured porous media." *Adv Water Resour*, 31(10), 1352-1363.

Grayson, R. B., Western, A. W., Chiew, F. H. S., and Bloschl, G. (1997). "Preferred states in spatial soil moisture patterns: Local and nonlocal controls." *Water Resour Res*, 33(12), 2897-2908.

Grigg, N. S. (2014). "The 2011-2012 drought in the United States: new lessons from a record event." *Int J Water Resour D*, 30(2), 183-199.

Guibas, L., and Stolfi, J. (1985). "Primitives for the Manipulation of General Subdivisions and the Computation of Voronoi Diagrams." *Acm T Graphic*, 4(2), 74-123.

Gupta, V. K., Castro, S. L., and Over, T. M. (1996). "On scaling exponents of spatial peak flows from rainfall and river network geometry." *J Hydrol*, 187(1-2), 81-104.

Gupta, V. K., Mantilla, R., Troutman, B. M., Dawdy, D., and Krajewski, W. F. (2010). "Generalizing a nonlinear geophysical flood theory to medium-sized river networks." *Geophys Res Lett*, 37.

Haga, H., Matsumoto, Y., Matsutani, J., Fujita, M., Nishida, K., and Sakamoto, Y. (2005). "Flow paths, rainfall properties, and antecedent soil moisture controlling lags to peak discharge in a granitic unchanneled catchment." *Water Resour Res*, 41(12).

Haitjema, H. M. (1995). "On the Residence Time Distribution in Idealized Groundwatersheds." *J Hydrol*, 172(1-4), 127-146.

Hamel, P., Daly, E., and Fletcher, T. D. (2013). "Source-control stormwater management for mitigating the impacts of urbanisation on baseflow: A review." *J Hydrol*, 485, 201-211.

Hancock, G. S., Holley, J. W., and Chambers, R. M. (2010). "A Field-Based Evaluation of Wet Retention Ponds: How Effective Are Ponds at Water Quantity Control?" *J Am Water Resour As*, 46(6), 1145-1158.

Hansen, A. L., Refsgaard, J. C., Christensen, B. S. B., and Jensen, K. H. (2013). "Importance of including small-scale tile drain discharge in the calibration of a coupled groundwater-surface water catchment model." *Water Resour Res*, 49(1), 585-603.

Heggen, R. J. (2001). "Normalized antecedent precipitation index." *J Hydrol Eng*, 6(5), 377-381.

Heppner, C. S., Ran, Q. H., VanderKwaak, J. E., and Loague, K. (2006). "Adding sediment transport to the integrated hydrology model (InHM): Development and testing." *Adv Water Resour*, 29(6), 930-943.

Hewlett, J. D., Fortson, J. C., and Cunningham, G. B. (1984). "Additional Tests on the Effect of Rainfall Intensity on Storm Flow and Peak Flow from Wild-Land Basins." *Water Resour Res*, 20(7), 985-989.

Hirt, U., Wetzig, A., Amatya, M. D., and Matranga, M. (2011). "Impact of Seasonality on Artificial Drainage Discharge under Temperate Climate Conditions." *Int Rev Hydrobiol*, 96(5), 561-577.

Hofer, M., Lehmann, P., Biemelt, D., Stahli, M., and Krafczyk, M. (2011). "Modelling subsurface drainage pathways in an artificial catchment." *Phys Chem Earth*, 36(1-4), 101-112.

HPRCC, H. P. R. C. C. (2015). "Crop Coefficients for Corn."

Huff, F., and Angel, J. (1992). "Rainfall Frequency Atlas of the Midwest." Midwest Climate Center.

Hultquist, J. M., and Best, L. B. (2001). "Bird use of terraces in Iowa rowcrop fields." *Am Midl Nat*, 145(2), 275-287.

Hutchinson, K., Christiansen, D., Geological Survey (U.S.), and Iowa. Department of Natural Resources (2013). *Use of the Soil and Water Assessment Tool (SWAT) for simulating hydrology and water quality in the Cedar River Basin, Iowa, 2000-10*.

IDALS, I. D. o. A. a. L. S. (2013). "IOWA NUTRIENT REDUCTION STRATEGY A science and technology--based framework to assess and reduce nutrients to Iowa waters and the Guld of Mexico."

IDNR, I. D. o. N. R. (2015). "Natural Resources Geographic Information Systems." IDNR, Iowa Department of Natural Resources.

IFC, I. F. C. (2014). "Hydrologic Assesment of the Upper Cedar River Watershed." *Technical Report*, IIHR - Hydroscience & Engineering.

IFC, I. F. C. (2014). "Hydrologic Assessment of the Upper Cedar River Watershed." *IIHR Technical Report*, I.-H. Engineering, ed., The University of Iowa, Iowa City, Iowa.

IGS, I. G. S. (2015). "GeoSam." The University of Iowa.

IGS, I. G. S., and IDNR, I. D. o. N. R. (2008). "Soils Requiring Tile Drainage for Full Productivity." IGS, Iowa Geologic Survey;
IDNR, Iowa Department of Natural Resources;, https://programs.iowadnr.gov/nrgislibx/.

IGWS, I. G. a. W. S. (2010). "One meter digital elevation model of Iowa." I. D. o. N. R. IDNR, ed., Natural Resources Geographic Information Systems Library.

ISU, I. S. U. (2015). "ISU AgClimate Network." ISU, Iowa State Univerisyt, Iowa State University Mesonet.

James, A. L., and Roulet, N. T. (2007). "Investigating hydrologic connectivity and its association with threshold change in runoff response in a temperate forested watershed." *Hydrol Process*, 21(25), 3391-3408.

Jaynes, D. B., Colvin, T. S., Karlen, D. L., Cambardella, C. A., and Meek, D. W. (2001). "Nitrate loss in subsurface drainage as affected by nitrogen fertilizer rate." *J Environ Qual*, 30(4), 1305-1314.

Johnson, B. L. (1995). "Assessment of the fate and transport of nitrate in groundwater within the Walnut Creek watershed." M.S., Iowa State University, Ames, IA.

Jones, J. P., Sudicky, E. A., Brookfield, A. E., and Park, Y. J. (2006). "An assessment of the tracer-based approach to quantifying groundwater contributions to streamflow." *Water Resour Res*, 42(2).

Jones, J. P., Sudicky, E. A., and McLaren, R. G. (2008). "Application of a fully-integrated surface-subsurface flow model at the watershed-scale: A case study." *Water Resour Res*, 44(3).

Kang, S. Z., Gu, B. J., Du, T. S., and Zhang, J. H. (2003). "Crop coefficient and ratio of transpiration to evapotranspiration of winter wheat and maize in a semi-humid region." *Agr Water Manage*, 59(3), 239-254.

Karlen, D. L., Kramer, L. A., James, D. E., Buhler, D. D., Moorman, T. B., and Burkart, M. R. (1999). "Field-scale watershed evaluations on deep-loess soils: I. Topography and agronomic practices." *J Soil Water Conserv*, 54(4), 693-704.

Kiesel, J., Fohrer, N., Schmalz, B., and White, M. J. (2010). "Incorporating landscape depressions and tile drainages of a northern German lowland catchment into a semi-distributed model." *Hydrol Process*, 24(11), 1472-1486.

Kim, S.-H., Hong, S. Y., Sudduth, K. A., Kim, Y., and Lee, K. (2012). "Comparing LAI Estimates of Corn and Soybean from Vegetation Indices of Multi-resolution Satellite Images." *Korean Journal of Remote Sensing*, 28(6), 597-609.

King, K. W., Fausey, N. R., and Williams, M. R. (2014). "Effect of subsurface drainage on streamflow in an agricultural headwater watershed." *J Hydrol*, 519, 438-445.

Kladivko, E. J., Frankenberger, J. R., Jaynes, D. B., Meek, D. W., Jenkinson, B. J., and Fausey, N. R. (2004). "Nitrate leaching to subsurface drains as affected by drain spacing and changes in crop production system." *J Environ Qual*, 33(5), 1803-1813.

Kladivko, E. J., Vanscoyoc, G. E., Monke, E. J., Oates, K. M., and Pask, W. (1991). "Pesticide and Nutrient Movement into Subsurface Tile Drains on a Silt Loam Soil in Indiana." *J Environ Qual*, 20(1), 264-270.

Kollet, S. J., and Maxwell, R. M. (2008). "Capturing the influence of groundwater dynamics on land surface processes using an integrated, distributed watershed model." *Water Resour Res*, 44(2).

Kollet, S. J., Maxwell, R. M., Woodward, C. S., Smith, S., Vanderborght, J., Vereecken, H., and Simmer, C. (2010). "Proof of concept of regional scale hydrologic simulations at hydrologic resolution utilizing massively parallel computer resources." *Water Resour Res*, 46.

Kramer, L. A., Burkart, M. R., Meek, D. W., Jaquis, R. J., and James, D. E. (1999). "Field-scale watershed evaluations on deep-loess soils: II. Hydrologic responses to different agricultural land management systems." *J Soil Water Conserv*, 54(4), 705-710.

Kristensen, K. J., and Jensen, S. E. (1975). "A model for estimating actual evapotranspiration from potential evapotranspiration." *Nordic Hydrology*, 6(3), 170-188.

Kurz, B. A., Wang, X., Silva, L. d., Hanson, S. K., Kurz, M. D., Peck, W. D., Simonsen, T. K., and Steadman, E. N. (2007). "An Evaluation of Basinwide Distributed Storage in the Red River Basin: The Waffle Concept." Energy & Environmental Research Center, University of North Dakota.

Laloy, E., and Bielders, C. L. (2009). "Modelling intercrop management impact on runoff and erosion in a continuous maize cropping system: Part I. Model description, global sensitivity analysis and Bayesian estimation of parameter identifiability." *Eur J Soil Sci*, 60(6), 1005-1021.

Levy, B., and McCuen, R. (1999). "Assessment of Storm Duration for Hydrologic Design." *J Hydrol Eng*, 4(3), 209-213.

Li, Q., Unger, A. J. A., Sudicky, E. A., Kassenaar, D., and Wexler, E. J. (2008). "Simulating the multi-seasonal response of a large-scale watershed with a 3D physically-based hydrologic model." *Journal of Hydrology*, 317-336.

Li, Q., Unger, A. J. A., Sudicky, E. A., Kassenaar, D., Wexler, E. J., and Shikaze, S. (2008). "Simulating the multi-seasonal response of a large-scale watershed with a 3D physically-based hydrologic model." *J Hydrol*, 357(3-4), 317-336.

Lo, M. H., and Famiglietti, J. S. (2010). "Effect of water table dynamics on land surface hydrologic memory." *J Geophys Res-Atmos*, 115.

Loague, K., and Vanderkwaak, J. E. (2002). "Simulating hydrological response for the R-5 catchment: comparison of two models and the impact of the roads." *Hydrol Process*, 16(5), 1015-1032.

Logan, T. J., Randall, G. W., and Timmons, D. R. (1980). "Nutrient Content of Tile Drainage from Cropland in the North Central Region." *Ohio Ardc Res Bull*(1119), 1-16.

Macrae, M. L., English, M. C., Schiff, S. L., and Stone, M. (2007). "Intra-annual variability in the contribution of tile drains to basin discharge and phosphorus export in a first-order agricultural catchment." *Agr Water Manage*, 92(3), 171-182.

Magner, J. A., Payne, G. A., and Steffen, L. J. (2004). "Drainage effects on stream nitrate-N and hydrology in south-central Minnesota (USA)." *Environ Monit Assess*, 91(1-3), 183-198.

Maidment, D. R. (1993). *Handbook of Hydrology*, McGraw-Hill, Inc.

Mandapaka, P. V., Krajewski, W. F., Mantilla, R., and Gupta, V. K. (2009). "Dissecting the effect of rainfall variability on the statistical structure of peak flows." *Adv Water Resour*, 32(10), 1508-1525.

Mantilla, R., Gupta, V. K., and Mesa, O. J. (2006). "Role of coupled flow dynamics and real network structures on Hortonian scaling of peak flows." *J Hydrol*, 322(1-4), 155-167.

Mattocks, C., and Forbes, C. (2008). "A real-time, event-triggered storm surge forecasting system for the state of North Carolina." *Ocean Model*, 25(3-4), 95-119.

McCuen, R. (2005). *Hydrologic Analysis and Design*, Peason Prentice Hall, Upper Saddle River, New Jersey.

Melvin, S., Seibel, D., Smith, V., Lucas, P., Frevert, W., and Nixon, J. (2012). "Iowa Drainage Guide." *Special Report*, ISU, Iowa State University, Extention and Outreach.

Menabde, M., and Sivapalan, M. (2001). "Linking space-time variability of river runoff and rainfall fields: a dynamic approach." *Adv Water Resour*, 24(9-10), 1001-1014.

Mertens, J., Stenger, R., and Barkle, G. F. (2006). "Multiobjective inverse modeling for soil parameter estimation and model verification." *Vadose Zone J*, 5(3), 917-933.

Meyles, E., Williams, A., Ternan, L., and Dowd, J. (2003). "Runoff generation in relation to soil moisture patterns in a small Dartmoor catchment, Southwest England." *Hydrol Process*, 17(2), 251-264.

Millington, R., and Quirk, J. P. (1961). "Permeability of Porous Solids." *T Faraday Soc*, 57(8), 1200-&.

Mitsch, W. J., Zhang, L., Fink, D. F., Hernandez, M. E., Altor, A. E., Tuttle, C. L., and Nahlik, A. M. (2008). "Ecological engineering of floodplains." *Ecohydrology & Hydrobiology*, 8(2–4), 139-147.

Mohanty, B. P., Ankeny, M. D., Horton, R., and Kanwar, R. S. (1994). "Spatial-Analysis of Hydraulic Conductivity Measured Using Disc Infiltrometers." *Water Resour Res*, 30(9), 2489-2498.

Mohanty, B. P., Horton, R., and Ankeny, M. D. (1996). "Infiltration and macroporosity under a row crop agricultural field in a glacial till soil." *Soil Sci*, 161(4), 205-213.

Montaldo, N., Mancini, M., and Rosso, R. (2004). "Flood hydrograph attenuation induced by a reservoir system: analysis with a distributed rainfall-runoff model." *Hydrol Process*, 18(3), 545-563.

Moriasi, D. N., Arnold, J. G., Van Liew, M. W., Bingner, R. L., Harmel, R. D., and Veith, T. L. (2007). "Model evaluation guidelines for systematic quantification of accuracy in watershed simulations." *T Asabe*, 50(3), 885-900.

Naz, B. S., Ale, S., and Bowling, L. C. (2009). "Detecting subsurface drainage systems and estimating drain spacing in intensively managed agricultural landscapes." *Agr Water Manage*, 96(4), 627-637.

NCDC, N. C. D. C. (2014). "Billion-Dollar Weather and Climate Disasters 1980-2014." *Billion Dollar Weather and Climate Disasters*, NOAA, ed.

NCRS, N. R. C. S. (2001). "Terraces: Iowa Job Sheet." USDA, United States Department of Agriculture
Des Moines, IA.

Nearing, M. A., Wei, H., Stone, J. J., Pierson, F. B., Spaeth, K. E., Weltz, M. A., Flanagan, D. C., and Hernandez, M. (2011). "A Rangeland Hydrology and Erosion Model." *T Asabe*, 54(3), 901-908.

Nikolopoulos, E. I., Anagnostou, E. N., Borga, M., Vivoni, E. R., and Papadopoulos, A. (2011). "Sensitivity of a mountain basin flash flood to initial wetness condition and rainfall variability." *J Hydrol*, 402(3-4), 165-178.

Nishat, S., Guo, Y., and Baetz, B. W. (2010). "Antecedent soil moisture conditions of different soil types in South-western Ontario, Canada." *Hydrol Process*, 24(17), 2417-2424.

NRCS (2014). "Gridded Soil Survey Geographic (gSSURGO)." United States Department of Agriculture, Natural Resources Conservation Service, Database for the United States of America and the Territories, Commonwealths, and Island Nations served by the USDA-NRCS.

NRCS, N. R. C. S. (2002). "USLE Erosion Prediction." *Section I, FOTG*, USDA, United States Department of Agriculture.

NRCS, N. R. C. S. (2004). "Soil Moisture/Soil Temperature Pilot Project." USDA, United States Department of Agriculture.

NRCS, N. R. C. S. (2011). "Part 650 (Engineering Field Handbook) Chapter 8." *Terraces*, USDA, United States Department of Agriculture.

NRCS, N. R. C. S. (2012). "Rapid Watershed Assesment Upper Cedar (MN/IA) HUC: 07080201." T. U. S. D. o. A. (USDA), ed.

NRCS, N. R. C. S. (2014). "Terrace: Code 600." *Natural Resource Conservation Service Conservation Practice Standard*, NRCS, Natural Resources Conservation Service, Iowa.

NRCS, N. R. C. S. (2015). "Maximum Terrace Spacing Charts." *Iowa Amendments to the Engineering Field Handbook*.

NRCS, N. R. C. S. (2015). "Soil Climate Analysis Network (SCAN)." USDA, United States Department of Agriculture, National Water and Climate Center.

O'Connell, E., Ewen, J., O'Donnell, G., and Quinn, P. (2007). "Is there a link between agricultural land-use management and flooding?" *Hydrol Earth Syst Sc*, 11(1), 96-107.

Ogden, F. L., and Dawdy, D. R. (2003). "Peak discharge scaling in small hortonian watershed." *J Hydrol Eng*, 8(2), 64-73.

Onstad, C. A., and Jamieson, D. G. (1970). "Modeling Effect of Land Use Modifications on Runoff." *Water Resour Res*, 6(5), 1287-&.

Opolot, E., Araya, T., Nyssen, J., Al-Barri, B., Verbist, K., and Cornelis, W. M. (2014). "EVALUATING IN SITU WATER AND SOIL CONSERVATION PRACTICES WITH A FULLY COUPLED, SURFACE/SUBSURFACE PROCESS-BASED HYDROLOGICAL MODEL IN TIGRAY, ETHIOPIA." *Land Degradation & Development*, n/a-n/a.

Or, D., and Wraith, J. M. (1999). "Temperature effects on soil bulk dielectric permittivity measured by time domain reflectometry: A physical model (vol 35, pg 371, 1999)." *Water Resour Res*, 35(7), 2283-2283.

Packman, J. C., and Kidd, C. H. R. (1980). "A Logical Approach to the Design Storm Concept." *Water Resour Res*, 16(6), 994-1000.

Panday, S., and Huyakorn, P. S. (2004). "A fully coupled physically-based spatially-distributed model for evaluating surface/subsurface flow." *Adv Water Resour*, 27(4), 361-382.

Pathiraja, S., Westra, S., and Sharma, A. (2012). "Why continuous simulation? The role of antecedent moisture in design flood estimation." *Water Resour Res*, 48.

Pebesma, E. J., Switzer, P., and Loague, K. (2005). "Error analysis for the evaluation of model performance: rainfall-runoff event time series data." *Hydrol Process*, 19(8), 1529-1548.

Penman, H. L. (1948). "Natural Evaporation from Open Water, Bare Soil and Grass." *Proc R Soc Lon Ser-A*, 193(1032), 120-&.

Penna, D., Tromp-van Meerveld, H. J., Gobbi, A., Borga, M., and Dalla Fontana, G. (2011). "The influence of soil moisture on threshold runoff generation processes in an alpine headwater catchment." *Hydrol Earth Syst Sc*, 15(3), 689-702.

Perez-Pedini, C., Limbrunner, J. F., and Vogel, R. M. (2005). "Optimal location of infiltration-based best management practices for storm water management." *J Water Res Pl-Asce*, 131(6), 441-448.

Perez, A. J., Abrahao, R., Causape, J., Cirpka, O. A., and Burger, C. M. (2011). "Simulating the transition of a semi-arid rainfed catchment towards irrigation agriculture." *J Hydrol*, 409(3-4), 663-681.

Perica, S., Martin, D., Pavlocic, S., Roy, I., St. Laurent, M., Trypaluk, C., Unruh, D., Yekta, M., and Bonnin, G. (2013). "NOAA Atlas 14: Precipitation-Frequency Atlas of the United States ", NOAA, Silver Spring, Maryland.

Peterson, T. C., Heim, R. R., Hirsch, R., Kaiser, D. P., Brooks, H., Diffenbaugh, N. S., Dole, R. M., Giovannettone, J. P., Guirguis, K., Karl, T. R., Katz, R. W., Kunkel, K., Lettenmaier, D., McCabe, G. J., Paciorek, C. J., Ryberg, K. R., Schubert, S., Silva, V. B. S., Stewart, B. C., Vecchia, A. V., Villarini, G., Vose, R. S., Walsh, J., Wehner, M., Wolock, D., Wolter, K., Woodhouse, C. A., and Wuebbles, D. (2013). "Monitoring and Understanding Changes in Heat Waves, Cold Waves, Floods, and Droughts in the United States: State of Knowledge." *B Am Meteorol Soc*, 94(6), 821-834.

Petrucci, G., Rioust, E., Deroubaix, J. F., and Tassin, B. (2013). "Do stormwater source control policies deliver the right hydrologic outcomes?" *J Hydrol*, 485, 188-200.

Pfletschinger, H., Prommel, K., Schuth, C., Herbst, M., and Engelhardt, I. (2014). "Sensitivity of Vadose Zone Water Fluxes to Climate Shifts in Arid Settings." *Vadose Zone J*, 13(1).

Pilgrim, D. H., and Cordery, I. (1973). "Rainfall Temporal Patterns for Design Flood Estimation." *Eos T Am Geophys Un*, 54(11), 1081-1082.

Ponce, V. M., and Hawkins, R. H. (1996). "Runoff Curve Number: Has It Reached Maturity?" *J Hydrol Eng*, 1(1), 11-19.

Prior, J. C., NetLibrary Inc., and Iowa. Department of Natural Resources. (1991). "Landforms of Iowa." *A Bur oak original*, University of Iowa Press for the Iowa Dept. of Natural Resources,, Iowa City, xi, 153 p.

Radatz, T. F., Thompson, A. M., and Madison, F. W. (2013). "Soil moisture and rainfall intensity thresholds for runoff generation in southwestern Wisconsin agricultural watersheds." *Hydrol Process*, 27(25), 3521-3534.

Rasoulzadeh, A., and Yaghoubi, A. (2014). "Inverse modeling approach for determining soil hydraulic properties as affected by application of cattle manure." *Int J Agr Biol Eng*, 7(2), 27-35.

Ravazzani, G., Gianoli, P., Meucci, S., and Mancini, M. (2014). "Assessing Downstream Impacts of Detention Basins in Urbanized River Basins Using a Distributed Hydrological Model." *Water Resour Manag*, 28(4), 1033-1044.

Rihani, J. F., Maxwell, R. M., and Chow, F. K. (2010). "Coupling groundwater and land surface processes: Idealized simulations to identify effects of terrain and subsurface heterogeneity on land surface energy fluxes." *Water Resour Res*, 46.

Rittenburg, R. A., Squires, A. L., Boll, J., Brooks, E. S., Easton, Z. M., and Steenhuis, T. S. (2015). "Agricultural Bmp Effectiveness and Dominant Hydrological Flow Paths: Concepts and a Review." *J Am Water Resour As*, 51(2), 305-329.

Rosso, R. (1994). "An introduction to spatially distributed modeling of basin response." *Advances in Distributed Hydrology*, 3-30.

Rozemeijer, J. C. (2015). "Description of PEST calibration of Equivelnt Medium Parameters, for a field site." N. W. Thomas, ed.

Rozemeijer, J. C., van der Velde, Y., McLaren, R. G., van Geer, F. C., Broers, H. P., and Bierkens, M. F. P. (2010). "Integrated modeling of groundwater-surface water interactions in a tile-drained agricultural field: The importance of directly measured flow route contributions." *Water Resour Res*, 46.

Rozemeijer, J. C., van der Velde, Y., van Geer, F. C., Bierkens, M. F. P., and Broers, H. P. (2010). "Direct measurements of the tile drain and groundwater flow route contributions to surface water contamination: From field-scale concentration patterns in groundwater to catchment-scale surface water quality." *Environ Pollut*, 158(12), 3571-3579.

Sahu, R. K., Mishra, S. K., Eldho, T. I., and Jain, M. K. (2007). "An advanced soil moisture accounting, procedure for SCS curve number method." *Hydrol Process*, 21(21), 2872-2881.

Sanford, W. E., and Selnick, D. L. (2013). "Estimation of Evapotranspiration Across the Conterminous United States Using a Regression With Climate and Land-Cover Data." *J Am Water Resour As*, 49(1), 217-230.

Santanello, J. A., Peters-Lidard, C. D., Garcia, M. E., Mocko, D. M., Tischler, M. A., Moran, M. S., and Thoma, D. P. (2007). "Using remotely-sensed estimates of soil moisture to infer soil texture and hydraulic properties across a semi-arid watershed." *Remote Sens Environ*, 110(1), 79-97.

Schaap, M. G., and Leij, F. J. (1998). "Database-related accuracy and uncertainty of pedotransfer functions." *Soil Sci*, 163(10), 765-779.

Schaap, M. G., and Leij, F. J. (1998). "Using neural networks to predict soil water retention and soil hydraulic conductivity." *Soil Till Res*, 47(1-2), 37-42.

Schaap, M. G., and Leij, F. J. (2000). "Improved prediction of unsaturated hydraulic conductivity with the Mualem-van Genuchten model." *Soil Sci Soc Am J*, 64(3), 843-851.

Schaap, M. G., Leij, F. J., and van Genuchten, M. T. (1998). "Neural network analysis for hierarchical prediction of soil hydraulic properties." *Soil Sci Soc Am J*, 62(4), 847-855.

Schaap, M. G., Leij, F. J., and van Genuchten, M. T. (2001). "ROSETTA: a computer program for estimating soil hydraulic parameters with hierarchical pedotransfer functions." *J Hydrol*, 251(3-4), 163-176.

Schilling, K., and Zhang, Y. K. (2004). "Baseflow contribution to nitrate-nitrogen export from a large, agricultural watershed, USA." *J Hydrol*, 295(1-4), 305-316.

Schilling, K. E., and Helmers, M. (2008). "Effects of subsurface drainage tiles on streamflow in Iowa agricultural watersheds: Exploratory hydrograph analysis." *Hydrol Process*, 22(23), 4497-4506.

Schilling, K. E., Jha, M. K., Zhang, Y. K., Gassman, P. W., and Wolter, C. F. (2008). "Impact of land use and land cover change on the water balance of a large agricultural watershed: Historical effects and future directions." *Water Resour Res*, 44.

Schilling, K. E., Jindal, P., Basu, N. B., and Helmers, M. J. (2012). "Impact of artificial subsurface drainage on groundwater travel times and baseflow discharge in an agricultural watershed, Iowa (USA)." *Hydrol Process*, 26(20), 3092-3100.

Schilling, K. E., and Libra, R. D. (2003). "Increased baseflow in Iowa over the second half of the 20th century." *J Am Water Resour As*, 39(4), 851-860.

Schlesinger, W. H., and Jasechko, S. (2014). "Transpiration in the global water cycle." *Agr Forest Meteorol*, 189, 115-117.

Sciuto, G., and Diekkruger, B. (2010). "Influence of Soil Heterogeneity and Spatial Discretization on Catchment Water Balance Modeling." *Vadose Zone J*, 9(4), 955-969.

Secchi, S., Gassman, P. W., Jha, M., Kurkalova, L., Feng, H. H., Campbell, T., and Kling, C. L. (2007). "The cost of cleaner water: Assessing agricultural pollution reduction at the watershed scale." *J Soil Water Conserv*, 62(1), 10-21.

Seck, A., Welty, C., and Maxwell, R. M. (2015). "Spin-up behavior and effects of initial conditions for an integrated hydrologic model." *Water Resour Res*, 51(4), 2188-2210.

Seo, H. H. (1996). "Hydraulic properties of Quaternary stratigraphic units in the Walnut Creek watershed." M.S., Iowa State University.

Seyfried, M. S., Grant, L. E., Du, E., and Humes, K. (2005). "Dielectric loss and calibration of the hydra probe soil water sensor." *Vadose Zone J*, 4(4), 1070-1079.

Shen, Z. Y., Hong, Q., Chu, Z., and Gong, Y. W. (2011). "A framework for priority non-point source area identification and load estimation integrated with APPI and PLOAD model in Fujiang Watershed, China." *Agr Water Manage*, 98(6), 977-989.

Simonovic, S. P. (1992). "Reservoir Systems-Analysis - Closing Gap between Theory and Practice." *J Water Res Pl-Asce*, 118(3), 262-280.

Sims, J. T., Simard, R. R., and Joern, B. C. (1998). "Phosphorus loss in agricultural drainage: Historical perspective and current research." *J Environ Qual*, 27(2), 277-293.

Singh, R., Helmers, M. J., and Qi, Z. M. (2006). "Calibration and validation of DRAINMOD to design subsurface drainage systems for Iowa's tile landscapes." *Agr Water Manage*, 85(3), 221-232.

Singh, V. P., and Woolhiser, D. A. (2002). "Mathematical modeling of watershed hydrology." *J Hydrol Eng*, 7(4), 270-292.

Skaggs, R. W., Breve, M. A., and Gilliam, J. W. (1994). "Hydrologic and Water-Quality Impacts of Agricultural Drainage." *Crit Rev Env Sci Tec*, 24(1), 1-32.

Soltani, A., and Hoogenboom, G. (2007). "Assessing crop management options with crop simulation models based on generated weather data." *Field Crop Res*, 103(3), 198-207.

Squillace, P., Caldwell, J., Schulmeyer, P., and Harvey, C. (1996). "Movement of Agricultural Chemicals Between Surface Water and Ground Water, Lower Cedar River Basin, Iowa." *Water Supply Paper*.

Stamm, C., Sermet, R., Leuenberger, J., Wunderli, H., Wydler, H., Fluhler, H., and Gehre, M. (2002). "Multiple tracing of fast solute transport in a drained grassland soil." *Geoderma*, 109(3-4), 245-268.

Steffens, K. J., and Franz, K. J. (2012). "Late 20th-century trends in Iowa watersheds: an investigation of observed and modelled hydrologic storages and fluxes in heavily managed landscapes." *Int J Climatol*, 32(9), 1373-1391.

Stillman, J. S., Haws, N. W., Govindaraju, R. S., and Rao, P. S. C. (2006). "A semi-analytical model for transient flow to a subsurface tile drain." *J Hydrol*, 317(1-2), 49-62.

Strauch, M., Lima, J. E. F. W., Volk, M., Lorz, C., and Makeschin, F. (2013). "The impact of Best Management Practices on simulated streamflow and sediment load in a Central Brazilian catchment." *J Environ Manage*, 127, S24-S36.

Strock, J. S., Kleinman, P. J. A., King, K. W., and Delgado, J. A. (2010). "Drainage water management for water quality protection." *J Soil Water Conserv*, 65(6), 131a-136a.

Therrien, R., McLaren, R., Sudicky, E. A., and Panday, S. (2013). "HydroGeoSphere: A three-dimensional nuermical model describing fully-integrated subsurface and surface flow and solute transport: User's guide." Groundwater Simulations Group, Waterloo, ON, Canada.

Therrien, R., and Sudicky, E. A. (1996). "Three-dimensional analysis of variably-saturated flow and solute transport in discretely-fractured porous media." *J Contam Hydrol*, 23(1-2), 1-44.

Therrien, R., and Sudicky, E. A. (2000). "Well bore boundary conditions for variably saturated flow modeling." *Adv Water Resour*, 24(2), 195-201.

Tomer, M. D., Meek, D. W., Jaynes, D. B., and Hatfield, J. L. (2003). "Evaluation of nitrate nitrogen fluxes from a tile-drained watershed in central Iowa." *J Environ Qual*, 32(2), 642-653.

Tomer, M. D., Meek, D. W., and Kramer, L. A. (2005). "Agricultural practices influence flow regimes of headwater streams in western Iowa." *J Environ Qual*, 34(5), 1547-1558.

Tuppad, P., Kannan, N., Srinivasan, R., Rossi, C. G., and Arnold, J. G. (2010). "Simulation of Agricultural Management Alternatives for Watershed Protection." *Water Resour Manag*, 24(12), 3115-3144.

Tuppad, P., Santhi, C., Srinivasan, R., and Williams, J. R. (2009). "Best Management Practice (BMP) Verification using Observed Water Quality Data and Watershed Planning or Implementation of BMPs " *TSSWCB PROJECT 04-18*.

US-EPA, U. S. E. P. A. (2012). "Climate Change Indicators in the United States, 2012."

Vache, K. B., Eilers, J. M., and Santelmann, M. V. (2002). "Water quality modeling of alternative agricultural scenarios in the US corn belt." *J Am Water Resour As*, 38(3), 773-787.

van den Eertwegh, G. A. P. H., Nieber, J. L., de Louw, P. G. B., van Hardeveld, H. A., and Bakkum, R. (2006). "Impacts of drainage activities for clay soils on hydrology and solute loads to surface water." *Irrig Drain*, 55(3), 235-245.

van der Velde, Y., Rozemeijer, J. C., de Rooij, G. H., van Geer, F. C., and Broers, H. P. (2010). "Field-Scale Measurements for Separation of Catchment Discharge into Flow Route Contributions." *Vadose Zone J*, 9(1), 25-35.

Van Genuchten, M. T. (1980). "A Closed-Form Equation for Predicting the Hydraulic Conductivity of Unsaturated Soils." *Soil Sci Soc Am J*, 44(5), 892-898.

VanderKwaak, J. E., and Loague, K. (2001). "Hydrologic-response simulations for the R-5 catchment with a comprehensive physics-based model." *Water Resour Res*, 37(4), 999-1013.

Vellidis, G., Smith, M. C., Leibowitz, S. G., Ainslie, W. B., and Pruitt, B. A. (2003). "Prioritizing wetland restoration for sediment yield reduction: A conceptual model." *Environ Manage*, 31(2), 301-312.

Verbist, K. M. J., Pierreux, S., Cornelis, W. M., McLaren, R., and Gabriels, D. (2012). "Parameterizing a Coupled Surface-Subsurface Three-Dimensional Soil Hydrological Model to Evaluate the Efficiency of a Runoff Water Harvesting Technique." *Vadose Zone J*, 11(4).

Verma, A. K., Cooke, R. A., and Wendte, L. (1996). "Mapping subsurface drainage systems with color infrared aerial photographs." *American Water Resource Association's 32nd Annual Conference and Symposium "GIS and Water Resources"*Ft. Lauderdale, Florida

Viglione, A., Merz, R., and Bloschl, G. (2009). "On the role of the runoff coefficient in the mapping of rainfall to flood return periods." *Hydrol Earth Syst Sc*, 13(5), 577-593.

Villarini, G., Smith, J. A., Baeck, M. L., and Krajewski, W. F. (2011). "Examining Flood Frequency Distributions in the Midwest U.S." *J Am Water Resour As*, 47(3), 447-463.

Villarini, G., Smith, J. A., Baeck, M. L., Vitolo, R., Stephenson, D. B., and Krajewski, W. F. (2011). "On the frequency of heavy rainfall for the Midwest of the United States." *J Hydrol*, 400(1-2), 103-120.

Villarini, G., Smith, J. A., and Vecchi, G. A. (2013). "Changing Frequency of Heavy Rainfall over the Central United States." *J Climate*, 26(1), 351-357.

Villarini, G., and Strong, A. (2014). "Roles Of climate and agricultural practices in discharge changes in an agricultural watershed in Iowa." *Agr Ecosyst Environ*, 188, 204-211.

Vivoni, E. R., Entekhabi, D., Bras, R. L., and Ivanov, V. Y. (2007). "Controls on runoff generation and scale-dependence in a distributed hydrologic model." *Hydrol Earth Syst Sc*, 11(5), 1683-1701.

Vrugt, J. A., Schoups, G., Hopmans, J. W., Young, C., Wallender, W. W., Harter, T., and Bouten, W. (2004). "Inverse modeling of large-scale spatially distributed vadose zone properties using global optimization." *Water Resour Res*, 40(6).

Wang, L., and Yu, J. H. (2012). "Modelling detention basins measured from high-resolution light detection and ranging data." *Hydrol Process*, 26(19), 2973-2984.

Wang, L. X., Niu, S. L., Good, S. P., Soderberg, K., McCabe, M. F., Sherry, R. A., Luo, Y. Q., Zhou, X. H., Xia, J. Y., and Caylor, K. K. (2013). "The effect of warming on grassland evapotranspiration partitioning using laser-based isotope monitoring techniques." *Geochim Cosmochim Ac*, 111, 28-38.

Wischmeier, W. H., and Smith, D. D. (1978). "Predicting Rainfall Erosion Losses - A Guide to Conservation Planning." *Agriculture Handbook No. 537*, USDA, United States Department of Agriculture.

Woodhouse, C. A., and Overpeck, J. T. (1998). "2000 years of drought variability in the central United States." *B Am Meteorol Soc*, 79(12), 2693-2714.

Wu, W. R., and Dickinson, R. E. (2004). "Time scales of layered soil moisture memory in the context of land-atmosphere interaction." *J Climate*, 17(14), 2752-2764.

Yang, Q., Meng, F. R., Zhao, Z. Y., Chow, T. L., Benoy, G., Rees, H. W., and Bourque, C. P. A. (2009). "Assessing the impacts of flow diversion terraces on stream water and sediment yields at a watershed level using SWAT model." *Agr Ecosyst Environ*, 132(1-2), 23-31.

Zhang, Z. Q., Wang, S. P., Sun, G., McNulty, S. G., Zhang, H. Y., Li, J. L., Zhang, M. L., Klaghofer, E., and Strauss, P. (2008). "Evaluation of the MIKE SHE model for application in the Loess Plateau, China." *J Am Water Resour As*, 44(5), 1108-1120.

Zhou, X., Al-Kaisi, M., and Helmers, M. J. (2009). "Cost effectiveness of conservation practices in controlling water erosion in Iowa." *Soil Till Res*, 106(1), 71-78.

Zucker, L. A., and Brown, L. C. (1998). "Agricultural Drainage: Water Quality Impacts and Subsurface Drainage Studies in the Midwest." *Ohio State University Extension Bulletin 871*, T. O. S. University, ed.Columbus, Ohio, USA.